Dissertation
submitted to the
Combined Faculties for the Natural Sciences and for Mathematics
of the Ruperto-Carola University of Heidelberg, Germany
for the degree of
Doctor of Natural Sciences

presented by
M.Sc. Oskar Staufer
born in: Wiesbaden, Germany
oral examination date: 28.07.2020

Bottom-up Assembly of Functional Extracellular Vesicles – Implications for Synthetic Biology and Biomedical Applications

Referees: Prof. Dr. Hilmar Bading

Prof. Dr. Joachim P. Spatz

Danksagung

Diese Arbeit ist nicht lediglich das Produkt meiner eigenen Anstrengungen, sondern wäre ohne zahlreiche und hingebungsvolle Unterstützung von Kollegen, Freunden und Kollaborateuren nicht möglich gewesen.

Ich möchte mich daher zunächst bei Prof. Dr. Joachim Spatz bedanken, der mich nun seit vielen Jahren in meiner wissenschaftlichen Laufbahn begleitet und unterstützt. In dutzenden anregenden Diskussionen mit ihm, formten sich viele der hier umgesetzten Ideen. Seit Beginn meines Studiums bot er mir die Möglichkeit in seinem Arbeitskreis meiner wissenschaftlichen Neugier mit großer Freiheit nach zu gehen und stand mir bei wissenschaftlichen Entscheidungen mit Rat zur Seite.

Weiterhin möchte ich Prof. Dr. Hilmar Bading dafür danken, dass er bereitwillig die Begutachtung meiner Arbeit übernahm. Er und zahlreiche Mitarbeiter seines Arbeitskreises boten mir in den Jahren meines Studiums und der Doktorarbeit eine heimische Atmosphäre sowie Inspiration für meine Forschungsarbeiten.

Auch möchte ich mich bei Prof. Dr. Stefan Wölfl, Prof. Dr. Michael Boutros und Dr. Alessia Ruggieri dafür bedanken, dass Sie bereitwillig als Mitglied in meinem thesis advisory comittee beziehungsweise als Prüfer/in in meiner Verteidigung teilgenommen haben.

I would like to especially thank Dr. Ilia Platzman, who supervised my PhD work in the last years. Only through intensive hours of discussion and his precise, constructive and on-point criticism, my PhD work was made possible. I´m deeply grateful that he always provided me with elaborate feedback on my ideas, concepts and plans. It was a great pleasure to closely work together with him as within the last three years he formed me to become a better scientist.

I would also like to thank Omer Adir as well as Prof. Dr. Avi Schroeder and his whole laboratory at the Isreal Institute of Technology for hosting me during the winter of 2019 for our collaborative research work.

Zahlreiche Experimente wären ohne die Hilfe von Andrea Hellwig (Elektronenmikroskopie), Sebastian Fabritz (Massenspektrometrie), Ulrike Mersdorf (Elektronenmikroskopie), Franziska Dietrich (organotypische Hautmodelle) Silvia Antona (Durchflusszytometrie), Martin Schröter (Surfactantsynthese) und Sabine Grünwald (Zellkultur) nicht möglich gewesen. Hiermit möchte ich mich herzlich für Eure Arbeit und Engagement bedanken.

Mein besonderer Dank gilt auch den Bachelor- und Masterstudenten, Dennis Zhang, Julius Fichtler, Julia Csatari, Xingyi Cheng und Jochen Hernandez, die mich während meiner Arbeite in den vergangenen Jahren begleitet haben. Mit viel Freude konnte ich in enger Zusammenarbeit mit Ihnen wissenschaftlich wachsen. Für die kritischen Kommentare zu meiner Thesis und für das sorgfältige Korrekturlesen meiner Doktorarbeit möchte ich mich außerdem bei Isabelle Kajzar, Jochen Hernandez und Dr. Ilia Platzman bedanken.

Dem gesamten Arbeitskreis von Prof. Joachim Spatz und insbesondere der Forschungsgruppe für Mikrofluidik gilt mein besonderer Dank. Ich habe hier in den Jahren meines Studiums in Heidelberg eine geistreiche Arbeitsatmosphäre gefunden, welche mich stets antrieb meine wissenschaftlichen Interessen zu verfolgen. Ich möchte mich auch bei der Administration sowie bei den technischen Abteilungen und Einrichtungen des Max-Planck-Instituts für medizinische Forschung bedanken, welche zahlreiche meiner Arbeiten sehr unbeschwert gestalteten.

Während all meiner bisherigen akademischen und wissenschaftlichen Tätigkeiten in und außerhalb Heidelbergs, habe ich viele Menschen kennen lernen dürfen, welche mich in meiner wissenschaftlichen Entwicklung maßgeblich geprägt haben. Deshalb möchte ich mich insbesondere bei Dr. Amin Rustom, Drs. Katharina und Dominik Niopek, Dr. Kerstin Göpfrich, Prof. Dr. Imre Berger, Dr. Dimitris Missirlis sowie Dr. Katrin Platzer und dem gesamten Heidelberger Life Science Lab für zahlreiche anregende Gespräche sowie für ihre Unterstützung bei wissenschaftlichen und nicht wissenschaftlichen Themen bedanken.

Mein größter Dank gilt jedoch meiner Freundin Isabelle Kajzar für ihre immerwährende liebevolle Zuwendung, sowie meinen Eltern Petra und Gerhard Staufer für ihre hingebungsvolle lebenslange Unterstützung.

Contributions

If not disclosed in the specific passages of the materials and methods section, experiments were carried out by myself under the supervision of Dr. Ilia Platzman and Prof. Dr. Joachim Spatz at the Max Planck Institute for Medical Research.
The concept for GUV-based baculovirus delivery was initiated by Prof. Dr. Imre Berger, Prof. Dr. Joachim Spatz and Dr. Ilia Platzman. Based on this, I designed the corresponding experiments together with Dr. Ilia Platzman and Prof. Dr. Joachim Spatz. The dynamic light scattering measurements of SUV and GUV zeta-potentials were partially performed by Dennis Zhang under my supervision.

I designed the concept of fully-synthetic extracellular vesicles and their application for wound healing. The experimental validations of the concept were designed and elaborated together with and under supervision of Dr. Ilia Platzman and Prof. Joachim Spatz. RNA sequencing, RNA-extraction, library preparation, sequencing, sequence alignment and data post-processing was performed by Genewiz GmbH (Germany). The data analysis was performed by myself. I designed the concept of functional intracellular synthetic organelles and performed the according experiments and analysis.

All surfactants used in this study were either purchased from RUN Biotechnologies or synthesized by Dr. Jan Willi-Janiesch or Martin Schröter. The preparation of baculovirus samples was performed by Martin Pelosse in the laboratory of Prof. Dr. Imre Berger. All animal work needed for the establishment of primary hippocampal cultures was performed by Iris Bünzli-Ehret in the laboratory of Prof. Dr. Hilmar Bading.

The funding for all the facilities and the experimental setups as well as for publication of the results was provided by Prof. Dr. Joachim Spatz and the Max Planck Institute for Medical Research. My research work was further supported by fellowships from the Heidelberg Biosciences International Graduate School, the Max Planck School Matter to Life and the Elisabeth Meurer Foundation awarded to me as well as by the Young Investigator Award of the International Society of Extracellular Vesicles.

Publications

Parts of the data and experiments leading to the results presented in this thesis as well as other research activities pursued during my PhD work at the Max Planck Institute for Medical Research have been published in peer-reviewed journals. Any peer reviewed publications currently under revision but not accepted for publication yet are not listed.

1. **Staufer O.**, Schröter M., Platzman I., Spatz J.P (2020) Bottom-up assembly of functional intracellular synthetic organelles by droplet-based microfluidics. *Small* https://doi.org/10.1002/smll.201906424

2. Luo R., Pashapour S., **Staufer O.**, Platzman I., Spatz JP. (2020) Polymer-Based Porous Microcapsules as Bacterial Traps. *Advanced Functional Materials* https://doi.org/10.1002/adfm.201908855

3. Göpfrich K., Haller B., **Staufer O.**, Dreher Y., Mersdorf U., Platzman I., Spatz JP. (2019) One-Pot Assembly of Complex Giant Unilamellar Vesicle-Based Synthetic Cells. *ACS Synthetic Biology* 17;8(5)

4. **Staufer O.**, Weber S., Bengtson CP., Bading H., Rustom A., Spatz JP. (2019) Adhesion stabilized en masse intracellular electrical recordings from multicellular assemblies. *Nano Letters* 8;19(5)

5. **Staufer O.**, Hernandez B JE., Rustom A. (2018) Protease-resistant cell meshworks: An indication of membrane nanotube-based syncytia formation. *Experimental Cell Research* 15;372(2)

The following publications relate to research I performed prior to my PhD studies:

1. Niopek K., Üstünel BE., Seitz S., Sakurai M., Zota A., Mattijssen F., Wang X., Sijmonsma T., Feuchter Y., Gail AM., Leuchs B., Niopek D., **Staufer O.**, Brune M., Sticht C., Gretz N., Müller- Decker K., Hammes HP., Nawroth P., Fleming T., Conkright MD., Blüher M., Zeigerer A., Herzig S., Berriel Diaz M. (2017) A Hepatic GAbp-AMPK Axis Links Inflammatory Signaling to Systemic Vascular Damage. *Cell Reports* 8:20(6)

2. **Staufer O.**, Weber S., Bengston CP., Bading H., Spatz JP., Rustom A. (2016) Functional fusion of living systems with synthetic electrode interfaces. *Beilstein Journal of Nanotechnology* 7, 296- 301

Parts of this thesis have been presented as posters and oral presentations in the following symposia and conferences:

1. International Conference of the SFB1036 Networks of Cellular surveillance mechanisms, Heidelberg (Germany), 22.-24. October 2018 (Poster)

2. Max-Planck Croucher Symposium: Matter to Life, Okinawa (Japan), 19.-21. November 2019 (presentation)

3. Materials Research Society Fall Meeting 2019, Boston (USA), 1.-6. December 2019 (presentation)

4. Spring Meeting of the German Society of Extracellular Vesicles, Frankfurt (Germany), 5.-6. March 2020 (presentation)

5. WebEVTalks, International online Seminar, 7. May 2020 (presentation)

6. Annual Meeting of the International Society of Extracellular Vesicles (online seminar), 20.-22. July 2020

Two European patent-application related to this work have been filled:

1. EP Application No. EP 19 218 881.1. on “Microfluidic production of biofunctionalized giant unilamellar vesicles for targeted intracellular cargo delivery”

2. EP Application No. EP 20 155 012.6. in “Bottom-up assembly of synthetic extracellular vesicles

Abstract

Formation of lipid-based compartments is a distinguishing feature of eukaryotic life forms. These compartments play a crucial role in orchestrating independent and self-contained metabolic, signalling or synthesis processes. Moreover, cell-derived lipid compartments, like extracellular vesicles (EVs), have been shown to be essential for intercellular signalling and are involved in a wide variety of disease states. Although attaining a holistic understanding of EV-based communication is a compelling goal, the extensive molecular and structural complexity of these vesicles as well as a lack of reliable EV isolation techniques, have impaired detailed mechanistic insights. Inspired by bottom-up synthetic biology principles, the central goal of my interdisciplinary research was the development of a bio-inspired EV model system, which serves as a platform to study EV-based intercellular signalling and empowers novel EV-inspired therapeutics.

In this thesis, I present two major methodologies developed for the controlled high-throughput assembly of synthetic vesicles. First, I describe a droplet-based microfluidic approach for the production of giant unilamellar vesicles (GUVs) with well-controlled biophysical and biochemical properties. I report on systematic investigations of GUV interactions with living cells and present concepts on how fine-tuning of the vesicles surface characteristics can be applied for targeted cellular delivery of macromolecular cargos. Moreover, I show how these vesicles can be reconceptualised as synthetic organelles, functioning within living cells and providing them with synthetic functionalities. Based on these fundamental characterizations, in the second part of my thesis, I present a complementary and quantitative approach for the sequential bottom-up assembly of fully synthetic EVs (fsEVs). To exemplify the application of fsEVs for new therapeutic concepts, I show that they exert analogous functionalities to naturally occurring wound healing EVs. Furthermore, by combining the fsEV technology with whole-transcriptome analysis, I systematically decode the synergistic functionalities between individual EV components. This approach enabled me to perform an analytical dissection of the associated EV signalling processes mediated by tetraspanin proteins.

Bioinspired and biocompatible synthetic compartments with precisely controllable biophysical and biochemical properties are desirable tools for a wide range of living and synthetic cells research. This study makes it tempting to view EV-like compartments in a

broader perspective. For example, they have great application potential as on-demand drug delivery systems, paving the way for hitherto impossible approaches towards administration of advanced cargos such as microparticles, viruses or synthetic organelles. Moreover, I anticipate that the highly controlled assembly of fsEVs will provide a robust framework for innovative therapeutic applications of bottom-up assembled synthetic biological modules and will additionally allow for new insights into fundamental EV-related principles that govern cellular communication.

Zusammenfassung

Die Ausbildung lipidbasierter Kompartimente ist eines der bedeutendsten Kennzeichen eukaryotischer Lebensformen. Diese Kompartimente spielen eine zentrale Rolle bei der Orchestrierung von unabhängigen und selbsterhaltenden metabolischen Prozessen in der Biosynthese und Zellkommunikation. Darüber hinaus ist bekannt, dass lipidbasierte extrazelluläre Kompartimente, wie zum Beispiel extrazelluläre Vesikel (EV), essenziell für die interzelluläre Kommunikation sind und zahlreichen pathologischen Veränderungen zu Grunde liegen. Auch wenn ein holistisches Verständnis der EV-basierten Signalweiterleitung für zahlreiche Anwendungen von fundamentaler Bedeutung ist, konnte auf Grund der außerordentlichen molekularen und strukturellen Komplexität dieser Vesikel bisher kaum detaillierte mechanistische Erkenntnisse erlangt werden. Inspiriert durch das Bottom-up Prinzip der synthetischen Biologie, war daher die Entwicklung von synthetischen EV-Imitaten das zentrale Ziel meiner interdisziplinären Forschungsarbeiten. Diese künstlichen Vesikel sollten als originalgetreue Nachahmungen natürlicher EVs zur Untersuchung von EV-basierten interzellulärer Kommunikationsmechanismen dienen und darüber hinaus neuartige EV-inspirierte Therapeutika ermöglichen.

Ich stelle in dieser Arbeit die Entwicklung zweier Technologien zur kontrollierten Hochdurchsatzproduktion von synthetischen Vesikeln vor. Zuerst präsentiere ich einen Tröpfchen-basierten mikrofluidischen Ansatz zur Herstellung von großen unilamellaren Vesikeln (GUV) mit definierbaren biophysikalischen und biochemischen Eigenschaften. Auf dieser Grundlage stelle ich eine systematische und strukturierte Untersuchung der Interaktionen dieser Vesikel mit lebenden Zellen vor und zeige Möglichkeiten zur Feinjustierung der Vesikeleigenschaften auf. Letztendlich untersuche ich ihr Potenzial zur Anwendung im gezielten Wirkstofftransport von makromolekularen Therapeutika, sowie als vollsynthetische, intrazellulär aktive Organellen. Basierend auf diesen grundlegenden Charakterisierungen präsentiere ich im zweiten Teil der Arbeit einen komplementären und quantitativen Ansatz zur sequenziellen Bottom-up Konstruktion von vollsynthetischen EVs (fsEVs, *fully-synthetic Extracellular Vesicles*). Um den therapeutischen Wert der fsEVs zu unterstreichen zeige ich außerdem, dass sie analoge Funktionalitäten zu natürlichen EVs aufweisen und verwende sie als Wirkstoffe zur Förderung der Wundheilung. Des Weiteren zeige ich durch Kombination der fsEVs-Technologie mit

Transkriptom-Analysen die systematische Dekodierung synergistischer Funktionalitäten zwischen einzelnen Proteinbestandteilen der EVs auf. Dieser Ansatz ermöglichte es mir detaillierte Analysen der Tetraspanin-basierten EV Signalprozesse durchzuführen.

Bioinspirierte und biokompatible synthetische Kompartimente mit feinjustierbaren biophysikalischen und biochemischen Eigenschaften stellen ein universelles Werkzeug für eine Vielzahl von Untersuchungen an lebenden und synthetischen Zellen dar. Diese Arbeit zeigt die Anwendung von EVs in einem breiteren Kontext. Beispielweise können EV-inspirierte Vesikel ihr Potenzial im zielgerichteten Wirkstofftransport entfalten und damit Therapieansätze, basierend auf Mikropartikeln, Viren oder synthetischen Organellen, ermöglichen. Darüber hinaus erwarte ich, dass die kontrollierte *in vitro* Konstruktion von fsEVs einen Rahmen für innovative, auf synthetischer Biologie basierende, Therapeutika bietet. Zusätzlichen könnte die fsEV-Technologie fundamental neue Einsichten in die Wirkprinzipien natürlicher EVs erlauben und somit unser Verständnis interzellulärer Kommunikationswege vertiefen.

Table of Contents

1 Introduction

1.1 Principles of intercellular communication

Intercellular communication is a pivotal requirement for correct information exchange and physiological functioning in multicellular organisms and multicellular communities. Mammalian cells can apply a plethora of different information exchange mechanisms and routs, depending on the amount of information to be transmitted, the time scale in which the transmission should proceed and the distance over which the information needs to be transferred. Spatial and temporal scales of intercellular communication can span several orders of magnitude, e.g. electric signals can be transmitted by direct intracellular coupling of adjunct cells through gap-junctions (distance of ~10^{-9} meters)(Nielsen et al., 2012), while hormones released by endocrine glands can distribute within the whole body of an organism (distance of ~1 meter) (Weiss et al., 2016). Similarly, neuronal information processing, which mostly relays on electrochemical signals that propagate through complex wired neuronal networks, allows signal exchange in the range of <10^{-6} seconds (Kress and Mennerick, 2009), while bioactive signalling peptides and proteins (e.g. antibodies) can circulate for days or weeks within the body (10^{6} - 10^{7} seconds)(Tabrizi et al., 2010). Therefore, intercellular communication routes can be classified according to their spatiotemporal mode of action.

Short-distance intercellular communication routs mostly require direct contact between the interacting cells. For example, receptor-ligand interactions at the cell-cell interface are involved in a multitude of cellular signalling processes inducing and regulating a diverse set of physiological action like ICAM-LFA1 binding in T-cell rolling on the vascular endothelium (Sigal et al., 2000), NCAM-NCAM (CD56-CD56) binding involved in directional signalling during axonal cone growth (van den Pol et al., 1986) or MHC-TCR recognition in antigen presentation between antigen presenting cells and T-cells (Rossjohn et al., 2015). Contact-depended intercellular communication is also fundamental for regulation of tensile force-distribution within multicellular assemblies, e.g. in leader-cell formation during collective epithelial migration, where local intercellular forces are integrated to coordinate global tissue dynamics (Vishwakarma et al., 2018). Cells can establish long-distance intercellular communication in a contact-dependent manner by extending cellular-protrusions that span several cell diameters, e.g. neuronal axons and dendrites that mediate electric signalling between the central nervous

system and peripheral organs (Overland et al., 2016) or by intercellular bridges termed tunnelling nanotubes that allow for direct transfer of cytoplasmic material between distant cells (Rustom et al., 2004; Staufer et al., 2018). However, also non-contact dependent long-distance intercellular communication can be established, e.g. by release of soluble signalling molecules like low-molecular weight compounds and protein-based hormones (like insulin, thyroxin, steroids or GLP1). These signalling molecules are either distributed through the blood-capillary system or passively diffuse in the extracellular environment to coordinate multicellular actions involved in inflammation (Rauch et al., 2013), metabolic-homeostasis (Warner and Mittag, 2012) or tissue remodelling (Dioufa et al., 2010). Moreover, especially prokaryotic life forms can employ non-chemical, long-distance and contact independent messengers in the form of light-pulses emitted by oxidation of luciferin in a luciferase-catalysed and ATP/ O_2 dependent reaction (Fuqua et al., 1994).

Encoding and compression of the transmitted information is also highly variable between the distinct communication forms. While axonal signal-propagation is based on digital information encoding in the form of local and temporary membrane depolarizations (action potentials), hormone-based communication mostly acts in the form of analogue signals (continuous time-varying changes in hormone levels). Moreover, several mechanisms enable for amplification and regulation of the transmitted signals, e.g. amplifying signalling cascades which involve proteolytic cleavage or phosphorylation of signalling moieties (like C3 hydrolysis in complement system signalling (Lachmann, 2009)) and voltage-gated ion channels that allow for regulation of action-potential propagation by threshold potentials (Platkiewicz and Brette, 2010).

Eventually, intercellular communication leads to specific cellular responses in the receiving cell or cell collective. These responses might be of limited duration only, like muscle contraction upon intracellular calcium release from the sarcoplasmic reticulum after depolarization of myocytes (Fearnley et al., 2011). However, manifestation of long-lasting effects after signal-propagation can occur, e.g. in the form of epigenetic and transcriptomic changes by increase of nuclear calcium in active neurons (Zhang et al., 2009) or by transfer of regulatory epigenetic elements like microRNAs through tunnelling nanotube connections (Thayanithy et al., 2014). Taken together, this demonstrates that cells live in a multi-dimensional information space, subjected to various kinds of signal-inputs *via* different “channels” originating form proximal and distant senders. These

signals are not mutually exclusive but rather set an information environment for cells which results in interdependent feedback-response loops.

As it can be seen from the examples and descriptions given above, communication lays at the heart of life. The variety of communication routs explored by organisms and cells is as multi-faceted as life itself and new mechanisms of cellular communication pathways are still discovered. One of the most controversially discussed para- and endocrine signalling routs described in the recent biological literature are extracellular vesicles (van Niel et al., 2018). These "packages" of compressed cellular information are not only expected to greatly impact on therapeutic and diagnostic procedures but also hold great potential to answer yet unsolved questions of cell biology (Kalluri and LeBleu, 2020). However, these vesicular structures of cellular origin, their biogenesis, extracellular spreading, uptake, information encoding and their relevance *in vivo* remain poorly understood and partially mysterious. This is in part because of the lack of appropriate isolation and purification techniques, their intrinsic biological variability and their similarity to other extracellular structures. Therefore, novel complementary approaches, that revise current concepts of extracellular vesicle-research are critical to disentangle the fundamental aspects of extracellular vesicle biology (Garcia-Manrique et al., 2018). If successful, such technologies will not only advance the scientific field itself but also open new horizons for the application of extracellular vesicles in diagnostic and therapeutic procedures. In future, EV-inspired liposomal drug-delivery system could be engineered which potentially surpass current liposomal carrier systems in terms of biocompatibility, delivery-efficiency, targeting or immune-tolerance (Garcia-Manrique et al., 2018).

1.2 Intercellular communication *via* extracellular vesicles

In 1983, two independent publications reported on the secretion of transferrin receptors into the extracellular space on vesicles released from maturing reticulocytes (Harding et al., 2013). These reports are widely considered as one of the first descriptions of extracellular vesicles (EVs). However, it required several decades of intense research in order to demonstrate that vesicular content released from cells into the extracellular environment is not only a mechanism to discharge cellular waste but indeed a highly regulated information-transfer mechanism employed by cells. Today, release of EVs and their enrolment in intercellular signalling has been described in species across the whole phylogenetic tree, from prokaryotic to eukaryotic and even archaea organisms. Since their

first description, over 1000 scientific studies on EVs have been published, several national and international societies have been formed (e.g. the International Society of Extracellular Vesicles (ISEV) or the German, Spanish, UK and Austrian Societies of Extracellular Vesicles) and numerous publicly-funded, open-access data banks for storage and distribution of EV-related information have been established. Moreover, in 2013 the Nobel Prize in Physiology or Medicine was jointly awarded to James Rothman, Randy Schekman and Thomas Sudhof for their studies on intracellular vesicle transport, which also provided some knowledge on EV maturation and secretion mechanism.

The term "extracellular vesicles", is a collective-term covering a broad range of water filled lipid vesicles that are enclosed by a unilamellar membrane and contain a variety of biomolecular content (e.g. nucleic acids, proteins, carbohydrates, salts or low molecular weight compounds like ATP or NADH) in their lumen (Thery et al., 2018). This term includes all kinds of lipid membranous structures released by cells like exosomes, microvesicles (MVs), microparticles, ectosomes, oncosomes, apoptotic bodies and many more. Following the ISEV definition, EVs represents "the generic term for particles naturally released from the cell that are delimited by a lipid bilayer and cannot replicate, i.e. do not contain a functional nucleus" (Thery et al., 2018). EVs can be isolated from almost all kind of bio-fluids ranging from blood-serum (Fernando et al., 2017), saliva (Michael et al., 2010) and urine (Street et al., 2017) to microbial fluid-biofilms (Chebotar et al., 2013) and cell culture supernatants (Patel et al., 2019a). When crude EV-preparation are observed by electron microscopy, several different class of vesicles can be distinguished by size: Small vesicles in the size range of 50 – 120 nm, medium-sized vesicles of approximately 1,000 nm and large vesicles of 1,000 – 5,000 nm (Figure 1a). Historically, EVs were mostly classified according to their size as exosomes (small vesicles), microvesicles (medium-sized vesicles) and apoptotic bodies (large vesicles). However, considerable overlap between these classes exist wherefore working with these entities could arise specific issues. ISEV has therefore published a position statement for minimal information required for studies of EVs and particularly recommends the usage of the term "extracellular vesicles" for all these vesicular structures in combination with further description of the EV origin, purification and molecular finger-print (e.g. surface markers like CD9, CD63 or CD81) (Thery et al., 2018).

As for now, the most reliable classification of specific EV-subsets can be achieved by considering their cellular origin. In this case, vesicles with endosomal origin are generally termed "exosomes" (Figure 1b), while plasma membrane derived vesicles are commonly referred to as "ectosomes" or "microvesicles". In practice, however, assigning an EV-preparation to a specific biogenesis-pathway is extremely challenging as most isolation and purification techniques only yield crude vesicular extracts containing severe contaminations with plasma or serum proteins, other types of microparticles like lipoproteins and various kinds of other EV-subtypes.

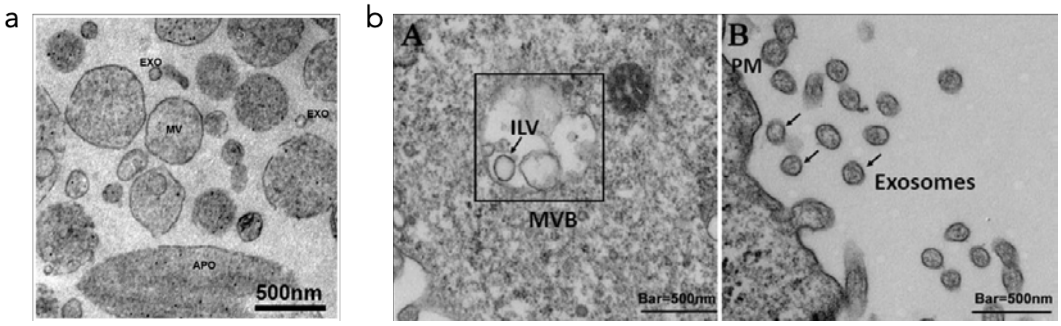

Figure 1 | Electron microscopy of extracellular vesicles. (**a**) Transmission electron microscopy of EVs isolated from conditioned THP-1 cell culture medium by ultracentrifugation. Size-based EV-subpopulations are labelled as EXO: exosomes, MW: microvesicles and APO: apoptotic bodies. Adopted with permission from (Osteikoetxea et al., 2015b). (**b**) Transmission electron microscopy of intraluminal vesicles and multivesicular bodies (left) and exosomes released by a cell into the extracellular space (right). Adopted with permission from (Wang et al., 2019a).

EVs explore several mechanisms for intercellular information transfer and mediate contact dependent (e.g. vesicle transfer at the immunological synapse) as well as contact independent (e.g. vesicles directing migration of follower cells) signalling between proximal and distant cells (Finetti et al., 2017; Kriebel et al., 2018). For instance, vesicles containing (epi-)genetic information in the form of mRNA, miRNA, tRNA or DNA, protect their intraluminal cargo from extracellular degradation and mediate intercellular transfer to recipient cells by membrane fusion or endocytotic uptake of the vesicle. However, EV do not only transfer (epi-)genetic information between cells but also function as protein presentation platforms and protein-presenting carries. For example, EVs released from multivesicular bodies (MVBs) of antigen presenting B-cells are loaded with antigen-presenting MHC II molecules which can signal to distant T-cells(Muntasell et al., 2007). Therefore, EVs can be viewed as structurally complex, compressed "packages" of information released by cells to convey homeostatic or pathological messages to their surroundings.

1.2.1 Cellular biogenesis pathways of extracellular vesicles

1.2.1.1 Biogenesis of exosomes

Exosomes originate from intraluminal vesicles (ILVs) inside endosomal compartments and mature during the process of multivesicular body (MVB) formation (van Niel et al., 2018). The formation and maturation process is based on a vastly complex protein machinery that orchestrates the accumulation and sorting of exosomal cargo and membrane components. This level of control and the sheer amount of proteins involved in exosome-formation, indicate that exosome signalling is of major importance to cells as a considerable effort is put into their correct maturation, release and uptake.

The first step in exosome maturation is the formation and sorting of cargos or membrane proteins into microdomains within MVBs, inducing inward budding and vesicle fission into the MVB lumen (Figure 2). The endosomal sorting complex required for transport (ESCRT) is a cytosolic protein complex of central importance for MVB and ILV function, as it is crucial for membrane shaping and fission (Hurley, 2008). Together with clathrin, ESCRT-0 and ESCRT-I mediate clustering of ubiquitinated transmembrane proteins into MVB microdomains and ESCRT-II and ECRT-III perform budding and fission of the vesicle membrane (van Niel et al., 2018). However, there is also experimental evidence that exosomes can form in an ESCRT-independent manner, as exosome secretion is also observed in cells depleted of specific ESCRT components (Stuffers et al., 2009). This could be based on the spontaneous generation of highly curved membrane subdomains by local accumulation of ceramides produced from sphingomyelin *via* neutral type II sphingomyelinase (Trajkovic et al., 2008). Moreover, tetraspanins, a class of membrane-spanning proteins with a conserved structure that mostly act as scaffolding and organizing elements (Termini and Gillette, 2017), together with syntenin, have been shown to mediated sorting of membrane proteins into MVB subdomains in an ESCRT-independent manner (van Niel et al., 2011). The mechanisms of exosomes formation might not only vary between individual cell types but is also likely to depend on the exosomal cargo. In particular, it has been shown that sorting of specific cargos into ILVs requires chaperones like the heat shock 70 kDa protein (HSP70) and heat shock cognate 71 kDa (HSC70)(Geminard et al., 2004), which are highly enriched in exosomal preparations compared to their cytosol of origin. Moreover, proteins post-translationally modified by ubiquitination and farnesylation have been shown to be specifically sorted into exosomes (Buschow et al., 2005; Luhtala et al., 2017). Especially the fact that exosomes can contain RNA (e.g. mRNA or miRNA) and DNA moieties is of interest for

studies focusing on intercellular communication and regulation (Thakur et al., 2014; Valadi et al., 2007). Albeit contradictive reports on this aspect exist, the mechanism and factors controlling a possibly specific sorting of nuclei acids into MVBs and subsequently into exosomes are studied intensively (Mateescu et al., 2017; Villarroya-Beltri et al., 2013). So far, several candidates that coordinate and regulated the incorporation and integration of RNAs into exosomes have been proposed: the ESCRT-II subcomplex, tetraspanin enriched microdomains, miRNA-induced silencing complex (miRISC) or argonaute 2 (Gibbings et al., 2009; Irion and St Johnston, 2007; Perez-Hernandez et al., 2013; van Niel et al., 2018).

1.2.1.2 Biogenesis of microvesicles

In contrast to exosomes, which are release through fusion of MVBs with the cells´ plasma membrane, MVs form by directed outward budding and fission of plasma membrane microdomains. As for exosomes, the initial formation of these plasma membrane subdomains involves a multitude of molecular machineries that coordinate and facilitate the local accumulation of MV components (Figure 2). Here, Ca^{2+}-dependent enzymes like aminophospholipid translocases, scramblases and calpain promote the local exposure of phosphatidylserine on the outside membrane (flipping from the inner to the outer membrane leaflet), leading to an intrinsic bending of the plasma membrane and subsequent rearrangement of cytoskeletal components under this microdomain inner membrane leaflet (Piccin et al., 2007). This eventually promotes MV budding and explains the comparably high concentrations of phosphatidylserine found in many EV preparations (Matsumura et al., 2019). However, also other lipids are enriched in MVs and are thought to be crucial for their generation and secretion by forming lipid rafts. For example, cholesterol is highly abundant in EVs and cholesterol depletion from cells by treatment with methyl-beta-cyclodextrin impairs MV release (Del Conde et al., 2005). However, the formation of such lipid microdomains appears to be necessary but not sufficient for MV biogenesis. Rather, as the activation of small GTPase from the RHO family of proteins and RHO associated protein kinases appears to be crucial for MV formation, a direct involvement of the actin cytoskeleton has been proposed (Li et al., 2012). Moreover, the localization of myosin 1a to microvilli of enterocytes has been linked to MV release, further supporting the central role of actin dynamics is MV biogenesis (McConnell et al., 2009).

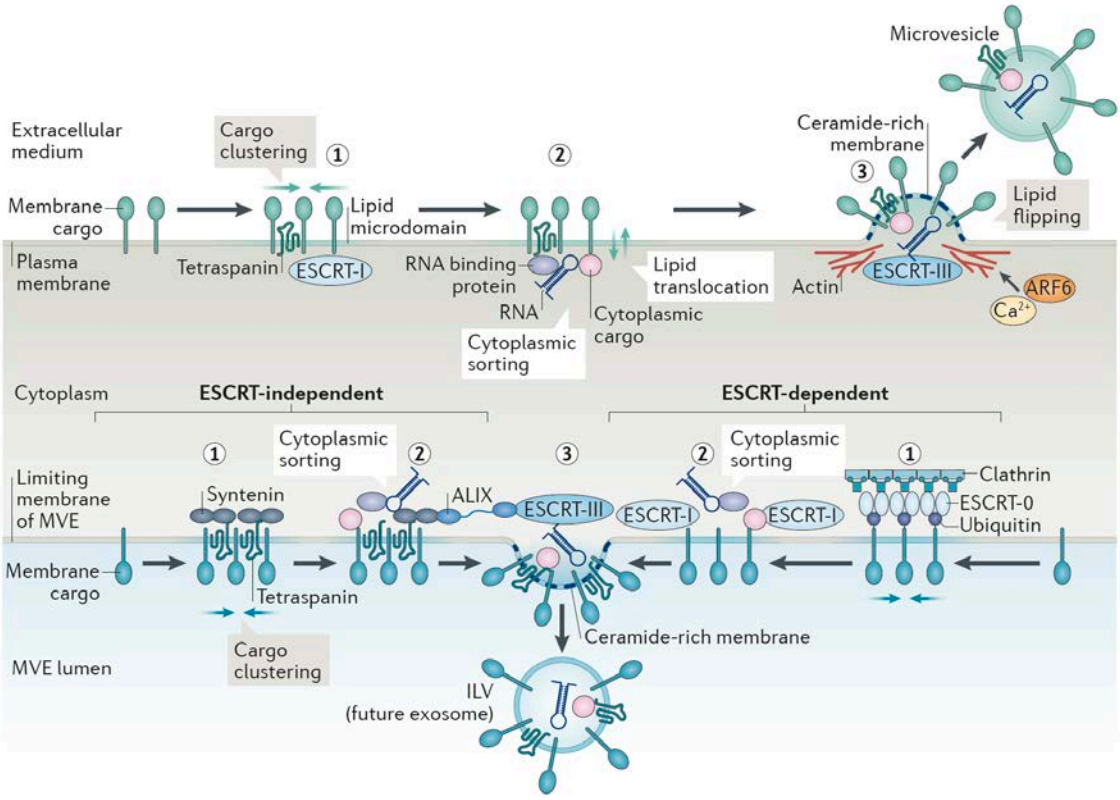

Figure 2 | Biogenesis pathways of exosomes and microvesicles. Schematic representation of microvesicles (upper panel) and exosome (lower panel) biogenesis pathways and incorporation mechanisms for membrane cargo and nucleic acids. Microvesicles biogenesis is initiated by lipid microdomain formation on the plasma membrane, followed by ESCRT-mediated cargo clustering and lipid translocation. Eventually, budding of RNA-containing vesicles is mediated by cytoskeletal elements in a Ca^{2+} dependent process. Intrinsic bending of the membrane microdomain is induced by incorporation of ceramides. Exosomal maturation at the MVE membrane can be initiated by ESCRT-dependent (right) or independent (left) processes. In the ESCRT-independent process, tetraspanins can act as scaffolding and structuring elements that initiated membrane cargo clustering and accumulation of cytoplasmic cargo before ceramide promoted membrane bending and vesicle fission. In the ESCRT-dependent mechanism, ESCRT-0 and ESCRT-I together with clathrin initiate aggregation of ubiquitinated membrane cargo and ESCRT-II and ESCRT-III mediated budding and fission of the vesicle into the MVB lumen. Modified with permission from (van Niel et al., 2018)

The mechanisms that conquer the selective loading of cytoplasmic cargos into MVs are barely understood. For loading of membrane-associated cargos, the respective components need to localize to the MV budding sites either by direct anchoring to membrane lipids or through their intrinsic affinity towards lipid membrane rafts (Shen et al., 2011; Yang and Gould, 2013). Interestingly, these mechanisms are also explored by several viruses, which is one of the reasons why viruses and MVs have been proposed to

be closely related (Nolte-'t Hoen et al., 2016). Other cytoplasmic components might be sorted into MVs by their interaction with the inner leaflet of a membrane microdomain through direct anchoring *via* myristoylation, prenylation or palmitoylation (Shen et al., 2011; Yang and Gould, 2013). However, the mechanisms by which nucleic acids are sorted and packed into MVs are still elusive and only a few experimental links, like the involvement of conserved zipcode RNA sequence motifs at the 3´-untranslated region of mRNA, have been proposed (Bolukbasi et al., 2012).

The current state of research only allows for one clear conclusion: EV-maturation and regulation of EV-formation is not only highly complex but also tightly regulated and involves a multitude of different protein complexes. Moreover, EV production might not only differ between cell types from the same organism but also depends on pathological states and other cellular conditions (e.g. cell cycle, growth arrest or the extracellular matrix composition). Furthermore, even technical replicates of EV preparations show intrinsically high, qualitative and quantitative, variations (Tiruvayipati et al., 2020). This not only limits efforts which set out to explore exosome biology but also impairs the reliable application for therapeutic and diagnostic procedures based on EVs. Therefore, in the hope to circumvent or compensate the variations of natural EV preparations, techniques and procedures for recombinant or chemical engineering of natural or semi-synthetic EVs have been developed (Garcia-Manrique et al., 2018).

1.2.2 Isolation and purification of EVs

According to a recent literature survey, precipitation of EVs in PEG solutions is one of the most commonly applied isolation methods (Konoshenko et al., 2018). This method is based on the addition of superhydrophilic PEG polymers to biofluids, decreasing the solubility of compounds (e.g. EVs) present in the solution, eventually leading to precipitation of the vesicles. Obviously, this partially destructive approach only delivers very crude EV preparations harbouring wide-ranging biomolecular contaminations (Van Deun et al., 2014) and exemplifies the current lack of suitable isolation and purification procedures which combine high yields, throughputs and reproducibility with economical up-scaling options, superior purity and additivity. Moreover, it highlights the current "primitive" state of EV isolation methods applied and underscores the need for advanced EV analysis approaches.

The population of EVs released by a single cell is widely divers, containing vesicles differing in size by several orders of magnitude. Moreover, their biophysical

surface characteristics (like charge or fluidity), their biomolecular surface decoration (like proteins and carbohydrates) as well as their density is greatly variable. This also applies to vesicles of the same cellular origin (e.g. large variations in exosome density have been described (Konoshenko et al., 2018)). Additionally, among lipoproteins, low molecular weight signalling molecules and soluble proteins, EVs are only of type of cellular products released into the extracellular environment and therefore present in biofluids. Therefore, robust and reproducible isolation of specific EV subset with high yield, throughput and purity, is a highly challenging task. Consequently, various isolation and purification approaches have been developed. Some of these, relay on recognition of specific molecular surface patterns on the EV surface and are therefore very specific but with low yield and throughput. Others are based on EV size differences and therefore perform with high throughput but low specificity. In the following, the most commonly applied isolation and purification methods will be summarized. The particular isolation or purification methods are not mutually exclusive but, in many cases, applied complementary and sequentially.

1.2.2.1 Ultracentrifugation

The most commonly applied method for EV isolation from biofluids builds on separation according to their buoyant density (Konoshenko et al., 2018). Most protocols based on ultracentrifugation apply differential centrifugation stages in order to isolate cell debris, apoptotic bodies and other aggregates before sedimenting the EVs (Livshits et al., 2015). Commonly applied accelerations range between 100,000-120,000 g for several hours (Konoshenko et al., 2018). However, no standard protocol has been defined yet, wherefore most studies develop and apply own ultracentrifugation routines. Although these procedures can be easily implemented in most laboratories, the major drawback still looms in the very heterogeneous EV mixtures obtained. EV populations isolated by ultracentrifugation not only harbour many different kinds of EV subtypes but also contain substantial contaminations which co-sediment with EVs (e.g. protein aggregates or viruses). In order to purify these sample, the EV pellet can be repetitively resuspended and re-centrifuged, resulting in purer EV fractions (Théry et al., 2006). However, this comes to the expense of reduced overall yield (Livshits et al., 2015). Moreover, subsequent filtration through 0.1 µm, 0.22 µm or 0.45 µm filters can be performed to further purify the EV samples. Several protocols have been designed to improve the purity of EV preparations obtained by ultracentrifugation. For instance, density gradient

ultracentrifugation applies a sucrose cushion as a density gradient which effectively separates EVs by their specific density (most exosomes range between 1.1 and 1.19 g/ml) from other contaminant moieties (Webber and Clayton, 2013). However, this purification method is even more laborious compared to classic ultracentrifugation and moreover requires complex, time-consuming and hardware extensive procedures, rendering the technique inapplicable for clinical settings (Zeringer et al., 2015).

1.2.2.2 Ultrafiltration

As described in section 1.2, several different types of EVs, with different molecular compositions and sizes, exist. Therefore, many techniques applied for EV isolation are based on their separation by size. Importantly, this does not allow for a precise isolation of vesicles according to their cellular origin (e.g. exosomes and microvesicles) but rather makes use of an apparently weak correlation between EV type and their size range (Cheruvanky et al., 2007). An easily implementable method for EV isolation by size is sequential filtration, where usually track-etched polycarbonate filter membranes with narrowly defined pore sizes between 0.8 µm and 0.1 µm (±20%), are applied (Xu et al., 2016). Hereby, specific EV fractions can be enriched by sequential ultrafiltration. Also in this case, EV purity and yield are directly and inversely proportional to the number of filtrations steps, respectively.

1.2.2.3 Size exclusion chromatography

Several publications describe the combination of ultrafiltration and ultracentrifugation with size exclusion chromatography, which purifies particles according to their hydrodynamic radius (Gámez-Valero et al., 2016). This comprise two specific advantages: First, chromatography is easily scalable and can therefore be incorporated into existing industrial pipelines. Secondly, size exclusion chromatography is a non-destructive method (Gámez-Valero et al., 2016), implying that the EVs are preserved in their natural physical state. Most literature reports based on this isolation technique show high purities, with only minor lipoprotein contaminants (Taylor and Shah, 2015). However, the resulting EV preparations are significantly diluted, reducing the overall isolation yield and the whole procedure requires substantial financial investments for the chromatographic solvents.

1.2.2.4 Isolation based on affinity interactions

The EV surface is densely decorated with a wide variety of ligands, suitable for affinity capture techniques. For instance, antibodies directed towards specific EV protein biomarkers, lectins (carbohydrate binding proteins) and lipid binding proteins can identify and bind to specific EV surface moieties. Several protocols have been developed which apply antibodies against tetraspanins for immunoprecipitation of EVs subsets with predefined surface markers (Greening et al., 2015; Oksvold et al., 2015). In these cases, the antibodies are immobilized on a solid phase or on magnetic nanoparticles, capturing EVs and allowing for subsequent washing and pull-down. This comprises several advantages over methods based on ultracentrifugation or filtration but also induces unspecific adsorption of non-EV associated compounds to the solid phase.

Although EVs comprise a significant amount of proteins, their major scaffolding elements are lipids. This feature has been explored to highly enriched vesicular particles from complex biofluids by applying lipid binding proteins as capture moieties. For instance, annexin V, a phosphatidylserine binding protein, has been used to bind EVs to solid phases, which contain considerable amounts of this lipid exposed on their surface (Shih et al., 2016). Similarly, lectins such as wheat germ agglutinin or *solanum tuberosum* lectin have been applied to isolate EVs based on their carbohydrate coating (Kosanović and Janković, 2014).

All the above-mentioned affinity-based methods allow for high quality enrichment of vesicles with >80% purity (Heinemann et al., 2014) and comprise fast turn-around times. However, the overall yield is very reduced and does still not allow to produce EV samples with purities reaching those of protein or nucleic acid preparations. In summary, it can be concluded that the currently available EV purification and isolation methods do not generate EVs of adequate quality and yield for large-scale industrial or clinical applications.

1.3 Diagnostic and therapeutic procedures based on extracellular vesicles

EVs hold several key features that renders them as promising candidates for therapeutic and diagnostic procedures. First, their protein and nucleic acid cargos mirrors, at least to some extent, the physiological state of their cell of origin. As several diseased tissues and organs are not easily accessible for diagnostic biopsies or inspections, EVs have been extensively studied as sources for liquid biopsies because they can be conveniently retrieved from patients bio-fluids (Halvaei et al., 2018). So far, several prognostic and

diagnostic markers have been identified. For instance, for liquid biopsy diagnosis of glioblastoma based on EVs, the presence of EGFRvIII, $IDH1^{R132H}$ or miR-21 have been studied (Santiago-Dieppa et al., 2014). Moreover, in prostate cancer patients, not only the total plasma concentration of CD63 positive vesicles was increased but also markers like CK18 and PTEN were elevated in plasma EVs (Pang et al., 2020). Even though EVs show partially outstanding sensitivity, specificity and positive predictive values, the use of EVs as biomarkers in liquid biopsies is still limited due to variations in their isolation procedures (Pang et al., 2020).

Considerable progress has been made for therapeutic administration of EVs. For instance, several administration routs for therapeutic EVs have been investigated: intravenous injection (e.g. to target macrophages in injured spinal cord (Lankford et al., 2018)), subcutaneously injection (e.g. to suppress parasitic infections (Trelis et al., 2016)), transdermal application (e.g. for acceleration of wound-healing in diabetic mice (Geiger et al., 2015a)), intrathecal injection (e.g. for therapy of nerve injuries (Shiue et al., 2019)), intranasal (e.g. for treatment of neuroinflammatory diseases (Lakhal and Wood, 2011)) or intramuscular injection (e.g. for therapy of Duchenne muscular dystrophy (Aminzadeh et al., 2018)). Also, circulation times as well as organotropism of EVs after systemic administration have been extensively and systematically characterized (Lee et al., 2018a; Wiklander et al., 2015). Therefore, EV-based therapies are raising high hopes in many medical fields, as they display an intrinsically low immunogenicity, a certain degree of organotropism, high cellular uptakes rates as well as considerably low side effects (Liu and Su, 2019).

1.3.1 Fibrocyte derived therapeutic exosomes for wound healing

Of special importance to this thesis are previously described human exosomes derived from primary $CD45^{+}[CD3/CD19/CD20/CRTH2]^{-}CD16^{-}CD115^{-}CD11b^{+}CD34^{+}$ fibrocyte cultures that increase wound-healing speed and efficiency in diabetic mice (Geiger et al., 2015b). The study of Geiger *et al*. was based on isolated circulating fibrocytes that were stimulated with platelet-derived growth factor-BB, transforming growth factor-b1 and fibroblast growth factor 2. EVs produced by these cultures were isolated by ultracentrifugation and their morphology was analysed by transmission electron microscopy (TEM), their size (89 ± 34 nm) as well as nanoparticle tracking analysis and their EV-marker expression (CD9, CD63, CD81, CD80, CD86, MHC-I, MHC-II, TSG101 and flotillin-1) by flow cytometry and immunoblotting. The study determined several

crucial moieties present in the EVs, like heat shock protein-90α, total and activated signal transducer and activator of transcription 3, proangiogenic miRNAs miR-126, miR-130a, miR-132, anti-inflammatory miRNAs miR-124a and miR-125b as well as the regulator of collagen deposition miRNA-21. The authors could show that these EVs do not possess any considerable immunogenicity and that they exhibited pro-angiogenic properties *in vitro*. Moreover, they found increased *in vitro* proliferation and migration of keratinocytes and activation of dermal fibroblasts. Finally, an accelerated wound closure of artificial wounds in mice was observed. Based on this study, a pharmaceutical company was established (DreiRosen Pharma, now acquired by Regenesis Therapeutics) that performed pre-clinical evaluation for therapeutic administration of the described EVs.

1.3.2 Artificial and engineered extracellular vesicles

Especially with the ulterior motive that EVs could serve as potential nanocarries for therapeutic compounds, considerable efforts have been made in order to manipulate EV compositions and function either during their intracellular biogenesis and shedding or after isolation. In particular, the incorporation of targeting moieties that provide EVs with increased "organotropism" as well as loading of endo- and exogenous compounds into the vesicle lumen have been pursued (Johnsen et al., 2014). One of the first approaches developed in this direction, was the extrusion of cultured cells over polycarbonate membrane filters with pore-dimensions in the size-range of natural EVs (Jang et al., 2013). This produces high yields of drug-loaded vesicles that retain a certain natural targeting ability due to their plasma membrane-like composition and topology. A similar procedure, based on artificial tearing of cultured cell within microfluidic devices, has been used to deliver endogenous RNA inside mimetic nanovesicles to target cells in culture (Jo et al., 2014). However, in these setups, specific and selective sorting of defined exogenous cargos is not possible and the very same purification procedures applied to EVs are used. Other methods relay on the recombinant expression of proteins-of-interest that are either fused to EV-targeting peptide sequences (Di Bonito et al., 2017) or to proteins know to localize within MVBs (e.g. CD63) (Liu and Su, 2019; Stickney et al., 2016). This leads to the preferential sorting of potentially therapeutic cargos into natural EVs. Such approaches are not only applicable in therapeutic setting but also supportive for studies aiming to perform quantitative characterizations of EVs (Hikita et al., 2018). However, again laborious and imprecise EV purification procedures need to be performed and potential interfering EV constituents cannot be eliminated from the final EV preparation.

Several approaches for post-production modification of EVs have been developed. In this way, synthetic targeting moieties and functional groups can be attached to the EV outer membrane in order to increase target-specificity or cellular uptake. Moreover, therapeutic compounds can be introduced into the vesicles´ lumen and thereby be protected from degradation or selectively released in the target tissue or cell type (Liu and Su, 2019). For instance, cholesterol-linked DNA has been incorporated into EV membranes in a simple one-step process. This allows to coupled horseradish peroxidase and perform hybridization chain reactions for EV quantification (He et al., 2017). Moreover, cholesterol-linked DNA has been used to functionalize isolated EVs with FasL, enabling the suppression of proliferative alloreactive T cells *in vivo* (Yerneni et al., 2019). For specific and quantitative loading of isolated EVs with therapeutic biomolecules (e.g. miRNAs) or low molecular weight drugs (e.g. the chemotherapeutic doxorubicin), electroporation protocols have been designed (Tian et al., 2014). Mild electroporation can achieve efficient incorporation of anti-tumour miRNAs (e.g. miR-31 or miR-451a) into EVs, which subsequently display pro-apoptotic properties when incubated with cancer cell lines (Pomatto et al., 2019). However, the quality of post-production modified and functionalized EVs is still dependent on cell-derived EVs and therefore influenced by their intrinsic variation in terms of composition and quantity. This especially limits their approval by regulatory authorities as constant and reproducible production parameters cannot be guaranteed and therefore large product fluctuations with only limited quality control can be expected (Yamashita et al., 2018). So far, all EV-based therapies are limited by the insufficient quality of the applied EV production, isolation and purification procedures, wherefore completely new approaches need to be implemented in order to explore the full potential of EV-based and EV-inspired therapies.

1.3.3 Liposomes and EVs for drug delivery

From a “biomaterials” point of view, EVs can be classified as cell-derived natural liposomes. Liposomes are spherical vesicles with one (unilamellar) or more (multilamellar) double lipid membranes with a typical size range of 50 – 800 nm and an aqueous lumen (Figure 3). They have been extensively used for drug delivery purposes (e.g. chemotherapeutic, anti-inflammatory agents or imaging probes) and for studies on lipid membrane biophysics and membrane interactions (Niehage et al., 2014; Sercombe et al., 2015). In contrast to synthetic liposomes, EVs display significantly higher complexity as they contain more building blocks and therefore also potentially possess a

higher entropy according to Claude Shannon mathematical theory of communication (Shannon, 1948). Therefore, comparted to synthetic liposomes, their biomolecular structure confers them with a very distinct biological identity. However, liposomes are commonly more defined on a quantitative and qualitative level and handling as well as storage of liposomal formulations is in many cases more compatible with clinical routine procedures (Chang and Yeh, 2012). Consequently, a wide variety of liposomal production strategies, with high yields and compatible with GMP-production regulations, have been developed (Has and Sunthar, 2019). Among these, vesicle extrusion through a porous polycarbonate membrane filter is one of the most commonly used, as it allows for precise regulation of liposomal size, on-line encapsulation of therapeutic agents, high throughputs and only requires limited handling skills or equipment. However, in recent years, microfluidic approaches for liposome generation have been developed (Yu et al., 2009). Although current microfluidic strategies for liposome assembly do not offer industrial mass-production throughputs, they allow for precise adjustment of liposome dimensions, formulation and cargo (Carugo et al., 2016).

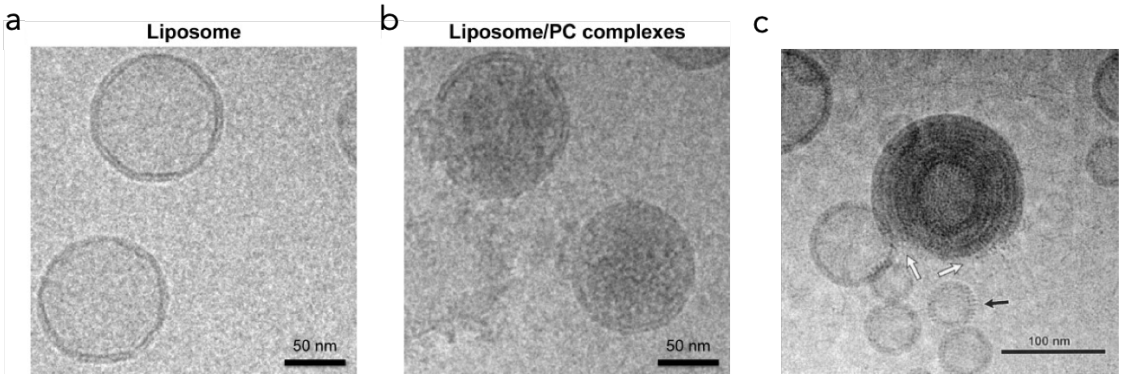

Figure 3 | Electron microscopy of liposomal-preparations. (**a and b**) Cryo-electron microscopy images of liposome preparation without (a) and with (b) a plasma protein corona. Adopted from (Corbo et al., 2016). (**c**) Cryo-electron microscopy images of multilamellar liposomes with DNA-coating. Adopted with permission from (Huebner et al., 1999)

Intracellular uptake of liposomes can proceed through several endocytic pathways (e.g. clathrin- and caveolae-mediated endocytosis, phagocytosis or micropinocytosis), depending on liposome size, charge, surface-biofunctionalization or opsonin coating (Figure 4) (Hillaireau and Couvreur, 2009). Moreover, fusogenic (e.g. cationic) liposomes can undergo direct fusion with the plasma membrane and directly deliver their cargo into the cytoplasm (Cavalcanti et al., 2018). Which of these uptake mechanisms will take place is not mutually exclusive but influenced by the physical and chemical properties (e.g. size

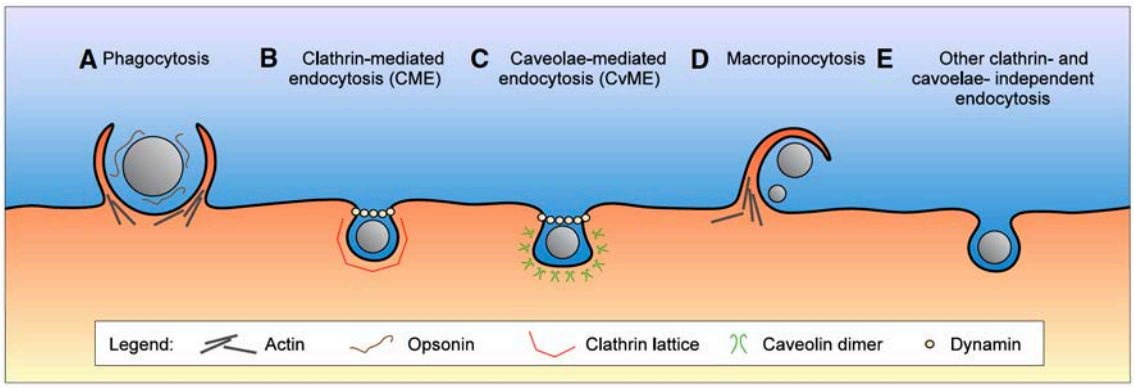

Figure 4 | Uptake mechanisms of liposomes. Liposomes can be internalized by cells through several different mechanisms depending on their size, charge or coating. Actin cytoskeleton-depended phagocytosis (A) is mostly performed for liposomes of larger size with opsonin coating. Clathrin- (B) and caveolin (C)-dependent endocytosis is performed for smaller vesicles and requires aggregation of a clathrin-complexes or caveolin-dimers under the inner membrane leaflet inducing inward budding of the membrane. Macropinocytosis (D) is an actin-dependent process by which various particles can be engulfed and captured by cellular protrusions for intracellular uptake. However, also other (E) processes can lead to liposome uptake like liposome-induced intrinsic bending of the plasma membrane or liposomes fusion. Adopted with permission from (Hillaireau and Couvreur, 2009).

and charge) of the liposomes, where for instance clathrin-mediated endocytosis is preferentially applied to particles <200 nm (Rejman et al., 2004). Moreover, as the physical and chemical liposome properties influence uptake (which also holds true for EVs (Whitehead et al., 2015)), they *vice versa* dramatically impact on the systemic circulation times and clearance of liposomes from blood and tissue by renal, hepatic or the mononuclear phagocyte systems (Ishida et al., 2002; Juliano and Stamp, 1975). Therefore, several strategies to dampen liposome clearance and therefore increase delivery efficiency have been implemented. For instance, coating the liposome surface with polyethylene glycol (so-called stealth liposomes) has been shown to prolong their circulation times and decrease their immunogenicity (Mohamed et al., 2019). Moreover, in combination with targeting moieties, like antibodies, attached to their surface, respective liposomes can be preferentially accumulated in selected tissues (e.g. lymph nodes) (Immordino et al., 2006). Interestingly, also passive targeting of non-functionalized liposomes into solid tumours has been observed. This effect is based on the enhanced permeability of the vascular endothelium inside tumorous tissue and their decreased lymphatic drainage (Deshpande et al., 2013). Moreover, several liposomal modification and functionalization strategies, which increase uptake efficiency in target

tissue and provide stimulus-controlled (e.g. pH or temperature) on-demand release of cargo, have been devised (Abri Aghdam et al., 2019; Heath et al., 1983).

1.3.3.1 Lysosomal degradation of liposomes and nanoparticles

If endocytosed liposomes are not conjugated to specific intracellular sorting signals, they are usually sorted into early endosomes and subsequently degraded during lysosomal maturation together with their cargo (Figure 5) (Hillaireau and Couvreur, 2009). Several strategies exist to overcome or by-pass lysosomal degradation in order to achieve cytoplasmic cargo release after liposome uptake: the attachment of pH-sensitive fusogenic peptides derived from viral fusogenic proteins (El-Sayed et al., 2009; Nakase et al., 2011), lysosomal osmotic swelling through proton-sponge mechanism of synthetic protonable polymers like polyethylenimine (El-Sayed et al., 2009) or ionizable pH-sensitive lipids with low pK_a incorporated into liposome membranes that allow for invers intralysosomal

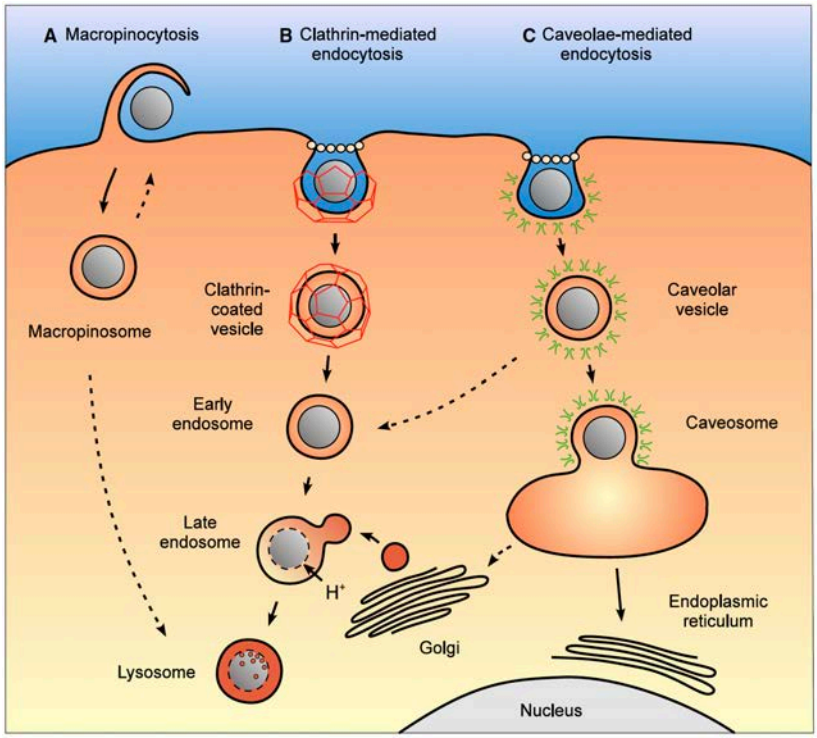

Figure 5 | Intracellular sorting of internalized liposomes. After intracellular uptake of liposomes *via* micropinocytosis (A) or clathrin-(B) and caveolin (C)-mediated endocytosis, liposomes can be directed towards the Golgi apparatus and the endoplasmic reticulum or destroyed by lysosomal degradation. Endosomal sorting through signalling moieties on the cargo directs macropinosomes and early endosomes. To avoid cargo degradation, lysosomal escape mechanisms need to be implemented into the liposomes. Modified from(van Niel et al., 2018).

fusion and delivery of cargos like mRNAs (Draffehn and Kumke, 2016; Patel et al., 2019b). However, liposome-based delivery still encompasses some fundamental drawbacks, like the comparably high (liver-)toxicity of some lipid formulations (Knudsen et al., 2015), low encapsulation efficiencies and considerably high leakiness of many liposome formulations for therapeutics of interest (Colletier et al., 2002; Gonzalez Gomez et al., 2019). Most importantly, current liposome preparations are limited in their size and therefor in the total amount and breadth of cargo they can transport. Because of this, the desired therapeutic dose in the targeted tissue can often not be reached and many pharmaceuticals of future interest like nanoparticles, viruses or synthetic supramolecular constructs (e.g. DNA-origami nanomachines) cannot be entrapped and delivered with state-of-the-art liposomes.

1.4 Bottom-up synthetic biology

Every organism alive today - from single-celled archaea to multicellular mammals - once originated from pre-existing life forms. As for now, no evidence for the spontaneous re-emergence of life on earth has been reported. It follows, that at specific point in time, life emerged from simple chemical building blocks and evolved from this state on, to form the living nature found on earth today. This raises a merely curiosity-driven scientific question: Can life-like entities, or fractions thereof, be recreated *de novo* and brought to life? In other words: can chemical building blocks be assembled one by one in order to create a synthetic biological system with life-like properties? Can matter be brought to life?

The academic field pursuing these questions is generally termed “bottom-up synthetic biology” (Gopfrich et al., 2018; Jia and Schwille, 2019) and is currently mostly centred around the creation of a synthetic cell or cellular functions that features characteristics attributed to living matter (e.g. as defined by the National Aeronautics and Space Administration (NASA)(Benner, 2010)). Efforts directed towards the assembly of such synthetic cells have yielded compartmentalized systems able to undergo division (Xu et al., 2019), sense and react to chemical gradients (Tian et al., 2019), apply protein-based effector molecules (Weiss et al., 2017) or use transcription-translation systems and genetic circuits for synthesis of biomolecules (Yue et al., 2019). Moreover, subcellular structures like mitochondria (Biner et al., 2018), light-harvesting chloroplasts (Lee et al., 2018b) and other organelles have been recreated (Simmel, 2019; Staufer et al., 2020).

1.4.1 Bottom-up assembly of synthetic cells

Recreating an artificial cell and artificial subcellular structures from simple molecular building blocks is, at best, a complex engineering problem. Cells possess an intrinsic hierarchical order of structures and processes which perform interdependent, spatiotemporally organized chemical reactions to remain in an out-of-equilibrium thermodynamic state. However, because of the redundancy, the shear abundance and the level of complexity of the involved biochemical pathways, there is still no holistic understanding of a cell – not even of the minimal set of components needed to operate a cell (Jia and Schwille, 2019). Also in this regard, bottom-up synthetic biology could provide novel means to abstract the intricate molecular complexity of living cells in favour of a highly defined and therefore controllable system.

Although bottom-up synthetic biology will certainly provide more in-detailed knowledge on fundamental biological matters also beyond evolutionary biology, for instance on the emergence of future life-forms, this field is not solely curiosity-driven research. In contrary, several technological breakthroughs are expected to originate based on bottom-up synthetic biology principles (Gopfrich et al., 2018). In particular, synthetic cells have been designed for therapeutic interventions in cancer treatment (Krinsky et al., 2018) or as synthetic platelets for the therapy of thrombocytopenia and lymphoproliferative syndrome (Majumder and Liu, 2017). Therefore, while pursuing questions of elemental importance for our self-conception, which could also transform our perspective on life itself, bottom-up synthetic biology might produce a multitude of spin-off technologies that impact on application-driven research.

A major breakthrough for the field of bottom-up synthetic biology was the implementation of transcription-translation systems inside compartmentalized micro-systems. For instance, the DNA replication machinery of Φ29 viruses has successfully been reengineered to perform in cell-free expression systems incorporated into liposome-based minimal cells (van Nies et al., 2018). Such pathways are not only able to transmit genetically encoded information to daughter cells but also to mediate genetic circuit interactions between communicating synthetic cells (Adamala et al., 2017). Based on studies in such micro-compartmentalized systems, meaningful mechanistic insights into the dynamics of cellular organizations can be gained. For instance, the importance of limited diffusion rates and crowded environments on the efficiency of transcription-translation systems has been assessed in reversibly shrinking monodisperse liposomal protocells (Deng et al., 2018). Also, stochastic effects in gene expression noise have been

studied in such minimal synthetic cells (Hansen et al., 2016). Taken together, these and other scientific synthetic cell efforts have shown that bottom-up synthetic biology can recapitulate one of the most central aspects of life in synthetic cells: Storage, processing and transmission of genetically encoded information.

1.4.2 Bottom-up assembly of synthetic organelles

The controlled assembly of artificial structures mimicking living cells has revolutionized the field of bottom-up synthetic biology. Especially, the application of droplet-based microfluidics has allowed to generate several well-defined compartmentalized systems to mimic the cell-like discrimination between the intra- and extracellular milieu based on water-in-oil droplets. Apart from the controlled assembly of synthetic cells, several scientific bottom-up synthetic biology endeavours have focused on the synthesis of sub-cellular structures, for instance on organelles. These are considered to be some of the central hallmarks of eukaryotic life forms which provide confined reaction space inside the cell body. Dozens of different organelles have originated since the first emergence of eukaryotes, most of them with a highly complex and intriguing structure-function relation. Recently, phase-separated, membraneless organelles have been described, a finding which is still controversially discussed (Boeynaems et al., 2018). However, most eukaryotic organelles are surrounded by one lipid bilayer (for instance the endoplasmic reticulum, the endosomes or the Golgi apparatus) or two lipid bilayers (for instance the nucleus, the mitochondria and the chloroplasts). Producing compartmentalized systems which closely mimic these enclosed reaction spaces has turned in to an important ambition within the field of bottom-up synthetic biology. Hereby, not only academic research, aiming to gain deeper insights into the mechanical functioning of organelles, has been pursued but also several efforts aiming to develop cellular "implants" which are able to restore or rescues dysfunctional organelles within living cells arose (Staufer et al., 2020; van Oppen et al., 2018). One important example for this approaches is the design of synthetic peroxisome-like compartments based on polymerosome structures. In their study, Einfalt *et al.* reported on the entrapment of horseradish peroxidase enzymes inside these polymerosomes, which are able to support cellular redox homeostasis not only in cultured cells but also living zebra fish (Einfalt et al., 2018). Another important report on bottom-up assembled synthetic organelles was published by Lee *et al.*, who showed the reconstitution of plant photosystems into synthetic lipid vesicles to create artificial chloroplast able to produce ATP by light harvesting (Lee et al., 2018b). Moreover, several

efforts have been made to also recreate membraneless organelles. For instance, phase separated protein condensates working inside living cells have been reported. These synthetic structures were are able to mediated orthogonal translation of specific RNAs, expanding the canonical set of amino acids and producing artificial proteins (Reinkemeier et al., 2019).

However, approaches aiming to constructor synthetic organelles, either to study their physiology or to developed new therapy options, still suffer from two major drawbacks: very low production throughput and comparably low control over the molecular composition. Once these drawbacks could be overcome, single properties of the organelles, e.g. their membrane composition, their size or their protein load could be systematically varied. Moreover, if enough synthetic organelles could be produced at reasonable production costs, this could empower their integration into clinical procedures. Furthermore, investigations on the uptake and integration dynamics of lipid-enclosed synthetic organelles could provide valuable insights into the emergence of natural organelles as postulated by the endosymbiotic theory (Martin et al., 2015).

1.4.3 Application of bottom-up synthetic biology for intercellular signalling studies

Apart from insights into the genetic basis of life, bottom-up synthetic biology principles have also been applied to investigate fundamental mechanisms of intercellular communication. For instance, epithelia-like tissue collectives of synthetic cells have been produced by incorporation of recombinant claudin-4 into giant unilamellar vesicle (GUV) membranes (Figure 6a) (Belardi et al., 2019). Thereby, synthetic cells, interconnected by tight-junction-like intercellular adhesions, have been produced and applied for studies on epithelial polarization. Moreover, the spatiotemporal regulation of immune-cell interactions and immune-synapse formation has been studied by recreating synthetic, GUV-based antigen presenting cells featuring immune-cell surface markers like pMHC, CD58, ICAM-1 and CD45 (Figure 6b) (Jenkins et al., 2018). Furthermore, communication across larger scale consortia of synthetic cells has been implemented to study fundamentals of reaction-diffusion morphogen gradients (Figure 6c). By this, uni-directional and counter-directional artificial-morphogenesis and spatial patterning was recreated in populations of synthetic cells leading to differential enzyme activities within the assemble (Tian et al., 2019; Wang et al., 2019). These efforts demonstrate the value of bottom-up synthetic biology to entangle the complexity of intercellular communication

processes module-by-module and thereby decipher fundamental aspects of cellular communication by applying quantitatively defined life-like components.

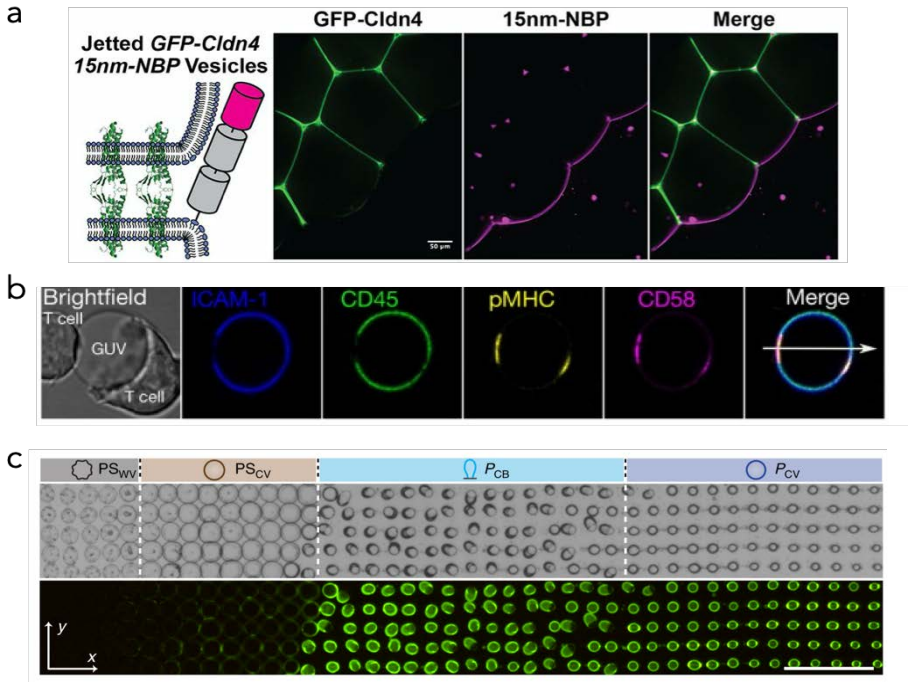

Figure 6 | Synthetic cells applied for studies of intercellular communication. (**a**) Schematic illustration and fluorescence microscopy images of GUVs containing fluorescent lipids as well as homophilic GFP-tagged claudin-4 and 5 nm non-binding proteins. Formation of tight-junction like cell collectives between the synthetic cells can be observed. Adopted with permission from (Belardi et al., 2019). (**b**) Bright field and fluorescence microscopy images of an artificial antigen-presenting cells in contact with two T-cells. Distribution of ICAM-1, CD45, pMHC and CD58 on the GUV is visible. Adopted with permission from (Jenkins et al., 2018). (**c**) Bright field and fluorescence microscopy images of a 2D array of differentiated protocells exposed to an intersecting "morphogen" gradient of sodium dodecylsulfate (from left to right) and polyoxometalate (right to left). Scale bar is 500 µm. Adopted with permission from (Tian et al., 2019).

1.4.4 Droplet-based microfluidics for synthetic-biology

The use of droplet-based microfluidics for the assembly of synthetic cells is of special importance for bottom-up synthetic biology as is allows for a very precise manipulation of small amounts of fluids (typically in the nanoliter to attoliter range) comparable to those of living cells. A wide variety of previously developed advanced microfluidic manipulation modules are applicable for the production of GUVs (e.g. pico-injection systems or controlled release modules (Frey et al., 2020; Weiss et al., 2017)) which offers a divers toolkit and further expands the level of control over such minimal cell-like compartments (Figure 7). The droplet-based microfluidic technology was originally

developed for high-throughput and multiplex chemical analysis (Whitesides, 2006) but was soon adopted for biological studies like organ-on-a-chip technologies (Zhang et al., 2018). As microfluidic chips combine reduced costs due to inexpensive reagents and low consumption volumes with fast and precise analysis, their application has enabled a multitude of further key scientific technologies like (single cell-) next-generation sequencing (Thompson et al., 2014) and portable, point-of-care therapeutic and diagnostic devices (Nightingale et al., 2019).

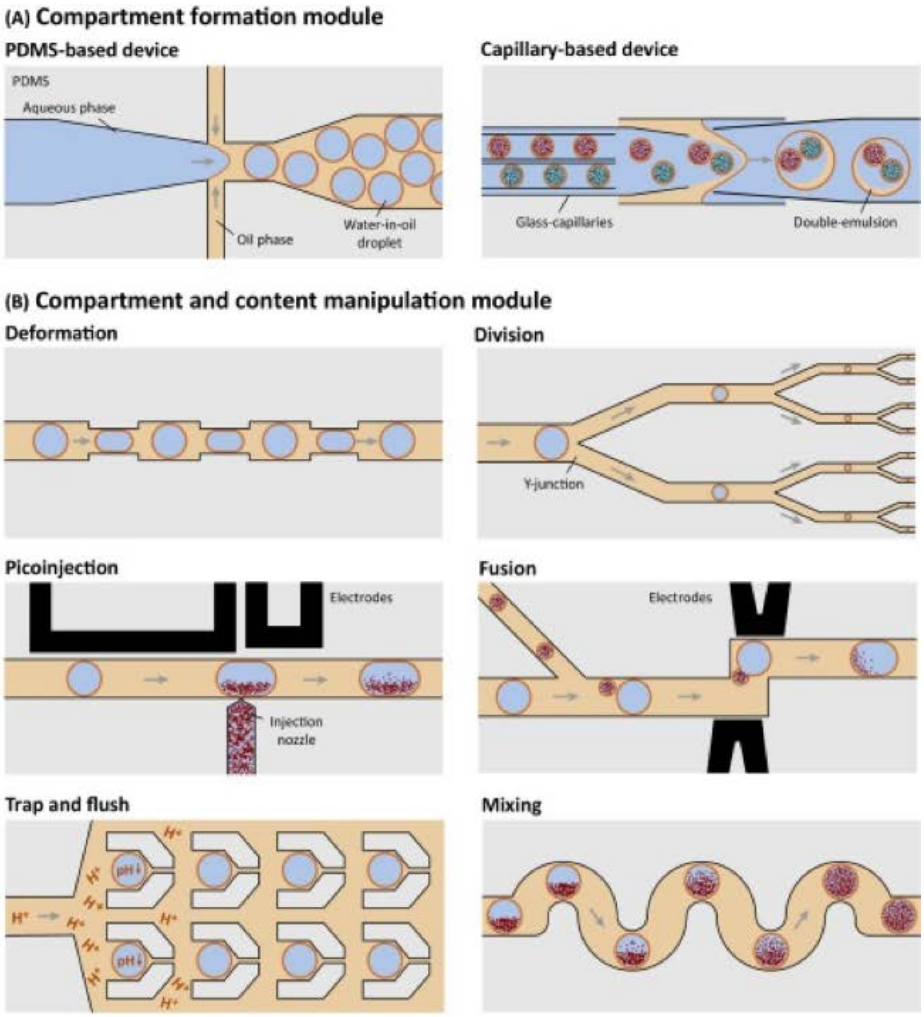

Figure 7 | Microfluidic modules for water-in-oil droplet manipulation. Schematic illustrations of PDMS-based microfluidic chip architectures applicable for droplet formation (A) and droplet-content manipulation (B). Aqueous phases are indicated in blue, oil-phases are indicated in yellow. Adopted with permission from (Gopfrich et al., 2018).

Droplet-based microfluidics exploits the laminar flow of liquids inside micrometer-sized channels for the generation of separated, usually water-filled, segmented droplets immersed in an immiscible oil-phase. For this purpose, special T-junction or flow-focusing junction architectures, which allow for the generation of monodisperse droplets

based on shear-forces, are implemented into the microfluidic devices. Most device architectures are produced from polydimethylsiloxane (PDMS) polymers as this material is mostly bio-inert, allows for the diffusion of oxygen and CO_2 and is compatible with negative imprinting of the channel architectures by photo-lithographic wavers (Friend and Yeo, 2010; Fujii, 2002). The resulting droplets are stabilized by amphiphilic block-copolymer surfactants which prevent entropy-driven droplet fusion and coalescence (Baret, 2012). With the help of microfluidic devices, a high degree of control over these droplets can be achieved. This is not only possible based on the pressures applied on the oil and aqueous inlet-channels but especially by smart designed and combination of different channel architectures. Moreover, as the generation and the stabilization of the droplet-emulsions is achieved by simple mechanical and "robust" thermodynamic principles, respectively, the droplet production rate can reach kilohertz frequencies. This not only empowers technologies like digital PCR (Quan et al., 2018) but is of special importance for the field of bottom-up synthetic biology. The generation of thousands of well-defined homogenous synthetic cells in short-time periods can for instance allow to study stochastic effect of biological processes across a wide cell-population (Hansen et al., 2016).

1.4.5 Charge-mediated formation of giant unilamellar vesicles

GUVs are frequently used model membrane compartments for the construction of protocells and synthetic cell compartments (Gopfrich et al., 2018; Göpfrich et al., 2019; Weiss et al., 2017). These cell-sized, usually spherical, water-filled lipid vesicles are enclosed by a doubled lipid membrane which is commonly composed of phospholipid mixtures and therefore mimics key characteristics of cell and organelle membranes (e.g. composition, thickness or fluidity). Several techniques for GUV production have been reported, including: (1.) electroformation of GUVs from supported lipid bilayers on indium tin oxide or platinum electrodes (Meleard et al., 2009), (2.) a centrifugation-based inverted emulsion technique (Moga et al., 2019), (3.) octanol-assisted formation of GUVs in microfluidic chips (Deshpande et al., 2016) and, most important for this work, (4.) droplet-stabilized formation of GUVs inside water-in-oil droplets (Figure 8).

The formation of droplet-stabilized GUVs (dsGUV) is a simple, flexible and high yield process that can be performed within microfluidic devices (Haller et al., 2018) or in bulk (Göpfrich et al., 2019) ( ). It is based on the formation of water-in-oil (perfluorinated, bioinert oils are commonly used) droplet-emulsifications that are stabilized by non-

charged di- or triblock fluorosurfactants (Janiesch et al., 2015) and at least one type of fluorosurfactant that provides a negative charge to the droplet periphery (e.g. COOH-perfluoropolyether)(Haller et al., 2018). When negatively charged liposomes or small unilamellar vesicles (SUVs), suspended in a Mg^{2+} containing aqueous solution, are entrapped within the droplet lumen, the Mg^{2+}-ions accumulate at the negatively charged droplet periphery and in turn recruit the negatively charged liposomes. This leads to charge-mediated liposome fusion and the formation of a dsGUV by creation of a supported lipid bilayer around the droplet periphery. There are several advantages associated with the production of GUVs inside water-in-oil droplets. First of all, it is compatible with other microfluidic modules and therefor allows for sequential assembly of GUVs (Weiss et al., 2017). In contrast to electroformation, a wide variety of lipids can be applied e.g. positively and negatively charged lipids, saturated and poly-unsaturated lipids, ceramides or lipids with large head groups (Göpfrich et al., 2019; Haller et al., 2018). Moreover, this method can be used with several different buffer compositions

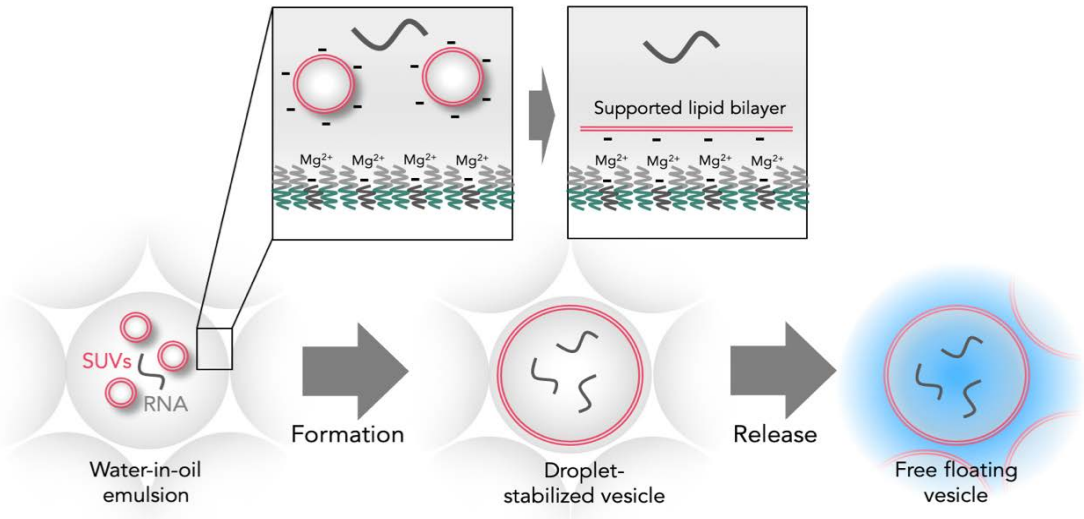

Figure 8 | Schematic illustration of the charge-mediated GUV formation process inside water-in-oil droplets. Negatively charged SUVs together with other biomolecules (e.g. RNA) to be incorporated into the final GUV, are entrapped inside water-in-oil droplet emulsifications by microfluidic technology or mechanical emulsification. The aqueous buffer is further supplemented with a mM concentration of Mg^{2+} ions. The emulsion is stabilized by a PFPE-PEG surfactant and PFPE carboxylic acid, which introduces a negative charge to the droplet periphery. SUV attachment to the droplet periphery is mediated by Mg^{2+} ions, inducing vesicles fusion to create a supported lipid bilayer along the periphery. During this process, other components can be entrapped inside the dsGUV. For release of the GUV into an aqueous environment, a destabilizing surfactant is added, transferring the GUV from the stabilizing polymer-shell into a suitable isotonic buffer.

(applied as aqueous phases) and can therefore be operated under isotonic, physiological conditions (Göpfrich et al., 2019). Also, during the GUV formation, biomolecular components (e.g. proteins, nucleic acids or organelles) suspended in the aqueous phase that do not accumulate at the droplet periphery, can be encapsulated inside the GUV (Göpfrich et al., 2019). This makes the use of in-droplet GUV formation an attractive technique for the bottom-up assembly of synthetic cells based on GUV membranes.

After dsGUV formation, a release procedure can be performed, which transfers the dsGUV from its stabilizing polymer- and oil shell into an aqueous environment. This involves the addition of an aqueous release buffer, providing further suspension volume for released GUVs, and a low-molecular weight destabilizing surfactant which drives demulsification based on its lower interfacial tension. In this way, GUVs suspended in an aqueous buffer can be produced and for example interfaced with living cells in a physiological environment.

2 Aims and Motivation

EVs are fundamental for intercellular communication and involved in a multitude of cellular processes. Consequently, EVs activate multiple signalling pathways that, in concert, initiate, drive and regulate single and collective cellular responses. These in turn, underlay nearly all facets of multicellular organisms, underscoring the central physiological role of EV-mediated intercellular communications and its involvement in a wide variety of disease states. Although attaining a holistic understanding of EV-signalling mechanisms is a compelling goal for biological research and biomedical applications, little insights have yet been accomplished, mainly due to intricate molecular complexity of the EVs. Therefore, I made the engineering of biomimetic systems for controlled manipulation of EV-mediated intercellular communications *in vitro,* the central goal of my interdisciplinary research. Particularly, I aimed to design and develop lipid-based synthetic EVs that would allow pinpointing the central physical, chemical and biological factors that conquer the interactions between vesicles and cells. My motivation was to understand and to optimise a mechanistic cross-correlation between these factors in order to design and assemble bioinspired synthetic liposomes with superior functions. Such endeavours required the development of new technologies that allow for a precisely controlled construction and manipulation of vesicles in order to permit systematic, comparative and thorough investigations. Therefore, inspired by bottom-up synthetic biology principles and the associated microfluidic technology, I set out to pursue two major research directions with the following aims:

1. The development and characterization of a microfluidic-based technology for precise assembly of GUVs suitable for cellular interaction studies as well as the implementation of a molecular toolbox for GUV-biofunctionalization.
2. The implementation of a systematic and comparative analysis of crucial GUV properties (e.g. charge, biomolecular coating or polymer-decoration) and their impact on the GUV-cell interplay.
3. The development of a hierarchical GUV-based system for intracellular cargo delivery.
4. Based on these findings, the implementation of GUV-based synthetic organelles functioning within living cells.

Based on the findings, insights and conclusions obtained from the investigations and developments pursued above, I aimed to conceptualization, design and assemble fully-synthetic EVs (fsEVs) with the following goals:

5. Application of bottom-up synthetic biology design principles for assembly of fsEVs consisting of lipid-, proteins and nucleic acid building blocks.
6. Following the natural blueprint of wound-healing therapeutic EVs, investigate the therapeutic potential of their fsEV-doppelgangers in dermal-wound healing.
7. Perform a systematic assessment of individual fsEV protein- and nucleic acid-components in order to dissect their individual contribution to the phenotypic changes induced in dermal cells.
8. Apply fully-synthetic EVs to systematically dissect their functional mechanisms by RNA-sequencing transcriptome analysis.

3 Materials and Methods

3.1 Materials

3.1.1 Lipids

EggPG L-α-phosphatidylglycerol (Egg, Chicken), EggPC L-α-phosphatidylcholine (Egg, Chicken), 18:1 DOPG 1,2-dioleoyl-sn-glycero-3-phospho-(1′-rac-glycerol), 18:1 DOPC 1,2-dioleoyl-sn-glycero-3-phosphocholesteroline, 18:1 DOPE 1,2-dioleoyl-sn-glycero-3-phosphoethanolamine, LissRhod PE 1,2-dioleoyl-sn-glycero-3-phosphoethanolamine-N-(lissamine rhodamine B sulfonyl), 18:1 DGS-NTA(Ni) 1,2-dioleoyl-sn-glycero-3-[(N-(5-amino-1-carboxypentyl)iminodiacetic acid)succinyl] (nickel salt), 18:1 DOTAP 1,2-dioleoyl-3-trimethylammonium-propane, 18:1-12:0 Biotin PE 1-oleoyl-2-(12-biotinyl-(aminododecanoyl))-sn-glycero-3-phosphoethanolamine, DSPE-RGD 1,2-distearoyl-sn-glycero-3-phosphoethanolamine-N-[4-(p-(cysarginylglycylaspartate-maleimidomethyl)-cyclohexane-carboxamide], 18:1 1,2-dioleoyl-sn-glycero-3-phospho-(1'-myo-inositol) (ammonium salt), 18:1 1,2-di-(9Z-octadecenoyl)-sn-glycero-3-phospho-L-serine (sodium salt), 18:1 1,2-di-(9Z-octadecenoyl)-sn-glycero-3-phosphate (sodium salt), cholesterol, 18:1 1-2-di-(9Z-octadecenoyl)-sn-glycerol, 18:0 N-stearoyl-D-erythro-sphingosylphosphorylcholin, 18:1 PEG350 PE 1,2-dipalmitoyl-sn-glycero-3-phosphoethanolamine-N-[methoxy(polyethylene glycol)-350], 18:1 PEG750 PE 1,2-dioleoyl-sn-glycero-3-phosphoethanolamine-N-[methoxy(polyethylene glycol)-750], 18:1 PEG1000 PE 1,2-dioleoyl-sn-glycero-3-phosphoethanolamine-N-[methoxy(polyethylene glycol)-1000], and extrude set with 50 nm pore size polycarbonate filter membranes were purchased from Avanti Polar Lipids, USA. NHS Palmitic acid N-hydroxysuccinimide ester and N-(4-carboxybenzyl)-N,N-dimethyl-2,3-bis(oleoyloxy)propan-1-aminium (DOBAQ) were purchased from Sigma Aldrich, Germany. Atto488 conjugated 1,2-dipalmitoyl-sn-glycero-3-phosphoethanolamine was purchased from Atto-Tec GmbH, Germany. All lipids were stored in chloroform at -20 °C and used without further purification.

3.1.2 Dyes and staining agents

DyLight 405 NHS Ester, AlexaFluor647-NHS, Anti CD3 (16-0038-81), Anti CD3-Alexa488 (53-0037-42), Hydroxypyrene-1,3,6-trisulfonic acid trisodium salt (HPTS),

Vybrant DiI Cell-Labelling Solution, Alexa Fluor 488 NHS Ester, Hoechst 33342, CellTracker Blue CMAC dye, CellTracker Green CMFDA dye, CellRox Green reagent, Fluo-4 AM-ester, o-nitrophenyl EGTA tetrapotassium, LysoTracker Green DND-26 dye and wheat germ agglutinin (WGA)-AlexaFluor conjugates were purchased from Thermo Fischer Scientific, Germany. Atto425-Biotin, <50 nm Fe2O3 nanoparticles and Phalloidin-FITC were purchased from Sigma Aldrich, Germany. Fluoresbrite YG Microspheres 1.00 µm were purchased from Polysciences Europe, Germany.

3.1.3 Cell culture materials

Dulbecco's Modified Eagle Medium (DMEM) high Glucose, 1:1 DMEM:F12, RPIM-1640, FluoroBrite DMEM (high glucose), trypsin-EDTA (0.05 %) with phenol red, GlutaMax Supplement, L-Glutamine (200 mM), phosphate buffered saline, heat-inactivated as well as exosome-depleted fetal bovine serum and penicillin/streptomycin (10,000 U/mL) were purchased from Thermo Fischer Scientific, Germany. Heat-inactivated horse serum, menadione and human male serum were purchased from Sigma Aldrich, Germany. 8-well cell exclusion inserts were purchased from Ibidi, Germany. The ELISA kit for the quantification of human pro-collagen I alpha was obtained from Abcam, UK.

3.1.4 Purified proteins, peptides, antibodies, recombinant proteins and RNAs

Recombinant N-terminal His-tagged human CD63 (amino acids 103-203), basic fibroblast growth factor (aa 10-155), Epithermal growth factor, AlexaFluor405 dye and custom synthesized GALA peptide (EAALAE ALAEALAEHLAEALAEALEALA) were purchased from Thermo Fischer Scientific, Germany. Lectin (Wheat Germ Agglutinin), bradykinin, human Interleukin 2, recombinant insulin, bovine catalase, fibronectin from bovine plasma and poly-L-lysine were purchased from Sigma Aldrich, Germany. His-tagged Protein G was purchased from BioVision, USA. His-tagged NrCAM 8425-NR-050 and human recombinant cadherin were purchased from R&D Systems, USA. Anti-VE-Cadherin and anti-alpha4-integrin (CD49d) antibodies were purchased from Santa Cruz (Sc-28644) and Millipore (MAB1383). Recombinant human CD95L was purchased from BioLegend, USA. Bovine albumin fraction V (BSA) was obtained from Carl Roth, Germany. Tat-HIV-GFP peptides were a generous gift from Rüdiger Arnold (Life Science Lab, German Cancer Research Centre). Recombinant N-terminal His-tagged human CD9 (amino acids 112-195) was purchased from Novus Biologicals, Germany. Recombinant

N-terminal His-tagged human TSG101 (amino acids 1-145) was purchased from Fitzgerald, USA. Recombinant N-terminal His-tagged human CD81 (amino acids 113-201) was purchased from MyBioSource, USA. miRIDIAN micro RNA mimics (hsa-miR-21-5p, hsa-miR124-3p, hsa-miR-125b-5p, hsa-miR-126-5p, hsa-miR-130a-3p, hsa-miR-132-3p) were purchased from Horizon Dharmacon, USA.

3.1.5 Cell lines, primary cell cultures and viruses

A431, Hela, Hs386, SH-SY5Y, Jurkat and BJ cell lines were obtained from the American Type Culture Collection, USA. REF52 cell lines (Missirlis et al., 2016) were a generous gift from Prof. Benjamin Geiger (Weizmann Institute, Rechovot). PC12 cells were a generous gift from Amin Rustom (Institute for Neurobiology, Heidelberg). HaCaT cells were obtained from CLS cell line service, Germany. Primary mouse hippocampal neurons were obtained from the Institute of Neurobiology, Interdisciplinary Center for Neurosciences in Heidelberg, Germany. Purified baculovirus specimens were obtained from Martin Pelosse (Commissariat à l'énergie atomique et aux énergies alternatives, CEA Grenoble, France). Purified K562 exosomes (HBM-K562) were obtained from Hansa BioMed/Lonza, Switzerland. Pre-wounded full thickness human organotypic skin cultures, respective culture media, and histological sample preparation services were obtained from MatTek Cooperation, USA.

3.1.6 Mass Spectrometry

Methanol LC_MS Chromasolv (≥99.9) was purchased from Honeywell/Riedel-de Haën. Dichloromethane SupraSolv for gas chromatography MS was purchased from Merck Millipore. ammonium acetate for mass spectrometry, eluent additive for LC-MS, polyethylenimine (branched, Mw ~25,000) were obtained from Sigma Aldrich, Germany. Rotisolve water was purchased from Carl Roth, Germany.

3.1.7 Microfluidics

Polydimethylsiloxan (PDMS) Sylgard 184 was purchased from Dow Corning, USA Perfluoropolyether-polyethylene glycol (PFPE-PEG) block-copolymer fluorosurfactant was purchased from Ran Biotechnologies, USA. FC-40 oil was purchased from io-li-tec, Germany. 1H,1H,2H,2H-Perfluoro-1-octanol (PFO) de-emulsifier was purchased from Sigma Aldrich, Germany. 97 % L-cysteine and 50 nm Au nanoparticles were purchased from Sigma Aldrich, Germany.

3.2 Methods

3.2.1 Microfluidic-based GUV production

DsGUVs were produced from SUV liposomal precursors with lipid compositions detailed in Table 5 following previously published protocols (Haller et al., 2018; Weiss et al., 2017). Lipid stocks were kept in chloroform, sealed with polytetrafluorethylen tape and stored at -20°C in the dark. Chloroform dissolved lipids were mixed at desired ratios according to the pre-designed lipid formulation in glass vials and dried under a gentle nitrogen stream or in a vacuum desiccator. Subsequently, the dried lipid films were rehydrated for 30 min with the production buffers specified in Table 5 to a final lipid concentration of 3 mM. In order to produce liposomes, these mixtures were shaken on a horizontal shaker at 600 rpm for 5 min. To produce SUVs, the liposome solution was extruded through a 50 nm pore size polycarbonate filter. In order to achieve homogeneous size distribution, extrusion was performed at least 9 times. Obtained solution were either used directly after production or stored at 4°C for up to 3 days.

Microfluidic devices (regular T-junction droplet production devices and droplet-splitting devices) were fabricated from PDMS. Production was performed following previously published protocols using photo- and soft-lithography methods (Janiesch et al., 2015; Weiss et al., 2017). An Elveflow OB1 MK3-microfluidic flow control system was used to adjust and control flow in the microfluidic devices. If not specified otherwise, GUVs were formed within microfluidic droplets using SUV solutions diluted to a final lipid concentration of 1.5 mM introduced into the aqueous channel of the devices. 1.25 mM $PFPE_{(7000\ g/mole)}$-$PEG_{(1500\ g/mole)}$-$PFPE_{(7000\ gr/mole)}$ triblock surfactant dissolved in FC-40 was used for the formation of negatively charged GUVs. 0.5% RAN Biotechnologies PEG-based fluorosurfactant diluted in FC-40 was used for formation of positively charged GUVs. 1.25 mM $PFPE_{(2500\ g/mole)}$-$PEG_{(600\ g/mole)}$-$PFPE_{(2500\ g/mole)}$ triblock surfactant diluted in FC-40 was used to produce GUVs containing DOBAQ lipids. For all microfluidic droplet production procedures, a water to oil phase ratio of approximately 1:4 was used. Droplets formed at the flow-focusing junction, and if desired splitted by a subsequent splitting architecture, were collected from the outlet of the microfluidic device and collected in a microcentrifuge tube. dsGUV were equilibrate at 4°C for a minimum of 120 min before release.

For the release procedure, excess oil phase was removed from the microcentrifuge tube and the remaining droplet layer was mixed in a volume ratio of 1:1:1 (aqueous production buffer : aqueous release buffer (see Table 5) : destabilizing PFO). After 30 min

of equilibration, the upper aqueous layer containing the released GUVs, was transferred into a microcentrifuge tube. Release buffer was added to a final volume of 2 ml and this GUV solution was centrifuged at >10,000 g for 15 min in order to remove any ruptured vesicles, debris or free floating SUVs from the sedimented GUV population. Subsequently, the supernatant was removed and the GUV pellet was resuspended in PBS to the desired concentration.

3.2.2 Production of fsEVs

For the production of fsEVs, a previously published protocol for one-pot bulk assembly of dsGUVs was adopted for shear stress emulsification (Göpfrich et al., 2019). For this, a triblock PEG2500-PFPE600-PEG2500 surfactant was diluted to a final concentration of 1.25 mM in FC-40 oil and used as the oil phase for w/o-droplet production. The water-phase was composed of SUVs and, if desired, miRIDIAN RNAs. For fsEV formation, SUVs were produced as detailed for microfluidic dsGUV production (see section 3.2.1): lipid chloroform stock solutions were mixed in glass vials and dried with a gentle nitrogen stream or in a vacuum desiccator before rehydration with PBS (supplemented with 10 mM $MgCl_2$) to a final lipid concentration of 6 mM. After 15 min incubation, the glass vials were sequentially shaken for 5 min at 1000 rpm on a horizontal shaker and the resulting liposomes were extruded at least 9 times through a 50 nm pore size filter. The final SUV solution was diluted in PBS containing 10 mM $MgCl_2$ to a final concentration of 3 mM and if desired, the miRIDIAN RNAs. The liquid was added to the oil phase in a 1:2 ratio and emulsified with an Ultra Turrax IKA T10 basic emulsifier for 60 sec at approximately 26,300 rpm. The resulting dsGUVs were incubated in the dark at 4°C for at least 120 min. The release and cleaning procedures were performed following the protocols for dsGUV release and cleaning of GUVs (see section 3.2.1).

The total amount of NTA-(Ni^{2+})-coupled lipids for coupling CD peptides was calculated from the lipid ratio. A 1:2 molar excess of the His-tagged peptides was added to the fsEV solutions and allowed to couple at 37°C protected from light for 60 min. The fsEV solution was then centrifuged at >10,000 rpm for 15 min. The supernatant, which contained unbound peptides was removed and the fsEV pellet resuspended in PBS. If not specified otherwise, miRIDIAN miRNA mimics were added to the SUV mixture at a final concentration of 145 nM.

For confocal microscopy and TEM analysis, fsEVs were produced from SUV containing 41mol% cholesterol, 16mol% SM, 15mol% DOPC, 11mol% DOPS, 6mol%

DOPE, 5mol% DOPG, 2mol%PA, 1mol% DAG, 1mol% PI, 1mol% LissRhod PE, and 1mol% DGS-NTA(Ni^{2+}) in PBS containing miRIDIAN RNA and 10 mM $MgCl_2$. In order to block unspecific protein-lipid interactions, fsEVs were transferred to a 0.1% BSA solution and Alexa488 labelled CD9 as well as 500 nM Hoechst33342 were added to the GUVs. For this analysis, miRIDIAN mimics were used in a total of 40 nM.

3.2.3 Microfluidic production of synthetic organelles

For the production of GUVs harbouring catalase in their lumen, purified bovine catalase was added to a final concentration of 2.7 µM to the SUV solution used for dsGUV production. For the production of GUVs which contained np-EGTA, np-EGTA and $CaCl_2$ were mixed at equimolar concentrations of 10 µM. This mixture was also added to the SUVs solution applied as aqueous phase for droplet production. During these procedures, all possible steps were carried out in the dark or under red light. For the incorporation of Fe_2O_3 nanoparticles into the dsGUVs, the nanoparticles were dissolved to a final concentration of 100 µg/ ml in 0.1% w/v bovine serum albumin in PBS. This mixture was applied together with the SUV solution was aqueous phase for droplet production.

3.2.4 Dynamic Light scattering

For measurements of fsEVs, GUV and SUV hydrodynamic radii and zeta potentials, a Malvern Zetasizer Nano ZS (Malvern Panalytical, Germany) was used. Measurements were performed in PBS at a total lipid concentration of 15 µM. The temperature of the cuvette and the measurement chamber was equilibrated for 600 sec (300 sec for fsEVs) to 25°C. Measurements were performed in three technical replicates at a scattering angle of 173° and individual runs per measurement were automatically selected by the build-in run-number selection of the Malvern Software. For analysis of lipid vesicles, a refractive index of 1.42 was set and die solvent properties were set to $\eta = 0.8882$, $n = 1.33$ and $\varepsilon = 79.0$. For GUV zeta potential measurements, the chamber and sample were equilibrated for at least 120 sec and at least two individual measurements were performed. To analyse the pH dependent zeta potential of DOBAQ containing GUVs, GUVs were dissolved to a final concentration of 15 µM in PBS adjusted to the desired pH with 4 N NaOH or 10% HCl. The DLS measurements on SUVs and GUVs were partially performed by Dennis Zhang in the course of his Bachelor thesis in our Department.

3.2.5 Cryogenic transmission electron microscopy

For cryogenic transmission electron microscopy, GUV samples were prepared by applying 2.5 µL of the GUVs solution onto a glow-discharged 200 mesh C-flat holey carbon-coated multihole grid (Protochips, USA) or ultrafoil goldgrids R 2/2 (Quantifoil GmbH, Germany). The grids were then blotted for 4 seconds and subsequently plunge-frozen at 100% humidity in liquid ethane using a Vitrobot Mark IV (FEI NanoPort, The Netherlands) and stored in liquid N_2. The grids were imaged using a FEI Tecnai G2 T20 twin transmission electron microscope (FEI NanoPort, The Netherlands) operated at 200 kV. Micrographs were recorded using a FEI Eagle 4k HS, 200 kV CCD camera at a dose of ≈40 electrons/$Å^2$.

3.2.6 Assessment of droplet homogeneity

In order to assess the transmission heterogeneity of the intraluminal droplet content, w/o droplets were formed at a flow-focusing junction of a 5x droplet splitting device or of a simple droplet formation device without further splitting architecture. A PBS solution supplemented with 10 mM $MgCl_2$, 1 mM AlexaFluor405, 1 µM His-tagged GFP, $1.08x10^9$ particles/ ml Fluoresbrite YG Microspheres (D=1.00µm) and 1.5 mM Rhodamine-labelled SUVs was applied as aqueous phase through the water-inlet channel. Droplets were collected in a microcentrifuge tubes and imaged by confocal microscopy in a custom-build observation chamber (one cover slip mounted in top of a glass slide with a double-sided sticky-tape spacer (approx. 200 µm)). Mean droplet-lumen fluorescence intensity was measured from single plane fluorescence confocal microscopy images by automated global threshold segmentation and the ImageJ particle analyser plug-in. The coefficient of variation was calculated by dividing the standard deviation of the droplet-intensities through their average intensity.

3.2.7 Quantification of GUV release efficiency and stability

GUV and fsEV concentrations (vesicles/ ml) were determined with a Neubauer chamber mounted on a fluorescence microscopy. For release efficiency measurement, the concentration of dsGUVs was assessed by manual counting of a homogeneously dispersed droplet emulsion. Prior to the measurements, the droplets were collected in a microcentrifuge tube and placed on a horizontal shaker at 100 rpm for 5 min in order to disperse the droplets in the oil phase. Released GUVs were visualized inside the Neubauer chamber by fluorescence excitation of Rhodamine B conjugated lipids incorporated into

the SUV formulation. GUV concentration after mechanical agitation was measured accordingly in regular time intervals.

For incubation of fsEVs and GUVs with cells, a specific final concentration of total lipids, rather than a specific amount of vesicles was added. To this end the total lipid concentration after GUV/ fsEV release was quantified using the total lipid fluorescence (of Rhodamine B- or Atto488-conjugated lipids introduced in the initial SUV formulation) of the obtained GUV/ fsEV solution with a fluorescence Infinite M200 TECAN plate reader (TECAN, Switzerland) controlled by TECAN iControl software with an in-built gain optimization and excitation/emission setting adjusted to 550/585 nm. The obtained fluorescence value was referred to a standard SUV dilution series produced from the same SUV batch used for dsGUV production, which was also measured with the same setting in a concentration range between 750 µM and 11.7 µM and fitted to a one-phase exponential decay curve (Figure 9). Typical lipid concentrations used for incubation with cells were 1.5 µM – 50 µM.

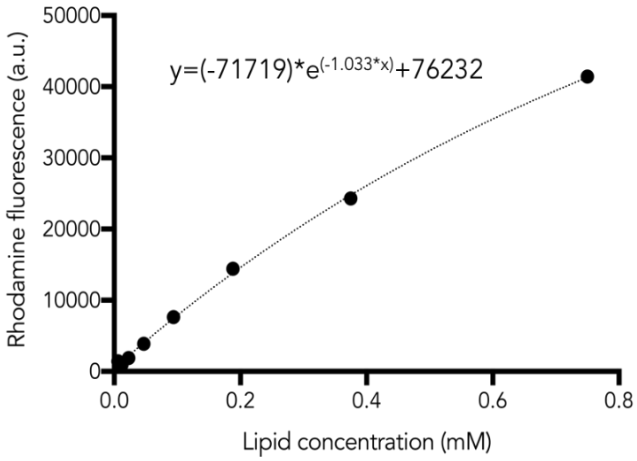

Figure 9 | Fluorescence intensity measurement of SUV dilution series. Mean rhodamine fluorescence intensities of an exemplary SUV (series containing 1mol% LissRhod PE lipids) dilution at 8 different concentrations are shown. The dotted line is the one-phase exponential decay curve fit and the corresponding equation is given in the graph. For example, for GUVs produced with these SUVs a mean fluorescence signal intensity of 5888 was measured, which corresponds to a concentration of 72 µM on this

3.2.8 Cell culture

REF52 cells, MDCK cells, A431, A431D, HaCaT, BJ (primary dermal foreskin fibroblasts), Hela and Hs386 cells were routinely cultured in Dulbecco's Modified Eagle Medium supplemented with 1% L-glutamine, 4.5 g/l glucose, 1% penicillin/streptomycin and 10% fetal bovine serum. SH-SY5Y cells were cultured in a 1:1 mixture of

DMEM:F12 supplemented with 1% penicillin/streptomycin, 1% L-glutamine and 10% fetal bovine serum. Jurkat cells were cultured with RPMI-1640 medium supplemented with 1% penicillin/streptomycin and 10% fetal bovine serum. PC12 cells were cultured with RPIM-1640 medium supplemented with 1% penicillin/streptomycin, 1% L-glutamine, 5% fetal bovine serum and 10% heat-inactivated horse serum. K562 cells were cultured in suspension in Iscove's modified Dulbecco's Medium supplemented with 10% exosomes free fetal bovine serum. Cell lines were incubated at 37°C and 5% CO_2 humidified atmosphere and passaged at ~80% confluency by treatment with 0.05% trypsin/EDTA. Suspension cells were passaged every other day by transferring 3 ml of the cell suspension to 10 ml of fresh cell culture medium. Cell culture routines were performed with the help of Sabine Grünewald (Department for Cellular Biophysics, MPI for Medical Research)

3.2.9 Assessment of cell proliferation

In order to perform high-throughput assessment of cell proliferation, a previously published well-plate based protocol for quantitative assessment of Hoechst33342 staining was applied (Gilbert et al., 2011). For this, 15,000 HaCaT or A431 cells per well were seeded in a flat-bottom transparent 96-well plate in 200 µl culture medium. The fsEVs to be tested were added just after cell seeding and incubated for 48 hours. All wells were subsequently washed twice with PBS using a multichannel pipette and subsequently incubated with ice-cold culture medium supplemented with 10 µM Hoechst33342. Then, the culture medium was removed and the wells were washed twice with 100 µl PBS in order to remove any excess Hoechst33342. The Hoechst 33342 signal (corresponding to the number of cells) in each well, correlating with the number of cells, was afterwards measured with an Infinite M200 TECAN plate reader controlled by TECAN iControl software with an in-built gain optimization and excitation/emission setting adjusted to 380/460 nm. All measurements were performed in biological triplicates.

3.2.10 Cell staining

For visualization of the nuclei of living cells, Hoechst33342 at a final concentration of 5 µg/ml was added either directly to the cell culture medium of the. Cell cytoplasm was stained with CellTracker Blue CMAC dye and CellTracker Green CMFDA dye following the manufacturer's recommendations. For analysis of lysosomal degradation, lysosomes were stained with the green-emitting LysoTracker Green DND-26 dye following the

manufacturer's instructions. For staining of cell membranes, wheat germ agglutinin (WGA)-AlexaFluor conjugates were used. To this end, a final concentration of 50 µg/ml WGA conjugates was directly added to the fully supplemented growth medium for 10 min at room temperature. In order to reduce endocytic dye uptake in the course of plasma membrane turn-over, once stained, cells were handled at room temperature for imaging. To stain endosomal membranes and compartments, 5 µg/ ml WGA-AlexaFluor conjugate was added to the cell cultures together with the GUVs or fsEVs and incubated for 24 hours before analysis. In this procedure, cell membranes are consecutively stained with WGA and when endosomal compartments, macropinocytomes or caveolae are formed, the fluorescent WGA is incorporated alongside.

3.2.11 Induction of oxidative stress and ROS quantification

To induce oxidative stress in HaCaT cell cultures, cells were seeded in 96-well plates to form a confluent monolayer (≈50 000 cells per well) after 24 hours of incubation. Subsequently, peroxisome-like SOs were added to the cells and incubated for another 24 hours to allow SOs internalization. Afterwards, non-internalized SOs were washed away by rinsing twice with PBS. Next, 25 µM menadione was added and the plates were incubated for 1 hour. CellRox Green was then added following the manufacturer's instructions and the CellRox Green fluorescence was quantified using an Infinite M200 TECAN plate reader controlled by TECAN iControl software with an in-built gain optimization and excitation/emission setting adjusted to 488/525 nm.

3.2.12 Assessment of SOs Containing npEGTA-Caged Ca^{2+}

To introduce npEGTA-caged Ca^{2+} containing SOs into BJ dermal fibroblast, the cells were seeded to form a confluent monolayer in LabTek glass-bottom microscopy chamber slides after 24 hours. Subsequently, respective SOs were added to the cells and incubated overnight to allow internalization. In order to avoid uncontrolled npEGTA cleavage, all procedures were carried out if possible in the dark or under red light illumination. Cells were then stained with cell permeable fluo-4 AM ester following the manufacturer's recommendations and analysed by fluorescence confocal microscopy. For UV-induced Ca^{2+} uncaging, cells were first rinsed twice with PBS in order to remove non-uptaken GUVs and then illuminated with a laser scanning confocal microscope (Zeiss LSM 800 with a 20× Plan-Apochromat 0.8 M27 objective) in the region of interest which contained

the uptaken SOs. Illumination was performed at full laser power for five iterations and the fluo-4 signal was subsequently recorded over 20 minutes.

To introduce npEGTA-Ca^{2+}-containing GUVs into water-in-oil droplets, a $MgCl_2$-free PBS solution containing the respective GUVs was employed as aqueous phase. Moreover, this solution contained a final concentration of 200 µM fluo-4 to image the Ca^{2+} release. In order to prevent dsGUV formation or attachment of the introduced GUVs at the droplet periphery, a FC40 solution containing 1% w/v commercially available PFPE carboxylic acid-free surfactant was applied as oil phase. Finally, the water-in-oil emulsion was produced following a previously published manual shaking protocol (Göpfrich et al., 2019). Quantification of the fluo-4 mean fluorescence intensities was performed by manual selection of areas of interest using ImageJ software in the time-laps microscopy series.

3.2.13 EV isolation from K562 cell cultures

Extracellular vesicles from K562 cultures were isolated by differential (ultra-) centrifugation from conditioned cell culture medium. K562 cells were cultured as suspension cultures in 50 ml Iscove's modified Dulbecco's Medium containing 10% exosome free serum at 37°C and 5% CO_2 atmosphere for 48 hours to a final cell concentration of $5x10^5$ cells/ ml. Subsequently, a first centrifugation step of 300 g at 4°C for 10 min was performed to pellet the cells and cell debris. The supernatant was then passed through a 0.22 µm pore size filter and EVs were pelleted at 100,000 g at 4°C for 75 min with a Beckmann Coulter Optima XE-100 ultracentrifuge (Beckmann Coulter Life Sciences, Germany) in a JA-20 fixed angle rotor (k-factor 770). The supernatant was afterwards discarded and the EV-pellet was washed with 50 ml ice cold PBS before performing another ultracentrifugation step under the same conditions as before. The final EV pellet was resuspended in 1 ml PBS. For quantification of the total protein concentration of the EV solution, the absorbance at 280 nm was measured with a Nanodrop ND-1000 spectrophotometer (Thermo Fischer Scientific, Germany). K562 EVs were fluorescently stained with Vybrant DiI cell labelling solution diluted 1:1000 with the isolated EV solution for 15 min at room temperature in the dark. In order to remove and residual DiI, the solution was afterwards centrifuged at 100,000 g at 4°C for 75 min and the final EV pellet was resuspended in 1 ml PBS.

3.2.14 Quantitative assessment of collagen deposition

In vitro collagen deposition of BJ dermal fibroblast was quantified by enzyme-linked immunosorbent assay (ELISA). For this, BJ dermal fibroblasts were seeded in 96-well, flat-bottom transparent cell culture plates at a density of 20,000 cells/ well and cultured for 24 hours. Cells were then washed twice with PBS and 200 µl fresh cell cultured medium supplemented with 10 µM (total lipid concentration) of the fsEV-formulations to be tested. The fsEVs were incubated together with the cells for 24 hours and subsequently ELISA analysis for human pro-collagen Iα was performed following the manufacturer's instructions.

3.2.15 Confocal microscopy and live cell imaging

Fluorescence confocal microscopy was performed with a LSM 800 (Carl Zeiss AG, Germany) laser scanning microscope For imaging, a 20x (Objective Plan-Apochromat 20x/ 0.8 M27, Carl Zeiss AG) or a 63x immersion oil objective (Plan-Apochromat 63x/ 1.40 Oil DIC, Carl Zeiss AG) was used. Image analysis was performed with ImageJ (NIH) and special care was taken not to obscure or eliminate any information from the original image. Image adjustments like brightness and contrast corrections or background corrections for image quantification were always performed on the whole image. Images showing speckled noise signals were processed with a 2-pixel median filter. 8-well Nunc LabTeK glass bottom culture slides (Thermo Fischer Scientific, Germany) with a total culture volume of 400 µl were used for culturing cell lines for subsequent analysis by confocal microscopy. If aldehyde fixation was required during sample processing for confocal microscopy, cell cultures were washed twice with PBS and afterwards fixed with 2-4% PFA for at least 20 min.

For epifluorescence microscopy and live cell fluorescence time-laps imaging, a Leica DMi8 inverted fluorescent microscope (Leica Microsystems, Germany) equipped with a sCMOS camera and 10x HC PL Fluotar (NA 0.32, PH1) objective was used. For epifluorescence microscopy, cells were cultured in 8-well Nunc LabTeK glass bottom culture slides and if green emitting fluorophores (e.g. CellTracker Green CMFDA) were imaged, FluoroBrite DMEM (high glucose) medium supplemented with GlutaMAX, 10% FBS and 1% enicillin/ streptomycin was used in order to reduce the background signal.

3.2.16 Analysis of magnetotactic behaviour

To analyse the deflection of Fe2O3 nanoparticle inside dsGUVs, time-lapse confocal microscopy recordings were performed. While avoiding any mechanical shaking of the setup to prevent vibration-induced deflections, an AlNiCo magnet was placed next to the sample during acquisition. To verify the intracellular uptake of magnetosome-mimicking SOs, normal rat kidney cells were seeded in 24 well plates at a density of 300,000 cells per well and cultured overnight. SOs were then added and incubated for 24 hours to allow internalization to proceed. Cell layers were subsequently washed twice with PBS in order to remove any non-uptaken SOs. Next, an AlNiCo magnet was placed alongside to the culture plates. The cultures were maintained in this configuration 48 hours and afterwards fixed with 4% para-formaldehyde for 20 min. Cells were then stained with 2 µg/ mL Hoechst 33342 and phalloidin-TRITC for 1 hour before performing bright field and epifluorescence microscopy. The same procedure was applied for the experiment performed with primary hippocampal neurons with the exception that the incubation time was prolonged to 96 hours in order to account for the reduced migration of the neurons. For automated analysis of the local cell densities within the wells, images segmentation based on global histogram-based intensity thresholding was performed with nuclear staining images. The images were separated manually into the corresponding regions before the analysis and particles (corresponding to individual nuclei) were counted with the built-in particle counter from ImageJ software after watershed separation of overlaying nuclei.

3.2.17 Transmission electron microscopy

For TEM analysis, cells were incubated for 16 hours with GUVs and subsequently fixed in 2.5% glutaraldehyde dissolved in a 0.1 M Na_3PO_4 buffer at room temperature for 30 min. A second fixation step with 0.4% uranyl acetate was subsequently performed overnight. For dehydration of the sample, an ethanol series with 50%, 60%, 70%, 80%, 90% and 100% ethanol was performed and samples were afterwards embedded in resin over night at 60°C. After complete polymerization, 85 nm ultrathin sections were prepared and contrasted by staining with lead acetate and osmium tetroxide. Images were acquired with a Zeiss EM 10 CR transmission electron microscope (Carl Zeiss AG, Germany). If needed, brightness, image contrast or sharpness was adjusted using the built-in ImageJ plug-ins. All TEM experiments were performed with technical assistance of Andrea

Hellwig (Interdisciplinary Centre for Neurosciences, Dept. of Neurobiology, University of Heidelberg).

3.2.18 Flow cytometry

To analyse the attraction of RDG-functionalized GUVs and Jurkat suspension cells, flow cytometry analysis was performed. For this, RDG- and rhodamine-functionalized GUVs were incubated with Jurkat cells for 24 hours and subsequently centrifuged for 5 min at 250 g in order to separate the unbound GUVs from the Jurkat cells. The cell pellet was subsequently resuspended in fully-supplemented cell culture medium and GUV fluorescence originating from GUVs bound to or uptaken by the cells was quantified using a BD LSRFortessa Cell Analyzer (BD Bioscience, Germany) in the PE channel ($\lambda_{em\ max}$= 575). Based on the forward- and side scatter intensities, the cell population of Jurkat cell was gated to discriminate between debris, clumps and free-floating GUVs. With this selected cell population, the GUV-fluorescence intensity was quantified for all conditions tested. All flow cytometry experiments were performed with the help of Silvia Antona (Dept. Cellular Biophysics, MPI for Medical Research).

3.2.19 Attraction assay

For quantification of GUV- and fsVE-cell interactions and uptake fsEVs, quantification assays were performed. For this, cells cultures were seeded in triplicates in 100 µl of their corresponding growth medium at cell densities resulting in confluent monolayer after 24 hours of incubation in 96 flat-bottom well-plates. Subsequently, fsEVs or GUVs (labelled with LissRhod PE lipids) to be tested for cell-interactions, were added to a final lipid concentration of 1.5 µM. After incubation for 24 hours, rhodamine fluorescence intensity in each well was measured using an Infinite M200 TECAN plate reader (TEACAN, Germany) controlled by TECAN iControl software with excitation/emission setting adjusted to 550/585 nm and the built-in gain optimization. Afterwards, in order to remove non-bound or non-up taken GUVs and fsEVs, cells were washed 3x with 100 µl PBS using a multichannel pipette and residual fluorescence intensity in each well was measured again as described above. In order to account for any variation in sample preparation, fluorescence intensity after washing (corresponding to GUVs/ fsEVs with strong attraction to cells) was normalized to the intensity before washing (corresponding to the total amount of GUVs/ fsEVs added). All samples were measured at 4 individual positions per well in order to account for variations in cell monolayer density and in triplicates. In

order to compare the specific attraction of GUVs biofunctionalized with proteins to specific cell lines, the corresponding attraction values (= intensity after washing divided by intensity before washing) were normalized to the attraction value of BSA functionalized GUVs obtained for each cell line. This was done, in order to reference all attraction values for each cell type, which could display variations e.g. in uptake-kinetics, surface topology, membrane turn-over, to a common moderately non-reactive protein.

For the analysis of attraction and binding between Jurkat cells and anti-CD3 functionalized GUVs, 3 µM of GUVs were incubated with the cells for 24 hours and fluorescence confocal microscopy was performed afterwards. Before imaging, Jurkat cells were labelled with Hoechst33342 and WGA-AlexaFluor647.

3.2.20 Quantification of preferential GUV uptake in co-culture

In order to assess and quantify preferential uptake of NrCam-functionalized GUVs in co-culture experiments, SH-SY5Y/ Hs683 co-cultures were produced. For this, SH-SY5Y and Hs683 cell lines were stained individually with CellTracker Blue CMAC and CellTracker Green CMFDA, respectively. After staining, cells were seeded in 8-well Nunc LabTeK glass bottom culture slides as co-cultures in a 10:1 (SH-SY5Y:Hs683) ratio in F12:DMEM (1:1) culture medium supplemented with 1% penicillin/ streptomycin, 1% L-glutamine and 10% fetal bovine serum. Subsequently, GUVs composed of 1mol% LissRhod PE, 20mol% PEG750 PE, 58mol% EggPC, 20mol% EggPG and 1mol% palmitic acid-NHS coupled to 1.5 µM His-tagged recombinant NrCAM were added to the cultures. Cell cultures were then washed 3x with PBS and fixed with 4% PFA for 20 min at room temperature and fluorescence confocal microscopy imaging was performed with appropriate laser excitation and emission filter settings. Form respective single plane confocal images of the CellTracker staining, the total area of Hs683 and SH-SY5Y cells in a field of view was deduced by automated global thresholding. Moreover, the total number of GUVs in respective cell areas was counted and normalized to the total cell area.

3.2.21 Organotypic dermal cultures

Pre-wounded, single donor, human organotypic full thickness skin models derived from neonatal-foreskin tissue were obtained from a commercial distributer (MatTek Corporation, USA). The 3D organotypic models were composed of an “epidermal” keratinocyte layer wounded by punching and a “dermal” layer composed of fibroblast embedded in a collagen matrix. The models were pre-incubated and cultured at an air-liquid interface as recommended by the manufacturer. For analysis of wound closure,

tissues were equilibrated for 16 hours at 37°C in 5% CO_2 atmosphere. After equilibration, a total volume of 2 µl PBS containing fsEVs (1 µM total lipids) with the desired composition (or PBS-only buffer controls or 2% human male serum), were added directly onto the 3 mm wound side. Wound healing was allowed to proceed for 48 hours at 37°C in 5% CO_2 atmosphere. Tissues were subsequently removed from their holders, tipped in PBS and fixed with 10% formalin solution overnight at 4°C. Wound size was quantified from histological slides stained with haematoxylin/eosin by measuring the distance from the last visible epidermal cells of the wound periphery, as marked by strong eosin staining, with ImageJ (NIH, USA). For quantification of the thickness of the regenerated epidermal layer, the epidermal thickness was measured in a 100 µm distance from the wound periphery with ImageJ (NIH, USA). For each tissue, histological slides were prepared by sectioning the wound in the middle and cutting three subsequent slices on each wound side. All experiments with organotypic cultures were performed with the help of Franziska Dietrich (Dept. Cellular Biophysics, MPI for Medical Research).

3.2.22 Cell exclusion assay

In vitro 2D wound healing assays were performed with 4-well silicone cell exclusion inserts for 12-well cell culture plastic plates with a gap width of 500 µm. HaCaT or A431 cells were seeded at a cell density of 40,000 cells/ well and incubated over night with 110 µl DMEM cell culture medium supplemented with 10% fetal bovine serum, 1% L-glutamine, 4.5 g/l glucose and 1% penicillin/streptomycin. In order to avoid evaporation from this small culture volume, 2 ml of medium was added to the wells outside of the inlets. Afterwards, 10 µM final lipid concentration of respective fsEV-formulations were added to the monolayers and incubated for 24 hours. Subsequently, the exclusion inserts were carefully removed using sterile stainless-steel tweezers. The artificial wound was allowed to close for 16 hours. In order to quantify the cell free area after “healing”, cells were fixed by removing the cell culture medium and adding 4% PFA for a minimum of 20 min. Phase contrast images of the fixed cultures were taken using a Leica DMi8 inverted fluorescent microscope equipped with a sCMOS camera and 10x HC PL Fluotar (NA 0.32, PH1) objective and the cell free areas were quantified manually with ImageJ software. For each condition, four “artificial” wound sides were quantified.

3.2.23 RNA-sequencing transcriptome analysis

For RNA-sequencing analysis, 500,000 HaCaT cells were seeded into 12-well plates and allowed to adhere for 24 hours in 1 ml of culture medium. Subsequently, fsEVs with the desired compositions were added to the cells to a final total lipid concentration of 30 µM and incubated for 24 hours. Cells were either treated with the soluble fsEV components or left untreated as control conditions. The well-plates were then transferred on ice and washed twice with ice-cold PBS. Afterwards, 1 ml of ice-cold PBS was added to each well and the cell layers were scraped off with a spatula. The solution was then transferred into 2 ml microcentrifuge tubes and an additional 1 ml of ice-cold PBS was added to the wells in order to recover residual cells. This 1 ml residue was then also transferred to the microcentrifuge tubes and the cells were pelleted at 13,000 rpm for 2 min. As much as possible supernatant was removed and the tubes were transferred into liquid nitrogen for snap-freezing of the cell pellets. All steps until snap-freezing were performed as fast as possible and whenever applicable on ice.

The frozen pellets were then shipped on dry-ice for RNA-sequencing to Genewiz (Germany). Briefly, the RNA-sequencing workflow after RNA isolation consisted of initial PolyA selection-based mRNA enrichment, mRNA fragmentation and random priming followed by first and second strand cDNA synthesis. Subsequently, end-repair 5´phosphorylation and dA-tailing was carried out. Finally, adaptor ligation, PCR enrichment as well as Illumina NovaSeq technology-based sequencing with 2x 150pb read length was performed. Trimmomatic v.0.36 software was used to remove possible adaptor sequence reads and nucleotide reads with poor quality. STAR aligner v.2.5.2b was used to align reads to the *Homo sapiens* GRCh38 reference genome available on ENSEMBL. To calculate unique gene hit counts, feature Counts from the Subread package v.1.5.2 were used. Hit counts are reported by using the gene ID feature in the annotation file. For this, only those unique reads which fall within exon regions were counted. Since the library preparation was strand-specific, the reads were counted strand-specifically. Comparison of gene expression levels between the different sample groups was performed using DESeq. To generate p-values and log2 fold changes (FC) the Wald test was applied. Genes with an adjusted p-value (padj) <0.05 were referred to as DEGs for each comparison. No DEG were found when HaCaT cells were treated with fsEVs containing CD63 only. Based on the DEG analysis, pathway enrichment analysis was performed using the reactome pathway knowledgebase (Jassal et al., 2020). The enrichment reports

generated by with these DEGs using with the reactome database can be accessed under https://osf.io/qpr4j/?view_only=de4bb4d5c25e452a95171a1518896fe3.

Two separate sequencing analysis rounds were performed. The first analysis included the evaluation of differentially expressed genes (DEG) between non-treated cultures and cultures treated either with fsEVs (composed of CD9, CD63 and CD81 as well as hsa-miR-21, hsa-miR-124, hsa-miR-125, hsa-miR-126, hsa-miR-130, hsa-miR-132) or the soluble protein and miRNA compounds. A second sequencing analysis was performed for the comparison of DEG between cultures treated only with vesicles lacking any protein or miRNA components and cultures treated with vesicles harbouring different combinations of proteins and miRNAs. The technical specifications and quality reports for the RNA-sequencing can be accessed under https://osf.io/5tvk7/?view_only=f1998ad90ba444a39bb7a2337f1b29fa and https://osf.io/kwgam/?view_only=85f8a79e8135438d8f2e712f9d496f2b for the first and second analysis, respectively. The sample specifications are given in Table 1 and Table 2. For coupling of recombinant human ED2 of the CD9, CD63 and CD81 proteins, 1mol% DGS-NTA(Ni^{2+}) was introduced into the initial SUV solution.

Table 1 | Sample specification for the first RNA-sequencing analysis

Sample A	**Untreated HaCaT cells**
Sample B	HaCaT cells treated with fsEVs harbouring recombinant human ED2 of CD9, CD63 and CD81 as well as hsa-miR-21, hsa-miR-124, hsa-miR-125, hsa-miR-126, hsa-miR-130 and hsa-miR-132
Sample C	HaCaT cells treated with soluble forms of recombinant human ED2 of CD9, CD63 and CD81 as well as hsa-miR-21, hsa-miR-124, hsa-miR-125, hsa-miR-126, hsa-miR-130 and hsa-miR-132 at the same final concentration as in C

Table 2 | Sample specification for the second RNA-sequencing analysis

Sample A	**HaCaT cells treated with the fsEVs without any protein or miRNA components (lipid constituents only)**
Sample B	HaCaT cells treated with fsEVs harbouring recombinant human ED2 of CD9, CD63 and CD81 as well as hsa-miR-21, hsa-miR-124, hsa-miR-125, hsa-miR-126, hsa-miR-130 and hsa-miR-132

Sample C	HaCaT cells treated with fsEVs harbouring recombinant human ED2 of CD9
Sample D	HaCaT cells treated with fsEVs harbouring recombinant human ED2 of CD63
Sample E	HaCaT cells treated with fsEVs harbouring recombinant human ED2 of CD81
Sample F	HaCaT cells treated with fsEVs harbouring recombinant human ED2 of CD9 and CD63
Sample G	HaCaT cells treated with fsEVs harbouring recombinant human ED2 of CD9 and CD81
Sample H	HaCaT cells treated with fsEVs harbouring recombinant human ED2 of CD63 and CD81
Sample I	HaCaT cells treated with fsEVs harbouring recombinant human ED2 of CD9, CD63 and CD81
Sample J	HaCaT cells treated with fsEVs harbouring recombinant human ED2 of CD9, CD63 and CD81 as well as hsa-miR-21, hsa-miR-124, hsa-miR-125, hsa-miR-126 and hsa-miR-130

3.2.24 Encapsulation of baculoviruses

For encapsulation of baculoviruses (BV) into GUVs, MultiBac baculovirus encoding recombinant mito-dsRed produced in insect cells (kindly provided by Prof. Imre Berger, University of Bristol) were used. The SUV solution applied as aqueous phase for GUV production was mixed in a 1:100 ratio with the baculovirus containing solution. Importantly, this solution was supplemented with 60 mM $MgCl_2$ as manganese concentrations below did not results in successful dsGUV formation. After release, GUVs containing baculoviruses, were incubated with REF cells for 24 hours and cells were subsequently incubated with 8 µg/ ml Hoechst33342 to stain nuclear and viral DNA. On respective cultures, fluorescence confocal microscopy was performed to analyse GUV uptake and expression of mito-dsRed as well as BV localization by oversaturation of the Hoechst33342 channel.

3.2.25 GUV Biofunctionalization and PEGylation

If not specified otherwise, GUV biofunctionalization was performed on released GUVs dissolved in PBS on a horizontal shaker at room temperature and protect from light. After all functionalization steps, GUVs were centrifuged at >10,000 g for a minimum of 15 min in order to remove unbound coupling agents and the GUV pellet was resuspended in PBS. For coupling reactions based on NHS-chemistry, all reagents were kept at 4°C whenever possible and dsGUV-release was performed not longer than 1 hour after droplet formation. Coupling of proteins to GUVs *via* NHS-chemistry was performed for a minimum of 3 hours. A 2-5 fold excess of proteins and lipids was added to the GUVs for NHS- and NTA-based biofunctionalization. The concentration of NHS- and NTA-lipids was deduced from the total GUV concentration considering the lipid formulation used for SUV production. For instance, when fluorescence quantification resulted in a total lipid concentration of 150 µM and SUVs were produced from SUVs with 1mol% palmitic acid NHS lipids, then at least 1.5 µM of the protein to be coupled was added. Hereby it was assumed that approx. 50% of the NHS-coupled lipids reside within the inner membrane leaflet of the GUV and are therefore not accessible for coupling. For coupling of WGA via NHS-chemistry, WGA was added only at 0.1 M deficit. For biofunctionalization of GUVs with RGD peptides, a desired amount of DSPE-RGD lipids was introduced into the lipid mixture for SUV production. For decoration of fsEVs with Alexa488-labled CD9, NHS-functionalized AlexaFluor488 was incubated with recombinant CD9 for 2 hours at 37°C in PBS in a two-fold molar excess. Unreacted NHS was quenched by adding glycine in a 10-fold molar excess.

For sequential functionalization of GUVs with Au-nanoparticles, 3 µM L-cysteine was incubated for 6 hours together with GUVs containing 1mol% NHS. Afterwards, Au nanoparticles with a size of 50 nm were added at 10 µg/ ml final concentration and the mixture was shaken at 300 rpm on a horizontal shaker overnight. For the production of GUVs coated with IgG antibodies, 3 µM His-tagged Protein G was incubated for 1 hour with GUVs containing 1mol% 18:1 DGS-NTA(Ni) lipids. Afterwards, 3 µM of the desired IgG, dissolved in 1% BSA, was added to the mixture and incubated for 1 hour. Whenever multiple functionalization-steps were performed (e.g. triple functionalization with biotin-, NHS- or NTA- containing lipids), the coupling step involving NHS-reactions was performed first in order to avoid any undesired cross reactions. PEG coated GUVs were produced by introducing the desired amount of PEG350, PEG750 or PEG1000 coupled PE lipids into the SUV formulation used for dsGUV production.

3.2.26 Lysosomal escape mechanisms

Three different approaches were assessed in order to achieve lysosomal escape of endocytosed GUVs. For all formulations, PBS containing 10 mM $MgCl_2$ and 50 mM 8-hydroxypyrene-1,3,6-trisulfonic acid trisodium salt was used as aqueous phase buffer and 1.25 mM triblock PFPE-PEG-PFPE 2500-600-2500 surfactant dissolved in FC-40 as oil phase. GUVs were cleaned after release by centrifugation and sequentially incubated with REF cells for 24 hours. Distribution of HPTS inside the cells was analysed by fluorescence confocal microscopy. Special care was taken to acquire images with constant imaging parameters in order to compare the different approaches with each other.

1. Poly-ethylene-imine approach: GUVs composed of 20mol% EggPG, 79mol% EggPC and 1mol% LissRhod PE were produced. To the SUV mixture used for dsGUV production, 44 µg/ ml poly-ethylene-imine was added.
2. GALA peptide approach: For intralysosomal fusion with GALA-peptide, GUVs composed of 1mol% LissRhod PE, 1mol% palmitic acid NHS, 20mol% EggPG and 78mol% EggPC were produced and coupled after release to 1.5 µM GALA peptide EAALAE ALAEALAEHLAEALAEALEALA in PBS.
3. DOBAQ approach: For intralysosomal fusion with DOBAQ lipids, GUVs composed of 1mol% LissRhod PE, 60mol% DOBAQ, 20mol% EggPG and 19mol% EggPC were produced in PBS supplemented with 50 mM HEPES for stabilization of pH during dsGUV formation.

3.2.27 Protein analysis by gel electrophoresis

For a gel-electrophoretic analysis of the proteins contained in K562 exosomes and fsEVs, NuPAGE bold Bis-Tris 4-12% gradient gels with MES running buffer were used. Electrophoresis was performed under denaturing conditions with a total of 3 µg and 500 ng of protein from fsEVs and natural exosomes, respectively, at 200 V for 35 min. Membranes were stained with Coomassie R250 dye following a previously published method (Laemmli, 1970). Line intensity profiles plots were measured using the profile-plot plug-in of ImageJ software. Gel-electrophoresis was performed with technical assistance of Cornelia Weber (Dept. Cellular Biophysics, MPI for Medical Research).

3.2.28 Quantitative Mass-Spectrometry of GUVs

Comparative quantitative mass spectrometry of GUVs and their SUV lipid precursors was performed with a Sciex QTRAP 4500 mass spectrometer (AB Sciex, Germany)

hyphenated with a Shimadzu Nexera HPLC system (Shimadzu, Japan) and controlled by Sciex Analyst 1.7 software. Lipid formulations of 33mol% DOTAP, 33mol% DOPE, 33mol% DOPC and 1mol% LissRhod PE were used for dsGUV production with 0.5% RAN Biotechnologies PEG-based fluorosurfactant (RAN Biotechnologies, USA) diluted in FC-40. Samples were sonicated for 3 min before analysis and diluted 1:1000 in LC-MS grade MeOH. A Supelco Titan C18 (Sigma Aldrich, Germany) column (0.21 x 10 cm, 1.9 µ) operated at 45°C was used for subsequent fractionation. A flow rate of 0.5 ml/ min using a 10 mM NH_4Ac solution in 98% MeOH aq. was applied for this isocratic method. The following instrument settings were used for the analysis in multi-reaction monitoring mode: curtain gas 35 psi, ionization voltage 5500 V, nebulizer gas 30 psi, heater gas 60 psi, heater temperature 180°C and a CAD gas set to 9. The compound-specific parameters used are shown in Table 3.

Table 3 | Compound specific parameters for comparative quantitative mass spectrometry of GUVs.

ID	Precursor mass [Da]	Fragment mass [Da]	Dwell time [msec]	Declustering potential [V]	Collision Energy [V]	Cell exit potential [V]
DOPE	744.498	603.500	110	91	33	16
DOTAP	662.528	603.500	50	166	41	20
DOPC	786.528	184.000	50	161	39	14
LissRhod	1301.605	682.000	110	40	67	24

All quantifications were performed in technical triplicates and data analysis was performed using Sciex Analyst 1.7 (AB Sciex, Germany) and MultiQuant 3.0.2 software. The obtained concentrations were normalized to a SUV sample containing DOPE:DOTAP:DOPC:LissRhod PE with lipid molar ratios of 33:33:33:1.

3.2.29 Quantitative Mass-Spectrometry of fsEVs

Lipid ratios of fsEVs were analysed by multi reaction monitoring analysis using a Sciex QTrap 4500 system with a Shimadzu Nexera UPLC front-end system set up for flow injection analysis (FIA). For instrument control, the Analyst 1.7.0 software from Sciex (AB Sciex, Germany) was used. As FIA-MS based lipid analysis could be affected by aggregation, adsorption and suppression, heavy isotope-labelled internal standards were used to ensure reproducible and precise results. For LC-MS experiments 9 different lipids

were monitored. The Avanti SPLASH LIPIDOMIX Mass Spec Standard, which contains representative deuterated forms of the analysed lipids, were used as internal standards. The internal standard mix was diluted 1:100 in 98% DCM/MeOH aq. + 10 mM NH_4Ac (50:50 v/v, LCMS grade) and then used to dilute the samples and calibrator. For calibration and normalization, an unprocessed PBS sample supplemented with the target lipid ratios was diluted 1:10000, 1:5000 and 1:2500. Before analysis, samples were sonicated for 3 min and diluted 1:5000 afterwards. Calibrator and samples were injected in triplicates or quintuplicates into a 450 µL/ min 98% MeOH aq. + 10 mM NH_4Ac stream with 0.1 µL air gaps.

Measurements were performed in negative and positive ionization mode (Table 4). As cholesterol showed increasing signal intensities with decreasing ion source temperature, the ionization temperature was lowered to 180°C for positive mode. For isolation of lipid precursors either de-/protonated or NH_4Ac-derived adducts were chosen. Precursors and MS2 fragments for MRM measurements together with the optimized parameters are shown in Table 4. As the lipids of the Avanti SPLASH LIPIDOMIX Mass Spec Standard mix showed unequal concentrations and ionization efficiencies, the PG-d7, PC-d7 and SM-d9 signal intensities were considered to be susceptible to detector saturation effects, wherefore their second isotopes (15:0-18:1(d7) PG, 15:0-18:1(d7) PC and d18:1-18:1(d9) SM) were selected as MRM precursors. All Mass-Spectrometry analysis were performed with the help of Dr. Sebastian Fabritz (MassSpec Core Facility at the MPI for Medical Research).

Table 4 | Parameters for mass spectrometry quantification of fsEV lipids. Ionization, precursor selection and fragmentation parameters are shown for the quantification of lipids by LCMS. (CUR = curtain gas, TEM = temperature, GS1= nebulizer gas, GS2= heater gas, CAD = collision gas, IS = ionization voltage, DP= declustering voltage, CE= collision energy, CXP= cell exit potential).

A: Source and ionization parameters

	+ polarity	- polarity
CUR [psi]	35	35
TEM [°C]	180	600
GS1 [psi]	70	70
GS2 [psi]	60	60
CAD	9	9
IS [V]	5500	-4500

B: MRM parameters

Q1 [m/z]	Q3 [m/z]	Dwell Time [ms]	ID	DP [V]	EP [V]	CE [V]	CXP [V]
786.5	281.3	25	18:1 PS	-120	-10	-55	-8.5
753.4	288.3	20	15:0-18:1(d7) PS	-100	-10	-56	-10
699.5	281.3	25	18:1 PA	-160	-10	-46	-9
666.4	288.3	20	15:0-18:1(d7) PA	-170	-10	-46	-10
861.4	281.3	25	18:1 PI	-185	-10	-60	-11
828.4	288.3	20	15:0-18:1(d7) PI	-90	-10	-60	-11
773.4	281.3	25	18:1 PG	-135	-10	-52	-11
741.4	289.3	20	15:0-18:1(d7) PG	-100	-10	-48	-10
844.5	281.3	25	18:1 PC	-90	-10	-54	-7
812.5	289.3	20	15:0-18:1(d7) PC	-115	-10	-50	-11
404.3	369.4	100	Cholesterol	121	10	13	12
411.2	376.3	60	Cholesterol (d7)	121	10	13	12
731.6	184.1	20	18:0 SM	120	10	34	5.4
739.5	185.0	20	d18:1-18:1(d9) SM	130	10	37	16
638.5	339.3	20	18:1 DAG	50	10	27	12
605.5	299.2	20	15:0-18:1(d7) DAG	91	10	21	6
744.5	603.5	20	18:1 PE	91	10	33	16
711.4	570.5	20	18:1(d7) Lyso PE	120	10	30	12

Table 5 | Specification of GUV and fsEV compositions.

Figure	Lipid composition	GUV lumen buffer and/ or composition	Release buffer and/ or GUV decoration
11	20 mol% EggPG, 79 mol% EggPC and 1 mol% LissRhod PE	PBS, 10 mM $MgCl_2$, 1 mM AlexaFluor405, 1 µM His-tagged GFP, 1.08x109 particles/ ml Fluoresbrite YG Microspheres, 1.5 mM SUVs	PBS
12	20 mol% EggPG, 79 mol% EggPC and 1 mol% LissRhod PE	PBS, 10 mM $MgCl_2$,1.5 mM SUVs	PBS

13	20 mol% EggPG, 79 mol% EggPC and 1 mol% LissRhod PE	PBS, 10 mM $MgCl_2$	PBS
14a and 14c	20 mol% EggPG, 79 mol% EggPC and 1 mol% LissRhod PE	PBS, 10 mM $MgCl_2$,1.5 mM SUVs	PBS
14b	20 mol% EggPG, 79 mol% EggPC and 1 mol% LissRhod PE	10 mM $MgCl_2$, buffers as indicated in the figure,1.5 mM SUVs	buffers as indicated in the figure
15a and 15b	49mol% DOPC, 50mol% DOPG and 1mol% LissRhod PE	PBS, 10 mM $MgCl_2$,1.5 mM SUVs	PBS
15a	79mol% DOPC, 20mol% DOPG and 1mol% LissRhod PE	PBS, 10 mM $MgCl_2$,1.5 mM SUVs	PBS
15a and 15b	99mol% DOPC and 1mol% LissRhod PE	PBS, 20 mM $MgCl_2$,1.5 mM SUVs	PBS
15a	79mol% DOPC, 20mol% DOTAP and 1mol% LissRhod PE	PBS,1.5 mM SUVs	PBS
15a and 15b	49mol% DOPC, 50mol% DOTAP and 1mol% LissRhod PE	PBS,1.5 mM SUVs	PBS
16	79mol% DOPC, 20mol% DOPG and 1mol% LissRhod PE	PBS, 10 mM $MgCl_2$,1.5 mM SUVs	PBS
17a	20mol% EggPG, 76mol% EggPC, 1mol% LissRhod PE, 1mol% DGS-NTA(Ni^{2+}), 1mol%	PBS, 10 mM $MgCl_2$,1.5 mM SUVs	PBS, 1% BSA, 1.5 μM His-tagged GFP, Atto425-streptavidin, AlexaFluor647 NHS

	DOPE and 1mol% Biotin PE		
17b	20mol% EggPG, 78mol% EggPC, 1mol% LissRhod PE and 1mol% DGS-NTA(Ni^{2+})	PBS, 10 mM $MgCl_2$,1.5 mM SUVs	PBS, 1% BSA, 3 µM His-tagged Protein G, 3 µM anti-CD3-AlexaFluor488 IgG
17c	20mol% EggPG, 78mol% EggPC, 1mol% LissRhod PE and 1mol% palmitic acid-NHS	PBS, 10 mM $MgCl_2$,1.5 mM SUVs	PBS, 1% BSA, 6 µM L-cysteine, 10 µg/ml 50 nm Au-NPs
17d	20mol% EggPG, 78mol% EggPC, 1mol% LissRhod PE and 1mol% DGS-NTA(Ni^{2+})	PBS, 10 mM $MgCl_2$,1.5 mM SUVs	PBS, 1% BSA, 3 µM His-tagged Protein G, 3 µM anti-CD3 IgG
18b	79mol% DOPC, 20mol% DOPG and 1mol% LissRhod PE	PBS, 10 mM $MgCl_2$,1.5 mM SUVs	PBS
18b	78mol% DOPC, 20mol% DOPG, 1mol% LissRhod PE and 1mol% DSPE-RGD	PBS, 10 mM $MgCl_2$,1.5 mM SUVs	PBS
18b	77mol% DOPC, 20mol% DOPG, 1mol% LissRhod PE and 2mol% DSPE-RGD	PBS, 10 mM $MgCl_2$,1.5 mM SUVs	PBS
18b	69mol% DOPC, 20mol% DOPG, 1mol% LissRhod PE	PBS, 10 mM $MgCl_2$,1.5 mM SUVs	PBS

	and 10mol% DSPE-RGD		
18c	77mol% DOPC, 20mol% DOPG, 1mol% LissRhod PE and 2mol% DSPE-RGD	PBS, 10 mM $MgCl_2$,1.5 mM SUVs	PBS
19a	20mol% EggPG, 78mol% EggPC, 1mol% LissRhod PE and 1mol% DGS-NTA(Ni^{2+})	PBS, 10 mM $MgCl_2$,1.5 mM SUVs	PBS, 10 µM His-tagged FasL
19b	20mol% EggPG, 78mol% EggPC, 1mol% LissRhod PE and 1mol% DGS-NTA(Ni^{2+})	PBS, 10 mM $MgCl_2$,1.5 mM SUVs	PBS
20	98mol% EggPC, 1 mol% LissRhod PE and 1 mol% DGS-NTA(Ni^{2+})	PBS, 20 mM $MgCl_2$,1.5 mM SUVs	PBS
20	98mol% EggPC, 1 mol% LissRhod PE and 1 mol% DGS-NTA(Ni^{2+})	PBS, 10 mM $MgCl_2$,1.5 mM SUVs	PBS, 3 µM His-tagged NrCam
21b and 21c	15mol% or 50mol% DOPG, PEGylated lipids as enclosed in the figure, rest of the lipids of the respective formulations is EggPC	PBS, 10 mM $MgCl_2$,1.5 mM SUVs	PBS
21b and 21c	15mol% or 50mol% DOTAP, PEGylated lipids as enclosed in	PBS,1.5 mM SUVs	PBS

	the figure, rest of the lipids of the respective formulations is EggPC		
22	20 mol% EggPG, 79 mol% EggPC and 1 mol% LissRhod PE	PBS, 10 mM $MgCl_2$,1.5 mM SUVs	PBS
22	20 mol% EggPG, 29 mol% EggPC, 50mol% PEG1000 and 1 mol% LissRhod PE	PBS, 10 mM $MgCl_2$,1.5 mM SUVs	PBS
23b	20 mol% EggPG, 54 mol% EggPC, 20mol% PEG750, 5mol% palmitic acid-NHS and 1 mol% LissRhod PE	PBS, 10 mM $MgCl_2$,1.5 mM SUVs	PBS and 6 µM peptide or ligands as disclosed in the figure
24b	58mol% EggPC, 20mol% EggPG, 20mol% PEG750, 1mol% LissRhod PE and 1mol% DGS-NTA(Ni^{2+})	PBS, 10 mM $MgCl_2$,1.5 mM SUVs	PBS, 3 µM His-tagged NrCam
25a and 25b	20 mol% EggPG, 79 mol% EggPC and 1 mol% LissRhod PE	PBS, 10 mM $MgCl_2$,1.5 mM SUVs	PBS
26a	20mol% EggPG, 79mol% EggPC and 1mol%	PBS, 10 mM $MgCl_2$,1.5 mM SUVs, 50 mM HPTS and 44 µg/ml PEI	PBS
26a	1mol% LissRhod PE, 1mol% palmitic acid NHS, 20mol% EggPG and 78mol% EggPC	PBS, 10 mM $MgCl_2$,1.5 mM SUVs, 50 mM HPTS	PBS, 1.5 µM GALA peptide

26a	1mol% LissRhod PE, 60mol% DOBAQ, 20mol% EggPG and 19mol% EggPC	PBS, 10 mM $MgCl_2$,1.5 mM SUVs, 50 mM HPTS	PBS
26b	60mol% DOBAQ, 20mol% EggPG and 20mol% EggPC	PBS, 10 mM $MgCl_2$,1.5 mM SUVs	PBS
26b	20mol% EggPG and 80mol% EggPC	PBS, 10 mM $MgCl_2$,1.5 mM SUVs	PBS
27	20mol% EggPG, 60mol% DOBAQ, 1mol% LissRhod PE and 1mol% palmitic acid-NHS	PBS, 10 mM $MgCl_2$,1.5 mM SUVs, 50 mM HPTS	PBS, 10 mg/ ml WGA
28	1 mol% LissRhod PE, 60 mol% DOBAQ, 20 mol% EggPG and 19 mol% EggPC	PBS, 60 mM $MgCl_2$, 1:100 dilution of Baculoviruses, 50 mM HEPS and 1.5 mM SUVs	PBS
29	1 mol% LissRhod PE, 60 mol% DOBAQ, 20 mol% EggPG and 19 mol% EggPC	PBS, 60 mM $MgCl_2$, 1:100 dilution of Baculoviruses, 50 mM HEPS and 1.5 mM SUVs	PBS
30	20mol% EggPG, 79mol% EggPC and 1mol% LissRhod PE	PBS, 10 mM $MgCl_2$, 2.7 µM bovine catalase	PBS
31	20mol% EggPG, 79mol% EggPC and 1mol% LissRhod PE	PBS, 10 mM $MgCl_2$, 10 µM npEGTA $CaCl_2$	PBS
32	20mol% EggPG, 79mol% EggPC and 1mol% LissRhod PE	PBS, 10 mM $MgCl_2$, 10 µM npEGTA $CaCl_2$	PBS

33	20mol% EggPG, 79mol% EggPC and 1mol% LissRhod PE	PBS, 10 mM $MgCl_2$, 10 µg/ ml Fe2O3 nanoparticles, 0.1% (w/v) BSA	PBS
34a	20mol% EggPG, 79mol% EggPC and 1mol% LissRhod PE	PBS, 10 mM $MgCl_2$, 10 µg/ ml Fe2O3 nanoparticles, 0.1% (w/v) BSA	PBS
34b	As in figure 34a	PBS, 10 mM $MgCl_2$	PBS
35	As in figure 34a	As in figure 34a	As in figure 34a
37b and 37c	20mol% EggPG, 79mol% EggPC and 1mol% LissRhod PE)	PBS, 10 mM $MgCl_2$, 3 mM SUVs	PBS
38	70mol% DOPC, 5mol% DOPE, 20mol% DOPG and 5mol% DOPS	PBS, 10 mM $MgCl_2$, 3 mM SUVs	PBS
39	69mol% DOPC, 5mol% DOPE, 20mol% DOPG, 5mol% DOPS and 1mol% DGS-NTA(Ni^{2+})	PBS, 10 mM $MgCl_2$, 3 mM SUVs	PBS, recombinant his-tagged ED2-CD9 (Ser112-Ile195) and TSG101 (Gly1-Pro145)
40	43mol% cholesterol, 16 mol% SM, 15 mol% DOPC, 11 mol% DOPS, 6 mol% DOPE, 5 mol% DOPG, 2 mol% PA, 1 mol% DAG and 1 mol% DOPI	PBS, 10 mM $MgCl_2$, 3 mM SUVs	PBS
41	42mol% cholesterol, 16mol% SM, 15mol% DOPC, 11mol%	PBS, 10 mM $MgCl_2$, 3 mM SUVs, miRIDIAN miRNA	PBS, recombinant his-tagged human ED2 of

	DOPS, 6mol% DOPE, 5mol% DOPG, 2 mol% PA, 1mol% DAG, 1mol% DOPI and 1mol% DGS-NTA(Ni^{2+})	mimics of hsa-miR-21, hsa-miR-124, hsa-miR-125, hsa-miR-126, hsa-miR-130 and hsa-miR-132 (50 nM each)	CD9 conjugated to AlexaFluor488
42a and 42b	As in figure 26	PBS, 10 mM $MgCl_2$, 3 mM SUVs	PBS, recombinant his-tagged human ED2 of CD9, CD63 and CD81
43	As in figure 26	PBS, 10 mM $MgCl_2$, 3 mM SUVs	PBS, recombinant his-tagged human ED2 of CD9, CD63 and CD81 as stated in the figure
43a and 43b	As in figure 26	PBS, 10 mM $MgCl_2$, 3 mM SUVs, miRIDIAN miRNA mimics of hsa-miR-21, hsa-miR-124, hsa-miR-125, hsa-miR-126, hsa-miR-130 and hsa-miR-132 (50 nM each) as stated in the figure	PBS, recombinant his-tagged human ED2 of CD9, CD63 and CD81, naïve vesicles are without conjugated proteins
44a	As in figure 26	PBS, 10 mM $MgCl_2$, 3 mM SUVs	As in figure 28
44b	As in figure 26	PBS, 10 mM $MgCl_2$, 3 mM SUVs	PBS, recombinant his-tagged human ED2 of CD9, CD63 and CD81 as stated in the figure, naïve vesicles are without conjugated proteins
44c	As in figure 26	As in figure 28	As in figure 27

45	As in figure 26	PBS, 10 mM $MgCl_2$, 3 mM SUVs, miRIDIAN miRNA mimics of hsa-miR-21, hsa-miR-124, hsa-miR-125, hsa-miR-126, hsa-miR-130 and hsa-miR-132 as stated in the figure (specific concentrations as shown in the figure)	As in figure 27
46	As in figure 26	As in figure 28	PBS, recombinant his-tagged human ED2 of CD9, CD63 and CD81, naïve vesicles are without conjugated proteins
47	As in figure 26	As in figure 26	As in figure 27
48	As in figure 26	As in figure 26	As in figure 27
49a, b and c	As in figure 26	As in figure 26	As in figure 27
49	-	As in figure 26	As in figure 27
50	As in figure 26	As in figure 26	As in figure 27
51a, b and c	As in figure 26	PBS, 10 mM $MgCl_2$, 3 mM SUVs	As in figure 28
51d	As in figure 26	As in figure 26	As in figure 27

4 Results

Microfluidic-based production of dsGUVs has proofed to perform with outstanding precision and versatility for the assembly of cell-sized lipid compartments. However, typical vesicle-dimensions produced with this method do not recapitulate the size spectrum of EVs or liposomal formulation needed for effective drug delivery. To overcome this current limitation of dsGUV assembly, in section 4.1, I describe the re-conceptualization of microfluidic droplet-splitting devices for dsGUV-based production and cargo-loading of lipid vesicles as well as their interaction-spectrum with cell cultures. In sections 4.2 and 4.3, I describe the development of new means for biorthogonal functionalization of the GUVs, approaches for their passivation and targeting, strategies for intracellular cargo release as well as their reconceptualization as synthetic intracellular organelles. Based on these findings, section 4.4 describes the development of fully-synthetic extracellular vesicles, their functional analysis and therapeutic potential as well as whole-transcriptome sequencing approaches to decipher underlying functional mechanisms.

4.1 Microfluidic assembly and characterization of droplet-splitted GUVs

4.1.1 Mechanical splitting of microfluidic droplets

The assembly of GUVs from SUV precursors within microfluidic w/o droplet-scaffolds not only offers high production rates but also excellent control over the molecular GUV composition. So far, microfluidic technologies previously presented in literature have been used to produce cell-sized GUVs in the size-range of ~ 50 µm (Gopfrich et al., 2018; Jia and Schwille, 2019; Weiss et al., 2017). These vesicles serve as durable, low-cost and excellent to handle mimics of living cells but are not representative for naturally occurring EVs, nor suitable for intracellular uptake by cells. Therefore, current microfluidic technologies need to be re-conceptualized in order to produce vesicles in the EV-size range. However, simply downsizing the flow focusing junctions, in order to produce droplets and GUVs of sizes smaller than 5 µm, requires sophisticated lithography procedures to imprint the complex and miniature channel architectures (Shim et al., 2013; Shui et al., 2011). These measures not only complicate the device-production process but also restrict reliable high-throughput small-droplet production. Therefore, in order to

overcome these limitations, the first effort of this work was directed towards the development of droplet-based PDMS microfluidic architectures, harbouring a flow-focusing T-junction (for w/o-droplet production) and a multi-V-shaped droplet splitting unit (Figure 10a). The devices additionally harboured one inlet channel for the oil phase and two inlet channels for aqueous phases which merged shortly before the droplet-generating T-junction, where two oil tunnels meet with the combined aqueous channel for droplet production. Moreover, filter structures were placed downstream of each inlet channel and a single outlet was positioned downstream of the splitting unit. This microfluidic design enabled for the production of w/o-droplets in the size range of 60 µm upstream of the splitting-unit and subsequent mechanical division of these droplets at the sharped bifurcation junctions. Multiple bifurcations can be connected in series for serial, high-throughput splitting of the droplets (Figure 10b). The microfluidic channels were designed in order to result in directly cantered chopping of the droplets (Figure 10b, inset), resulting in two equally sized daughter droplets. Hereby, five consecutive division steps, producing 32 daughter droplets from every droplet generated at the T-junction, result in droplets with a mean diameter of 2.90 µm (± 0.45 µm (SD), n = 202). The final channel width was approximately 2 µm, as employment of devices with more splitting units (>6) or narrower channels did not result in correctly formed lithographic wavers or non-

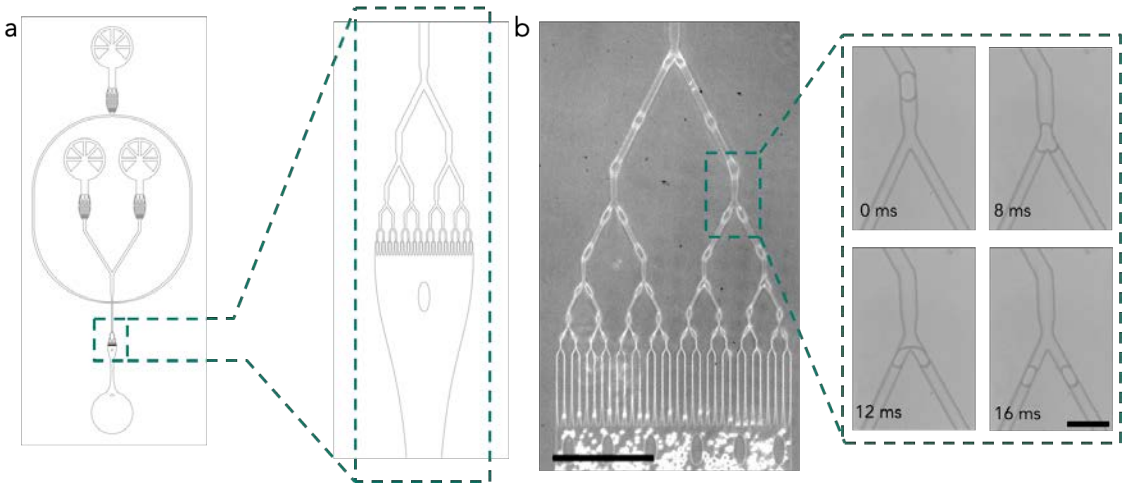

Figure 10 | Microfluidic droplet-splitting devices. (**a**) QCad design of the mechanical droplet splitting microfluidic device. Inset shows the magnification of the droplet-splitting unit. (**b**) Phase-contrast microscopy image of a microfluidic serial five-fold mechanical dsGUV splitting devise, producing 32 daughter droplets from a single 60 µm droplet formed at the upstream T-junction. The inset shows the mechanical division of a droplet at a V-junction over a time course of 16 msec. The scale bars are 300 µm and 60 µm, respectively.

cantered droplet splitting as well as persistent clogging of the PDMS-devices. Therefore, devices for 5-fold division were applied for further assessment and investigations on the assembly of droplet-splitted dsGUVs.

4.1.2 Assessment of droplet content after serial microfluidic splitting

High droplet-homogeneity is a pivotal requirement to produce GUV-batches with reproducible size and composition and as low as possible interdroplet-variation. However, heterogeneity into the droplet population could be introduced by non-uniform droplet-splitting or by microscopic variations in local concentration of larger particles. Therefore, the transmission homogeneity of intraluminal droplet-contents from the mother to the daughter droplets was assessed (see section 3.2.6). Towards this, fluorescent compounds of different sizes were loaded into the droplets by mixing them with the aqueous phase used for droplet production and the resulting droplets were analysed by fluorescence confocal microscopy. Mean fluorescent signal intensities for each fluorescent component among mother droplets were compared to mean fluorescent signal intensities among daughter droplets for the low-molecular weight fluorophore AlexaFluor 405, supramolecular complexes as represented by the green fluorescent protein, nanometre sized fluorescently labelled SUVs (composed of 20 mol% EggPG, 79 mol% EggPC and 1 mol% LissRhod PE) and 1 µm sized fluorescent polystyrene (PS) beads (Figure 11).
Only low inter-droplet variations of the fluorescence signal intensities were found, especially for the smaller compounds, suggesting tolerable heterogeneity in droplet composition (Table 6). Large variations were only found for the PS beads, presumably

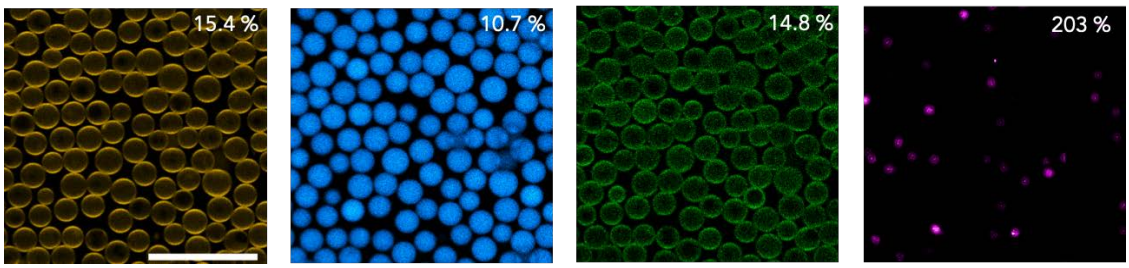

Figure 11 | Assessment of droplet-content homogeneity after splitting. Representative single plane fluorescence confocal microscopy images of droplets after mechanical splitting. Droplets were loaded with fluorescently labelled SUVs (1 mol% LissRhod PE, yellow), AlexaFluor 405 (blue), green fluorescent protein (green) and 1 µm fluorescent polystyrene beads (purple). Coefficients of variation (CV) of the droplets mean signal intensity are indicated in the upper right image corners (n = 665 single droplets). The scale bar is 40 µm.

because of their large size and the used concentration ($1.08x10^9$ particles/ ml) mostly results in Bernoulli-like splitting distributions. The overall production rate was approx. $2.5x10^5$ droplets/ min at the flow focusing T-junction and therefore approximately $8x10^6$/ min after five-fold serial splitting. This showcases that homogeny droplet populations can be produced at high-throughput.

Table 6 | Variation of inter-droplet mean fluorescence signal intensities of four differently sized compounds in droplets before and after five-fold splitting.

Compound	Coefficient of variation (%) before splitting n= 29 individual droplets	Coefficient of variation (%) after splitting n= 655 individual droplets
AlexaFluor 405	5.6	10.7
GFP	18.5	14.8
100 nm SUVs	68.0	15.4
1 µm PS beads	N.A.	203

4.1.3 Microfluidic mechanical splitting of droplet-stabilized GUVs

Interestingly, the fluorescence confocal microscopy analysis in section 4.1.2 also revealed peripheral distribution of the SUV fluorescence inside the droplets, suggesting successful formation of dsGUVs before, during or after mechanical splitting of the droplets. In order to verify the formation of dsGUVs, a release procedure was performed on collected droplets produced with SUVs composed of 20mol% EggPG, 79mol% EggPC and 1mol% LissRhod PE (see section 3.2.1 for details on the release procedure). After addition of the destabilizing surfactant, large quantities of free floating GUVs could be observed by confocal florescence microscopy (Figure 12a). Size-distribution analysis of the released GUVs revealed a mean diameter of 1.400 µm (± 0.202 µm (SD), n = 122 single GUVs) (Figure 12b), which is in the upper size range of natural EVs and liposomal drug-delivery formulations tested previously. This demonstrates the possibility to produce large amounts of uniform GUVs with predefined dimensions for EV- and liposomal delivery research.

Based on these observations, more detailed analysis of the dsGUV production parameters used for microfluidic splitting devices-based GUV assembly were performed. First, as smaller droplets have an increased surface-to-volume ratio and therefore a higher concentration of SUVs is needed in order to cover the complete droplet periphery, the

SUV concentration required for dsGUV formation inside these small w/o-droplets was optimized (Figure 13). An optimal SUV concentration (composed of 20mol% EggPG, 79mol% EggPC and 1mol% LissRhod PE) of 1.5 mM of total lipids, achieving over 50% GUV-release efficiency, was found result in the highest release- and presumably also formation-efficiency. These optimized production conditions, successfully producing approximately one GUV for every two droplets generated, enabled a production throughput of $3x10^6$ GUVs/ min.

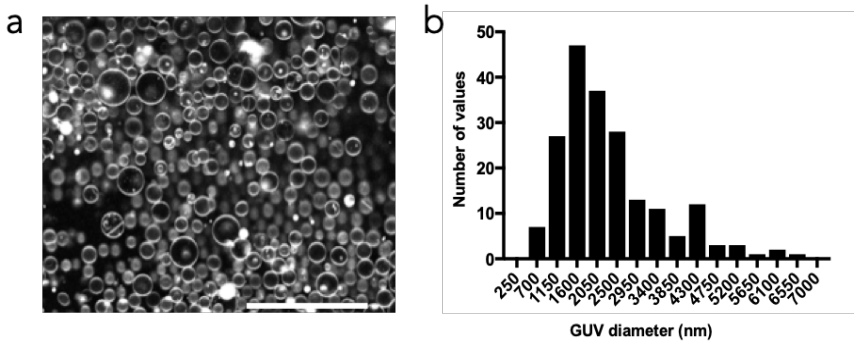

Figure 12 | GUVs produced from droplet-splitted dsGUVs. (**a**) Representative single plane fluorescence confocal microscopy images of free-floating GUVs released from mechanically-splitted dsGUVs. Droplets were produced with SUVs composed of 20 mol% EggPG, 79 mol% EggPC and 1 mol% LissRhod PE) and released into PBS. The scale bar is 25 µm. (**b**) Size distribution histogram of GUVs produced from droplet-splitted dsGUVs.

In order to assess whether the microfluidic handling procedures or mechanical splitting manoeuvres induces any changes in the lipid formulation (e.g. by loss of specific lipids into the oil phase during mechanical rupturing of the droplet), quantitative electrospray ionization tandem mass spectrometry of SUV- and GUV-lipids was performed (Table 7). The results revealed that the composition of the GUVs almost identically resembles the formulation of initial the SUV-mixtures. This not only demonstrates that the microfluidic dsGUV production and splitting does not change the lipid ratio and GUV formulation but also underscores the level of control provided by the microfluidic technology.

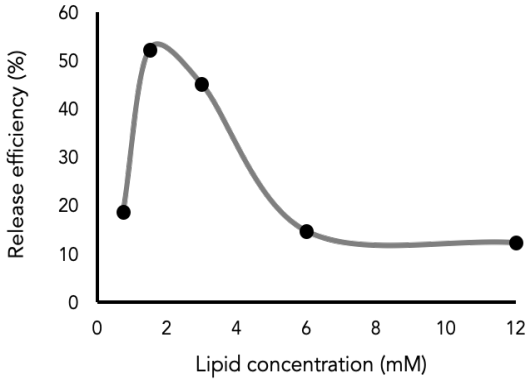

Figure 13 | Optimization of the intraluminal SUV concentration for producing mechanically splitting dsGUVs. Droplets containing SUV-lipid concentrations of 12 mM, 6 mM, 3mM, 1.5 mM and 0.75 mM were mechanically splitted and release efficiencies were calculated by counting the number of dsGUVs and released GUVs.

Table 7 | Quantification of SUV and GUV lipid ratios. Quantitative electrospray ionization tandem mass spectrometry was performed on SUVs containing DOPE, DOTAP, DOPC and LissRhod lipids as well as split GUVs produced from these SUVs (shown as LissRhod normalized concentration ratios). No considerable change in lipid ratios was found. MS experiments were performed in triplicates. All CVs for the SUV samples were <7.5 %. CVs for the GUV samples were <10 %.

	DOPE	**DOTAP**	**DOPC**	**LissRhod PE**
SUVs	1,00	1,00	1,00	1,00
GUVs	1,00	1,03	1,03	1,03

4.1.4 Application of droplet-splitted GUVs for in vitro *tissue culture studies*

As the droplet-splitted GUVs were designed for application in chemically complex biological environments which might further be subjected to higher shear stress (e.g. blood flow) and the potential GUV-administration routs could involve considerable mechanical stress, a basic assessment of their mechanical stability was performed. For this, a GUV solution (GUVs composed of 20mol% EggPG, 79mol% EggPC and 1mol% LissRhod PE) was incubated in a microcentrifuge tube at 37°C under constant mechanical agitation on a horizontal shaker at 800 rpm for 24 h in PBS. The GUV concentration in samples, taken from this solution at regular time intervals during the agitation, were analysed by counting the GUV number in a defined volume (see section 3.2.7 for details on the assessment of GUV concentrations). As a control, an identical sample was kept at 4°C in the dark

without mechanical agitation. The quantification revealed that 90% of the GUVs survived this procedure over a time-course of 24 hours (Figure 14a). This suggests that droplet-splitted GUVs with a diameter of approximately 2 µm tolerate considerable mechanical stress and are therefore probably robust enough for drug delivery applications *in vivo*.

Moreover, for the incorporation of functional biomolecular cargo into the GUV lumen, it is critical to assess whether the microfluidic production process can be performed under physiological buffer conditions. Therefore, a systematic assessment of the GUV release efficiency (used here as a measure of successful dsGUV production) was performed with three different aqueous phases based on water, PBS and serum-supplemented cell culture medium (Figure 14b). Moreover, each condition was also tested for optimal release buffer composition in order to estimate the osmotic stability of the produced GUVs. Under all conditions, GUV (GUVs composed of 20mol% EggPG, 79mol% EggPC and 1mol% LissRhod PE) release efficiency was the highest (45%) for dsGUVs produced in and released into cell culture medium. This demonstrates that droplet-splitting can produce GUVs under physiological buffer conditions which can subsequently also be maintained in cell-friendly environments. Based on these findings, time-laps microscopy analysis of GUVs incubated with rat embryonic fibroblast (REF) cultures was performed in order to assess the long-term stability of GUVs interacting with living cells. It was found that the GUVs remained stable and vigorously interacted and established contacts with cells over a time period of 20 h (Figure 14c). In summary, these results proof that sufficient amounts of defined GUVs, in a size-range suitable for cellular uptake, can be produced by droplet-splitting microfluidic approaches and that these GUVs can be maintained under cell culture conditions for several hours to days. This opens the door to apply GUVs produced by droplet-splitting for vesicle-cell interaction studies.

4.1.5 Charge-mediated GUV-cell interactions

Identifying the physical, chemical and biological factors that determine the interaction-spectrum of vesicles and cells, is of major importance to understand EV-cell interplay as well as liposomal uptake in drug delivery. One of the most important factors that conquers the interaction between lipid vesicles and cellular plasma membranes is the charge of the interacting lipid layers. Opposite charges can lead to membrane fusion or attachment while reduced interactions can be seen if both membranes display a similar charge state. Membrane charge, which is mostly determined by the lipid moieties (for natural cell

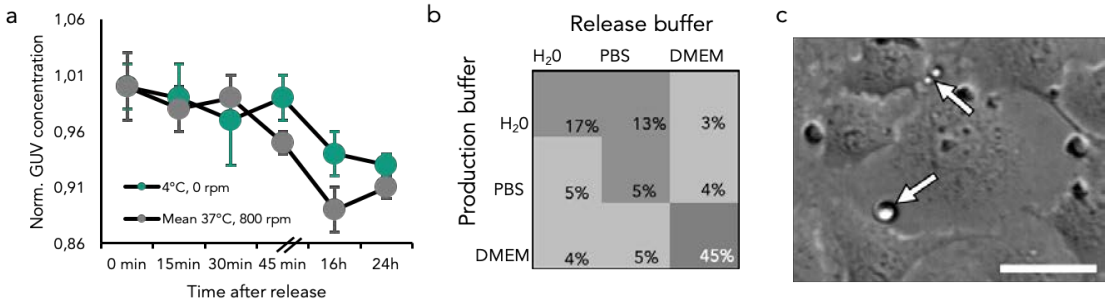

Figure 14 | Characterization of GUV stability under physiological-buffer conditions. (**a**) Assessment of the mechanical stability of droplet-splitted GUVs shaken at 800 rpm at 37 °C for 24 hours or kept as a control at 4 °C without mechanical agitation. Results are shown as average value with SD from three technical replicates. (**b**) Quantification of GUV release efficiency from droplet-splitted GUVs with different combinations of extraluminal release buffers and intraluminal (production) buffers. (**c**) Representative phase contrast image of GUVs produced by mechanical droplet-splitting and incubated with rat embryonic fibroblast cell cultures. White arrows indicate GUVs. The scale bar is 10 µm.

membranes also by carbohydrates attached on and glycoproteins embedded in the membrane) present in the outer leaflet, has been extensively studied for small vesicles of <100 nm radius. In order to evaluate if charge-based interactions can also be used to guide the GUV-cell interplay, a systematic comparative evaluation of the interaction spectrum of cells with differently charged, mechanically splitted GUVs was performed. Towards this end, GUVs with varying amounts of positively (DOTAP) and negatively (DOPG) charged lipids were produced. The GUV surface charge can be deduced by measuring their surface potential e.g. their zeta potential (ζ-potential). Dynamic light scattering (DLS) analysis revealed that by altering the lipid composition, the charge of the vesicles can be adjusted between highly negatively charged to highly positively charged GUVs (Table 8). This enables to characterize a wide spectrum of charge mediated interaction between cells and GUVs.

Table 8 | ζ-potential of released, droplet-splitted GUVs with varying lipid compositions measured by DLS. Different ratios of positively charged (DOTAP) and negatively charged (DOPG) lipids were incorporated into the SUV formulation.

ζ-potential (mV)	**-31**	**-19**	**+2**	**+20**	**+28**
DOTAP (mol%)	0	0	0	20	50
DOPC (mol%)	49	79	99	79	49
DOPG (mol%)	50	20	0	0	0
LissRhod PE (mol%)	1	1	1	1	1

In order to quantify various kinds of GUV-cell interactions (e.g. repulsion, attachment, uptake, engulfment or fusion) a plate-reader based attraction assay was established (see section 3.2.19). This assay quantifies the number of GUVs retained by cell monolayers cultured in well-plates, by measuring the fluorescence intensity of GUVs containing fluorophore-conjugated lipids. The five differently charged GUV-types described above were therefore interfaced with cell lines of endothelial (MDCK), epithelial (A431D and A431) and adrenal (PC12) origin. These specific cell lines were selected in order to cover a wide range of potential target cell types with varying surface markers, topologies, membrane turn-over rates, glycocalyx coating and endocytic activity. For all cell lines tested, a direct correlation between the GUV charge and the normalized cell attraction values was observed (Figure 15a). Hereby, an increase in GUV surface charge resulted in higher attraction, while non-charged GUVs displayed the lowest attraction values. For instance, in the frequently used carcinoma model cell line A431D, GUVs with a ζ-potential of -31 mV showed an almost 100 times higher attraction value compared to GUVs with +2 mV ζ-potential. Inversely, GUVs with +28 mV ζ-potential showed 50 times higher attraction values than +2 mV ζ-potential GUVs. Importantly, this quantitative assay does not discriminate between different types of GUV-cell interactions (e.g. GUV attachment, fusion, uptake or engulfment). Therefore, a qualitative assessment of the GUV-cell interplay, based on fluorescence confocal microscopy of A431D cells cultured together with respective droplet-splitted GUVs for 24 hours, was performed (Figure 15b). Three distinct types of interactions could be observed: GUV endocytosis, attachment and fusion. Moreover, it was found that the different types of interactions were distinctly associated with the differently charged GUVs. Endocytosis was primarily observed for negatively charged GUVs, attachment for non-charged GUVs and fusion for positively

charged GUVs. Fusion of the GUVs with the cellular plasma membrane was evident when the GUV lipid fluorescence co-localized with a cell membrane staining. In this state, most cells showed morbid cell morphologies, detachment from the substrate and deformed nuclear morphologies, suggesting considerable cytotoxicity.

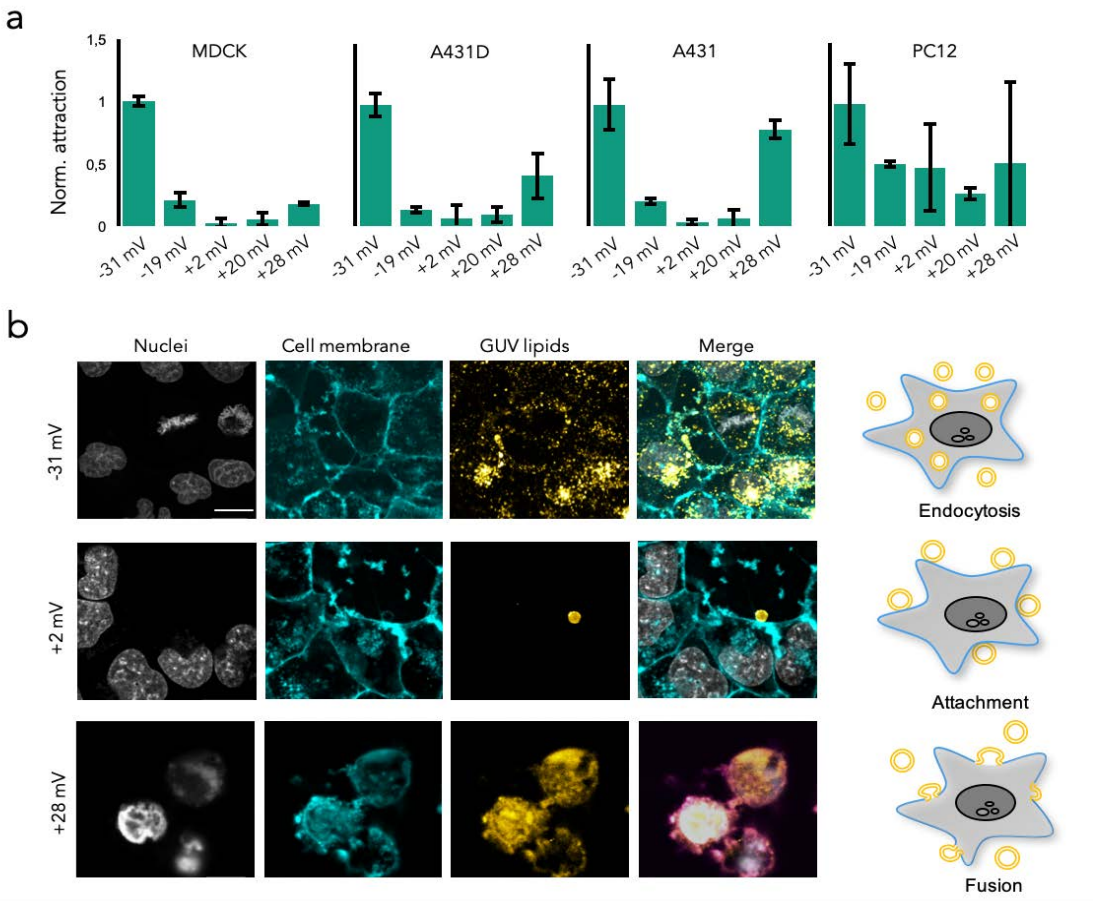

Figure 15 | Charge-mediated GUV-cell interactions. (**a**) Quantification of GUV-cell attraction with differently charged droplet-splitted GUVs (GUV ζ-potential indicated on x-axis) with endothelial (MDCK), epithelial (A431D and A431) and adrenal (PC12) cell lines. Droplet-splitted GUVs were incubated with cells for 24 hours and attraction assays were performed. Results are shown as average values normalized to the -31 mV average and SD from three technical replicates. (**b**) Representative single plane fluorescence confocal microscopy images and schematic illustrations of charge-mediated GUV-A431D cell interactions with differently charged, droplet-splitted GUVs (GUV ζ-potential indicated on the left). Nuclei (first column) were stained with Hoechst 33342, cell membranes (second column) were stained with WGA-AlexaFluor488 and GUVs (third column) were imaged by incorporation of LissRhod-PE fluorescent lipids into GUV formulation. Last column shows the merged channels. The scale bar is 20 µm.

In order to confirm that negatively charged, droplet-splitted GUVs are taken up into the intracellular environment, two additional analysis were performed: First, z-resolved fluorescence confocal microscopy of A431D cells with fluorescence cytoplasm (stained with CellTracker labelling dye) which were incubated with negatively charged GUVs (GUVs composed of 20mol% EggPG, 79mol% EggPC and 1mol% LissRhod PE) was performed (see supplementary video 1). This analysis revealed that the GUVs are located within the cell body and that they were absent of any cytoplasmic staining, which indicates that they reside within intracellular compartments (e.g. endosome). Second, cells incubated with negatively charged, droplet-splitted GUVs (composed of 20 mol% EggPG, 79 mol% EggPC and 1 mol% LissRhod PE) were fixed and analysed by transmission electron microscopy (TEM) (Figure 16a). In line with the previous results, this analysis showed that the droplet-splitted GUVs reside inside membrane-enclosed compartments within the cells´ body (Figure 16b). This could suggest endosomal processing of the GUVs after endocytic, phagocytic or pinocytic uptake. Taken together, these assessments proof that negatively charged GUVs are indeed taken up by cells. Moreover, these results reveal the pervasive influence of GUV charge on GUV-cell interactions and underscore the importance methods that allow for GUV charge control.

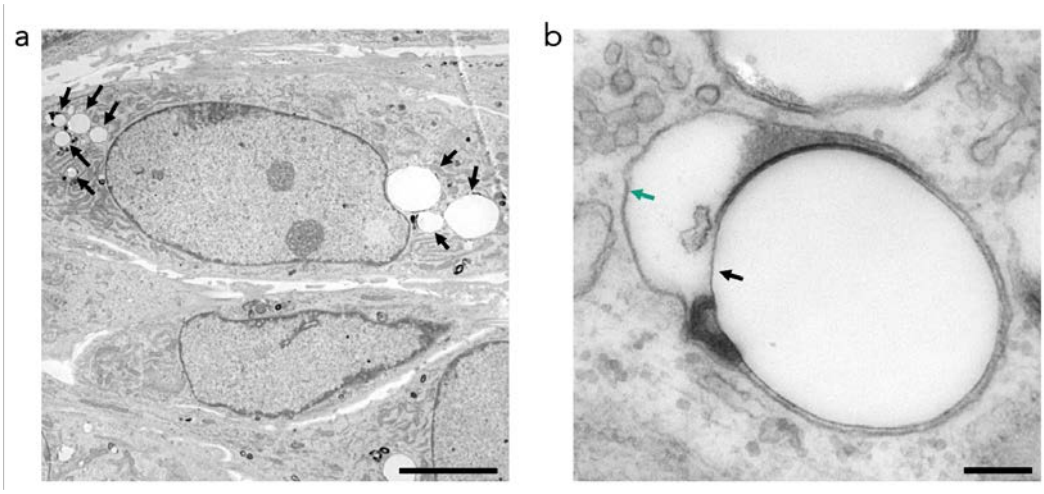

Figure 16 | Transmission electron microscopy analysis of GUVs internalized by cells. (**a**) Representative horizontal TEM section micrograph of REF cells incubated with negatively charged GUVs for 16 hours. GUVs inside the cytoplasm are marked by the black arrows. The scale bar is 2.5 µm. (**b**) Higher magnification of an internalized GUV. Black arrow indicates the GUV membrane and turquoise arrow indicates the endosomal membrane. The scale bar is 200 nm.

4.2 Molecular engineering of GUV-cell interactions

4.2.1 Biofunctionalization of droplet-splitted GUV membranes

Charge-mediated uptake of droplet-splitted GUVs appears to be an efficient process to direct the mode of GUV-cell interactions. However, it does not provide cell-type specific interactions or targeting of the GUVs. To achieve such a specific GUV-cell interaction, a toolbox for bio-orthogonal decoration of GUV membranes, based on different conjugation strategies, with targeting biomolecules was developed. Based on this, an additional ligand-directed targeting functionality can be introduced on the GUV surface. Three individual one-step biofunctionalization strategies were implemented by introducing functionalized lipids into droplet-splitted GUVs (GUVs composed of 20mol% EggPG, 76mol% EggPC, 1mol% LissRhod PE and 1mol% of the respective functionalized lipid): 1. biotinylated lipids, in order to bind streptavidin tagged proteins, 2. NTA-Ni^{2+}-functionalized lipids, in order to bind histidine-tagged proteins and 3. NH_2-containing DOPE lipids, for linking to N-hydroxysuccimid (NHS)-functionalized targeting moieties. These GUV-functionalization approaches can be implemented separately in different droplet-splitted GUV batches but because of their orthogonal nature, also in parallel on the same GUV membrane. For instance, triple orthogonal functionalization of droplet-splitted GUVs was achieved by adding Atto425-labelled streptavidin, histidine-tagged green fluorescent protein and NHS-functionalized Alexa647 to released droplet-splitted GUVs (Figure 17a). This demonstrates that GUV membranes can be specifically decorated with small functionalized biomolecules in simple one-step reactions.

However, also the immobilization of supra-molecular complexes like antibodies on the GUV surface is of special interest to achieve antigen-specific targeting. Also, coupling of complete (nano-)particles to the GUVs could offer great potential for *in vivo* imaging technologies (e.g. based on magnetic nanoparticles, Raman resonance or photothermal optical coherence tomography (Smith and Gambhir, 2017)). In order to achieve droplet-splitted GUV functionalization with such big moieties, sequential multi-step GUV functionalization strategies were implemented. For instance, AlexaFluor488-conjugated anti-CD3 immunoglobulins were immobilized on the GUV (GUVs composed of 20mol% EggPG, 78mol% EggPC, 1mol% LissRhod PE and 1mol% DGS-NTA(Ni^{2+})) surface *via* 6x His-tagged protein G bound to NTA-conjugated lipids (Figure 17b). Moreover, cysteine-functionalized gold nanoparticles were immobilized on the GUVs (GUVs composed of 20mol% EggPG, 78mol% EggPC, 1mol% LissRhod PE 1mol% palmitic acid-NHS) *via* NHS-reaction of palmitic acid-NHS lipids and the NH_2-groupe of

cysteine (Figure 17c and supplementary video 2). This demonstrates that droplet-splitted GUVs can not only be decorated with small molecular compounds but also with large, potentially multifunctional particles for advanced therapeutic and diagnostic applications.

In order to assess whether such macromolecular complexes remain functional once coupled to the GUV membrane and if they eventually provide any functionality to the GUVs, antibody-mediated GUV-cell interaction was assessed. Antibodies offer great selectivity for specific cell surface antigens, wherefore antibody-based targeting has previously been used to enhance specific SUV delivery (Sofou and Sgouros, 2008). To qualitatively assess the cell-binding properties of anti-CD3-coated GUVs (composed of 20mol% EggPG, 78mol% EggPC, 1mol% LissRhod PE and 1mol% DGS-NTA(Ni^{2+})), they were incubated with $CD3^{+}$ Jurkat T-lymphocytes. When imaged by fluorescence confocal microscopy, an attachment site between the cells and the GUVs, reminiscent of a "minimal" immunological synapse, could be observed (Figure 17d). This indicates successful GUV-cell coupling. In summary, this demonstrates that a multitude of strategies can be applied in order to design and produce droplet-splitted GUVs with biomolecular coatings which could achieve a more cell-type directed targeting or a more specific cell-GUV attraction.

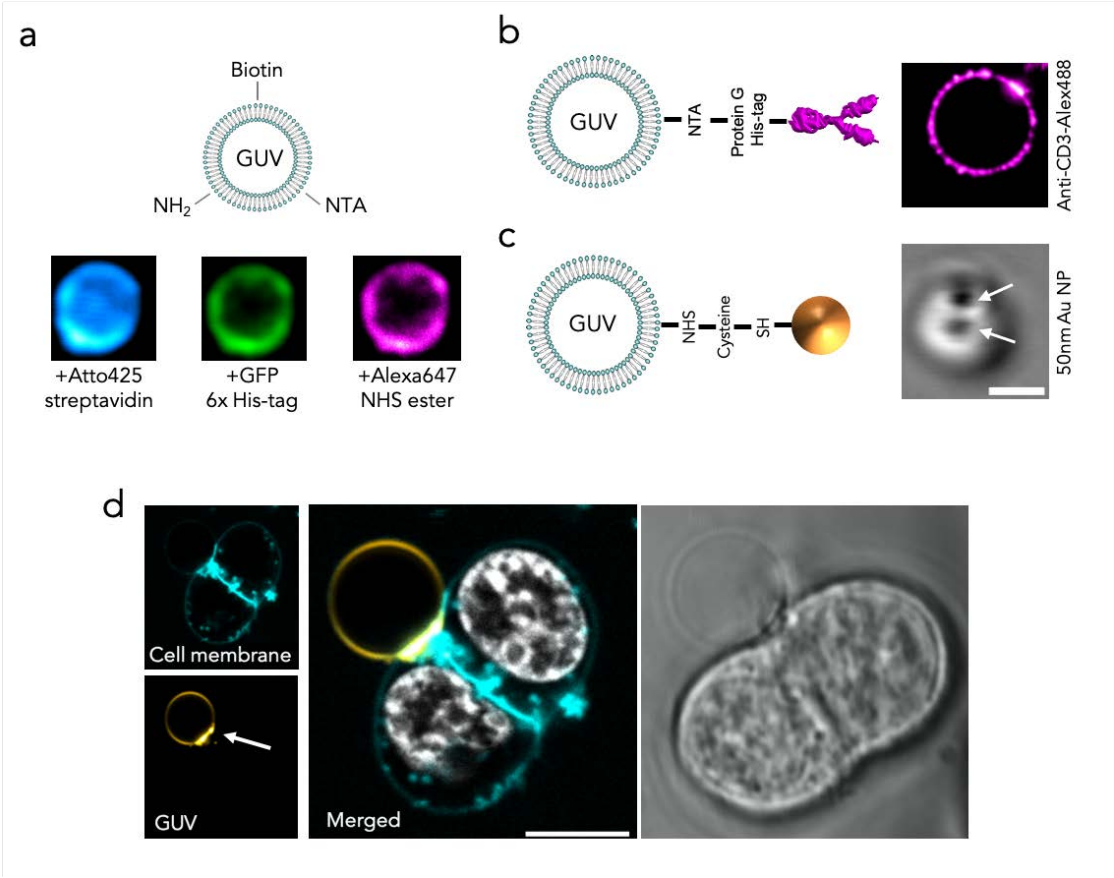

Figure 17 | Bio-functionalization of droplet-splitted GUV membranes. (**a**) Schematic illustration and representative single plane fluorescence confocal microscopy images of triple-functionalized GUVs produced by a droplet splitting microfluidic device. GUVs were coupled to Atto425-streptavidin, His-tagged GFP and NHS-Alexa647 *via* NTA-Ni^{2+}, biotin and NH_2-conjugated lipids, respectively. (b and c) Schematic illustrations and representative single plane fluorescence confocal microscopy images of sequential GUV functionalization with (**b**) anti-CD3 immunoglobulins or (**c**) 50 nm gold nanoparticles. Right panels show a fluorescence confocal image of droplet-splitted GUVs functionalized with AlexaFluor488-linked anti-CD3 IgG-immobilized to the GUV membrane *via* 6x His-tagged Protein G to NTA-Ni^{2+} lipids and a bright field image of gold nanoparticles immobilized to a GUVs (indicated by white arrows). Scale bar is 1 µm and 2 µm for (c) and (b), respectively. (**d**) Formation of an attachment site between CD3+ Jurkat T-lymphocytes and anti-CD3-functionalized GUVs after co-incubation for 24 hours. Cell membranes were stained with WGA-AlexaFluor488 (cyan), GUVs were imaged by incorporation of LissRhod-PE fluorescent lipids into the formulation (yellow) and nuclei in the merged image were stained with Hoechst 33342 (grey). The arrow points to the site of a lipid and WGA-stain cluster at the GUV-cell interface. Respective bright field image is shown in the right panel. The scale bar is 6 µm.

4.2.2 Ligand-mediated attractive GUV-cell interactions

In order to increase the interaction of GUVs and cells, further experiments were directed towards presenting protein and peptide ligands on the GUV surface which by binding to receptors expressed on cells, could foster specific attractive interactions. Receptor-ligand interactions exhibit a distance-dependent specific binding-energy, resulting in an attractive force (typically in the pN range) between the two binding partners. In order to systematically asses if such receptor-specific interactions can be employed to increase droplet-splitted GUV-cell attraction, negatively charged, RGD functionalized GUVs were produced (GUVs composed of 20mol% DOPG, either 79, 78, 77 or 69mol% DOPC, 1mol% LissRhod PE and 9, 1, 2 or 10mol% DSPE-RGD). The integrin binding motif RGD was used, since this tripeptide has been shown to enhance liposomal drug delivery through integrin initiated endocytosis (Wang et al., 2014). For this assessment, varying amounts of RGD-coupled lipids were introduced into the SUV formulation in order to produce droplet-splitted GUVs with varying RGD surface densities (Figure 18a). Respective GUVs were cultured together with three adherent cell lines (MDCK, A431 wt and A431D) that express integrin receptors for 24 hours. The GUV-cell interaction for these RGD-GUVs was subsequently assessed with attraction assays (see section 3.2.19). Naïve, non-decorated GUVs were used as a reference standard. For all tested cell lines, a correlation between GUV-cell attraction and GUV RGD-density was found (Figure 18b). For all three cell-types, an approximately 10% increase was found for GUVs composed of 10 mol%-RGD ligand compared to naïve vesicles. This effect was additionally studied with non-adherent Jurkat T-lymphocyte cells, which express high levels of integrin $\alpha_4\beta_1$, by flow cytometry quantification. Here, incorporation of 10 mol%-RGD into the droplet-splitted GUV formulation induced an approximately 15-fold increase in GUV-cell attraction, as measured by quantifying the mean GUV fluorescence signal intensity on single cells (corresponding to GUVs that have either attached to cells or reside within the cells).

In order to analyse the interaction and attraction of RGD-functionalized droplet-splitted GUVs with cells on a qualitative level, fluorescence confocal microscopy analysis of A431D cells incubated with RGD functionalized droplet-splitted GUVs (composed of 20mol% DOPG, 77mol% DOPC, 1mol% LissRhod PE and 2mol% DSPE-RGD) was performed. It was found that GUVs mostly accumulated in the perinuclear region of cells, suggesting intracellular uptake of the GUVs, and at the cell periphery, where high integrin densities can be found (Figure 18c). Taken together, these results demonstrate that GUV-

cell interaction and attraction can be increased by decorating the droplet-splitted GUV surface with cell receptor-specific ligands.

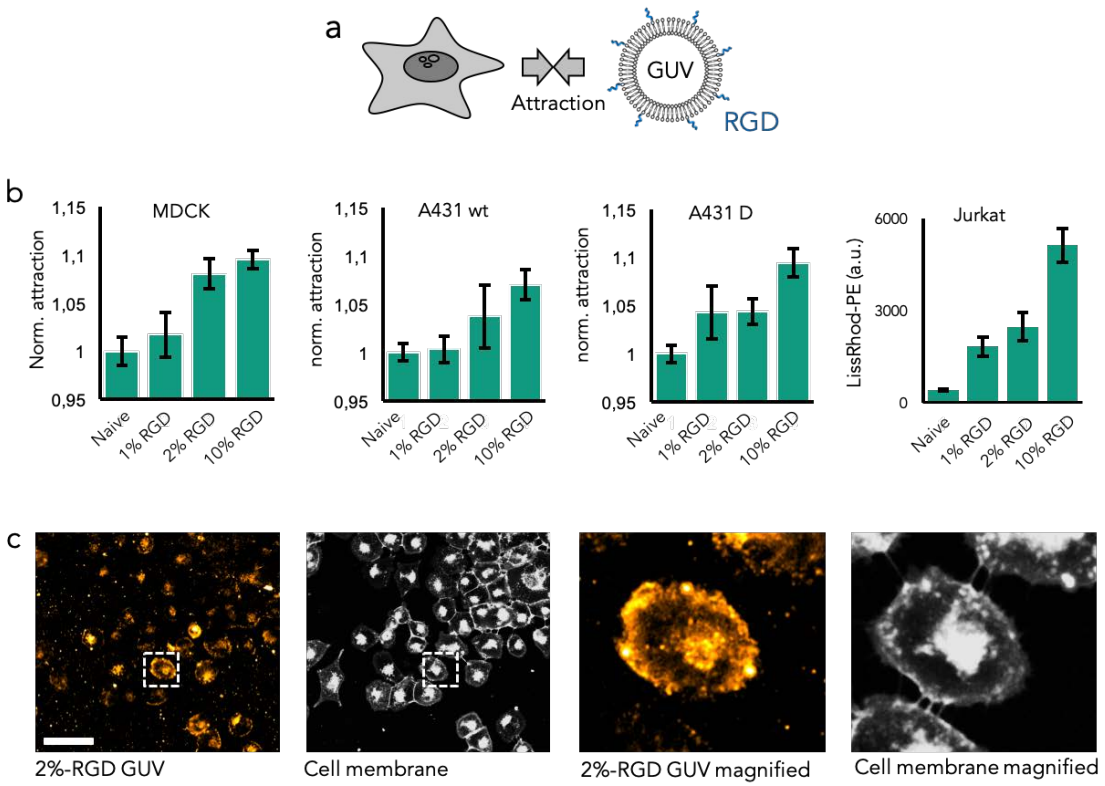

Figure 18 | Ligand mediated GUV-cell attraction. (**a**) Schematic illustration of RGD-mediated GUV-cell attraction at the GUV-cell interface by conjugation of integrin-specific RGD ligands to the GUV surface. (**b**) Attraction assay analysis of droplet-splitted GUVs functionalized with varying amounts of RGD-coupled ligands and incubated with different cell lines for 24 hours. The results are normalized to the mean attraction of naïve GUVs for each condition and shown as average value and SD from three technical replicates. For quantification of GUV-cell attraction of RGD-functionalized droplet-splitted GUVs and Jurkat T-lymphocytes, suspended cells were measured by flow cytometry. (**c**) Representative single plane fluorescence confocal microscopy images of droplet-splitted GUVs decorated with 2 mol% RGD ligands (and harbouring 1mol% LissRhod PE for imaging, yellow) and incubated with membrane-stained (grey) A431D cells for 24 hours. The scale bars are 60 µm. The two images on the right side show magnified view of the areas indicated by the dashed lines in the two left panels. Accumulation of GUVs in the perinuclear region and at the cell periphery can be observed.

Furthermore, in order to visualize and verify the correct immobilization of recombinant proteins and ligands on the GUV surface, cryogenic transmission electron microscopy (cryoTEM) was performed (Figure 19). For this, GUVs were produced by droplet-splitting of dsGUVs formed with SUV composed of 78mol% EggPC, 20mol% EggPG, 1mol% LissRhod PE and 1mol% DGS-NTA(Ni^{2+}). The released GUVs were subsequently

incubated with recombinant human 6xHis-tagged FasL and observed by cryoTEM. GUVs of the same composition were left uncoupled as a control. A protein brush corona of linear thread-like particles could be observed around the FasL coupled GUVs (Figure 19a). Comparable observations were not made for uncoupled GUVs (Figure 19b).

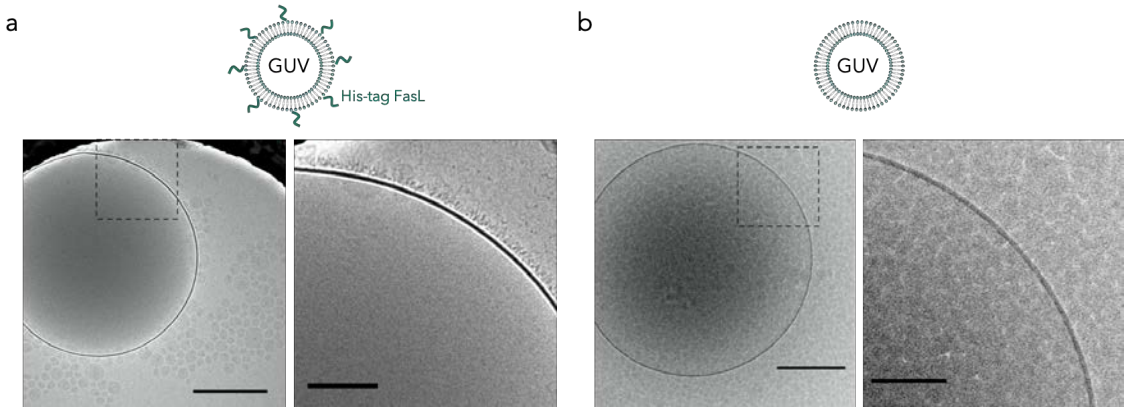

Figure 19 | CryoTEM analysis of protein-coated GUVs. (**a**) CryoTEM micrograph of a GUV composed of 78mol% EggPC, 20mol% EggPG, 1mol% LissRhod PE and 1mol% DGS-NTA(Ni^{2+}) coupled to recombinant human 6xHis-tagged FasL. Inset shows magnification of the protein thread-like corona on the GUV surface as indicated by the dashed lines in the overview image. Scale bars are 300 nm and 100 nm for the overview and magnified image, respectivly. (**b**) CryoTEM micrograph of a GUV composed of 78mol% EggPC, 20mol% EggPG, 1mol% LissRhod PE and 1mol% DGS-NTA(Ni^{2+}) without protein corona. Inset shows magnification of the plain GUV surface as indicated by the dashed lines in the overview image. Scale bars are 200 nm and 80 nm for the overview and magnified image, respectivly.

4.2.3 Regulation of repulsive GUV-cell interactions

Section 4.2.2 introduced functionalization strategies for GUV-decoration with RGD ligands and antibodies to enhance GUV-cell interactions. However, this biofunctionalization does not prevent other, for instance charge-driven non-specific interactions, at the GUV-cell interface. These non-specific attractive interactions could potentially be high enough to interfere with the specific ligand-based interaction. To assess this effect, non-charged droplet-splitted GUVs (composed of 98mol% EggPC, 1 mol% LissRhod PE, 1 mol% DGS-NTA(Ni^{2+})) coated with the neuronal cell-adhesion molecule NrCam (6x His-tagged), were incubated with SH-SY5Y neuroblastoma cells and the resulting attraction was compared to those of non-charged naïve vesicles. The attraction assay showed that both attraction values were comparably high (Figure 20). This could indicate that the attraction effect between droplet-splitted GUVs and cells is mostly based on the vesicle charge and that the ligand coating (e.g. RGD, NrCAM, antibody, etc.) does only play a role in e.g., 1. establishing the primary contact, 2. maintaining a stable

interface between the GUV and the cell or 3. in activating specific downstream signalling mediating GUV engulfment or uptake. It proofs however, that non-specific lipid-cell attraction can be considerably high and interfere with ligand-directed GUV targeting.
To overcome this limitation, poly-ethylenglycol (PEG)-coated GUVs were produced from

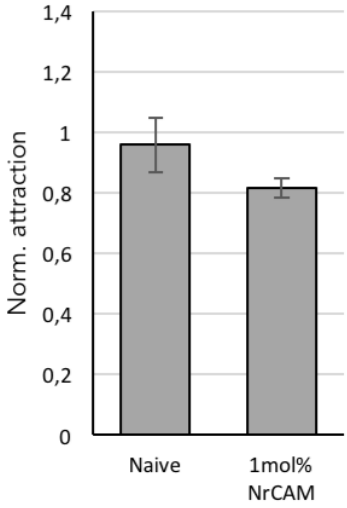

Figure 20 | Assessment of non-specific, lipid-based GUV-cell interactions. Attraction assay values for naïve and recombinant 6x His-tagged NrCAM-functionalized non-charged, droplet-splitted GUVs (GUVs composed of 98mol% EggPC, 1 mol% LissRhod PE, 1 mol% DGS-NTA(Ni^{2+})) incubated for 24 hours with SH-SY5Y neuroblastoma cells. No considerable increase in attraction is observed by NrCAM functionalization as the non-specific lipid-based attraction appears to be larger than the NrCAM ligand-receptor based attraction.

droplet-splitted dsGUVs in order to introduce a PEG-mediated repulsive force between the cells and the GUVs (Figure 21a). This could potentially shield and reduce the non-specific interactions. Covering small vesicles (<100 nm) with PEG has previously generated so-called "stealth" liposomes, which feature prolonged blood-stream circulation times because of reduced opsonin coating and cell interaction (Immordino et al., 2006). Also, if successfully applied on GUVs, this could lead to masking of electrostatic non-specific interactions and introduce a repulsive force between cells and GUVs. To assess this effect, GUVs harbouring 15mol% or 50mol% of negatively (DOPG) or positively (DOTAP) charged lipids were produced, to both GUV types PEG350, 750 or 1000 conjugated PE lipids were added additionally to the formulation. In order to assess successful PEG-coating and a potential charge shielding effect, the ζ-potential of respective SUVs and of the released GUVs were measured by DLS (Figure 21b). It was found that the ζ-potential of negatively and positively charged vesicles increased with decreasing PEG chain length and with lower PEGylation-rate of the formulation. This

shows that PEG conjugation to the droplet-splitted GUV surface exhibits the potential to shield the GUV-surface charge. Secondly, it was assessed to which extend GUV PEGylation and thereby masking of the GUV surface charge (and possibly also reduced opsonin coating), impacts on GUV-cell attraction. Therefore, the PEGylated GUVs were incubated with six different adherent cell lines and attraction values for each condition were measured (Figure 21c). For all tested cell lines, GUV PEGylation could decrease charge-mediated GUV-cell attraction to some extent. Albeit varying effectivity between the different cell lines, this effect was mostly more pronounced for GUVs with higher PEG-concentrations and higher PEG-molecular weight in their formulation. For instance, the interaction of GUVs composed of 5mol% PEG350 with A431D carcinoma cells, showed almost 50% more attraction as compared to GUVs composed of 50mol% PEG350. Moreover, especially an increase the PEGylation rate appeared to decrease the GUV-cell interaction.

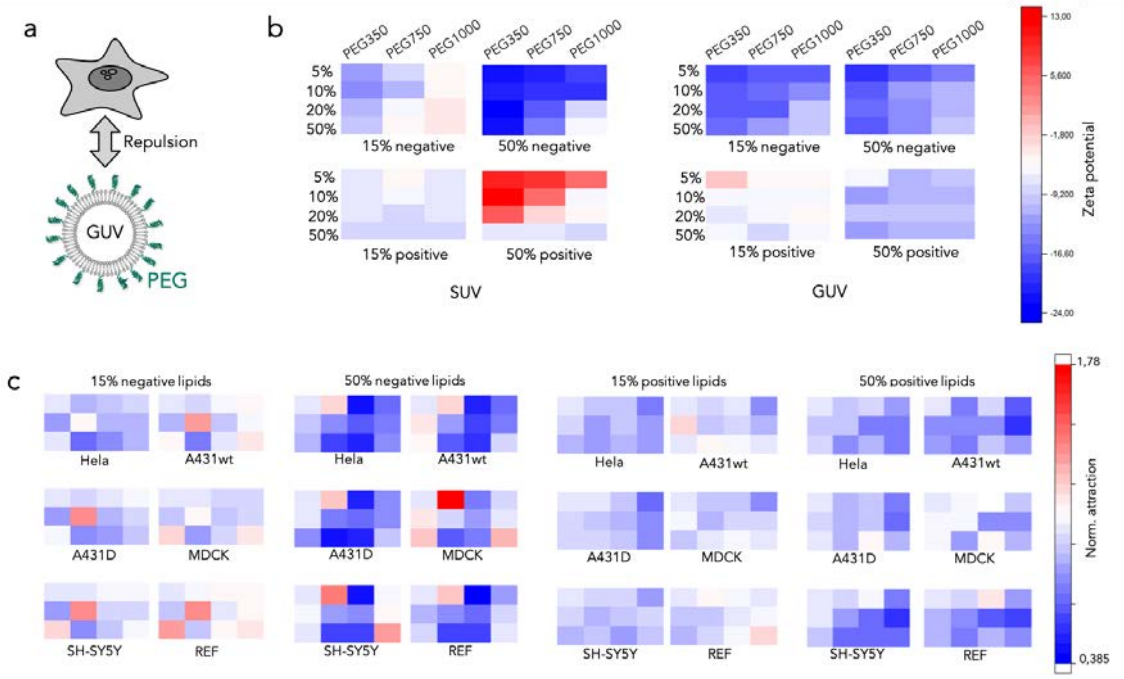

Figure 21 | Repulsive GUV-cell interactions by GUV PEGylation. (**a**) Schematic illustration of PEG-mediated GUV-cell repulsion. (**b**) Color-coded heat-map illustration of SUVs and droplet-splitted GUVs ζ-potentials for lipid formulations with varying amounts of positively (DOTAP) or negatively (DOPG) charged lipids as well as different concentrations of PEG and PEG-molecular weights. SUV and GUV ζ-potentials are shown on the left and right, respectively. Upper and lower row show ζ-potentials for negatively and positively charged GUV formulations, respectively. PEG concentration (mol%) is indicated on the left, PEG-molecular weight on the top. (**c**) Color-coded heat-map illustration of attraction values obtained with the GUVs from (b) for six different cell lines (specified below the respective heat-maps) after co-incubation for 24 hours. Results for negatively and positively charged lipid formulations are shown on the left and on the right, respectively. Results are normalized to the attraction value obtained for 5mol% PEG350 for each cell line separately. Upper, middle and lower row represent values for PEG350, PEG750 and PEG1000, respectively. First, second, third and fourth column represent values for 5mol%, 10mol%, 20mol% and 50mol%, respectively.

In order to analyse this repulsive interaction between cells and droplet-splitted GUVs on a qualitative level, fluorescence confocal microscopy imaging was performed. In line with the findings described above, this analysis showed that negatively charged, naïve GUVs incubated with A431 cells for 24 hours mostly co-localized with the cells and only a few of them were found between cell groups (Figure 22). Consistently, PEGylated GUVs could mostly be observed accumulated in the intercellular space, where they formed "contact inhibition zones" around individual cells. This mode of GUV-cell interplay might be traced back to repulsive interactions. In summary, these experiments show that GUVs

generated from droplet-splitted dsGUVs can be produced with PEGylated lipid-formulations and that these droplet-splitted GUVs will lead to reduced charge-mediated GUV-cell interactions.

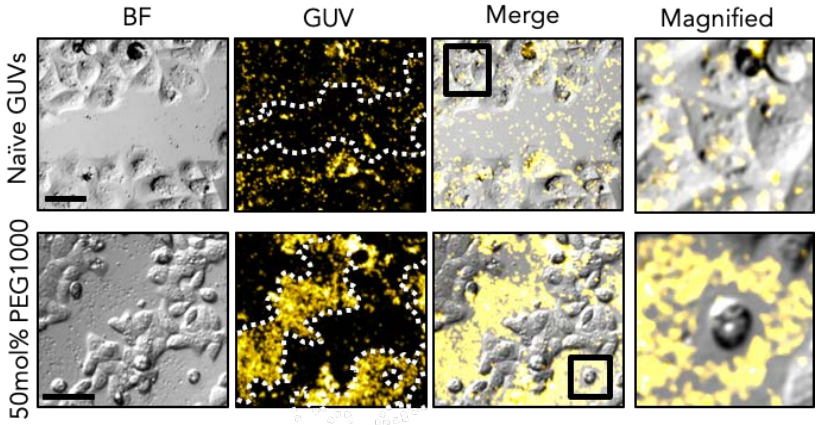

Figure 22 | Contact inhibition between cells and GUVs. Representative bright field (first column, grey) and fluorescence confocal microscopy (second column, yellow) images of A431 cells incubated with naïve, negatively charged, droplet-splitted GUVs (top row) or negatively charged, droplet-splitted GUVs containing 50mol% PEG1000 (bottom row) for 24 hours. The naïve GUVs co-localize with the cells, while the PEGylated GUVs mostly accumulate in the intercellular space (merged image, third column). Formation of PEGylated-GUV inhibition zones around the cells is observed (fourth column displays magnified images of the areas indicated by the black boxes in the merged images). In the fluorescent-channel images, borders of cells and cell groups are indicated by the white dotted lines as deduced from the bright field images. Scale bars are 15 µm.

4.2.4 Regulation of attractive and repulsive GUV-cell interactions

In order to achieve cell-type specific uptake of droplet-splitted GUVs, the strategies for GUV-cell attraction and repulsion described above, were implemented into a single GUV preparation. In this case, it was aimed to limit distorting, non-specific charge-mediated attractions between the cells and droplet-splitted GUVs by PEGylation, while simultaneously introducing GUV ligand-functionalization in order to promote specific attraction to desired cell-types. Therefore, droplet-splitted GUVs composed of 20mol% negatively charged EggPG lipids, 54mol% neutral EggPC lipids, 1mol% LissRhod PE, 20mol% PEG750-conjugated PE lipids and 5mol% NHS-coupled palmitic acid for ligand immobilization *via* NH_2 groups were produced. Following the attraction-repulsion concept, for targeted interaction with a specific cell-type, the ligand-receptor based attraction between a GUV and a cell needs to be high enough to overcome the PEG-mediated repulsion. Ideally, this is only given for cells that express the receptive receptor

or antigen (Figure 23a). Eventually, the charge mediated interaction could then lead to intracellular uptake of the droplet-splitted GUV or generation of a mature GUV-cell interface. In order to experimentally validate this concept, droplet-splitted GUVs with 15 different biomolecular (attached by the NHS group) coatings were produced and tested in attraction assays. Hereby, some coatings were expected to be specific for a given cell type (*e.g.* anti-cadherin antibodies or bradykinin) while others could potentially induce an attraction in all cell types (*e.g.* poly-L-lysine), serving as a positive control. Each GUV formulation, was tested with 6 different cell lines (human fibroblast BJ cells, neuroblastoma SH-SY5Y cells, endothelial MDCK cells, epithelial A431 cells, dexamethasone-treated epithelial transformed A431 cells and Hela cells) in order to cover a wide spectrum of potentially interesting targets for drug delivery. Each individual attraction value for a given cell type was normalized to the attraction value determined for BSA-coupled GUVs with the same cell type, in order to reference the attraction to a moderately unreactive protein (Figure 23b). The measurements showed that coating of droplet-splitted GUVs with peptides and proteins that do not bind to specific cell types – *e.g.* wheat germ agglutinin (WGA, which binds to the glycoproteins and the glycocalyx on the cell surface), poly-L-lysine (which establishes interactions based on its highly positive charge) or the HIV derived tat-peptide (a cell membrane penetrating, arginine-rich peptide) – display high attraction to almost all tested cell types. This could be based

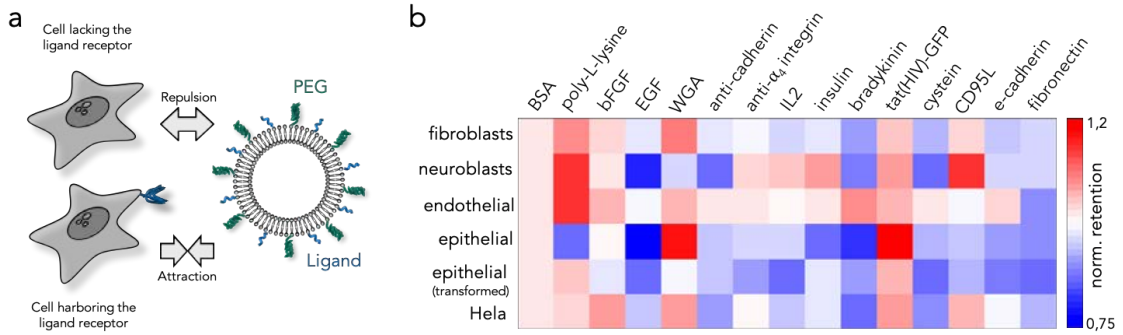

Figure 23 | Fine tuning of repulsive and attractive GUV-cell interactions for targeted delivery. (**a**) Schematic illustration of a GUV biofunctionalized with a receptor-specific ligand and additionally decorated with PEG in order to achieve specific attraction to a cell expressing the respective receptor. (**b**) Attraction values obtained for PEG 750 PEGylated droplet-splitted GUVs coated with different non-specific (e.g., BSA, PLL, WGA and tat-peptide) and specific (e.g., anti-cadherin, recombinant cadherin and bradykinin) cell ligands (*via* 5mol% NHS lipids) to human fibroblast BJ cells, neuroblastoma SH-SY5Y cells, endothelial MDCK cells, epithelial A431 cells, dexamethasone-treated epithelial transformed A431 cells and Hela cells. Values for each condition were normalized to the attraction of BSA-coupled droplet-splitted GUVs for the respective cell line.

on the non-specific attractions mediated by these coatings, which successfully overcame the repulsive "PEG-barrier" in all cell types. However, proteins and ligands that target receptors more specifically, e.g. bradykinin which binds to the bradykinin-specific G-protein-coupled receptors (highly expressed on epithelial and endothelial cells), attraction specific to endothelial cells was achieved. In this specific case, the attraction value was increased up to 40% compared to other cell lines. When targeting cadherin proteins by coating the droplet-splitted GUVs with recombinant cadherin (which can establish homophilic interactions) or anti-cadherin antibodies, similar specific attractions towards endothelial cells could be obtained. This systematic and comparative assessment shows that PEG-based shielding of non-specific interactions, combined with ligand-based specific attractive interactions, can achieve a preferential GUV targeting to individual cell types.

To assess whether this strategy for targeted attraction is able to induce specific GUV-uptake by selected cells also in a more complex, multi-cell type environment, co-culture experiments were performed. For this, co-cultures of astrocyte (Hs683) and neuronal (SH-SY5Y) model cell lines were established, each stained with a distinct CellTracker probe in order to discriminate the cells by fluorescence microscopy. These two specific cell-types were chosen as astrocytes and neurons grow and interact in great proximity in mammalian brains. Selectively targeting one specific cell type of them, is of great interest for therapeutic approaches treating neuroblastoma or neurodegenerative diseases. These co-cultures were incubated with droplet-splitted GUVs composed of 58mol% EggPC, 20mol% EggPG, 20mol% PEG750, 1mol% LissRhod PE and 1mol% 18:1 DGS-NTA(Ni^{2+}) lipids. The GUVs were additionally coated with the neuronal adhesion molecule NrCAM (His-tagged extracellular domain aa20 - 630) which is able to bind to axonin-1 expressed preferentially on neuronal membranes (Figure 24a)(Stoeckli and Landmesser, 1995). After 24 hours of incubation, fluorescence confocal microscopy was performed in order to analyse the uptake of GUVs by each cell type individually (Figure 24b) (see section 3.2.20). The quantification did not only show that the GUVs were taken up by the cells but also that neuronal cells contained up to 520% more GUVs than astrocyte cells. This experiment suggests that preferential targeting of droplet-splitted GUVs can be achieved by fine-tuning the repulsive and attractive interactions to specific cell types.

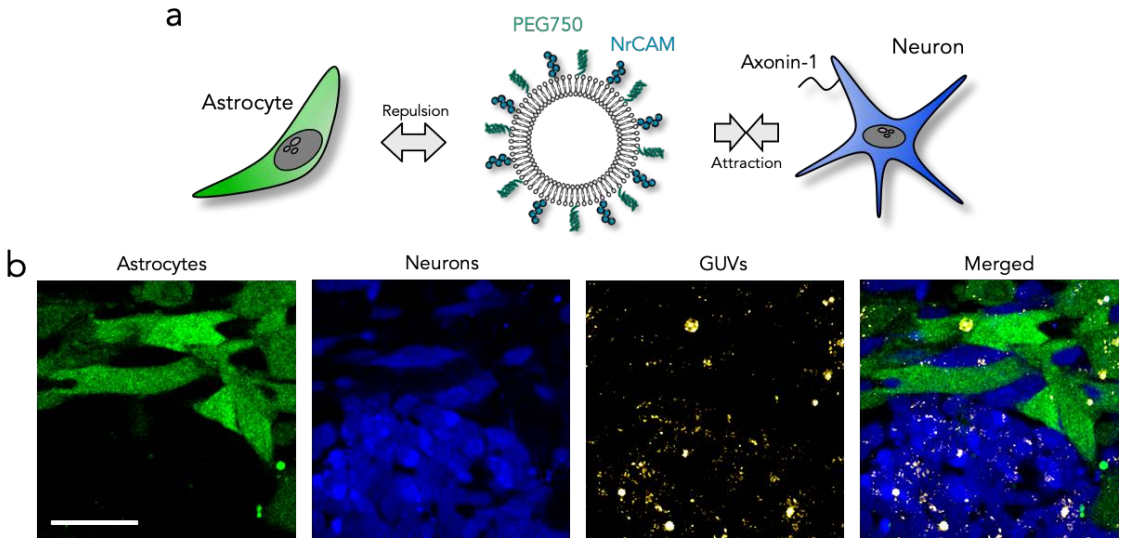

Figure 24 | Preferential targeting of GUVs by repulsive and attractive interactions. (**a**) Schematic illustration of GUVs with a repulsive PEG layer and biofunctionalized with NrCAM in a co-culture with neuronal cells and astrocytes, which express and lack the axonin-1 receptor, respectively. (**b**) Representative single plane fluorescence confocal microscopy images of the astrocytes (green) and neurons (blue) co-cultures following 24 hours of incubation with droplet-splitted GUVs biofunctionalized with recombinant NrCAM and coated with 20mol% PEG750 conjugated lipids. SH-SY5Y neurons and Hs683 astrocytes were stained with CellTracker Blue and Green, respectively. GUVs were imaged by incorporation of LissRhod-PE fluorescent lipids into the GUV formulation. The scale bar is 50 µm.

4.2.5 Lysosomal escape for GUV cargo delivery

As shown by the fluorescence confocal microscopy and transmission electron microscopy experiments in section 0, negatively charged droplet-splitted GUVs are taken up by cells into the intracellular space. However, most cargos that enter the intracellular environment by endocytosis, phagocytosis or micropinocytosis are usually degraded within lysosomal compartments by enzymatic decomposition. In order to analyse the endosomal sorting and a possible lysosomal degradation of droplet-splitted GUVs, negatively charged fluorescent GUVs were incubated with CellTracker labelled REF cells which were simultaneously stained with fluorescently conjugated WGA in order to stain plasma membrane derived endosomal compartments (see section 3.2.10). Fluorescence confocal microscopy observation of these cultures showed that most GUVs were located inside the cells, dispelling any cytoplasmic staining, surrounded by endosomal membranes (Figure 25a). This confirms that the entry pathway of droplet-splitted GUVs is *via* membrane mediated uptake (e.g. micropinocytosis or phagocytosis), which excludes other uptake routs like direct membrane penetration or sole engulfment of the GUVs by the plasma membrane. In order to follow a possible lysosomal degradation of the droplet-splitted

GUVs, cells were additionally stained with LysoTracker dye (Figure 25b). After 24 hours of incubation, the GUV fluorescence was found to co-localize with the lysosomal staining, suggesting sorting of the endosome-entrapped GUVs into lysosomal compartments and subsequent progressive degradation of the GUVs once inside the cells. This is most probably accompanied by degradation of the GUV cargo and therefore reduces the deliver-efficiency, potentially impairing any therapeutic valuable outcome. Moreover, many pharmacological active compounds used for therapeutic approaches target cytoplasmic components. Therefore, efficient and complementary lysosomal escape mechanisms applicable for intracellular GUV cargo discharging need to be implemented into the GUVs´ functional repertoire. If successful, once taken up by cells, the GUVs

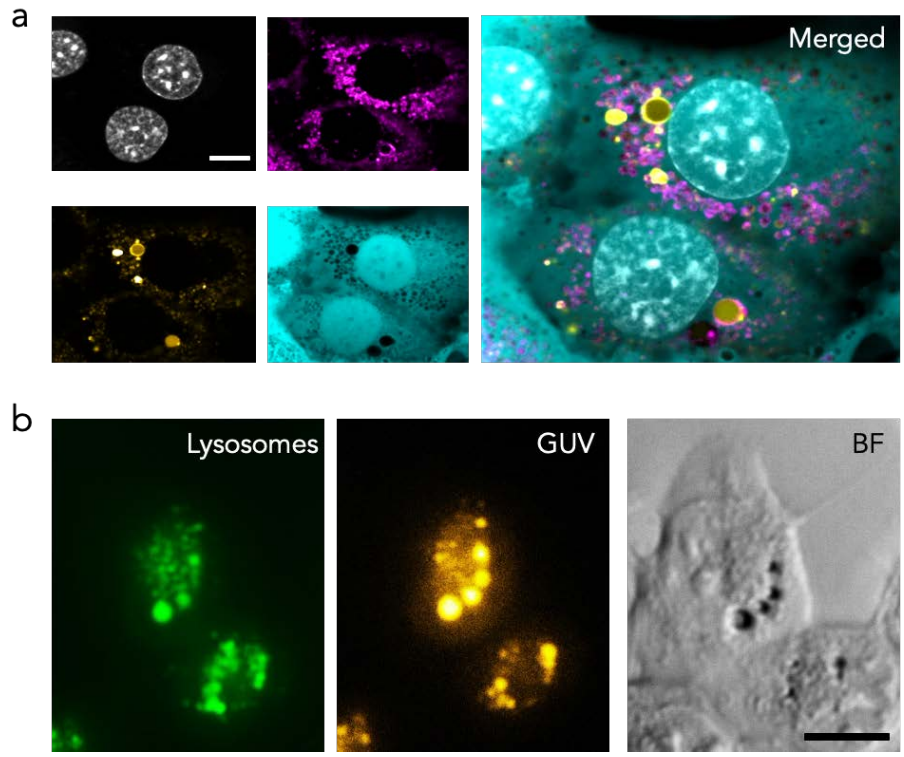

Figure 25 | Assessment of lysosomal GUV degradation. (**a**) Representative fluorescence confocal microscopy images of REF cells incubated with negatively charged GUVs. Nuclei (top left image) were stained with Hoechst 33342, endosomes (top center image) were labeled by addition of WGA-AlexaFluor488 together with the GUVs, GUVs (bottom left image) were imaged by incorporation of LissRhod-PE fluorescent lipids and the cytoplasm (bottom center image) was stained by CellTracker Green. The merged image (right image) demonstrates that GUVs reside within the cytoplasm, entrapped within endosomal compartments. The scale bar is 10 µm. (**b**) Representative fluorescence microscopy images of GUVs (yellow) incubated for 24 hours with REF cells (grey, bright field) that were stained with LysoTracker Green (green) in order to visualize lysosomal compartments. Co-localization of most GUVs with LysoTracker-positive compartments is observed. The scale bar is 10 µm.

would unload their intraluminal cargo into the cytoplasm during the lysosome-maturation process before and lysosomal degradation proceeds.

In order to circumvent lysosomal degradation, three different lysosomal escape mechanisms were implemented for assessment in droplet-splitted GUVs. All three mechanism are compatible with the production of droplet-splitted GUVs and are based on the rapid decrease of endosomal pH after lysosome fusion. The first tested mechanism has previously been used for delivery of nucleic acids (Zakeri et al., 2018) and is based on lysosomal rupturing *via* a proton sponge mechanism achieved by incorporation of high molecular weight poly-ethylene-imine (PEI) into the GUV lumen. The second approach is a biomimetic strategy based on the lysosomal escape of viral particles, which is mediated by pH-dependent fusiogenic peptides and intra-lysosomal fusion. These viral pore-forming peptides are hereby mimicked by a synthetic, arginine-rich GALA peptide attached to the GUV surface (Nakase et al., 2011). The third strategy achieves lysosomal escape of the GUV *via* intra-lysosomal membrane fusion through incorporation of the pH-sensitive, charge-switching lipid DOBAQ into the droplet-splitted GUV membrane. All three strategies have previously been verified and employed for drug delivery purposes, in many cases in combination with liposomal delivery. However, compared to most liposomes used previously, GUVs possess an increased surface to volume ratio, which is likely to affect the efficiency of these release strategies. Therefore, all three release strategies need to be revaluated for GUV-based systems.

For the next assessments, aiming to analyse and detect retention, degradation or release of droplet-splitted GUV cargo by lysosomal escape, the membrane impermeable dye 8-Hydroxypyrene-1,3,6-trisulfonic acid (HPTS) was incorporated into the GUV lumen. If successfully released, the dye is expected to distribute within the whole cell body, while when being retained inside the GUVs and lysosomes, only punctuated fluorescence is expected. As GUV membranes are non-permeable for HPTS (Dezi et al., 2013), a significant progressive leaking out of the GUVs neglected. Respective droplet-splitted GUVs were incubated with A431D cells for 24 hours and intracellular HPTS distribution was observed by fluorescence confocal microscopy (Figure 26a). For GALA-coupled and PEI-loaded droplet-splitted GUVs, the HPTS fluorescence inside the cells was exclusively detected in a punctuated form, co-localizing with the GUVs fluorescence. This indicates a stable HPTS retention inside the GUVs and lysosomes, suggesting unsuccessful cytoplasmic cargo release and endosomal or lysosomal entrapment (presumably followed by degradation). However, for droplet-splitted GUVs composed of

60mol% DOBAQ, the HPTS fluorescence could be found evenly distributed throughout the entire cell body, without co-localizing with the GUV fluorescence, therefore indicating successful release from the GUVs and the lysosomes into the cytoplasm. In order to confirm that DOBAQ containing GUVs indeed undergo a pH dependent charge switching, their ζ-potential was measured by DLS in a pH range of 2 to 8. At a pH between 8 and 4, the GUVs displayed a negative ζ-potential, while at lower pH, a positive ζ-potential was measured (Figure 26b). This proofs that DOBAQ containing GUVs undergo pH-dependent charge-switching and can be cationic at low pH, thereby possible inducing intraluminal inverse membrane fusion with lysosomal membranes.

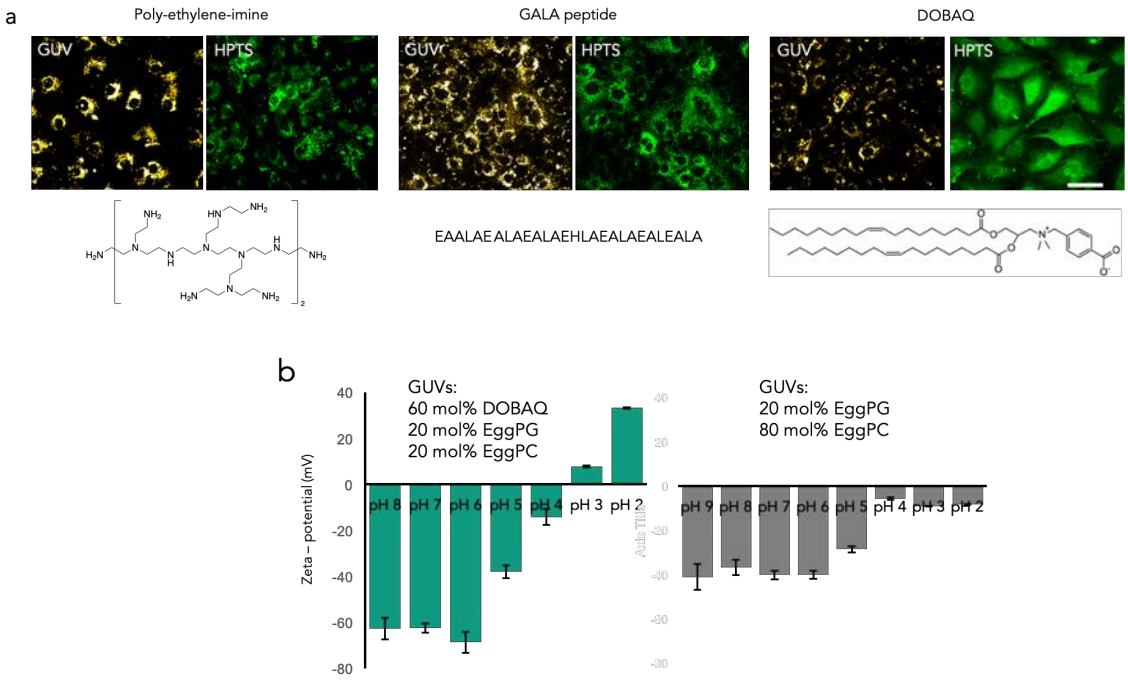

Figure 26 | Lysosomal escape of GUV cargo. (**a**) Representative fluorescence confocal microscopy images of PEI-, GALA peptide- and DOBAQ-mediated lysosomal escape of droplet-splitted GUVs (yellow) loaded with HPTS (green) and incubated with REF cells for 24 hours. The scale bar is 50 µm. (**b**) DLS ζ-potentials measurements of droplet-splitted GUVs at different pH conditions for GUVs containing 60mol% of the pH-sensitive lipid DOBAQ (left) or GUVs without pH-sensitive lipids (right). At low pH, the DOBAQ-containing GUVs undergo charge-switching from negatively to positively charged. Results are show as average and SD values from three technical replicates.

The experiments described above were carried out with cancerogenic cell lines. However, previous reports highlighted that the dynamics of particle uptake and lysosomal degradation significantly vary between transformed and untransformed cells (Elkin et al., 2015; Knecht et al., 1984). Therefore, the lysosomal escape efficiency of DOBAQ-based droplet-splitted GUVs was also analysed for *in vitro* cultured primary hippocampal neurons. Importantly, neurons represent an important target in many therapeutic procedures that aim to treat neurodegenerative diseases or neuronal tumours. Towards this end, negatively charged (20mol% EggPG), HPTS-loaded GUVs containing 60mol% DOBAQ were incubated for 24 hours with the neuronal primary cultures and subsequently observed by fluorescence confocal microscopy (Figure 27). For these experiments, the GUVs were additionally functionalized with WGA in order to enhance their attraction to the sialic acid-containing neuronal glycocalyx. Two important observations were made: First, the GUVs accumulated in the perinuclear region, suggesting intracellular uptake and further sorting by the intracellular membrane trafficking machinery. Second, when analysing the HPTS distribution, HPTS fluorescence was observed to be distributed within the whole cell body and dendrites, without co-localizing with the GUV fluorescence. These observations provide clear evidence that a DOBAQ-mediated lysosomal release of the GUV cargo is compatible and functional also in primary cells. Taken together, these experiments show that GUVs can be equipped with endosomal escape mechanisms to deliver their intraluminal cargo into the cytoplasmic space of cell lines and primary cells.

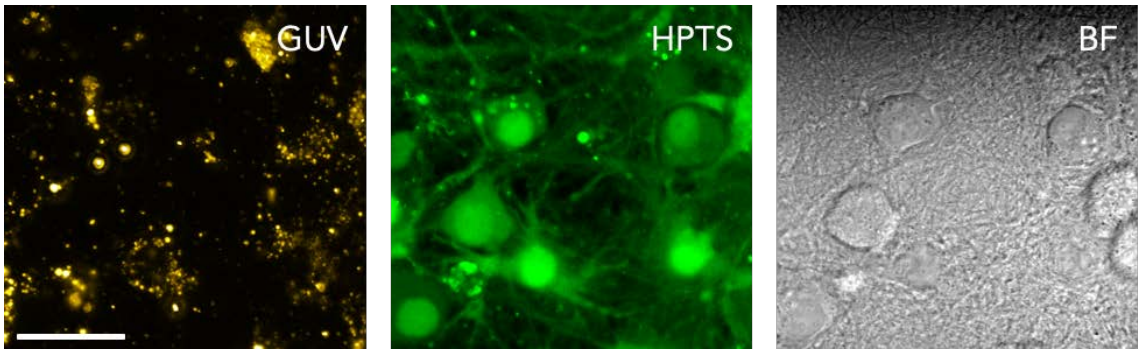

Figure 27 | DOBAQ-mediated lysosomal escape in primary neurons. Representative fluorescence confocal microscopy and bright field images of primary mouse hippocampal neurons cultured for 24 hours in the presence of HPTS (green) loaded droplet-splitted GUVs (visualized by incorporation of 1mol% LissRhod PE lipids, yellow) containing 60mol% of the pH-sensitive lipid DOBAQ. The scale bar is 30 µm.

4.2.6 GUV-based intracellular delivery of baculoviruses

One specific advantage of using droplet-splitted GUVs instead of SUVs and liposomes for targeted intracellular delivery of functional or therapeutic agents is that GUV can load significantly larger cargo. This not only expands the total cargo capacity but also allows to deliver a complete new set of theranostic compounds that are designed to be applied in future pharmacological procedures. For instance, many gene therapeutic approaches are based on viral transduction of the target cells. However, preventing recognition by the immune system as well as very restricted tissue selectivity of the applied viral particles, currently limit their administration and implementation in clinical routines. Outsourcing these functionalities on GUV membranes, in order to provide a taxi cabinet for the therapeutic virus, could offer new means to precisely deliver such largo cargos. One virus-type of special interest is the non-human but arthropod specific lipid enveloped dsDNA baculovirus (BV). This virus is especially interesting for future gene therapy applications, as it is characterized by a flexible rod-like protein capsid of approx. 200 nm length, which can accommodate large additional heterologous DNA insertions exceeding 100kb.

In order to assess the concept of GUV-mediated viral delivery, purified BVs were loaded into DOBAQ-containing (60mol%), negatively charged (20mol% EggPG) droplet-splitted GUVs by adding them directly to the SUV solution used for dsGUV production. Successful loading was confirmed by fluorescence confocal microscopy (Figure 28a). In order to assess the correct incorporation of BVs into the GUV lumen and the ultrastructure of the BV virions inside the droplet-splitted GUVs, cryoTEM analysis was performed (Figure 29). Based on previously published structural analysis of BVs (Wang et al., 2016), three major distinct conformations could be observed: 1. Incorporation of one or more viral capsids into the GUV lumen without any apparent surrounding viral lipid envelops, 2. relaxed viral capsids with extruded viral DNA and 3. GUVs with apparently completely "dissolved" viral capsules but with a particle (possibly protein-based) corona on the GUV lipid membrane. Subsequently, respective GUVs were incubated with REF cells for 24 hours and afterwards analysed by fluorescence confocal microscopy for BV intracellular distribution and cellular transduction (Figure 28b). The BV-loaded GUVs were successfully taken up by the cells and BV particles (as imaged by Hoechst 33342 staining, see section 3.2.24) were found within the cytoplasm. Moreover, the BVs encoded a recombinant dsRed fluorescent protein fused to a mitochondrial targeting sequence in order to assess successful cellular transduction. A prominent mitochondrial fluorescence could be observed in almost every cell analysed, proofing successful and efficient

transduction. This demonstrates transduction of mammalian cells with BVs mediated by carrier-GUVs and highlights the possibility of transporting large and complex cargos into the intracellular space.

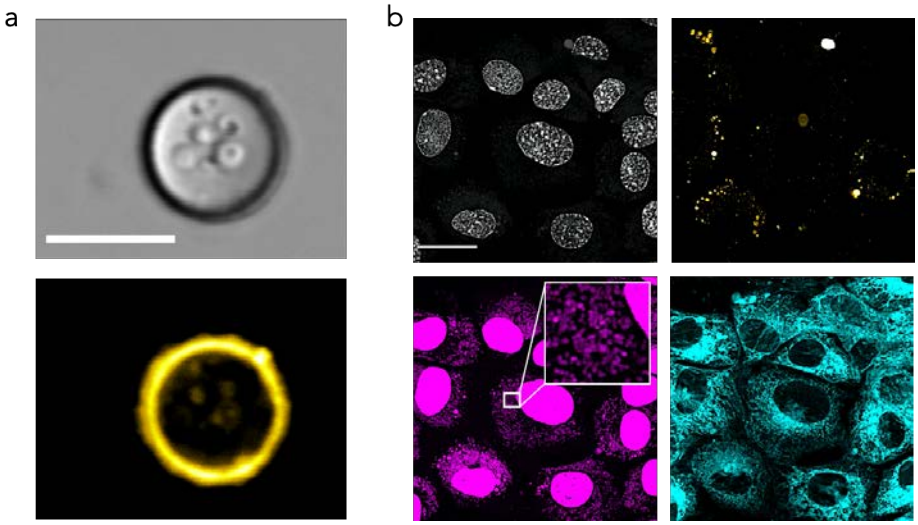

Figure 28 | GUV-based delivery of large viral particles. (**a**) Representative bright field (gray) and confocal microscopy (yellow) images of a BV-loaded droplet-splitted GUV. The scale bar is 10 µm. (**b**) Representative fluorescence confocal microscopy maximal z-projection images of REF cells incubated for 24 hours with BV-loaded, DOBAQ containing (60mol%), negatively charged (20mol% EggPG) GUVs produced by droplet-splitting. Nuclei (gray) were stained with Hoechst3334 (grey), GUVs were imaged by incorporation of 1mol% LissRhod PE (yellow) and BVs were imaged by oversaturation of the Hoechst33342 image (magenta). Note the expression of mitochondria-targeted dsRed (cyan). The scale bar is 25 µm.

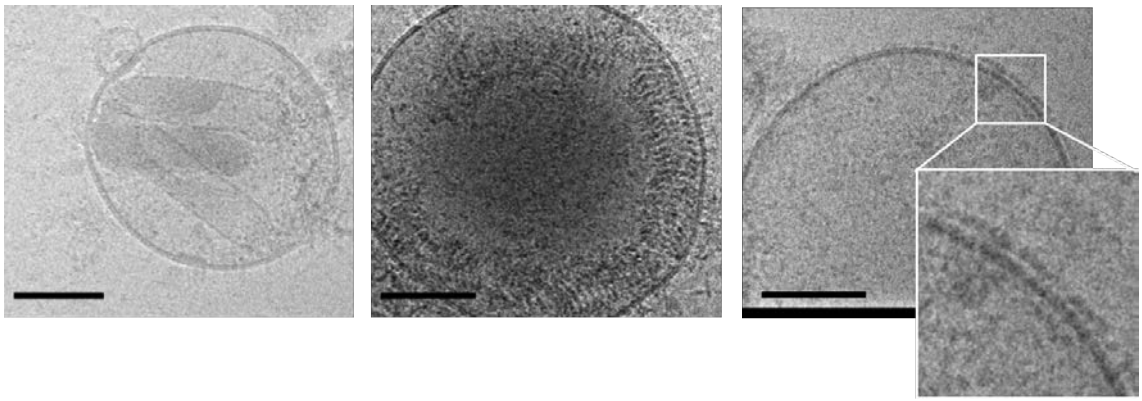

Figure 29 | Ultrastructural characterization of BV-loaded GUVs. CryoTEM micrographs of BV-loaded droplet-splitted GUVs. Three distinct BV-configurations were be observed: 1. One or more viral capsids without any apparent surrounding viral lipid envelops within the GUV lumen, 2. relaxed viral capsid with extruded viral DNA and 3. GUVs with apparently "dissolved" viral capsids featuring a particle corona on the GUV lipid membrane (from left to right). The scale bars are 100 nm.

4.3 Bottom-up assembly of GUV-based synthetic organelles

Based on the observations on intracellular GUV uptake and processing made in chapters 4.1 and 4.2, further studies on the application of the GUVs as synthetic organelles (SOs) were performed. As detailed in section 1.4.2, SOs have several important implications in biomedical and evolutionary biology research but current technologies for SOs production are either limited in their throughput, control or versatility. Therefore, GUV-based SOs could offer novel means to assemble SOs form the bottom up. Moreover, the results obtained in the previous sections highlight that GUVs are readily taken up by cells and remain intact in the intracellular space for several hours. Therefore, three separate concepts for SOs assembly based on GUVs were pursued:

4.3.1 Mimicking the natural functionality of peroxisomes

As a first approach, a peroxisome mimicking SOs was produced by incorporating purified catalase enzymes into the GUV lumen. Peroxisomes are one of the most important organelles for cellular redox homeostasis and regulated intracellular levels of reactive oxygen species. For instance, hydrogen peroxide can be degraded by means of catalase enzymes (Figure 30a). In order to mimic these organelles, GUVs composed of 20mol% EggPG, 79mol% EggPC and 1mol% LissRhod B containing micromolar amounts of purified bovine catalase were produced. These GUVs where then incubated with HaCaT keratinocytes for 24 hours and subsequently assessed by confocal fluorescence microscopy. In accordance with the results obtained for negatively charged GUVs in section 4.1.5, intracellular uptake of the SOs was observed (Figure 30b). Keratinocyte cells were selected as a model cell type for peroxisome-mimicking SOs, as several inflammatory skin diseases, carcinoma progression as well as deregulated wound healing are linked to dysregulation of cellular redox homeostasis (Kruk and Duchnik, 2014). To assess if these SOs are able to support cellular redox homeostasis under oxidative stress conditions, intracellular reactive oxygen (ROS) species levels were measured by CellRox Green (CRG) staining (see section 3.2.11) (Figure 30c). CRG is weakly fluorescent in its reduced form but emits a bright green fluorescence when oxidised by ROS. This allows

for quantification of intracellular ROS levels after loading of CRG into the cells. In order to induce oxidative stress, the cells were treated with 25 µM menadione, a potent ROS inducer (Loor et al., 2010), after loading of the SOs. This analysis revealed that cells containing peroxisome-like SOs show reduced CRG staining after exposure to menadione (Figure 30d). Quantitative analysis of this observation, showed that ROS levels of keratinocyte monolayers can be reduced to those of non-stress cells by incorporation of as little as 2.7 µM catalase into the GUV lumen (Figure 30e). This showcases the concept of GUVs as SOs and demonstrates the passive "implantation" of catalase-filled GUVs as functional peroxisome mimics inside living cells.

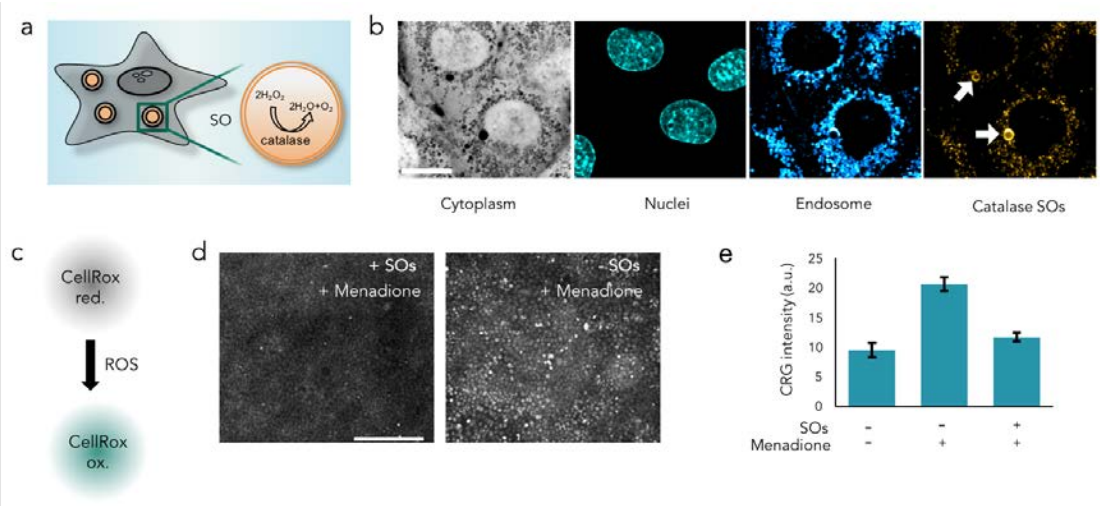

Figure 30 | Mimicking the natural functionality of peroxisomes. (**a**) Schematic illustration of catalase-loaded SO mimicking the peroxisome function. The SOs are produced from GUVs containing internalized bovine catalase, mediating the breakdown of hydrogen peroxide. (**b**) Representative fluorescence confocal microscopy images of HaCaT keratinocytes incubated for 24 hours with the peroxisome-mimicking SOs. Cytoplasm was stained by CellTracker Green (grey), nuclei were stained with Hoechst 33342 (cyan), endosomes were labelled with wheat germ agglutinin Alexa647-conjugate (blue) and SOs (yellow, white arrows) were imaged by incorporation of rhodamine B-conjugated. The scale bar is 15 µm. (**c**) Schematic illustration of CRG transformation induced by ROS-mediated oxidation of the weakly fluorescent molecule into a bright, green emitting fluorophore for ROS quantification. (**d**) Representative epifluorescence microscopy images of HaCaT monolayers treated for 1 hour with 25 µM menadione and subsequently stained with CRG. Cell monolayers either contained intracellular peroxisome-mimicking SOs (left image; +SOs) or no SOs (right image, -SOs). Those cells that did not contain SOs displayed an increased CRG staining, indicating elevated intracellular ROS levels. (**e**) Quantitative assessment of CRG staining of HaCaT monolayers treated either with 25 µM menadione for 1 hour or left untreated. Monolayers containing peroxisome-mimicking SOs harbouring 2.7 µM bovine catalase, showed comparable ROS levels to non-stressed monolayers. Results are shown as mean ± SD from three technical replicates.

4.3.2 Mimicking the natural functionality of the ER by synthetic mechanisms

The next approach aimed towards the assembly of SOs that mimic a function which is intrinsic to the cells but based on a synthetic operating mechanism. For this, SOs mimicking the Ca^{2+}-buffer capacity of the endoplasmic reticulum (ER) were assembled. The ER, and its close relative the sarcoplasmic reticulum, can act as a potent calcium storage organelles which are applied by many different cell types to regulate calcium signalling. Fibroblasts for instance, greatly relay on Ca^{2+} release from the ER to perform proper electrophysiological signalling and dysfunctional electrophysiology of fibroblasts has been closely associated with cardiac fibrosis and decreased wound-healing (Sebastian et al., 2011; Vasquez et al., 2011). To mimic the calcium binding properties of ER-proteins, synthetic calcium stores based on GUVs were assembled which contained the light-sensitive calcium chelator nitrophenyl EGTA (npEGTA). NpEGTA shows a nanomolar affinity to calcium ions but this affinity increased to approximately 3 mM after UV exposure and cleavage of the nitrophenyl group, eventually releasing the chelated Ca^{2+}. By this, UV light applied to npEGTA filled GUVs, can be used as externally trigger for calcium release from the GUVs (Figure 31a).

As a first assessment of this concept, the diffusion of UV-released Ca^{2+} from the inside of the GUVs to the outside of the GUVs was assessed. Towards this, npEGTA-Ca^{2+} loaded GUVs were encapsulated together with the fluorescent calcium indicator fluo-4 inside water in oil droplets (Figure 32), following previously published protocols (Göpfrich et al., 2019). The droplets were then irradiated with a 405 nm laser and the fluorescent signal of fluo-4 was monitored by fluorescence confocal microscopy. It was observed that after an initial increase of fluorescence inside the GUV lumen, corresponding to successful release of calcium from npEGTA and binding to fluo-4, also an increased fluorescence outside of the GUV was observed. This provides first evidence that Ca^{2+} successfully crossed the GUV membrane.

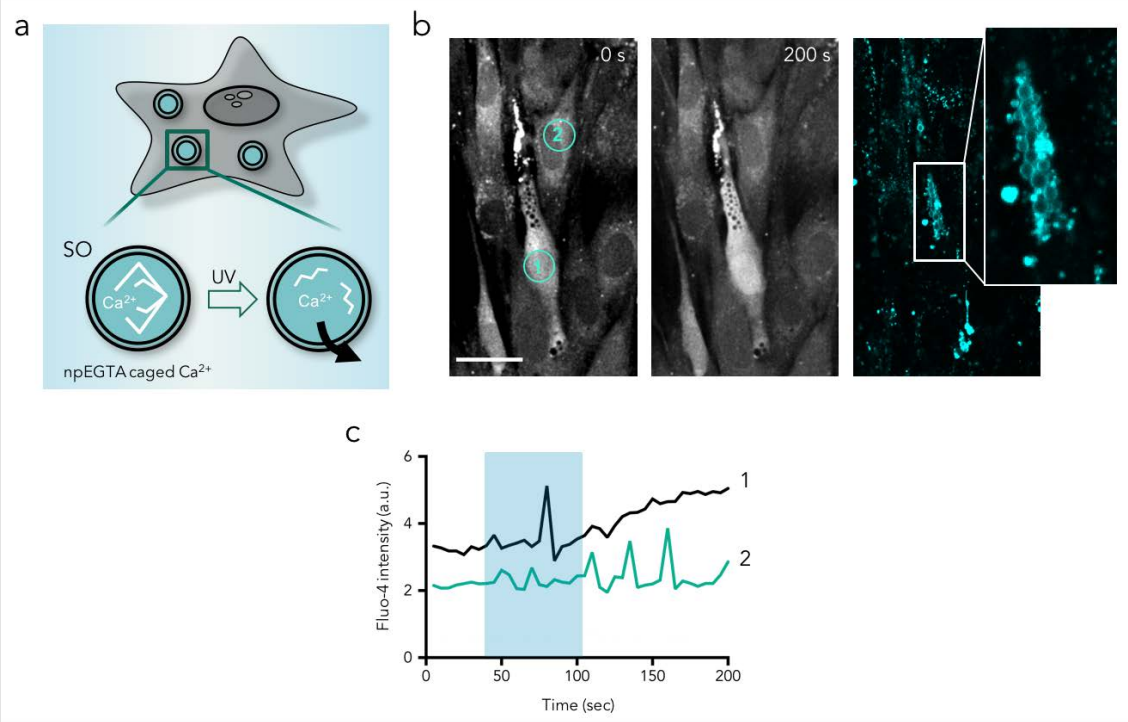

Figure 31 | Mimicking the natural, calcium-buffering functionality of the ER using a synthetic mechanism. (**a**) Schematic illustration of a cell containing ER-mimicking SOs with UV-sensitive npEGTA-chelated Ca^{2+} ions. After illumination with a 405 nm UV laser, Ca^{2+} is released from the synthetic SOs by cleavage of the npEGTA. (**b**) Time-lapse fluorescence confocal microscopy analysis of BJ fibroblast monolayers containing ER-mimicking SOs (cyan) and loaded with the calcium sensor fluo-4 (grey). Left image shows fluo-4 intensity before UV-illumination and right image after illumination. The scale bar is 30 µm. The illuminated region is displayed in the magnified inset. (**c**) Time course quantification of the fluo-4 intensity profile from cells marked in (b). The SOs in cell 1 were illuminated with 405 nm light (the turquoise background indicates the time-window of illumination), triggering successive Ca^{2+} increase in the cell cytoplasm and subsequently firing of calcium action potentials in cell 2.

In order to assess if this released is also functional within living cells, respective GUVs were incubated with fibroblast cells. After GUV uptake, the fibroblast electrophysiology was monitored by fluorescence confocal microscopy analysis of the fluo-4 intensity within the living cells. Interestingly, after illumination of the SOs with a 405 nm laser, a prominent but transient increase in the cytosolic fluo-4 fluorescence, as well as a sharp spike-like increase, reminiscent of a calcium action potential, was observed (Figure 31b). This was followed by a several spike-like increases of the fluo-4 intensity in adjunct cells (Figure 31c). Taken together, these results demonstrate the implementation of functional, synthetic calcium storing organelles into living cells and their employment to generate action-potential-like Ca^{2+} increases in target and "follower" cells by illumination.

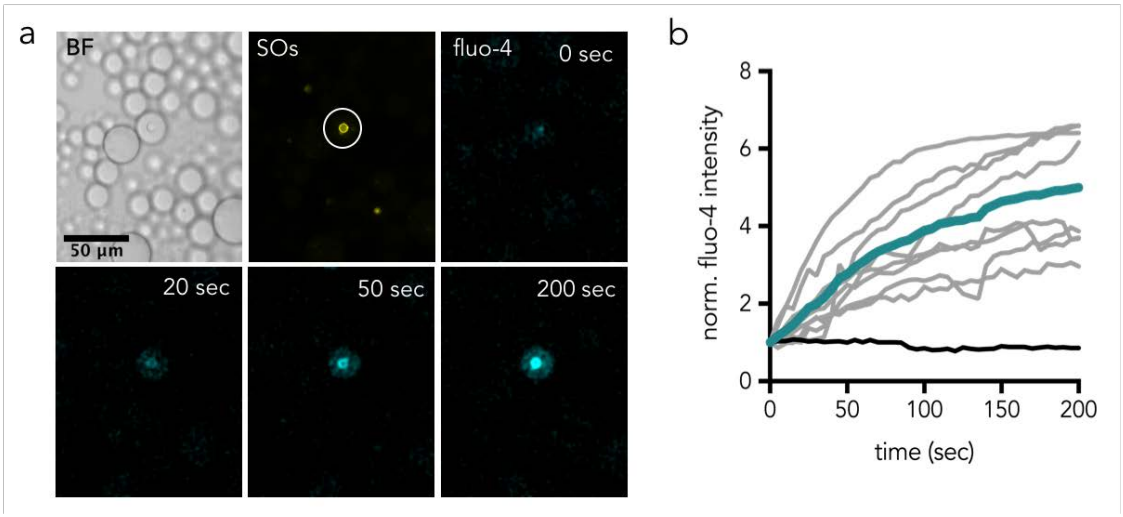

Figure 32 | Assessment of Ca^{2+} release from ER-mimicking SOs after UV-illumination. (**a**) Representative fluorescence confocal and bright field microscopy images of GUVs containing npEGTA-chelated Ca^{2+} encapsulated into water in oil droplets (upper left and middle image). The droplets further contained fluo-4 fluorescence calcium indicator (cyan images) for analysis of free Ca^{2+} levels. White circled area indicates the area of 405 nm illumination with a laser-scanning confocal microscope. Successive increase of fluo-4 intensity inside the GUV and inside the whole droplet is observed after illumination at time point 0 sec, indicating successful release of Ca^{2+} from the SO. (**b**) Quantification of fluo-4 intensity from 8 separate droplets containing ER-mimicking SOs. Time intensity profiles of individual droplets are shown in grey, green line shows the mean profile from the individual droplets. Black profile shows intensity of non-illuminated droplets.

4.3.3 Assembly of magnetosomes to equip cells with non-innate functionalities

Apart from mimicking pre-existing organelles and their functionalities in living cells, also completely new organelles can be "transplanted". For instance, mimics of organelles which originate from organism in a completely different part of the phylogenetic tree could be integrated into mammalian cells. This could significantly expand the functional repertoire of cellular "machineries" applied for industrial production of proteins and other metabolites or for novel theranostic interventions. An interesting organelle which can be found in several bacteria are magnetosomes. These membrane enclosed organelles contain magnetite or greigite magnetic particles which align as pearl-like strings inside the bacteria to provide them with a magnetotactic sense of the earth's magnetic field (Blondeau et al., 2018). Comparable organelles are not developed by mammalian cells but if synthetically incorporated, could provide new means to extrinsically direct cell migration or polarization by magnetic fields (Figure 33a). Therefore, the next approach aimed to produced SOs that contain magnetic particles by which, once taken up into the intracellular space, they can provide magnetotaxis to mammalian cells. For this, 50 nm

Fe_2O_3 nanoparticles were encapsulated into the GUVs to form magnetotactic SOs. When respective dsGUVs were analysed by bright field microscopy, an aggregation of the nanoparticles inside the dsGUV lumen was observed. Moreover, a sensitive deflection of these aggregates could be induced externally applied magnetic fields (Figure 33b).

After release of the respective dsGUVs, uptake by normal rat kidney cells was observed when incubated with these SOs for 24 hours. In order to verify that nanoparticles remain inside the GUV lumen after intracellular uptake, TEM analysis was performed. This revealed that not only did the GUVs stay intact after uptake but also that the nanoparticles still reside within their lumen (Figure 34a). Moreover, staining the cell actin cytoskeleton with phalloidin-FITC showed that the SOs are surrounded by a dense actin envelope which was linked to surrounding actin stress fibres, suggesting that any forces originating from inside the SOs by magnetic field deflection of the nanoparticles could be transmitted to the cellular cytoskeleton (Figure 34b).

As a next step, we “implanted” these SOs into fibroblast to analysis if they can sense, align or migrate within a magnetic field with the help of the nanoparticles inside the SOs. For this, respective cells were incubated next to an AlNiCo permanent magnet for 24 hours. Subsequently, bright field microscopy was performed to observe the conformation and intracellular distribution of the SOs. This revealed that the SOs aligned within the cytoplasm of the cells to form pearl-like strings (Figure 33c). Interestingly, this conformation was reminiscent of the bacterial magnetosome structures. This indicates that the iron nanoparticle containing SOs can be deflected by a magnetic field also within the intracellular environment. Whether this intracellular alignment can also impact on the migratory behaviour of the fibroblast, was analysed

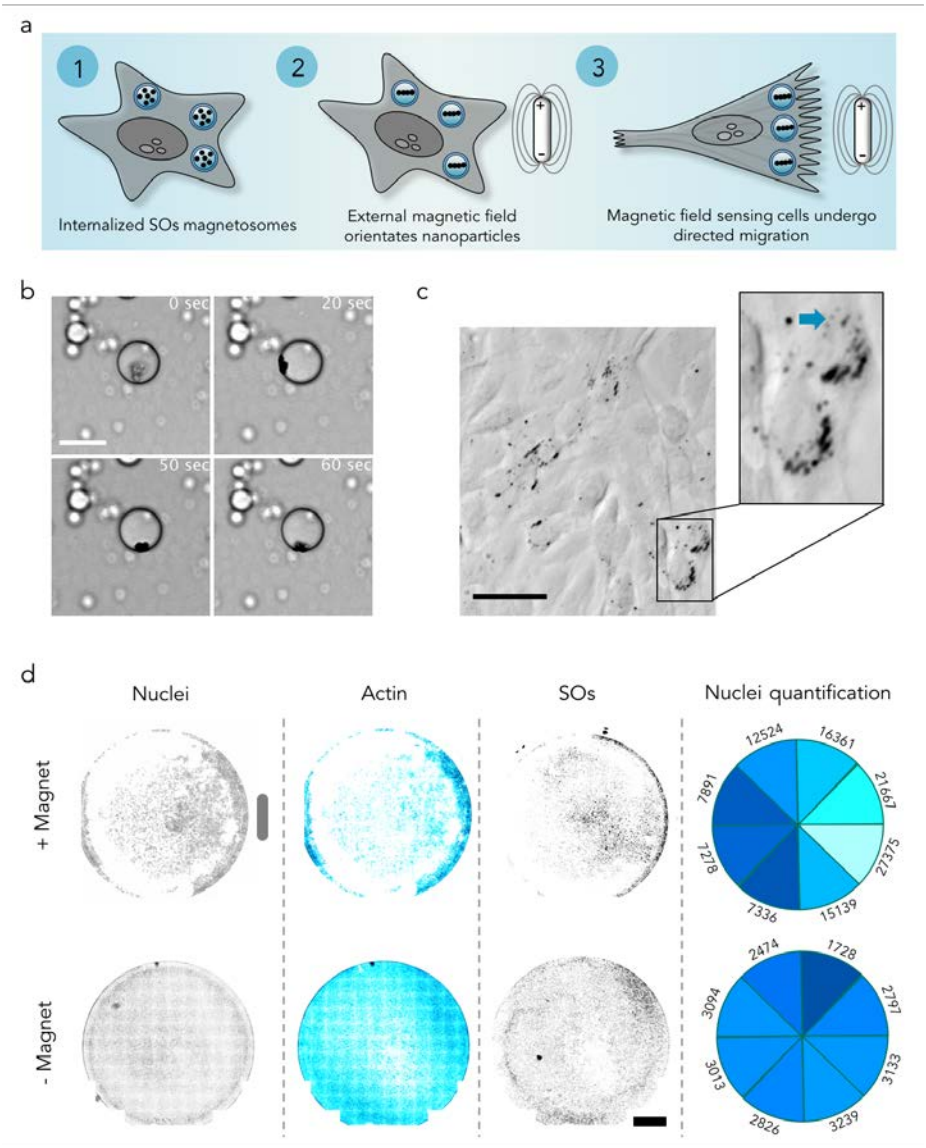

Figure 33 | Assembly of magnetosome-like SOs to equip cells with completely new, non-intrinsic functionalities. (**a**) Schematic illustration of synthetic magnetosome-induced polarization and migration of cells. (**b**) Bright field time-lapse series of dsGUVs containing Fe_2O_3 nanoparticles. To deflect the nanoparticles during the image acquisition, an AlNiCo magnet was placed next to the sample. The scale bar is 10 µm. (**c**) Representative bright field microscopy images of normal rat kidney fibroblasts containing magnetosome-mimicking SOs (black dots), incubated for 48 hours next to an AlNiCo magnet. Inset magnifies the string-like alignment of SOs (blue arrow) within the cells. The scale bar is 50 µm. (**d**) Epifluorescence microscopy images of normal rat kidney fibroblasts containing magnetosome-like SOs, cultured in 15.6 mm diameter wells next to (top row) or without (bottom row) an AlNiCo magnet for 72 hours. Phalloidin-FITC and Hoechst33342 was applied to stained actin and nuclei, respectively, and SOs were imaged by rhodamine B conjugated membrane lipids. Grey bar indicates AlNiCo magnet position. Right panels show colour-coded cell densities by automated counting of the nuclei in the respective regions. The scale bar is 3 mm.

by incubating them in a well-plate located next to an AlNiCo magnet form 72 hours and subsequently staining the cells with phalloidin-FITC and Hoechst33342. Afterwards, the complete wells were imaged to visualize the cell distribution within them. It was found that the cells were not evenly distributed within the wells but rather accumulated at the side where the magnet was placed (Figure 33d). Cells cultured for the same time period without a magnet next to them showed no comparable distribution. Automated counting of the cells by their nuclear staining showed that the cell density at the magnet side was approximately three times higher compared to the opposite side. This demonstrates how "implanting" magnetosome-like SOs into fibroblasts can provide them with a synthetic magnetotaxis and how this allows them to align and migrate within a magnetic field.

Fibroblast can be considered as intrinsically mobile cells (Petrie and Yamada, 2015), wherefore inducing a directed migratory behaviour in this cells does not allow to conclude a strong magnetotactic effect. In order to analyse if the SOs-mediated magnetotaxis can also be acquired by less mobile cells, primary neuronal cell migration after magnetosome-like SOs loading was studied. Inducing and directing the migration of these cells could have direct implications for the treatment of spinal cord injuries e.g. cross section paralysis or other neuronal palsy and damages (Shibuya et al., 2009). For this analysis, magnetosome SOs we incubated with primary rat hippocampal neurons and

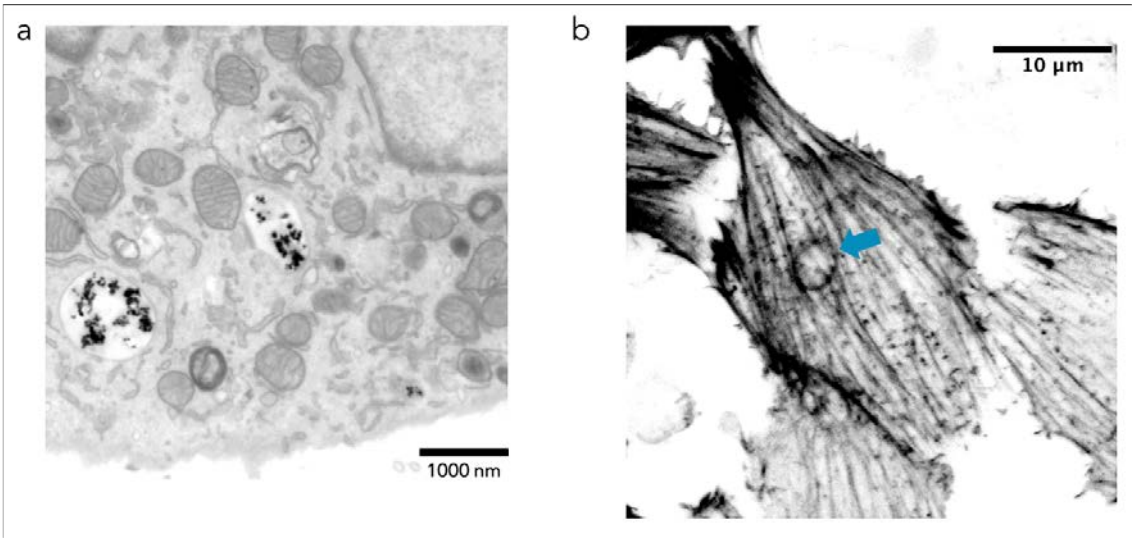

Figure 34 | Analysis of intracellular conformation of magnetosome mimicking SOs. (**a**) Representative transmission electron microscopy micrographs of magnetosome mimicking-SOs inside living normal rat kidney fibroblasts. Note that the iron nanoparticles are only found within the GUV lumen. (**b**) Representative fluorescence confocal microscopy images of phalloidin-FITC stained normal rat kidney fibroblasts incubated for 24 hours with magnetosome-mimicking SOs. Blue arrow indicates SO

subsequently cultured for 96 hours next to an AlNiCo paramagnet. Cell densities were subsequently analysed by Hoechst3342 and phalloidin-FITC staining. Again, it was found that the cell density next to the magnet was approximately 2x higher compared to the cell density on the opposite side of the well (Figure 35a). Moreover, higher magnification analysis revealed that the cells residing next to the magnet also showed an increased connectivity and actin enrichment (Figure 35b). This could potentially be deduced to the increased mechanical forces which have previously been described to stimulate neurite and axonal elongation (Raffa et al., 2018; Zheng et al., 1991).

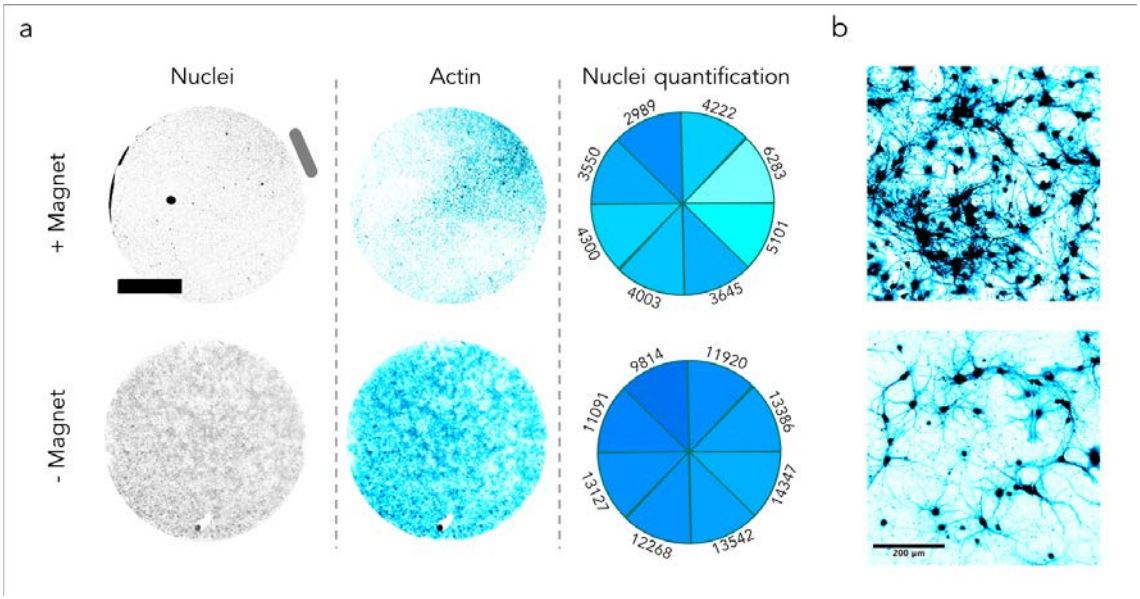

Figure 35 | Magnetosome-like SOs provide magnetotaxis to primary neurons. (**a**) Epifluorescence microscopy images of primary rat hippocampal neurons containing magnetosomes-mimicking SOs, cultured for 96 hours on 18 mm diameter glass cover slips either next to an AlNiCo magnet (top row) or without a magnet (bottom row). Nuclei and actin were stained with Hoechst33342 and phalloidin-FITC, respectively. AlNiCo magnet position is indicated by the grey bar. Right panels show colour-coded cell densities obtained by automated nuclei counting in the respective regions. The scale bar is 5 mm. (**b**) Representative fluorescence microscopy images of phalloidin-FITC stained primary hippocampal neuron incubated with (top image) or without (bottom image) SOs for analysis of neurite and axonal connectivity.

4.4 Bottom-up assembly of fully-synthetic extracellular vesicles

EVs, such as exosomes, microvesicles or apoptotic bodies present membrane-anchored proteins on their surface and shuttle genetic information (e.g. nuclear and mitochondrial DNA) and epigenetic regulatory elements (e.g. miRNAs) to distant cells. Thereby, they deeply impact on nearly every facet of cell-physiological processes including migration (Steenbeek et al., 2018), proliferation(Aiello et al., 2017) and differentiation (Cruz et al., 2018). Attaining a more fundamental understanding of EV-mediated intercellular

communication is a compelling goal not only for biosciences but also for the development of EV-based theranostics (El Andaloussi et al., 2013; van Niel et al., 2018). However, the error prone and time-consuming procedures required for EV isolation, purification and characterization from natural biofluids as well as their intricate molecular complexity and intrinsic biological variability have hindered an in-detailed understanding of the associated signalling events.

Based on the GUV-cell interactions studies described in the chapters 4.1 and 4.2, the hypothesis arose that by using in-droplet assembly of dsGUVs, fully-synthetic EVs (fsEVs) could be assembled from molecular buildings blocks with comparable functionality to their natural doppelgangers (Figure 36). This technology, which offers exquisite control over the vesicle preparation parameters and therefor over their composition, biochemistry and biophysical characteristics, could provide a minimalistic model system to study fundamental biophysical phenomena underlying EV-signalling. Moreover, as the resulting GUVs in many parts resemble the natural EV lipid carriers, they could trigger EV-equivalent therapeutic responses without being subjected to natural fluctuations like cell-derived EVs. This chapter introduces a high throughput assembly technique for fsEVs based on charge-mediated formation of dsGUVs, their molecular and structural characterization, an *in vitro* assessment of their functionality as well as a RNA-sequencing transcriptome approach to study their signalling mechanisms.

Figure 36 | Bottom-up assembly of fully-synthetic EVs. Schematic illustration of the isolation and purification process applied for EVs from natural resources (left) and for the assembly of fsEVs from defined molecular building blocks (right).

4.4.1 High-throughput assembly and structural characterization of fsEVs

For *in vivo* administration and analysis of fsEVs as well as for fsEV-based therapeutic interventions large amounts of fsEVs are needed. Therefore, a bulk method, based on shear stress mechanical emulsification of water-in-oil mixtures was designed (Figure 37a). Here, a perfluorinated oil phase containing a stabilizing surfactant as well as a negatively charged surfactant is mixed with an aqueous phase containing negatively charged SUVs

of desired (functionalized-) lipid composition, $MgCl_2$ and nucleic acids (e.g. miRNAs) to form water-in-oil droplets. As the emulsification process is mediated by a rapidly rotating shaft, it can be performed in very large volumes (~1 litre) and therefore produce within seconds enough dsGUVs and eventually fsEVs to perform in vivo analysis (Figure 37b). As for this process the same principals of charge-mediated dsGUV formation are applied, it can be viewed as an up-scaling production process for the droplet-splitting assembly of EV-sized GUVs. Moreover, using this technique the final droplet size is not determined by the microfluidic channel width or fluid flow pressure but by the rotation speed of the shaft where higher rotation speed results in higher shear-stress and therefore smaller droplets. Therefore, the final fsEV size can be easily adjusted from batch to batch without the need for a new device design and far smaller fsEVs can be produced (Figure 37c). For instance, emulsification at 30,000 rpm for 30 sec produced fsEVs with a mean radius of 292 nm (± 12 nm, n= 3 technical replicates) as measured by DLS. Emulsification at 14,000 rpm for 30 sec, however, resulted in fsEVs with a mean diameter of 627 nm (± 15 nm, n= 3 technical replicates). After release, recombinant EV surface proteins can be coupled to the outer fsEV leaflet *via* functionalized lipids following the protocols developed in section 4.2.1.

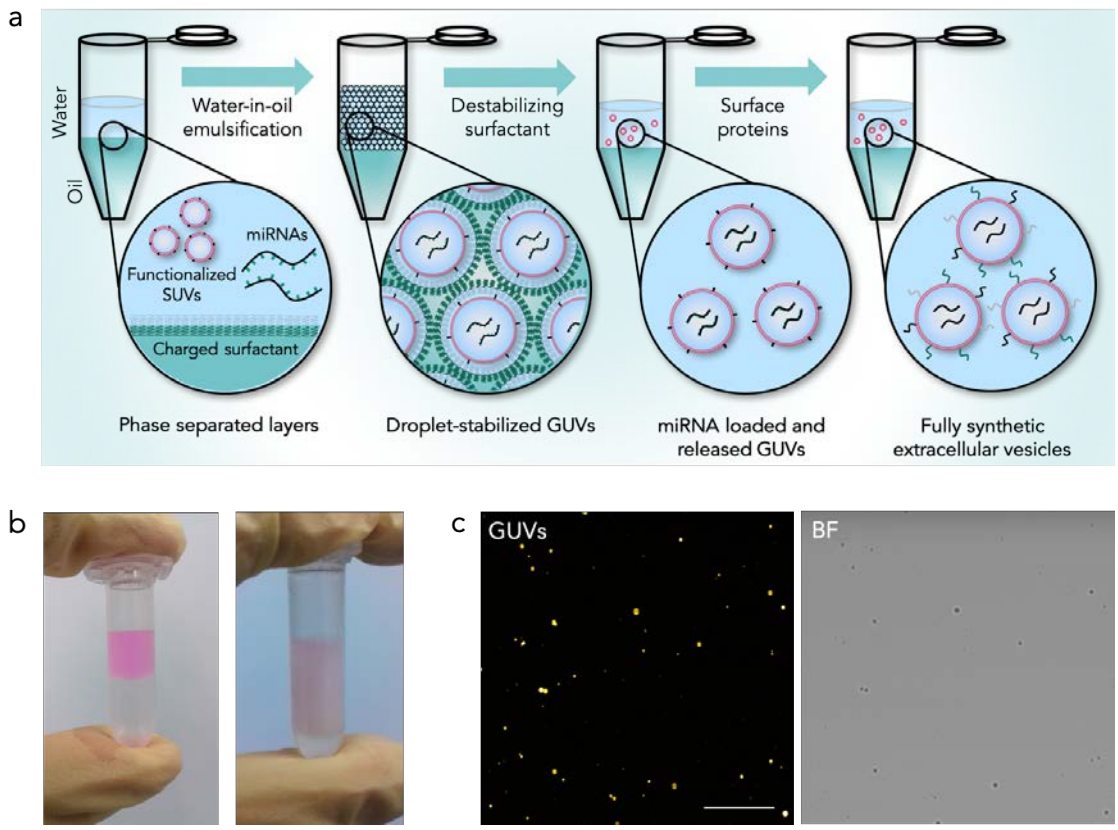

Figure 37 | Larger-scale production of fsEVs by mechanical emulsification. (**a**) Schematic illustration of the fsEVs charge-mediated production process inside w/o droplet-compartments formed by mechanical emulsification. MicroRNA containing fsEVs are formed on the droplet-periphery from SUV precursors containing functionalized lipids for subsequent decoration with recombinant EV-surface proteins. (**b**) Photographs of the phase-separated SUV/miRNA containing aqueous (top, pink) and surfactant-containing oil (bottom, transparent) layers before mechanical emulsification. Right image shows a photograph of the w/o droplet-emulsion after mechanical mixing for 30 sec at 30,000 rpm. (**c**) Representative fluorescence (left) confocal and bright field (right) microscopy images of dsGUVs produced by mechanical emulsification for 30 sec at 30,000 rpm from SUV precursors (20mol% EggPG, 79mol% EggPC and 1mol% LissRhod PE). The scale bar is 20 µm.

In order to investigate the purity and homogeneity of the produced fsEVs, transmission electron microscopy was performed on negative stained samples. Here, the fsEVs (composed of 70mol% DOPC, 5mol% DOPE, 20mol% DOPG, 5mol% DOPS lipids) were compared to EVs isolated by differential ultracentrifugation from conditioned cell culture medium of the erythroleukemia cell lines K562. Further, exosome preparation from the same cell lines obtained from a commercial distributor were analysed in parallel (Figure 38). Considerably fewer contaminating aggregates and non-vesicular particles were present in the fsEVs preparations.

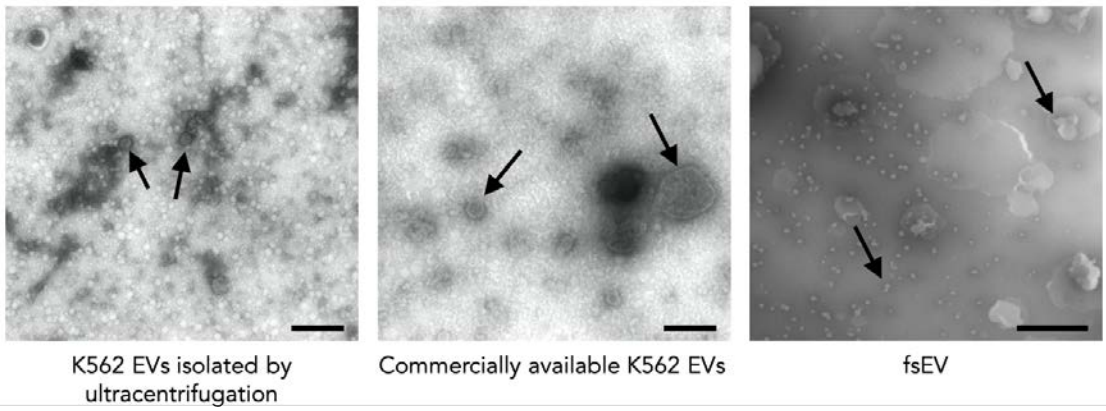

Figure 38 | TEM analysis of natural and fsEVs. Representative TEM micrographs of EVs (marked by black arrows) isolated by differential ultracentrifugation from K562 cell culture media conditioned for 48 hours (left). EVs isolated from conditioned K562 media by a commercial distributer (centre image). fsEVs (70mol% DOPC, 5mol% DOPE, 20mol% DOPG, 5mol% DOPS) produced by charge-mediated formation inside w/o droplets *via* mechanical emulsification (right image). Negative staining with uranyl acetate was applied to the vesicle preparations. The scale bars are (from left to right): 100 nm, 100 nm, and 1 µm.

Furthermore, the protein content and purity of the vesicles were analysed by denaturating SDS polyacrylamide gel electrophoresis (PAGE) (Figure 39). Both, K562 exosomes from the commercial distributer as well as EVs isolated from conditioned K562 media, differed greatly with regard to their protein composition, underscoring the degree of variations between different EV sample preparation methods. Moreover, when comparing two separately prepared exosome batches, substantial variation in the PAGE-protein profiles could be observed. In contrast to this, when analysing fsEVs decorated with recombinant His-tagged CD9-ED2 and His-tagged TSG101 (aa 1-145) (coupled *via* NTA(Ni^{2+}) lipids) by denaturating SDS PAGE, a clearly defined and characteristic band pattern could be observed. Moreover, when comparing to separately produced fsEV batches, the band patterns appeared to be nearly identical. This indicates, that fsEVs can not only be prepared more reproducibly but also that fsEV provide a more defined system compared to EVs isolated from natural sources.

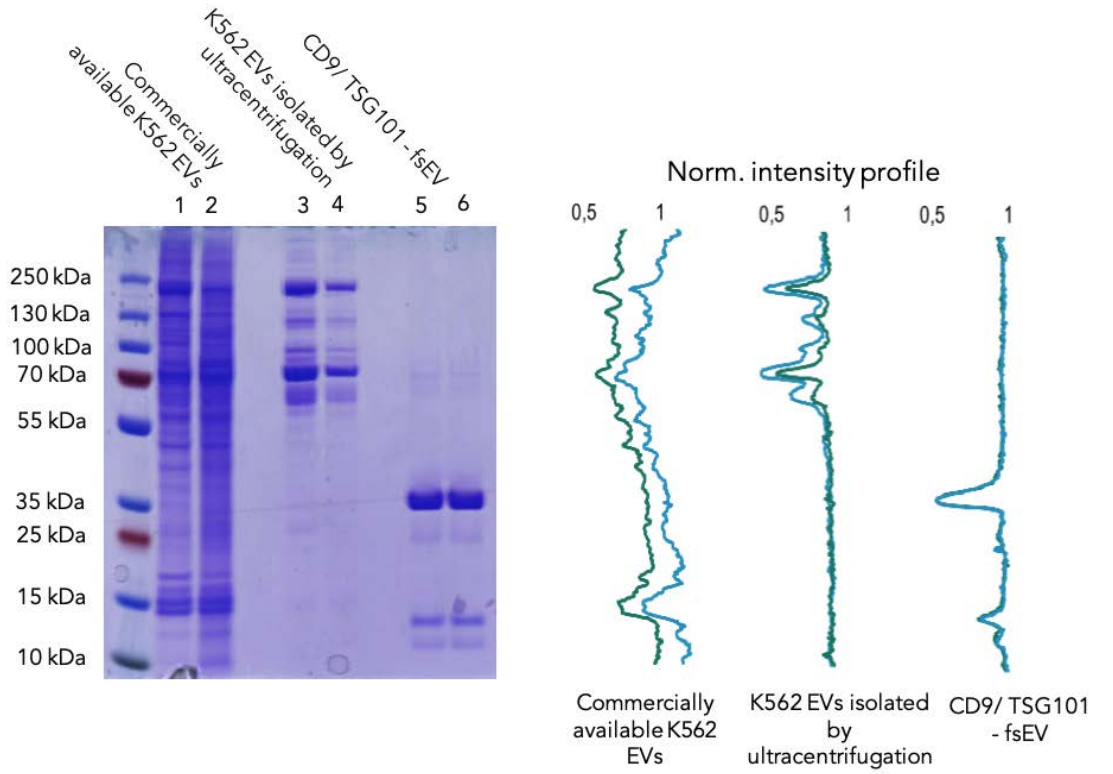

Figure 39 | Characterization of EV and fsEV protein content by denaturation SDS PAGE. Two separate production batches of K562 EVs isolated by a commercial distributer were loaded on lane 1 and 2. EVs from two separate isolations of K562 cells by differential ultracentrifugation were loaded on lane 3 and 4. fsEVs decorated with recombinant ED2-CD9 (Ser112-Ile195) and TSG101 (Gly1-Pro145), produced in two separate assemblies by mechanical emulsification, were loaded in lanes 5 and 6. 3 µg and 500 ng total protein content was loaded on each lane for natural and full-synthetic EVs, respectively. Normalized line profile intensities of the individual lanes are displayed on the right.

4.4.2 Characterization fsEV lipid composition

Lipids act as the major scaffolding elements of EVs and greatly contribute to their signalling capabilities. In order to assess whether the quantitative definition of fsEVs also holds true for their lipid composition, quantitative electrospray ionization tandem mass spectrometry was performed. The lipid composition of the fsEVs was designed to closely resemble the composition of natural EVs, wherefore a formulation based on a 43 : 16 : 15 : 11 : 6 : 5 : 2 : 1 : 1 ratio of cholesterol : SM : DOPC : DOPS : DOPE : DOPG : PA : DAG : DOPI lipids was used for their production. Although it is technically possible to assemble fsEV-membranes from an almost unrestricted selection of lipid types, these 9 lipids were selected as they represent some of the most abundant types found in EVs (e.g. cholesterol and SM) or possess important signalling functionality (DOPS and DAG). The quantitative mass spectrometry analysis of fsEVs and their SUV precursors revealed that

the fsEV composition is almost identical to the formulation of the applied SUVs (Figure 40). This proofs that the lipid ratio remains unchanged during the emulsification and release procedures and underscores the quantitative definition of the fsEVs. It also demonstrates, that fsEVs can be constructed from a desired lipid ratio that closely resembles the membrane composition of natural EVs.

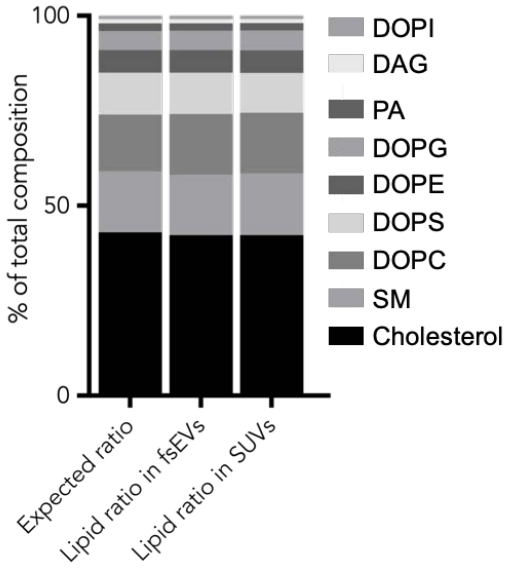

Figure 40 | Quantification of SUV and resulting fsEV lipid composition by ionization tandem mass spectrometry. SUVs were prepared from a lipid mixture containing an expected ratio of 43 : 16 : 15 : 11 : 6 : 5 : 2 : 1 : 1 of cholesterol : SM : (18:1)DOPC : (18:1)DOPS : (18:1)DOPE : (18:1)DOPG : PA : DAG : (18:1)DOPI lipids and fsEVs were prepared by mechanical emulsification within w/o-droplets from respective SUVs. The lipid composition of the SUVs and the resulting fsEVs samples were quantified by ionization tandem mass spectrometry. Results, as well as the expected lipid ratio of the designed formulation, are shown for the individual as percentage of the whole composition.

Moreover, DLS measurements showed that the ζ-potential of fsEVs with this lipid formulation was -12,3 mV (±0,7 mV, n= 3 technical replicates). These values are comparable to the ζ-potentials of natural EVs reported in literature (Vogel et al., 2017) and to those measured for commercially available K562 EVs (-11,8 mV ±0,9 mV, n= 3 technical replicates) and EVs isolated from conditioned K562 cell culture medium by ultracentrifugation (-11,3 mV ±0,5 mV, n= 3 technical replicates). Therefore, size (468 nm ± 199 nm and 240 nm ± 32 nm for commercially available K562 EVs and K562 EVs isolated by differential ultracentrifugation, respectively), ζ-potential and lipid composition precisely match the biophysical characteristics of natural EVs with even slightly higher homogeneity and reproducibility compared to their natural blueprints.

4.4.3 Characterization of fsEV protein-decoration and RNA-loading

Although lipids are considered crucial components of EVs, most of the specific EV-signalling functions are commonly associated with their lipid and nucleic acid cargo. Many therapeutic applications use or target EV miRNA cargo or peripheral membrane proteins and receptors (-ligands) on the EV surface. To demonstrate that fsEVs can also be assembled with these functional constituents, miRNAs and proteins were introduced into the dsGUVs and eventually into fsEVs. As a natural blueprint for the miRNA and protein composition of these fsEVs, the components found to be essential in wound-healing promoting exosomes derived from fibrocytes (see section 1.3.1), were used (Geiger et al., 2015a). To this end, fsEVs containing synthetic double-stranded RNA oligonucleotides miRNA mimics (miRIDIAN) of the natural exosomal miRNAs hsa-miR-21, hsa-miR-124, hsa-miR-125, hsa-miR-126, hsa-miR-130 and hsa-miR-132 were applied. A total miRNA concentration of approximately 750 pg/10^{12} vesicles is found in natural EVs(Li et al., 2014), wherefore a corresponding concentration 50 nM of each RNA mimic was added to the initial aqueous SUV solution used for dsGUV formation. Moreover, fsEVs membranes were decorated with recombinant histidine-tagged second extracellular domains of human tetraspanins CD9, CD63 and CD81 by applying Ni^{2+}-NTA coupling as described in section 4.2.1. A protein to lipid ratio of 1:200 was used as this closely resembles the ratio found in natural EVs (Osteikoetxea et al., 2015).

Correct assembly of final fsEVs samples (lipid membrane decorated with proteins and miRNAs in the lumen) was assessed by fluorescence confocal microscopy (Figure 41). For this, AlexaFluor488 labelled CD9 was used to assess immobilization of the tetraspanin proteins on the fsEVs, LissRhod PE conjugated lipids were additionally introduced into the lipid formulation to visualize the fsEV membrane and miRNAs were stained with Hoechst33342. The fsEVs showed a circular shape of the lipid membrane enclosing a bright Hoechst33342 fluorescence signal which indicates successful incorporation of the miRNAs. Moreover, the AlexaFluor488 CD9 signal was exclusively found on the fsEV membrane, suggesting correct membrane coupling and anchoring of the tetraspanin ED2-domain. Importantly, employment of bio-orthogonal surface chemistry (e.g. Ni^{2+}-NTA-polyhistidine tag coupling) allows for precise control of the membrane-anchored-protein to lipid ratio. In contrast to EVs engineered and produced inside living cells, this adjustment and quantitative fine-tuning capability, is a considerable improvement.

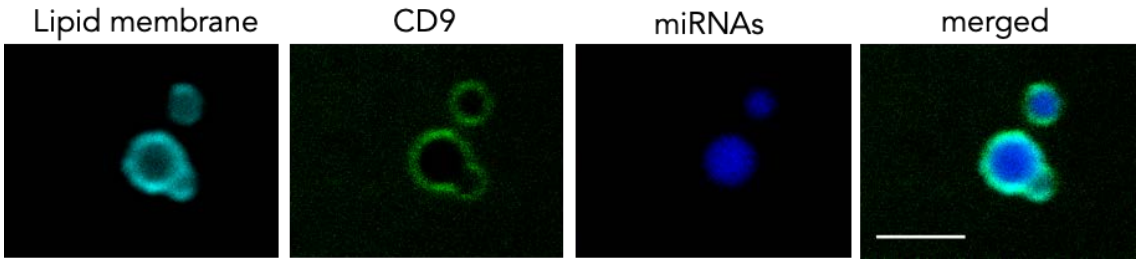

Figure 41 | Analysis of correct fsEV assembly. Representative fluorescence confocal microscopy images of fsEVs produced by mechanical emulsification. fsEV membranes were labelled by incorporation of LissRhod B PE-labelled fluorescent lipids. Membrane immobilization of recombinant tetraspanins ED2 was assessed by imaging of Alexa488-labeled CD9 and the incorporation of 300 nM miRNA mimics (hsa-miR-21, hsa-miR-124, hsa-miR-125, hsa-miR-126, hsa-miR-130 and hsa-miR-132) into the fsEV lumen was analyzed by Hoechst33342 staining. The scale bar is 2 µm.

Further, the uptake of these fsEVs by dermal cells was analysed by incubating them for 24 hours with spontaneously immortalized human keratinocytes (HaCaT cells). The HaCaT model cell-line was chosen as it features many key characteristics (cell-cell junction, collective migration etc.) of the keratinocytes responsible for wound-healing *in vivo* (Boukamp et al., 1988). When observed by fluorescence confocal microscopy, the fsEVs were found to be internalized into the cells and to co-localize with endosomal compartments, as analysed by co-staining with WGA-AlexaFluor488 conjugates (Figure 42a). This is in line with the results described in section 4.2.2, where negatively charged GUVs undergo comparable cellular uptake. Similar results were obtained when fsEVs were incubated with primary human dermal fibroblasts, which are also considered a crucial cell type involved in wound healing (Figure 42b). Here, fsEVs were also found to be bound to the cell membrane and within the perinuclear region, suggesting cellular uptake and subsequent processing by the intracellular trafficking machinery. Moreover, this interaction was comparable to that of natural EVs isolated from conditioned K562 cell culture medium, indicating that fsEVs are recognized and processed by cells in a similar way to natural EVs.

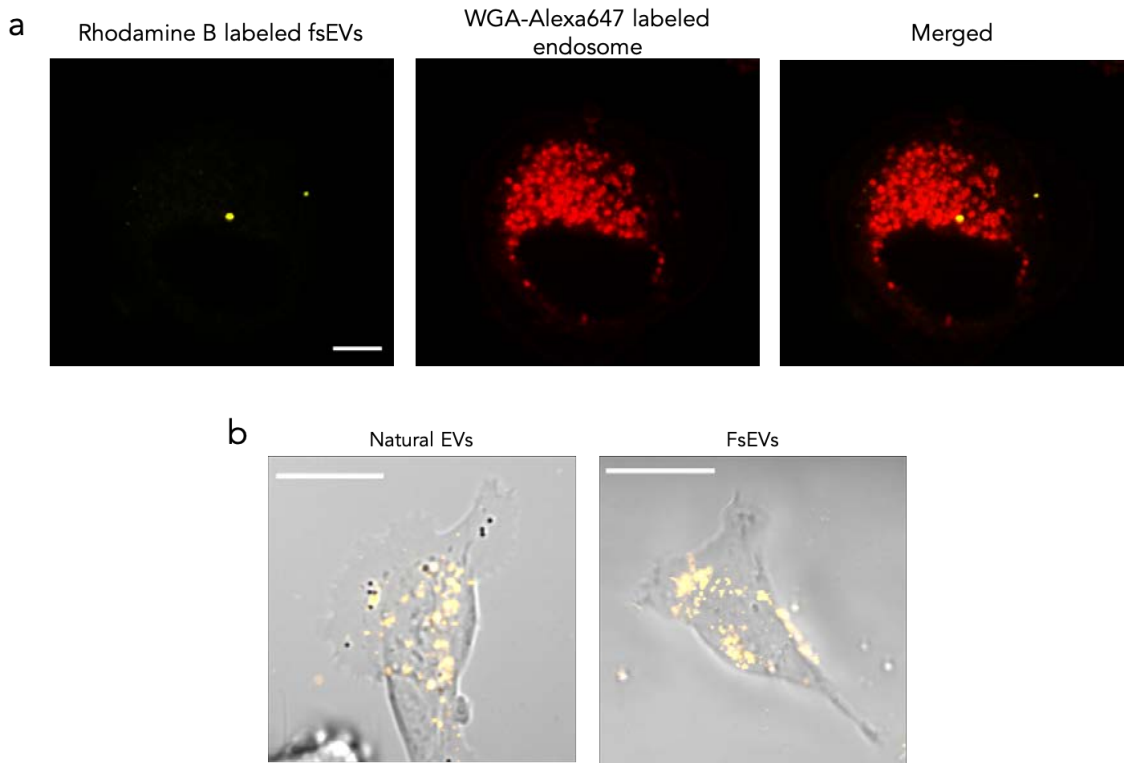

Figure 42 | Analysis of fsEV uptake by human dermal cells. (**a**) Single plan fluorescence confocal microscopy images of fsEVs incubated with WGA-Alexa647-stained immortalized HaCaT keratinocytes for 24 hours. fsEVs co-localized with WGA-stained endosomal compartments. The scale bar is 5 µm. (**b**) Representative merged bright field and fluorescence confocal microscopy images of primary dermal fibroblasts incubated for 24 hours with DiI labelled (yellow) natural EVs isolated from K562 media by differential ultracentrifugation (left) or incubated for 24 hours with fluorescent fsEVs (yellow) coated with recombinant histidine-tagged ED2 of CD9, CD63 and CD81 (at a 1:200 protein to lipid ratio) (right). Scale bars are 20 µm.

4.4.4 Functional assessment of wound-healing fsEVs

In their study on wound-healing promoting fibrocyte-derived exosomes (Geiger et al., 2015a) (see section 1.3.1), Geiger *et al.* report on their observations that these EVs induce phenotypic changes in keratinocytes and fibroblasts *in vitro*. Some of the prominent effects observed by Geiger *et al.* include: 1. higher proliferation rates as well as 2. acceleration of the collective migratory behaviour of dermal keratinocytes and 3. enhanced collagen deposition by dermal fibroblasts. Therefore, fsEVs were tested for their potential to induced comparable phenotypic effects.

4.4.4.1 Pro-proliferative effect of fsEVs on keratinocytes

The first assessment aimed to analyse a possible pro-proliferative effect of fsEVs on dermal keratinocytes. Towards this direction, spontaneously immortalized human keratinocytes cell lines (HaCaT cells) were incubated with fsEVs for 48 hours and the number of cells was subsequently assessed by a previously established Hoechst33342 staining assay (see section 3.2.9) (Figure 43a). In order to decipher the functional contribution of the individual protein components, fsEVs were decorated either with a single recombinant human CD9, CD63 and CD81 tetraspanin-ED2 (at a 1:200 protein to lipid ratio) or combinations of them but lacking miRNAs. The analysis not only revealed that fsEVs exhibit a pro-proliferative effect but also that co-presentation of tetraspanins leads to a synergistic response on proliferation. This effect was most pronounced for fsEVs which present all three tetraspanins, leading to an approximately 2-fold Hoechst33342 intensity increase when compared to cultures treated with naïve vesicles (lipid vesicles without proteins) only. This proofs that presenting the ED2 of human CD9, CD63 and CD81 on fsEVs membranes is already sufficient to achieve a pro-proliferative effect on keratinocytes.

As a next step, the contribution of single miRNAs to the pro-proliferative effect was evaluated. For this purpose, fsEVs biofunctionalized with the ED2 of human CD9, CD63 and CD81 (at a 1:200 protein to lipid ratio) and loaded with miRIDIAN mimics of either hsa-miR-21, hsa-miR-124, hsa-miR-125, hsa-miR-126, hsa-miR-130 and hsa-miR-132 or a combination of all six (50 nM of each mimic was added to the SUV mixture used for dsGUV assembly) were produced. Interestingly, the respective analysis of cell numbers revealed that every single miRNA enhanced proliferative to a different extent (Figure 43b). For instance, fsEVs loaded with hsa-miR-125 or hsa-miR-126 mimics displayed the most pronounced effect (approximately 1.7-fold Hoechst33342 intensity increase). However, compared to unloaded CD9, CD63 and CD81-biofunctionalized fsEV, the highest pro-proliferative effect (2.5-fold Hoechst33342 intensity increase), was observed when fsEVs were loaded with all six miRNAs at once. These results show, that fsEVs are appropriate carriers to convey miRNA-based epigenetic information and thereby reconstituting a central function of EV-based signalling.

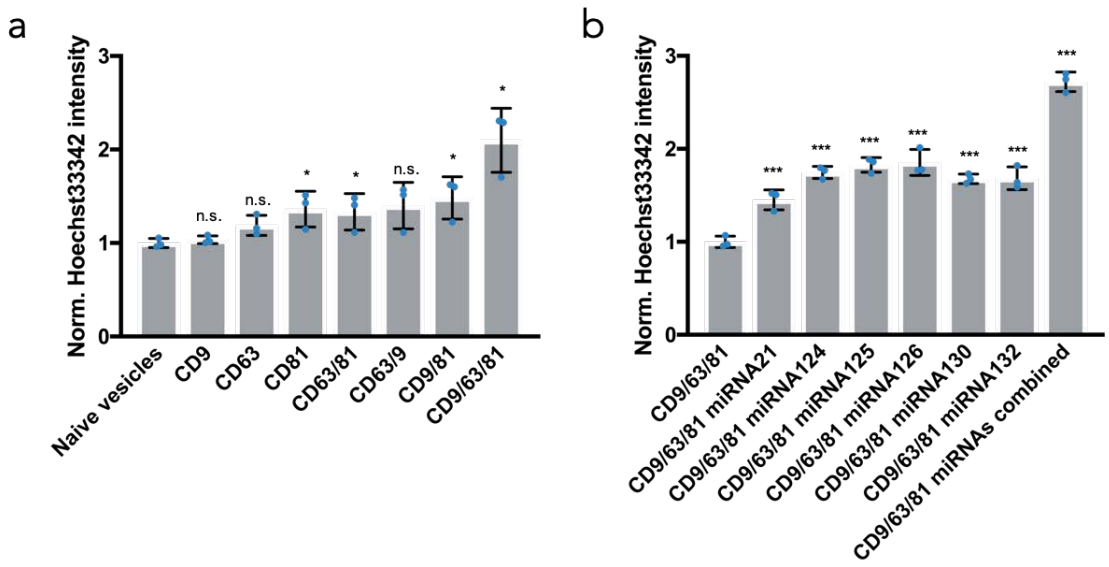

Figure 43 | Pro-proliferative effect of wound-healing fsEVs. (**a**) Fluorescence intensity quantification of Hoechst33342-stained human HaCaT keratinocyte cultures after treatment for 48 hours with fsEVs decorated with different recombinant tetraspanin ED2 domain variants (at a 1:200 protein to lipid ratio). (**b**) Fluorescence intensity quantification of Hoechst33342-stained human HaCaT keratinocyte cultures after treatment for 48 hours with fsEVs decorated with recombinant tetraspanin ED2 domains of human CD9, CD63 and CD81 (at a 1:200 protein to lipid ratio) and loaded with different miRNA mimics (50 nM each). Results are shown as mean ± SD; n=3 biological replicates. Statistical analysis was performed for significant difference compared to the control conditions "naïve vesicles" and "CD9/63/81" in a and b, respectively. T-test with *=p<0.01, **=p<0.001, ***=p<0.0001, n.s. not significant.

4.4.4.2 Enhancement of keratinocytes collective cell migration by fsEV treatment

In order to assess the effect of fsEVs on collective epithelial cell migration, *in vitro* cell exclusion wound healing assays were performed with artificially wounded keratinocyte monolayers. Cultures were treated with fsEVs decorated either with recombinant human CD9, CD63 or CD81 (at a 1:200 protein to lipid ratio) or a combination of them for 24h (Figure 44a). 16 hours after removal of the exclusion inserts, cell free area between the two advancing fronts was quantified (Figure 44b). This analysis not only revealed that protein-decorated fsEVs can promote keratinocyte collective migration into the cell free area but also that this effect was more pronounced when fsEVs presented all three tetraspanin ED2 at once. This is in good agreement with the results obtained for the proliferation analysis of fsEVs. Compared to "treatment" with fsEVs that were solely functionalized with CD9, CD63, and CD81, the addition of miRIDIAN miRNAs mimics effectively amplified this pro-migratory behaviour (Figure 44c). As observed in the pro-

proliferative analysis, some miRNAs were more effective in this regard (e.g. hsa-miR-132) compared to others (e.g. hsa-miR-124).

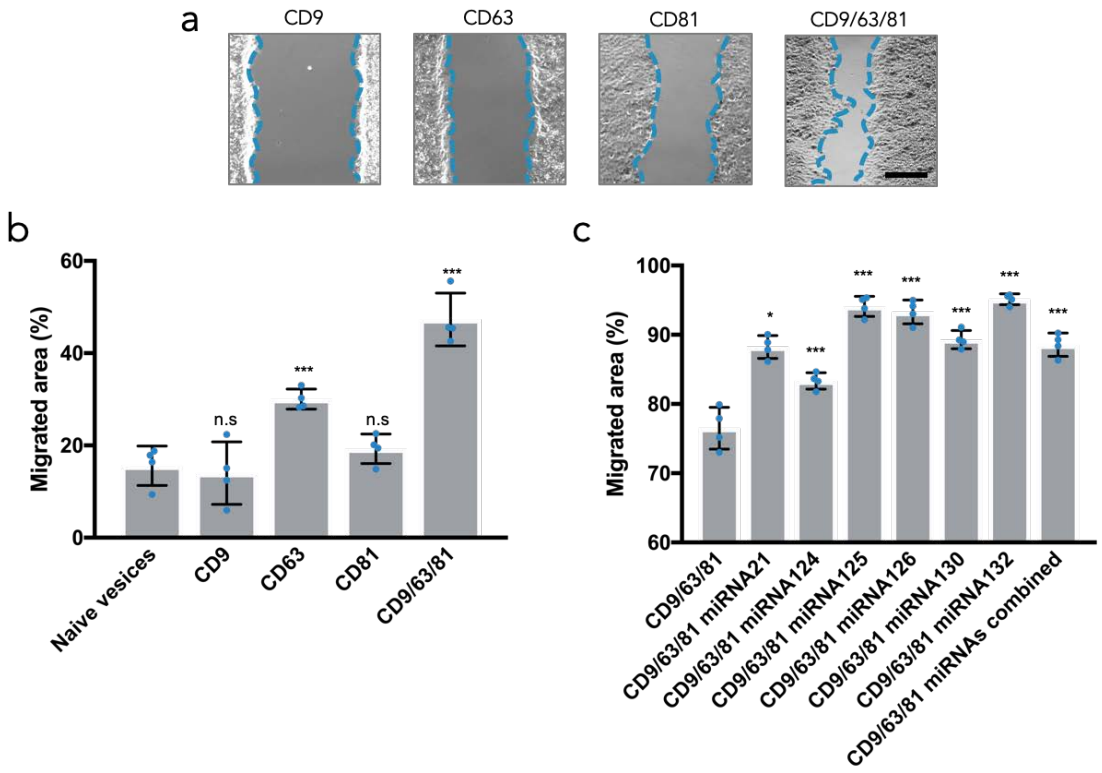

Figure 44 | *In vitro* collective migration of fsEV-treated keratinocytes. (**a**) Representative phase contrast images of HaCaT keratinocyte monolayers treated with fsEVs for 24 hours and after 16 hours of migration into an *in vitro* wound site. The boarders of the cell layers are highlighted by blue-dashed lines. Scale bar 185 µm. (**b**) Quantification of *in vitro* wound healing migration assays of keratinocyte monolayers treated for 24 hours with fsEVs presenting different human tetraspanin ED2 variants (at a 1:200 protein to lipid ratio). (**c**) Quantification of *in vitro* wound healing migration assays of keratinocyte monolayers treated for 24 hours with fsEVs decorated with recombinant tetraspanin ED2 domains of human CD9, CD63 and CD81 (at a 1:200 protein to lipid ratio) and loaded with different miRNA mimics (50 nM each). Results are shown as mean ± SD; n=4 individual wound sites. Statistical analysis was performed for significant difference compared to the control conditions "naïve vesicles" and "CD9/63/81" in b and c, respectively. T-test with *=p<0.01, **=p<0.001, ***=p<0.0001, n.s. not significant.

Importantly, a fundamental conceptual advancement, provided by the use of fsEVs compared to natural EVs, lays in their quantitative defined character. For instance, this allows to systematically vary their quantitative miRNA formulation and thereby to explore holistic effects EV-mediate miRNA signalling on a quantitative level. Therefore, concentration effects of miRNA132 mimics on *in vitro* keratinocyte migration were investigated by integrating different concentrations of hsa-miR-132 mimics (from 5-150 nM) into the fsEVs while keeping the other five miRNAs at a constant concentration of

50 nM each (Figure 45). Interestingly, the addition of 50 nM hsa-miR-132 mimic, which represents and equimolar concentration to the other five miRNAs, resulted in the most pronounced effect on *in vitro* wound closure. This indicates that in order to achieve a desired physiological EV-signalling, not only the sole presence of individual miRNAs is of importance but that a specific ratio needs to be kept. Taken together, these experiments show that alongside proliferation, fsEVs can also increase collective migration of keratinocytes.

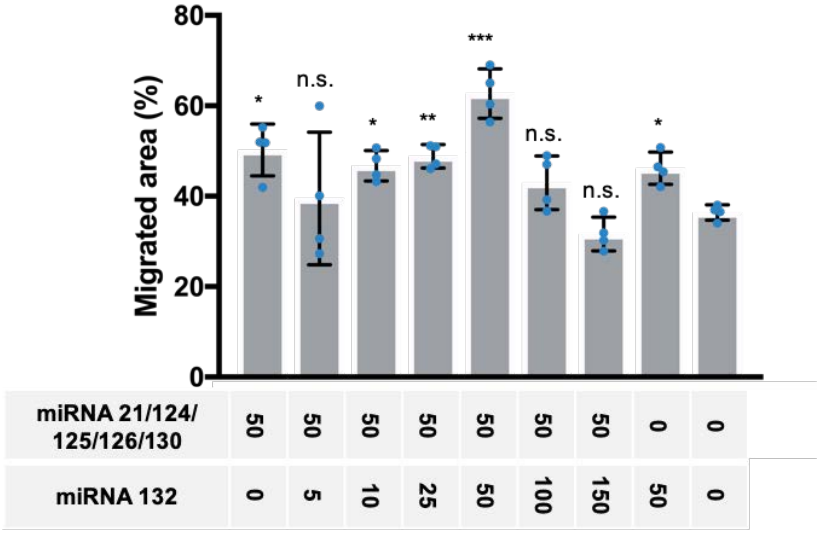

Figure 45 | miRNA concentration effects on collective cell migration of keratinocytes. Quantification of *in vitro* wound healing migration assays of keratinocyte monolayers treated for 24 hours with fsEVs decorated with recombinant tetraspanin ED2 domains of human CD9, CD63 and CD81 (at a 1:200 protein to lipid ratio) and loaded with miRNA mimics (concentrations given in nM). The miRNA mimics of hsa-miR-21, hsa-miR-124, hsa-miR-125, hsa-miR-126 and hsa-miR-130 in the fsEVs were added at a constant concentration of 50 nM, while the concentration of hsa-miR-132 was varied. Results are shown as mean ± SD; n=4 individual wound sites. Statistical analysis was performed for significant difference compared to the control conditions with no miRNA added. T-test with *=$p<0.01$, **=$p<0.001$, ***=$p<0.0001$, n.s. not significant.

4.4.4.3 Increase of collagen deposition by dermal fibroblasts upon fsEVs treatment

In order to assess the effect of fsEVs on dermal fibroblast collagen deposition, enzyme-linked immunosorbent assays (ELISA) were performed on primary human dermal fibroblast cells (BJ cells) treated with fsEVs for 24 hours (Figure 46). Although efforts to decode differential effects of individual miRNAs revealed no significant differences, treatment with fsEVs containing all six miRNA mimics (50 nM each) and recombinant tetraspanin ED2 domains of human CD9, CD63 and CD81 (at a 1:200 protein to lipid ratio) induced a higher collagen deposition compared to untreated cultures.

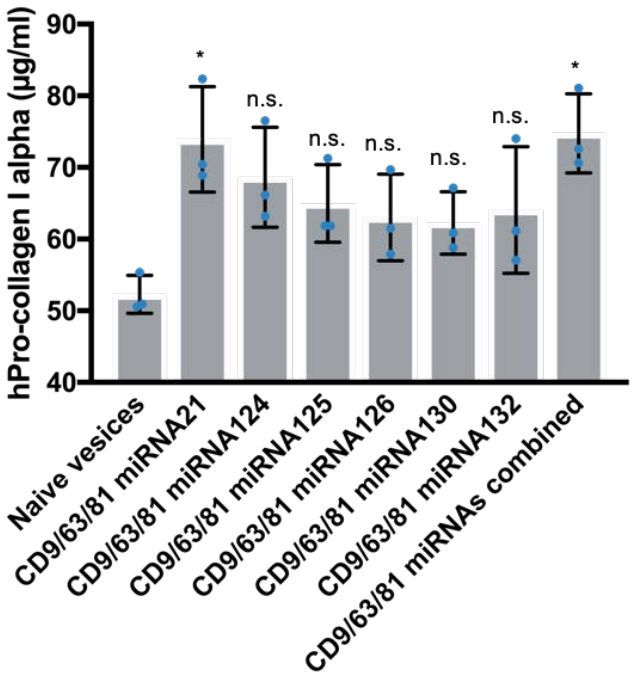

Figure 46 | ELISA-based quantification of human pro-collagen-Iα deposition. Primary human dermal fibroblasts were treated for 24-hours with fsEVs presenting recombinant tetraspanin ED2 domains of human CD9, CD63 and CD81 (at a 1:200 protein to lipid ratio) and loaded with different miRNA mimics. Results are shown as mean ± SD; n=3 biological replicates. Statistical analysis was performed for significant difference compared to the control conditions with naïve vesicles. T-test with *=p<0.01, **=p<0.001, ***=p<0.0001, n.s. not significant.

4.4.5 FsEVs enhance wound-healing of 3D organotypic skin models

Wound healing is a highly dynamic process involving several distinct cell types, signalling factors that mediated communication between them and three-dimensional rearrangements of these cellular architectures. Therefore, 2D *in vitro* models offer only a limited representation of these processes and do not effectively predict the response of a 3D human wound. In order to assess if the fsEVs´ *in vitro* 2D functionality can also lead to regeneration of wounded human skin, organotypic full-thickness skin models (Figure 47) from human donors with epidermal wounds were treated with fsEVs for 48h. The fsEV solution was directly applied onto the wound site at the air-liquid interphase. For this analysis, fsEVs containing mimics of the six miRNAs hsa-miR-21, hsa-miR-124, hsa-miR-125, hsa-miR-126, hsa-miR-130 and hsa-miR-132 (50 nM each) and presenting human recombinant ED2 of the tetraspanins CD9, CD63 and CD81 (at a 1:200 protein to lipid ratio) were used.

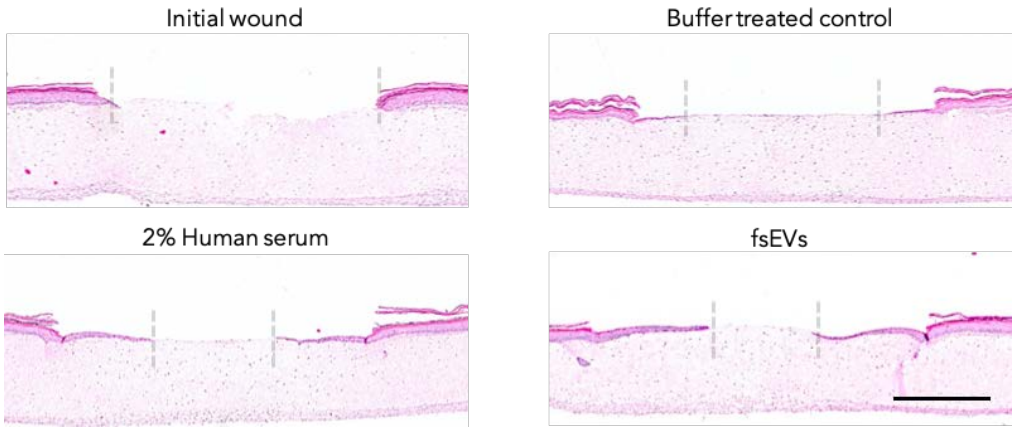

Figure 47 | Wound closure of 3D organotypic human skin models after fsEV treatment. Representative histological sections of organotypic human full-thickness epidermal skin models with a punched epidermal wound side (upper left). Wounds were either treated by applying 2 µl of buffer (PBS, upper right), 2% human serum dissolved in buffer (lower left) or with fsEVs (1 µM total lipids) containing mimics of miRNAs hsa-miR-21, hsa-miR-124, hsa-miR-125, hsa-miR-126, hsa-miR-130 and hsa-miR-132 (50 nM each) and presenting human recombinant ED2 of the tetraspanins CD9, CD63 and CD81 (at a 1:200 protein to lipid ratio) (lower right). Tissue were treated for 48 hours and haematoxylin-eosin stained sections were prepared afterwards. Dashed lines indicate epidermal wound edges. The scale bar is 1 mm.

Epidermal closure of the approximately 3 mm wound was quantified by measuring the epithelial wound bed-size in haematoxylin-eosin (H/E)-stained histological samples (Figure 48a). The fsEV treatment substantially augmented the healing processes as compared to buffer treated negative controls, reaching comparable effect as the human serum treated positive controls. Moreover, the thickness of the regenerated epidermal layer was significantly increased compared to buffer-treated negative controls. This indicates that not only the wound closure speed is increased by the wound-healing fsEVs but also that the regenerated epidermal layer is better developed after fsEV treatment. Taken together these data demonstrate that the bottom-up design and assembly of fsEVs using a droplet-stabilized approach, can produce artificial EVs with a therapeutic potential also in complex, in *in vivo*-like scenarios.

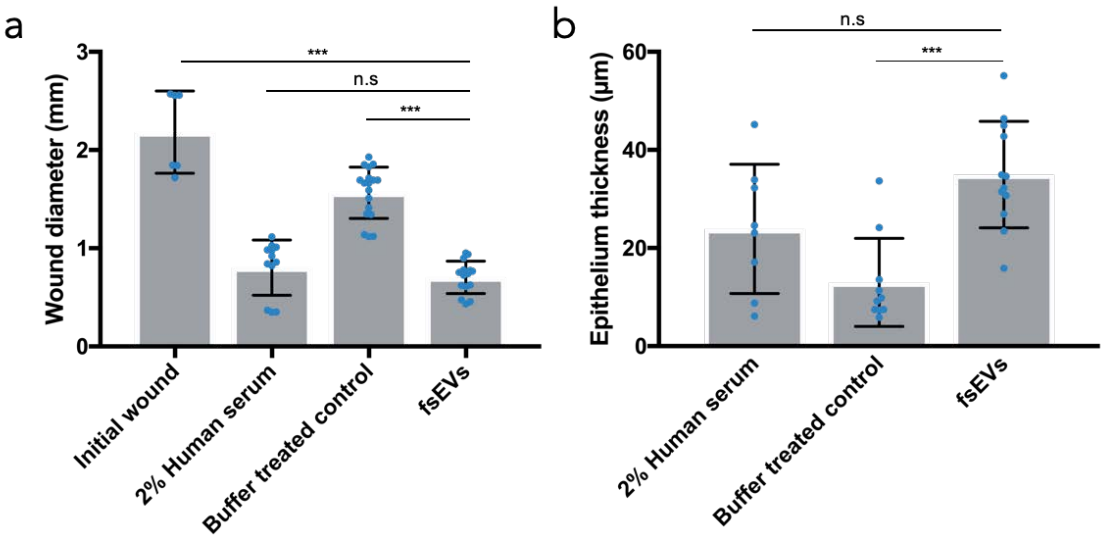

Figure 48 | Quantification of epidermal wound-bed closure in human organotypic skin models. (**a**) Epidermal wound-bed size after 48 hours treatment with 2% human serum (positive control), PBS buffer (negative control) and fsEVs loaded with miRNAs miR-21, miR-124, miR-125, miR-126, miR-130, and miR-132 (50 nM each) and decorated with recombinant human ED2 of CD9, CD63, and CD81 (at a 1:200 protein to lipid ratio). 6 slides from 1 skin, 12 slides from 2 skins (biological duplicate), 18 slides from 3 skins (biological triplicates) and 15 slides from 3 skin (biological triplicates) were measured for the initial wound and serum-, buffer- and fsEV-treat samples, respectively. (**b**) Quantification of the regenerated epidermal layer thickness after treatment for 48 hours with 2% human serum (positive control), PBS buffer (negative control) and fsEVs loaded with miRNAs hsa-miR-21, hsa-miR-124, hsa-miR-125, hsa-miR-126, hsa-miR-130, and hsa-miR-132 (50 nM each) and decorated with recombinant human ED2 of CD9, CD63, and CD81 (at a 1:200 protein to lipid ratio). 8 regenerated epithelia slides from 2 skins (biological duplicates), 10 regenerated epithelia slides from 3 skins (biological triplicates) and 12 regenerated epithelia slides from 3 skins (biological triplicates) were measured for serum-, buffer- and fsEV-treat samples, respectively. Results are shown as mean ± SD. Statistical analysis was performed for significant difference between the samples. T-test with *=$p<0.01$, **=$p<0.001$, ***=$p<0.0001$, n.s. not significant.

4.5 RNA-sequencing analysis of fsEV-treatment

In order to analysis the effect of fsEV-treatment on a functional-mechanistic level whole-transcriptome RNA-sequencing analysis was performed. By this, changes in gene expression can be investigated and the up- or down-regulation of specific gene sets can be correlated to specific functional effects detailed in section 4.4.4.

4.5.1 Transcriptional profiling of keratinocytes treated with wound healing fsEVs

In order to assess transcriptome-alterations induced by treatment with fsEV for wound-healing, HaCaT keratinocytes were incubated with fsEVs decorated with recombinant human ED2 of CD9, CD63, and CD81 (at a 1:200 protein to lipid ratio) and harbouring hsa-miR-21, hsa-miR-124, hsa-miR-125, hsa-miR-126, hsa-miR-130 and hsa-miR-132 (50 nM each) miRIDIAN miRNA mimics for 24 hours or left untreated as a control condition. Moreover, an additional treatment option was analysed which consisted of the soluble fsEV components, meaning that the same final concentration of proteins and RNAs were added to the cells without being bound onto or incorporated into the lipid vesicles. This was performed in order to analyse if these soluble components exert an effect by themselves and whether proteins presentation on the vesicle surface or vesicle-mediated intracellular delivery of the miRNAs is an actual requirement to fulfil their signalling properties. The technical summary and quality assessment of the RNA-sequencing procedure can be found in section 3.2.23.

Principle component (PC) analysis was performed to visualize the overall effect of the experimental covariants and to reveal the similarities between the different treatment groups (Figure 49a). When compared to the untreated keratinocyte cultures, cells treated with fsEVs showed a distinct grouping in the first two principle components (PC). In total 13045 genes were found to be expressed by the HaCaT cells, whereof 173 where found to be differentially expressed genes (DEG) (Figure 49b and supplementary table 1) with an adjusted p-value < 0.05 compared to the untreated cells. From these genes, 113 were upregulated and 60 were downregulated. Interestingly, when comparing cells treated with the soluble compounds, only 5 DEG were found, all of which were also identified in the cells treated with fsEVs (Figure 49b inset). In order to deduce the most central effect of fsEV treatment on the keratinocyte physiology, pathway enrichment analysis was performed using the reactome database (Jassal et al., 2020) database (Figure 49c and supplementary table 2). This analysis revealed that fsEVs impact on three major phenotypic changes in the keratinocytes: 1. cell cycle progression, 2. immune cell activation and regulation as well as 3. ECM remodelling, cell migration and keratinization. In total 70 different pathways were significantly enriched, some of which regulate pivotal phenotypic transitions involved in wound healing, for instance keratinization, formation of a cornified envelope, assembly and crosslinking of collagen fibres and other multimeric structures as well as the synthetises of hydroeicosatetraenoic-based tissue hormones.

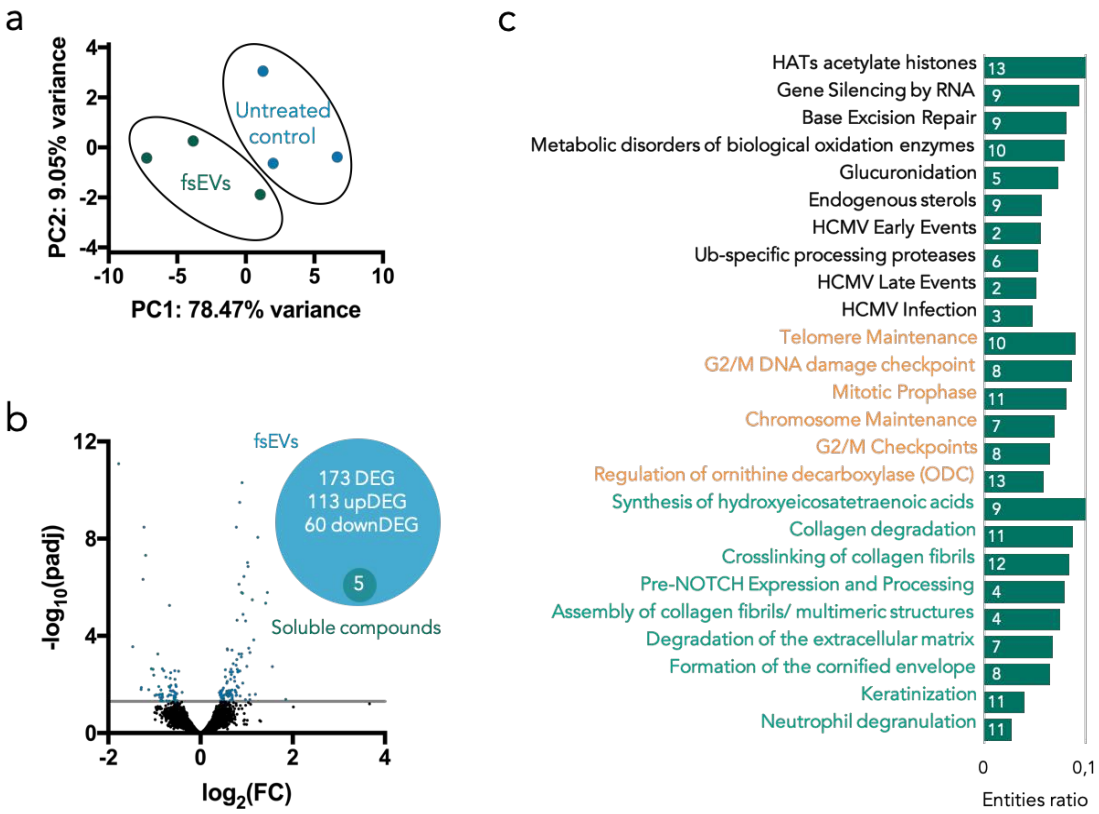

Figure 49 | RNA-sequencing transcriptome analysis of fsEV treatment. HaCaT keratinocytes were treated with fsEVs decorated with recombinant human ED2 of CD9, CD63, and CD81 (at a 1:200 protein to lipid ratio) and harbouring hsa-miR-21, hsa-miR-124, hsa-miR-125, hsa-miR-126, hsa-miR-130 and hsa-miR-132 (50 nM each) miRIDIAN miRNA mimics for 24 hours and compared to untreated cultures. (**a**) Principle component analysis of keratinocytes treated with fsEVs and control-treated with PBS. Every data point represents a single sample of the respective group. (**b**) Volcano plot of gene expression analysis of keratinocytes treated with fsEVs. DEGs are highlighted in blue and the p_{adj}<0.05 threshold is indicated by the grey line. Inset shows Venn diagram of DEGs from cultures treated with fsEV and cultures treated with the soluble components as well as a summary of the DEGs in fsEV treated cultures. Only 5 DEG could be detected when treating keratinocytes with the soluble fsEV compounds. (**c**) Top 25 enriched pathways of DEGs from fsEVs-treated HaCaT cultures. Pathway enrichment analysis was performed based on the reactome database and results are sorted by their entities ratio (entities present in the DEG list/total entities in the pathway). White numbers indicate the number of DEGs detected in the respective pathways. Pathways commonly associated with cell cycle progression are highlighted in orange and pathways commonly associated with cell migration, adhesion, ECM remodelling or wound-healing are highlighted in green.

Moreover, several genes were enriched which are associated with pathways that have previously been explored as important therapeutic targets in wound healing therapy. For instance, several genes involved in the "regulation of ornithine decarboxylase (ODC)" pathway were upregulated by fsEV treatment (Figure 50). Ornithine is decarboxylated to

putresceine, which is the rate limiting step in the synthesis of polyamines involved in cell proliferation (Kern et al., 1999). Therefore, ornithine supplementation itself has been widely explored in (pre-) clinical studies for improved wound healing therapy (Coudray-Lucas et al., 2000; Debats et al., 2003; Shi et al., 2002). Specifically, the genes encoding LRP8, TAP2 and NQO1 were significantly up-regulated with $\log_2$(FoldChange) of 0.811, 0.538 and 0.498, respectively. This indicates that fsEV treatment induces an intrinsic production of putrescine by keratinocytes, possibly supporting cell cycle progression and explaining the increased proliferation rates found in section 4.4.4.1. This is only one of many examples found in the RNA-sequencing analysis, which explains the observation of increased keratinocyte proliferation made in the functional assessments of fsEV treatment. For the sake of clarity, the ODC pathway was chosen as it is comparably straightforward. Other pathways providing mechanistic explanation for increased migration and collagen deposition were found to be affected accordingly. This is not only in good agreement with the functional analysis performed in section 4.4.4 but also reveals the transcriptional changes associated with EVs artificially assembled following the natural blueprint of fibrocytes-derived EVs. This demonstrates how quantitatively defined fsEVs can be employed to gain new functional insight into EV signalling principles.

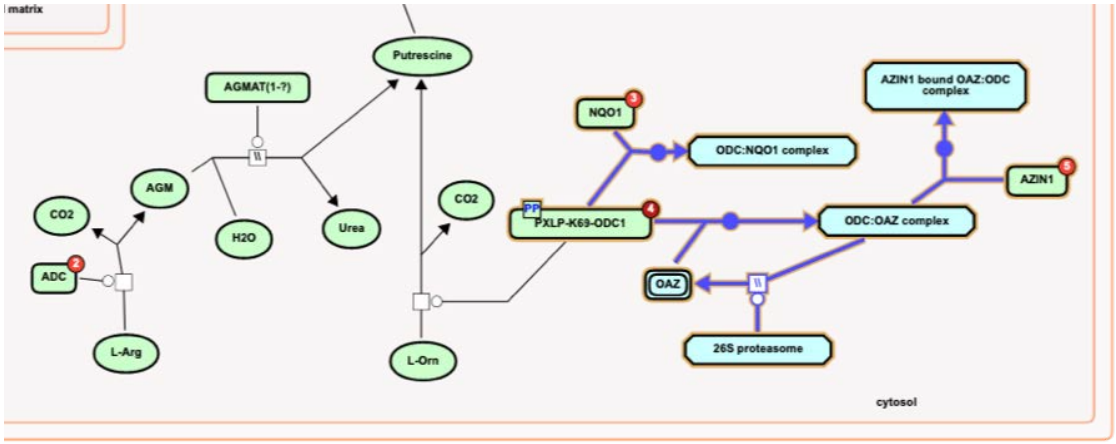

Figure 50 | Regulation of the ornithine decarboxylase pathway. Schematic illustration of the reactome pathway "regulation of ornithine decarboxylase". The pathway entities LRP8, TAP2 and NQO1 were significantly upregulated with $\log_2$(FC) of 0.811, 0.538 and 0.498, respectively, after treatment with fsEVs decorated with recombinant human ED2 of CD9, CD63, and CD81 (at a 1:200 protein to lipid ratio) and harbouring hsa-miR-21, hsa-miR-124, hsa-miR-125, hsa-miR-126, hsa-miR-130 and hsa-miR-132 (50 nM each) miRIDIAN miRNA mimics for 24 hours. The affected steps are highlighted in blue and the affected entities are highlighted with red-circled numbers indicating how many entities in the corresponding pathway steps were found in the submitted DEG set.

4.5.2 Deciphering EV-signalling pathways by *fsEVs*

In order to demonstrate the fundamental advantage of fsEVs for systematic decoding of EV signalling principles, a subsequent RNA-sequencing transcriptome analysis with differently decorated fsEVs was performed. Here, in order decipher the individual contributions of the fsEV proteins, the recombinant ED2 tetraspanins were either coupled together on the fsEV membrane or in pair and triple combinations of them. The transcriptome profile was then compared to keratinocytes cultures treated only with the lipid components of the fsEVs, lacking any proteins or miRNAs.

This analysis revealed, that when HaCaT keratinocytes were treated with fsEVs harbouring recombinant human ED2 CD9, CD63 and CD81 tetraspanins (at a 1:200 protein to lipid ratio) but lacking any miRNA mimics, 231 genes were differentially expressed compared to the lipid treated control cultures. From these genes, 168 were found to be up-regulated and 63 to be down-regulated (see supplementary table 3). Importantly, the fsEV technology now allows to decipher the contribution of each single tetraspanin to the differential regulation of each gene in this set (Figure 51a and supplementary table 3). For instance, cells treated with fsEVs presenting a combination of recombinant human ED2 CD9 and CD81, showed only 58 overlapping DEGs while fsEVs decorated with recombinant human ED2 CD9 or CD63 showed no overlap at all. Interestingly, fsEVs with recombinant human ED2 CD81 did show an overlap of 34 DEGs when compared to cultures treated with fsEVs harbouring recombinant human ED2 CD9, CD63 and CD81 tetraspanins. This exemplifies how fsEVs can be applied to decipher the contribution of individual EV components to differential expression of specific genes or gene sets.

This approach can further be applied to decipher the impact of EV components on individual pathways. Towards this direction, pathway enrichment analysis for DEGs of HaCaT keratinocyte cultures treated with different fsEVs variants was performed (Figure 51b and supplementary table 4). Among the top 25 enriched pathways of cultures treated with fsEVs harbouring recombinant human ED2 CD9, CD63 and CD81 tetraspanins (at a 1:200 protein to lipid ratio), several pathways associated to immune-regulatory mechanisms were identified. Moreover, again several pathways commonly associated with cell migration and ECM remodelling were identified as enriched. By combining this pathway enrichment analysis with the consideration of individual DEGs, specific tetraspanins can be correlated to specific phenotypic alterations. To exemplify this, the

"Type I hemidesmosome assembly" pathway was further investigated for the individual fsEV compositions (Figure 51c). Important to note, desmosome disassembly is of major importance for proper wound healing (Garrod and Chidgey, 2008; Hopkinson et al., 2014). Type I hemidesmosomes consist of 8 major proteins, 6 of which were found to be differentially expressed by fsEV treatment. It was found that the respective DEGs were specifically associated with individual tetraspanin combinations. This not only correlates with the functional assessments in section 4.4.4.2 but also shows the cumulative nature of the EV components, as the more EV proteins are united in a single fsEV preparation, the more diverse transcriptomic changes are observed. Taken together, these investigations demonstrate that EVs of complex composition induced more functional effect than simply the sum of their parts, highlighting their role as intercellular protein-presentation platforms.

The fsEV concept can not only be applied to the protein component of EVs but also to other moieties like the miRNAs. To demonstrate this, HaCaT keratinocyte cultures treated with fsEVs harbouring recombinant human ED2 CD9, CD63 and CD81 tetraspanins (at a 1:200 protein to lipid ratio) were compared to fsEVs harbouring recombinant human ED2 CD9, CD63 and CD81 tetraspanins and additionally carrying hsa-miR-21, hsa-miR-124, hsa-miR-125, hsa-miR-126, hsa-miR-130 and hsa-miR-132 miRNA mimics. This comparison revealed 57 DEGs (see supplementary table 5). Moreover, respective DEGs were found to be enriched in 12 pathways which were interestingly not associated to ECM remodelling, cell migration, adhesion or immune-regulation (Figure 51d and supplementary table 6). Rather, mostly pathways associated with mitochondrial physiology and metabolism were enriched. Upregulation of cellular energy metabolism in turn, is a prerequisite to boost cell proliferation.

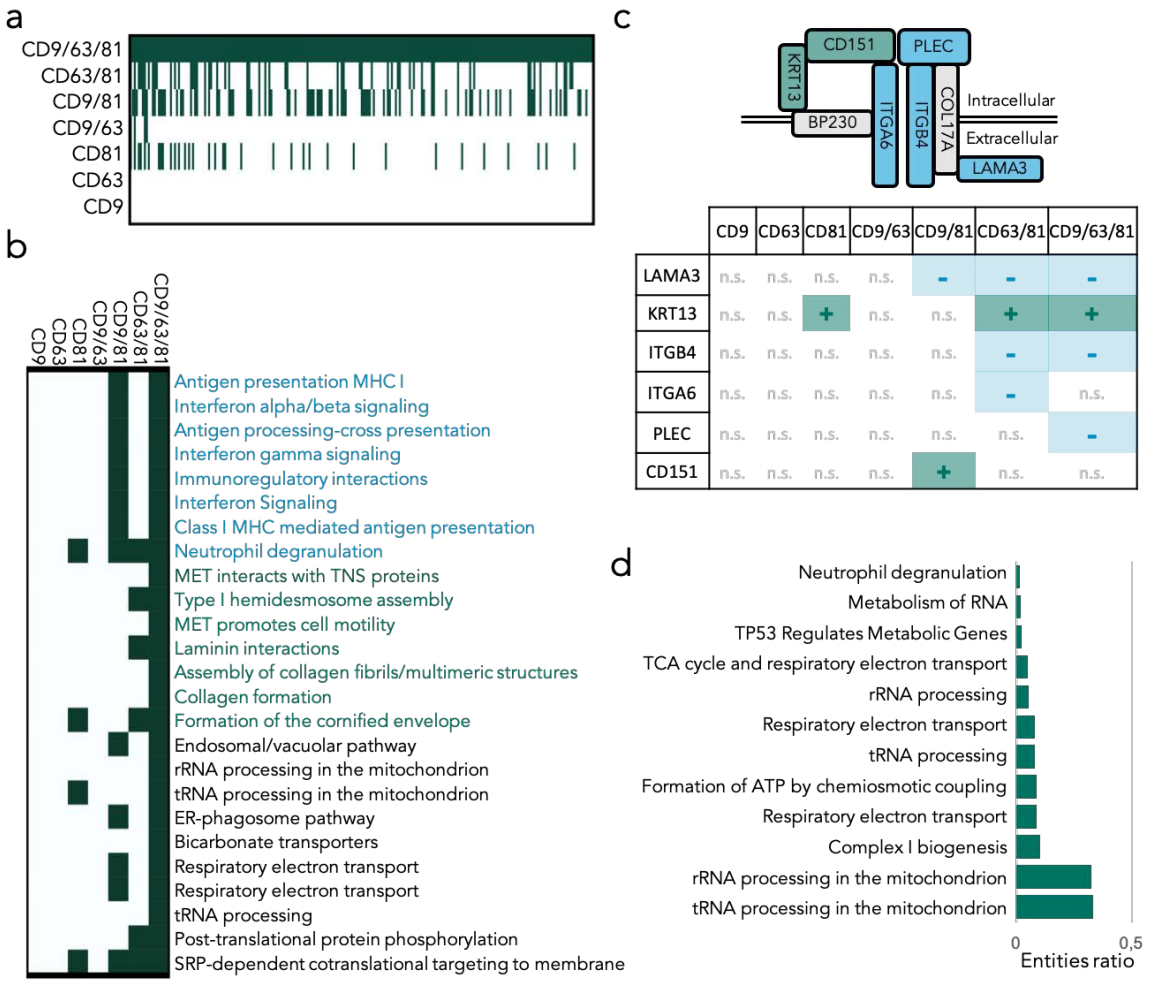

Figure 51 | Deciphering EV signalling by RNA-sequencing analysis of fsEV-treated cells. (**a**) Heat map of overlapping DEGs between cultures treated with fsEVs decorated with different combination of recombinant human tetraspanins ED2. Each column represents one of 231 DEGs found for HaCaT cells treated with fsEVs decorated with recombinant human ED2 CD9, CD63 and CD81. DEGs are marked in green. (**b**) Heat map of pathway enrichment analysis of the top 25 pathways enriched in HaCaT cells treated with fsEVs decorated with recombinant human ED2 CD9, CD63 and CD81 and overlapping enriched pathways for HaCaT cells treated with vesicles decorated with other tetraspanin combinations. Significantly ($p<0.05$) enriched pathways are marked in green. Pathways commonly associated with immune-regulation and cell motility are highlighted in blue and green, respectively. (**c**) Schematic representation of a type I hemidesmosome and summery of associated DEGs in HaCaT cells treated with fsEVs decorated with different tetraspanin combinations. Upregulations and downregulation of the respective genes are indicated with + and -, respectively. N.s. indicates no significant differential expression of the respective gene in the treatment condition. (**d**) Top 12 enriched pathways of DEGs from HaCaT cultures treated with fsEV decorated with recombinant human ED2 CD9, CD63 and CD81 and harbouring hsa-miR-21, hsa-miR-124, hsa-miR-125, hsa-miR-126, hsa-miR-130 and hsa-miR-132 miRNA mimics. DEGs were determined in comparison to HaCaT cultures treated with fsEVs decorated only with recombinant human ED2 CD9, CD63 and CD81. Results are sorted by their entities ratio (entities present in the DEG list/total entities in the pathway).

5 Discussion

In this thesis, I describe the characterization and manipulation of GUV-cell interactions and the assembly of fully-synthetic and functional extracellular vesicles. I describe bulk and microfluidic methods for the charge-mediated assembly of dsGUVs and the implementation of microfluidic splitting devices for serial miniaturization of dsGUVs. Moreover, I report on the application of bio-orthogonal functionalization strategies of GUV membranes. Based on the developed concepts, I describe the assembly of hierarchical GUV-based vesicular delivery systems for large supramolecular cargos and synthetic organelles. Moreover, I describe the bottom-up assembly of fully-synthetic but functional EVs for application in wound healing therapy and concepts for their deployment in studies aiming to decipher functional mechanisms of EV-signalling.

5.1 GUVs for intracellular cargo delivery

In the following, I summarize and critically discuss some key aspects and achievements involved in GUV-based intracellular cargo delivery:

Chapter 4.1 introduces a high-throughput droplet-based microfluidic production pipeline for the assembly of large amounts of well-defined carrier-GUVs suitable for cellular uptake with a diameter of approximately 2 µm. The described technology relays on three subsequent production steps: 1) well-controlled charge-mediated assembly of dsGUVs from SUV precursors 2) serial mechanical splitting of dsGUVs by V-shaped microfluidic channel-architectures and 3) the release of these droplet-splitted GUVs into an aqueous environment by destabilization of the droplet emulsion. As demonstrated in sections 4.1.2 and 4.1.5, this sequential assembly approach enables for very efficient loading of complex supramolecular cargos into the dsGUVs and moreover offers a high control over the physicochemical properties of the GUV-membranes. Specifically, the precise adjustment of GUV size, cargo and charge as well as the ability to adjust the strength of GUV-cell interactions, has allowed to undertake a systematic assessment of key factors that conquer the GUV-cell interaction and to explore concepts for targeted GUV delivery as described in chapter 4.2. Moreover, the highly reliable and diverse bio-orthogonal GUV-functionalization strategies implemented in section 4.2.1, empower the production of GUVs with a diverse functional repertoire. In particular, the work presented in this thesis shows how a combination of repulsive PEG-mediated interactions together

with charge-driven and specific ligand-receptor-based attractive GUV-cell interactions can be applied to regulate specific cellular GUV-uptake.

Moreover, a systematic evaluation of GUV-decoration with PEG polymers is presented (see section 4.2.3). This approach is inspired by PEGylation strategies previously applied for other small liposomal delivery systems (Immordino et al., 2006) and the integration of small amounts of PEG into GUV membranes (Yamashita et al., 2002). However, this thesis presents, to the best of my knowledge, the first characterization of GUV PEGylation at high concentrations of PEG (up to 50mol%), which was so far not achievable with current GUV-formation techniques. This does not only highlight a fundamental advantage provided by the formation of GUVs *via* dsGUV production but also allowed for the first systematic screening of PEGylated-GUV-cell interactions. It was observed that increased PEGylation rates of the GUVs resulted in a decrease GUV-cell attraction. DLS measurements revealed that corresponding GUVs feature a decreased ζ-potential, indicating that PEG polymers successively mask or shield the GUV-membrane charge. A directly decreased charge-mediated membrane-membrane interaction between the GUVs and cells could thereby explain the reduced attraction. However, this effect could also be deduced to a reduced opsonin coating of the GUVs by serum-proteins and therefore lead to a reduced receptor-mediated GUV uptake (Suk et al., 2016). As detailed in section 4.2.3, this effect was especially affected by the rate of PEGylation employed and less by the PEG-chain length. This observation might be explained by considering the two main structural conformations surface-immobilized PEG can form: 1) an extensively coiled “mushroom”-like conformation and 2) a more linearized, “brush”-like structure. While the brush-like form results in higher shielding capacity, the mushroom-like form has only limited capabilities in reducing liposomal-membrane interactions (Perry et al., 2012). Two of the key factors determining the actual PEG-conformation state on lipid membranes are the polymer length (assuming a non-branched polymer) and the membrane PEGylation density. As detailed in previous reports (Perry et al., 2012), experimental determination of the PEG density on a surface is highly challenging, wherefore most considerations in this regard are based on theoretical predictions and calculations (Cruje and Chithrani, 2014). For this, the Flory radius (R_F), the intermolecular-PEG distance on the surface (D) and the polymer length (L) need to be considered. At low polymer surface densities with $D>R_F$, a mushroom-like form, with non-fully extended PEG-chains, is preferred. As D decreases, the PEG polymers extend to a brush-like conformation providing denser coverage of the surface (Cruje and

Chithrani, 2014; Kaufmann et al., 2011; Perry et al., 2012; Suk et al., 2016). Moreover, when $L>2R_F$, a dense brush-like confirmation is formed (Damodaran et al., 2010). R_F can be approximated by $R_F=a*n^v$ (where a is the PEG monomer length of 3.5 Å, n is the number of monomers and v is the Flory constant of 3/5) (Cruje and Chithrani, 2014). For all PEG molecular weights tested (PEG350, PEG750 and PEG1000), L is larger than $2*R_F$, wherefore a dense brush conformation can be assumed in all cases. Increase from 5 to 50mol% induced a transition from a mushroom-like conformation to a brush-like conformation, this could potentially explain why increase in PEG length does not affect the GUV-cell repulsion as strong as the increase in PEGylation density. Successive increase of the PEG length however, results in a non-linear increase in the PEG layer thickness and therefor probably in a more efficient shielding of the GUV surface charge. To assess these matters, as well as possible opsonin-coating effects, future characterizations should not only include functional assessment like cell-attraction measurements but also involve (ultra-)structural evaluations based for instance on cryoTEM or QCM-D.

Based on these assessments, section 4.2.4 demonstrates how a combination of attractive and repulsive GUV-cell interactions can be employed to decrease nonspecific, electrostatic interactions and boost specific cell-targeting. Moreover, observations based on electron microscopy and z-resolved confocal fluorescence microscopy in combination with the endosomal compartment staining presented in sections 4.1.5 and 4.2.5 provide clear proof that negatively charged GUVs as well as ligand coupled GUVs are taken up by cells. Passage of this first biological barrier, the plasma membrane, opens the doors for further directed, possibly lossless intracellular release of cargo. This further highlights the application of dsGUV formation for the controlled module by module assembly of hierarchical cargo delivery systems with sequential release functionalities.

Further, section 4.2.5 describes the assessment of several lysosomal escape mechanisms and the implementation of an efficient cytoplasmic release strategy for GUV cargos, based on the pH-sensitive lipid DOBAQ. This analysis revealed that out of the three approaches tested, only DOBAQ showed efficient intracellular release of GUV luminal cargo. However, the PEI as well as the GALA-peptide-based approaches have previously been applied for efficient drug-release from nano-carriers (Nakase et al., 2011; Zakeri et al., 2018), raising the question why these approaches seem to be non-functional for GUV-based delivery. Therefore, two major structural differences between previously applied liposomal nano-carriers and GUVs need to be emphasised. First, the GUV

membrane curvature as well as the curvature induced membrane tension is almost neglectable and second, GUVs possess a significantly higher surface-to-volume ratio compared to SUVs. Particularly, the fusogenic properties of GUVs, in dependence of their membrane tension, have been assessed previously (Kliesch et al., 2017). These reports provided clear evidence that the "fusiogenicity" of GUVs increases with curvature induced membrane tension. Therefore, the GALA-based approaches might not provide sufficient inter-membrane attraction for intralysosomal fusion of GUV-membrane. Additionally, because of the reduced membrane curvature, the intrinsic "fusiogenicity" of the GUVs might be too low to allow spontaneous membrane fusion even if the two membranes are brought in close contact. However, this should not affect the PEI-based approach, as in this case lysosomal escape is achieved by lysosomal rupture and not by fusion. Therefore, the second key difference of GUVs compared to nano-size liposomes needs to be considered: the high surface-to-volume ratio. Potentially, the GUV lumen is to spacious to allow for a harsh unproportional proton-sponge like swelling and subsequent rupturing of GUV and lysosome. If true, this effect could be overcome by increasing the PEI intraluminal concentration. However, when concentrations higher than 44 µg/ml PEI were encapsulated into dsGUV, neither reliable dsGUV formation nor GUV release was observed.

Another important observation related to GUV-fusion was made when applying cationic GUVs on cells (see section 4.1.5). Incubation of GUVs containing cationic DOTAP lipids with cells induced severe cytotoxic effects. By co-localization of the GUV-lipid fluorescence with a plasma membrane staining, it could be shown that the GUVs most probably undergo direct fusion with the cells. This effect has been studied extensively for other cationic liposomal formulations under *in vitro* and *in vivo* conditions (Audouy et al., 2002; Bailey and Cullis, 1997; Cavalcanti et al., 2018; Cortesi et al., 1996; Mok and Cullis, 1997; Romoren et al., 2004), where cytotoxic side effects are well-known complications and several routs and mechanisms related to this cytotoxicity haven been proposed. Therefore, a very narrow therapeutic-window needs to be kept for such cationic liposomal systems. In the case of cationic GUV-based systems, this window might be even further narrowed. For instance, *in vitro* IC_{50} in the range of 100 – 300 µM have been reported for cationic liposomes (Vangasseri et al., 2006). In the experiments presented in section 4.1.5 however, lipid concentrations of 10 µM were applied and almost no cell survival was observed under these conditions. This indicates that cationic GUVs possess a comparable high cytotoxicity. This effect could be based on two different phenomena.

First, when direct GUV-cell fusion occurs, the amount of exogenous fluid released into the cytosol is orders of magnitude higher when compared to classical liposomal system. This could induced severe disturbance of the intracellular electrolyte homeostasis and cause inevitable cell death. Secondly, the number of exogenous lipids introduced into the cell membrane upon fusion of a single GUV is considerably high compared to nanometer-sized liposomes. This harsh disturbance of membrane homeostasis as well as the associated changes of the physical state of the cell membrane could lead to consequential disturbance of the cellular equilibrium. Therefore, for drug-delivery applications, an in-detail analysis of the dose-response and dose-cytotoxicity relation of cationic GUVs needs to be performed in future experiments. However, even though cationic GUVs potentially possess a lower IC_{50}, they could still outperform conventional cationic liposome formulations. In particular, because their total cargo capacity is orders of magnitude higher and therefore the total number of GUVs that need to be applied to reach a therapeutic drug dose could be very low, compensating their higher cytotoxicity.

Interestingly, GUVs with ζ-potentials close to 0 showed very reduced cell-attraction (see section 4.1.5). In accordance with the quantitative cell-attraction assay measurements, observations by fluorescence confocal microscopy showed that respective GUVs were "loosely" bound to cell membranes. Experimental setups based on respective GUVs, are very well suited to analyse the effect of protein presentation by vesicles as interfering effects by any substantial vesicle uptake can be diminished. Such systems might be very valuable to study intercellular signalling based on ligand-receptor interactions as performed laboriously in previous studies (Jenkins et al., 2018). However, as the dsGUV formation process is based on a charge-mediated lipid-surfactant interaction, the production rates of respective GUVs were considerably low, wherefore further optimization of the production parameters (e.g. increase of $MgCl_2$) should be performed.

Moreover, further in-depth characterization of some GUV characteristics might be performed in future studies. For instance, as the assessment presented in section 4.1.2 was solely based on average fluorescence intensity measurements, the inconsistencies in the assessment of the interdroplet variation (see Table 6) should be revaluated to better characterize the droplet-transmission homogeneity. Therefore, more quantitative experimental approaches, for instance techniques with single molecule resolution like TEM, should be applied.

The successful incorporation of BVs into GUVs by means of charge-mediated dsGUV formation (see section 4.2.6) together with the subsequent transduction of cell

culture cells based on GUV uptake, demonstrates the cargo loading capability of the droplet-splitted GUVs. This represents a significant advancement compared to the current size and load limitations of conventional liposomal drug-delivery systems. In future, freights could include ensembles of therapeutic viruses with multiple genome engineering modalities, drug-releasing porous microparticles, large quantities *in vivo* imaging agents, DNA origami nano-robots and other biological and synthetic nanodevices. In this case, the GUV shell could simultaneously allow for targeted delivery and also prevent cargo degradation inside the GUV lumen. Particularly for viruses, a GUV-based delivery system might not only prevent any eliminating immune-recognition but also "outsources" so far genetically engineered targeting functionalities of viral capsids to the GUV membrane. This in turn would "free" additional genetic space on the viral genomes for therapeutic exogenous genes. After arrival of the GUV at its cellular destination, the cargo would then be intracellularly discharged *via* the presented lysosomal escape mechanism. However, the purity of respective BV-loaded GUVs needs to be reassessed as free viruses released from the GUV "shell" during the deemulsification process could lead to a misleading GUV-independent transduction. Moreover, the structural properties of BVs loaded into the GUV membranes need to be critically assessed. The cryoTEM analysis (see section 4.2.6) showed that BV can undergo apparently progressive disassembly inside the GUVs. Other reports have found previously that "demounting" the BVs´ lipid envelop by surfactants, the viral capsid undergoes relaxation and DNA extrusion, potentially lowering or diminishing the viral transduction potential (Wang et al., 2016). The charge-mediated dsGUV assembly from SUV precursors for simultaneous BV incorporation could also include substantial Mg^{2+}-mediated attraction of the BVs themselves to the droplet-periphery and subsequent fusion of the viral lipid envelop with the SUVs to form a hybrid dsGUV (Figure 52). Therefore, in particular the immunogenicity of such BV-loaded GUV needs to be evaluated as viral membrane proteins could be presented on the GUV surface. Section 4.3 introduces how the unique capabilities of microfluidic-based GUV assembly can be employed to produced SOs as well as their uptake and functioning inside different mammalian cell lines and primary cells. Concepts on how GUV-based SOs can be equipped with several operational modules to mimic the natural organelle structure and function are presented. The application of microfluidics for the production of lipid enveloped SOs can be considered as an important advancement, as dsGUV technology is compatible with numerous different lipid types, which allows to precisely assemble the natural organelle membrane composition *in vitro*. Moreover, it emphasises the flexibility

of the dsGUV approaches as it allows the incorporation of compounds with varying sizes, ranging from low molecular weight npEGTA cages to large nanoparticles like iron nanoparticles. This also showcases the construction of complex, higher order machineries operable in the intracellular space which can also expand the boarders of natural design and building plans towards the intracellular implantation of new synthetic modules.

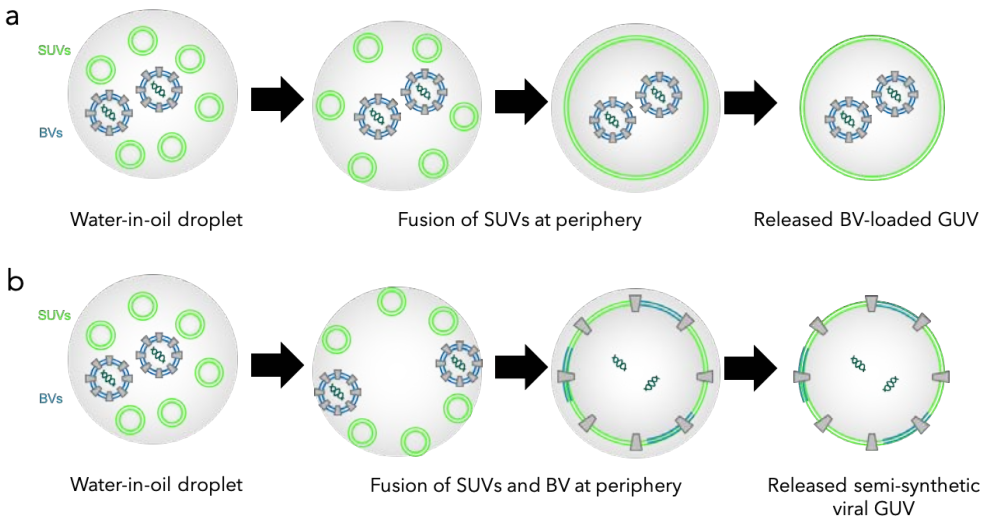

Figure 52 | Models of BV-loading into GUVs. (a) Schematic illustration of the incorporation of BVs into the lumen of a dsGUV. (b) Schematic illustration of the simultaneous fusion SUVs and BVs inside water-in-oil droplets, forming a hybrid GUV membrane.

However, further concept beside lysosomal escape will need to be developed in order to control the intracellular stability of the SOs. In the presented studies, SOs have been observed to be stable for approximately 72 hours. Although this represents a time window which is well-suited for *in vitro* studies on organelles functioning and some medical approaches, it does not implicate stable incorporation of the SOs into the cell machinery. Therefore, novel means, e.g. allowing for SOs replication during the cell cycle should be developed, which would then allow for a true fusion of synthetic organelles with living cells.

5.2 Limitations and outlook for GUV-based targeted delivery

In the following I will discuss future research directions empowered by the advancements presented in this thesis as well as the current drawbacks and limitations of the GUV-based delivery systems:

Although the work presented in this thesis has provided some fundamental advancements towards the use of droplet-splitted GUVs for cellular delivery purposes,

several challenges still loom on the way to their clinical applications. For instance, the (humoral-) immunogenicity of the GUVs needs to be assessed. The value of *in vitro* assays for this purpose is still controversially discussed wherefore only *in vivo* administration can provide clear evidence and conclusions in this regard. However, the *in vivo* application of such GUVs bears additional aspects that need to be meticulously assessed and considered during the GUV design. For instance, micron-sized particles, or aggregations thereof, could potentially lead to clogging of blood-vessels or other tubular structures like liver sinusoids. Moreover, there is an evident correlation between vesicle size and vesicle localization after injection (Carstens et al., 2011), their circulation time (Litzinger et al., 1994) and the type of immune response (Badiee et al., 2012) evoked. This size-correlation also holds true for liver and spleen uptake rates (Liu et al., 1992), which, if not reduced by repulsive-PEG coating, could further limit the targeting efficiency of the GUVs. Importantly, GUVs produced *via* microfluidic technologies exhibit a very low bending rigidity and are therefore highly flexible (Karamdad et al., 2015). Many blood-circulation depletion effects are based on the mechanical rigidity of the particles (e.g. filtration of old red blood cells by the spleen), making GUVs promising carrier particles for long blood-circulation times. Together with this, the GUV administration routs need to be evaluated as each individual application (e.g. intravenous, intramuscular, intraperitoneal, intracerebral, subcutaneous, intraocular, oral etc.) requires specific formulation features and GUV surface characteristics. For instance, intravenous injection demands high shear stress tolerance of the GUVs, while oral administration requires an increased chemical and osmotic stability. Which of these parameters can be engineered into droplet-splitted GUVs remains to be assessed.

Although GUV-based systems have been interfaced with cells previously to assess immune signalling of antigen-presenting cells (Jenkins et al., 2018), this thesis provides the first throughout study that sheds light on the fundamental factors that govern GUV-cell interaction spectrum. Based on this, new horizons open which not only allow to investigate the interactions of cells with GUVs applied for drug delivery but moreover empower systematic characterizations of intercellular signalling based on synthetic cells. The engineering strategies detailed in this thesis, characterizing GUV-cell interactions and GUV guidance, lay the foundation for such highly promising future applications. Importantly, the exquisite control over the GUV composition offered by the charge-mediated assembly as well as the developed toolbox of GUV functionalization strategies, enable for the construction of GUVs with an excessive functional diversity. Therefore, the

investigation of GUV-cell interactions will prove eminently useful for bottom-up synthetic biology approaches, aiming to create novel materials somewhere in between the living and synthetic states of matter (Figure 53a). By incorporation of such synthetic cells into living cell architectures, fundamental questions of bottom-up synthetic biology could be solved. For instance, an objectified cellular Turing-test towards *vivum ex vivo* could be implemented, where stable integration and the formation of a holistic semi-synthetic "self" is evaluated based on the establishment of bidirectional information exchange between the living and synthetic life forms (Levin, 2019). Hereby, interactions within hybrid tissues and therefore on the micro- and mesoscale architecture of these, could be tuned using the molecular-engineering strategies presented in this thesis (Figure 53b). Moreover, these detailed characterizations lay the foundations and clarify imminent requirements for the bottom-up assembly of defined fsEV structures.

5.3 GUVs as fully-synthetic extracellular vesicles

In the following, I summarize and critically discuss some key aspects and achievements associated with the first synthesis of fully-synthetic, functional and potentially therapeutic fsEVs.

Chapter 4.4 introduces a complementary and quantitative approach based on bottom-up synthetic biology principles for sequential *in vitro* synthesis of fully-synthetic extracellular vesicles with completely defined lipid, protein and nucleic-acid composition. Section 4.4.1 demonstrates how fsEVs can be assembled step-by-step from well-defined synthetic molecular building blocks *in vitro* using a mechanical emulsification approach for dsGUV production. This strategy for EV preparation circumvents the introduction of impurities by cellular production techniques. In sections 4.4.2 and 4.4.3, quantitative data on the fsEV lipid composition are provided and an assessment of the nucleic acid incorporation and protein decoration as well as the biophysical properties of the EVs is performed. These experiments demonstrate that fsEVs can be assembled from individually adjustable lipid precursors to precisely match the lipid composition and biophysical characteristics of EVs isolated from cells, even with slightly higher homogeneity and reproducibility than their natural blueprints. Section 4.4.4 describes fully-synthetic EVs with identical functionalities to natural exosomes and shows their administration on organotypic full-thickness human skins models for wound-healing therapy. Much like their natural doppelgangers, these *in vitro* assembled EVs are able to

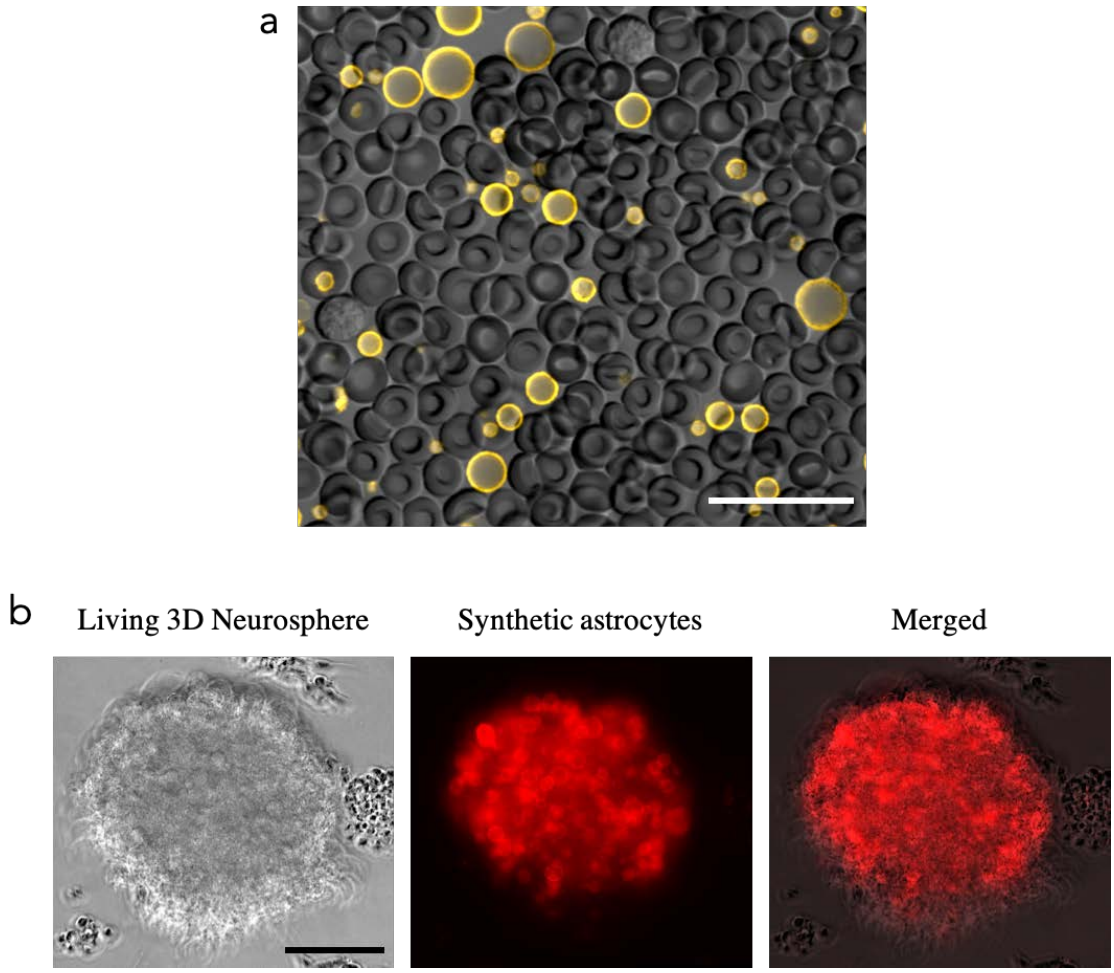

Figure 53 | Incorporation of synthetic cells into living system. (**a**) Merged fluorescence confocal microscopy and bright field image GUVs (yellow) incubated in 1:100 diluted blood. The scale bar is 25 µm. (**b**) Fluorescence confocal microscopy and bright field image of GUVs applied as synthetic astrocytes (red) by decoration of the GUV surface with NrCAM. Synthetic astrocytes were incorporated into living 3D Sh-SY5Y neurospheroids to create a hybrid-tissue architecture. The scale bar is 100 µm.

boost three of the most fundamental processes involved in proper wound healing: proliferation, migration and collagen deposition. This well-defined fsEV preparation methodology allowed to systematically decode synergistic functionalities between individual protein and miRNA exosome components (see sections 4.4.4.1 and 4.4.4.2). This, in combination with RNA-sequencing-based transcriptome analysis, enabled for an analytical dissection of the associated EV-function mechanisms and provided a versatile framework for innovative EV-therapeutics.

When treated with fsEVs, keratinocyte monolayer showed increased coverage of the cell-free space in *in vitro* wound healing experiments (see 4.4.4.2). Moreover, the same cells also showed increased proliferation rates when treated with fsEVs (4.4.4.1). Therefore, the increased closure of the artificial wound side is not necessarily explained

by increased collective cell migration speed but could be simply explained based on the increased number of cells in the monolayer after treatment. In order to analyse the exact changes in the monolayer migration dynamics, e.g. increased intercellular connectivity (Ollech et al., 2020), changes in leader-cell formation (Vishwakarma et al., 2018) or changes in cell adhesion (Ilina and Friedl, 2009), traction-force-microscopy analysis before, during and after fsEV treatment should be performed. This, in combination with differential regulation of signalling pathways associated with increased collective cell migration observed in the transcriptome analysis, could definitively proof the pro-migratory effect of fsEVs.

Moreover, most of the vesicle characterizations presented in this thesis were based on bulk measurements. In order to analyse the quantitative inter-vesicle variation of fsEVs in size, lipid composition, charge, protein coating or miRNA loading, analysis with single vesicles resolution should be implemented (Kim et al., 2020). Although favourable for several biomedical applications and for approval by regulatory agencies, the fsEV population would not necessarily need to be extremely homogeneous in order to exert a "correct" physiological effect. An intrinsic heterogeneity and variation of specific biological effector molecules is an eminent prerequisite for proper function of several signalling cascades (Altschuler and Wu, 2010). Therefore, a comparable feature-distribution to natural EVs should be programmable when designing fsEVs in order to offer means to accurately mimic disease states. This intercellular variance in fsEV composition could also influence the results presented in Figure 45, where stoichiometric effects of EV-based miRNA delivery were assessed. Such effects have been proposed but the experimental evidence from earlier reports has not been completely conclusive, demonstrating that the complementary fsEV-approach can provide valuable quantitative insights into EV-function (Alexander et al., 2015). However, if large variation in the miRNA content of fsEVs persist, also these results could suffer from inconsistencies originating from the population averaged-based results.

This work also introduces the application of mechanical shear stress-based emulsification of water and oil phases for the creation of water-in-oil droplets. By applying a rotation shaft, a SUV-containing water layer can be mixed with a surfactant containing oil phase in order to create large volumes of dsGUVs within seconds. This method thus provides an industrial-scale production method for fsEVs with dimeters down to approximately 300 nm. In this process, the principles of the charge-mediated dsGUV assembly are fundamentally the same as for the microfluidic-based production, offering

the same degree of control over the chemical and biological fsEV characteristics. However, the advantages of high-throughput bulk assembly, comes to the expense of the w/o-droplet size distribution, where typical preparations will deliver fsEVs with sizes between 50 µm and 300 nm. Therefore, additional purification procedures, like differential centrifugation, need to be applied in order to isolate the fsEVs with dimensions of interest.

Sections 4.4.4.1, 4.4.4.2 and 4.4.4.3 provide clear evidence that wound healing fsEVs trigger very comparable, if not equivalent, cellular responses as their natural blueprints. However, these characterizations should also be directly evaluated in comparison to the performance of natural exosomes which they are inspired from. Thereby, the efficiency of fsEVs for therapeutic applications could be put in better perspective. Moreover, the fsEV wound-healing capabilities have been tested as a proof-of-concept in human organotypic skin models (see section 4.4.5). Although these primary cell-derived 3D tissue-like architectures can accurately recapitulate some key features of human skin (Oh et al., 2013), they do not represent and preserve the full anatomical and physiological characteristics of human wounded skin (e.g. immunological inflammation factors and coagulated blood are not present). Therefore, an increased epidermal wound-healing speed and epithermal thickness of these models does not necessarily imply proper wound healing *restitutio ad integrum* under *in vivo* conditions. Here, many other factors like accurate matrix remodelling and ingrowth of skin associated cell types (e.g. dendritic cells and melanocytes) come into play. Therefore, the therapeutic potential of fsEVs should in future also be evaluated with human skin xenografts before translation into clinical testing.

The fundamental conceptual advantages associated with the employment of fsEV for EV research are highlighted in section 4.5. Here, whole-transcriptome analysis, based on RNA-sequencing is performed on HaCaT keratinocytes treated with fsEVs of varying composition. This assessment revealed some elemental principles on which EV signalling and cargo shuttling relays. First of all, section 4.5.1 shows clear evidence that when presented in their soluble form, the single fsEV constituents alone do not induce transcriptional changes to the same extend as fsEVs do. Rather, the individual components need to be presented to cells in a “vesicular context”. Simply incubating the cells with the soluble miRNA and proteins did not lead to a comparable alteration of the gene expression profiles. This observation may sound trivial in first place but is actually essential for the field of EV research as such an integral behaviour could not be experimentally validated

with natural EVs before. This is mostly due to the current lack of methods which allow to produce EVs with the highest purity, for instance comparable with protein purification methods, and the poor EV-engineering capabilities. The importance of the "vesicular context" therefore provides an experimental proof on why cells employ EV signalling at all: they substantially augment the signalling potential of the associated proteins and nucleic acids! In general, scientific efforts aiming to decipher EV-based signalling currently lack solid and robust biological reasoning on the advantages provided by EV-based intercellular signalling and are mostly based on the observation of academically interesting correlations in the form of: EVs from cell-type A, induce effect B in cells of type C. Therefore, such fundamental assessments are much needed not only in order to justify of the tremendous efforts currently undertaken in EV-research but also to demonstrate to the scientific community that EV account for important intercellular communications phenomena.

Moreover, section 4.5.2 demonstrates how highly-defined fsEVs allow to systematically decode synergistic functionalities between individual EV components, enabling analytical dissection of associated extracellular vesicle signalling. To exemplify this, a differential gene expression and pathway enrichment analysis was performed on keratinocytes treated with fsEV decorated with different tetraspanins and combination of them. Several specific gene sets and pathways were found to be triggered by the individual components. Importantly, it was found that the single tetraspanins on their own did only exert little to no significant differential gene expression. However, when the tetraspanins were presented on the fsEV surface together, large transcriptomic changes were observed. This is on good agreement with the functional assessments performed in section 44.4.4, where combinatorial effects between the tetraspanins were observed. However, this effect was not purely additive, rather synergistic signalling was observed when combining several different tetraspanins. Apparently also for EVs, the whole is more than the sum of its parts.

To describe this effect in greater detail, the influence of single tetraspanins on the assembly of hemidesmosomes was untangled. This specific example was chosen as the hemidesmosome structure is well studied and because hemidesmosomes have a significant impact on wound healing (Garrod and Chidgey, 2008; Hopkinson et al., 2014). By combining the defines of the fsEV technology with RNA-sequencing, the impact of every single tetraspanin present in the fsEVs could be followed on a molecular level, i.e. it could be revealed which hemidesmosome component was down- or upregulated by

which tetraspanin and therefore how they contribute to the increased migration of keratinocytes. In line with these observations, several fsEV triggered pathways could be identified which have previously been associated with proper wound healing and in many cases, like for the regulation of the ornithine decarboxylase pathway, already extensively explored in clinical studies for wound healing therapy (Coudray-Lucas et al., 2000; Shi et al., 2002). This demonstrates that wound-healing fsEVs can induce the intrinsic up-regulation of wound-healing promoting process without the need for pharmacological supplementation or administration of drugs. Rather, the integral biological processes appear to be triggered, thereby potentially rectifying deregulated or dysfunctional intercellular communication in wounds. This in turn, would establish fsEVs as completely new EV-based therapy, where not the pathological effector molecules or proteins themselves are targeted but rather the specific intercellular communication responsible for their regulation the is substituted or mimicked. Moreover, when applying the same experimental concepts to resolve the contribution of miRNAs to the wound-healing effect of the presented fsEVs, it was found that they predominantly trigger processes associated to the citric acid cycle and mitochondrial respiration. This demonstrates that fsEV are capable of transferring regulatory genetic elements which in turn can induce fundamental alteration in the cells´ energy homeostasis. Interestingly, even though five different miRNA mimics were applied in the fsEV formulation, only a small set of DEGs was found. This could point to a rather specific regulatory behaviour, or probably to a more targeted effect of these miRNAs. Taken together, these are important proof-of-concept investigations of how fsEVs can be applied to entangle complexly interwoven problems with high level of complication associated to intercellular signalling.

5.4 Limitations and outlook for the application of fsEVs

In the following I will discuss future research directions and the biomedical potential empowered by the fsEV-related advancements presented in this thesis as well as their current drawbacks and limitations:

FsEVs are almost inter-confusable mimics of natural EVs. In order to replace or even outperform their application in research and in therapeutic settings, they precisely recapitulate the molecular EV composition in a very quantitative manner. However, their molecular design is based on the know EV-composition they are inspired by. It follows, that they can only recapitulate described and known characteristics of EVs. If specific components or functionalities of a specific EV population are unknown or falsified by

impurities, the fsEVs design and application will likely suffer from this. Moreover, the purity, definition and functionality of the fsEVs depends on the purity of their molecular building blocks. Sophisticated *in vitro* synthetises and chromatographic purification methods exists for lipids, nucleic acids and other low-molecular weight components. However, high-grade purification of (recombinant) proteins is challenging, even when applying immune-precipitation or NTA(Ni^{2+}) columns. Therefore, the purity of the fsEVs will always be limited by the purity of the proteins applied. However, it also needs to be considered that the purity of such proteins is still orders of magnitude higher than that of EV preparations form cells. Moreover, this can be overcome in future by employment of synthetic peptides which harbour relevant tetraspanin (or other EV proteins) sequences. When employing recombinant expressed proteins, the fsEV functionality will also depend on the correct post-translational modification of these proteins. For instance, correct glycosylation of the tetraspanins appears to be of major important for their signalling capabilities. Therefore, the fsEVs functionalities and signalling capabilities could be falsified compared to their natural blueprints when employing recombinant proteins.

Even though the RNA-sequencing analysis as well as the functional assessment of fsEV treatment show substantial effects on keratinocyte and fibroblast physiology, the exact mechanisms by which for instance the tetraspanin components exert their function remain unknown. It is generally surprising that tetraspanins themselves have signalling capability when immobilized on a vesicular membrane. So far, they have mostly been considered as scaffolding elements which direct microdomain formation of proteins which reside in the same membrane layer. No direct experimental evidence has been presented which demonstrates “trans” acting tetraspanin signalling, i.e. binding of a tetraspanin embedded in one membrane (e.g. in a vesicle) to a receptor embedded in another membrane (e.g. in the target cell plasma membrane). The lack of such examples does of course not rule out the possibly of an interaction. However, respective receptors or binding partners will need to be uncovered in further investigations.

Nonetheless, fsEV provide well-controlled minimalistic models to study fundamental biophysical phenomena underlying EV-signalling. As they are not subjected to natural intrinsic fluctuations like cell-derived EVs and comprise a higher purity, fsEVs could provide a more secure therapy option in future. Moreover, “hybrid” vesicles, which are inspired by EVs released from different cell types under different conditions (e.g. immunological EVs released during inflammation and fibrocyte EVs released during wound-healing), can be created, combining several properties and functionalities of

interest in one single fsEV chassis. Additionally, non-natural therapeutic or diagnostic constituents, like radioactive probes, tracers or drugs can be easily engineered into the fsEVs.

In conclusion, the achievements presented in this thesis represent a major milestone for the field of bottom-up synthetic biology, opening doors for new approaches in applied and fundamental research. The design and assembly of fully-synthetic functional EVs, mimicking physiological functionality of natural EVs, was demonstrated using a complementary synthetic approach. Looking towards the clinical applications of fsEVs, I have identified key EV miRNA and protein compositions at a quantitative level, which in many ways overcome the technological challenges related to EV isolation and purification from living cells. The presented engineering strategies, based on charge-mediated assembly of dsGUVs, allow for the production of functional EVs based on bio-inspired blueprints and may move the boundaries of EV therapy beyond the limits of bio-derived EVs. More broadly speaking, this technology will potentially bring forward an entirely new class of therapeutics based on merging synthetic, life-like assemblies and living systems. This could include the installation of modular production pipelines which combine different microfluidic elements to enable rational structuring of functional fsEVs from standardized synthetic units. Such platforms could then empower the accurate and quantitative exploration of the principal biophysical mechanisms underlying EV-based intercellular signalling.

6 References

- Abri Aghdam, M., Bagheri, R., Mosafer, J., Baradaran, B., Hashemzaei, M., Baghbanzadeh, A., de la Guardia, M., and Mokhtarzadeh, A. (2019). Recent advances on thermosensitive and pH-sensitive liposomes employed in controlled release. Journal of Controlled Release *315*, 1-22.
- Adamala, K.P., Martin-Alarcon, D.A., Guthrie-Honea, K.R., and Boyden, E.S. (2017). Engineering genetic circuit interactions within and between synthetic minimal cells. Nature Chemistry *9*, 431-439.
- Aiello, S., Rocchetta, F., Longaretti, L., Faravelli, S., Todeschini, M., Cassis, L., Pezzuto, F., Tomasoni, S., Azzollini, N., Mister, M.*, et al.* (2017). Extracellular vesicles derived from T regulatory cells suppress T cell proliferation and prolong allograft survival. Scientific reports *7*, 11518.
- Alexander, M., Hu, R., Runtsch, M.C., Kagele, D.A., Mosbruger, T.L., Tolmachova, T., Seabra, M.C., Round, J.L., Ward, D.M., and O'Connell, R.M. (2015). Exosome-delivered microRNAs modulate the inflammatory response to endotoxin. Nature communications *6*, 7321.
- Altschuler, S.J., and Wu, L.F. (2010). Cellular heterogeneity: do differences make a difference? Cell *141*, 559-563.
- Aminzadeh, M.A., Rogers, R.G., Fournier, M., Tobin, R.E., Guan, X., Childers, M.K., Andres, A.M., Taylor, D.J., Ibrahim, A., Ding, X.*, et al.* (2018). Exosome-Mediated Benefits of Cell Therapy in Mouse and Human Models of Duchenne Muscular Dystrophy. Stem Cell Reports *10*, 942-955.
- Audouy, S.A.L., de Leij, L.F.M.H., Hoekstra, D., and Molema, G. (2002). In Vivo Characteristics of Cationic Liposomes as Delivery Vectors for Gene Therapy. Pharmaceutical Research *19*, 1599-1605.
- Badiee, A., Khamesipour, A., Samiei, A., Soroush, D., Shargh, V.H., Kheiri, M.T., Barkhordari, F., Robert Mc Master, W., Mahboudi, F., and Jaafari, M.R. (2012). The role of liposome size on the type of immune response induced in BALB/c mice against leishmaniasis: rgp63 as a model antigen. Experimental Parasitology *132*, 403-409.
- Bailey, A.L., and Cullis, P.R. (1997). Membrane fusion with cationic liposomes: effects of target membrane lipid composition. Biochemistry *36*, 1628-1634.

- Baret, J.-C. (2012). Surfactants in droplet-based microfluidics. Lab on a Chip *12*, 422-433.
- Belardi, B., Son, S., Vahey, M.D., Wang, J., Hou, J., and Fletcher, D.A. (2019). Claudin-4 reconstituted in unilamellar vesicles is sufficient to form tight interfaces that partition membrane proteins. Journal of Cell Science *132*, jcs221556.
- Benner, S.A. (2010). Defining life. Astrobiology *10*, 1021-1030.
- Biner, O., Schick, T., Ganguin, A.A., and von Ballmoos, C. (2018). Towards a Synthetic Mitochondrion. Chimia (Aarau) *72*, 291-296.
- Blondeau, M., Guyodo, Y., Guyot, F., Gatel, C., Menguy, N., Chebbi, I., Haye, B., Durand-Dubief, M., Alphandery, E., Brayner, R.*, et al.* (2018). Magnetic-field induced rotation of magnetosome chains in silicified magnetotactic bacteria. Sci Rep *8*, 7699.
- Boeynaems, S., Alberti, S., Fawzi, N.L., Mittag, T., Polymenidou, M., Rousseau, F., Schymkowitz, J., Shorter, J., Wolozin, B., Van Den Bosch, L.*, et al.* (2018). Protein Phase Separation: A New Phase in Cell Biology. Trends in Cell Biology *28*, 420-435.
- Bolukbasi, M.F., Mizrak, A., Ozdener, G.B., Madlener, S., Ströbel, T., Erkan, E.P., Fan, J.B., Breakefield, X.O., and Saydam, O. (2012). miR-1289 and "Zipcode"-like Sequence Enrich mRNAs in Microvesicles. Mol Ther Nucleic Acids *1*, e10.
- Boukamp, P., Petrussevska, R.T., Breitkreutz, D., Hornung, J., Markham, A., and Fusenig, N.E. (1988). Normal keratinization in a spontaneously immortalized aneuploid human keratinocyte cell line. J Cell Biol *106*, 761-771.
- Buschow, S.I., Liefhebber, J.M., Wubbolts, R., and Stoorvogel, W. (2005). Exosomes contain ubiquitinated proteins. Blood Cells Mol Dis *35*, 398-403.
- Carstens, M.G., Camps, M.G.M., Henriksen-Lacey, M., Franken, K., Ottenhoff, T.H.M., Perrie, Y., Bouwstra, J.A., Ossendorp, F., and Jiskoot, W. (2011). Effect of vesicle size on tissue localization and immunogenicity of liposomal DNA vaccines. Vaccine *29*, 4761-4770.
- Carugo, D., Bottaro, E., Owen, J., Stride, E., and Nastruzzi, C. (2016). Liposome production by microfluidics: potential and limiting factors. Sci Rep *6*, 25876.
- Cavalcanti, R.R.M., Lira, R.B., and Riske, K.A. (2018). Study of the Fusion Mechanism of Fusogenic Cationic Liposomes with Anionic Model Membranes. Biophysical Journal *114*, 606a.

- Chang, H.I., and Yeh, M.K. (2012). Clinical development of liposome-based drugs: formulation, characterization, and therapeutic efficacy. Int J Nanomedicine *7*, 49-60.
- Chebotar, I.V., Konchakova, E.D., and Maianskii, A.N. (2013). Vesicle formation as a result of interaction between polymorphonuclear neutrophils and Staphylococcus aureus biofilm. J Med Microbiol *62*, 1153-1159.
- Colletier, J.-P., Chaize, B., Winterhalter, M., and Fournier, D. (2002). Protein encapsulation in liposomes: efficiency depends on interactions between protein and phospholipid bilayer. BMC Biotechnology *2*, 9.
- Corbo, C., Molinaro, R., Taraballi, F., Toledano Furman, N.E., Sherman, M.B., Parodi, A., Salvatore, F., and Tasciotti, E. (2016). Effects of the protein corona on liposome-liposome and liposome-cell interactions. In International Journal of Nanomedicine, pp. 3049-3063.
- Cortesi, R., Esposito, E., Menegatti, E., Gambari, R., and Nastruzzi, C. (1996). Effect of cationic liposome composition on in vitro cytotoxicity and protective effect on carried DNA. International Journal of Pharmaceutics *139*, 69-78.
- Coudray-Lucas, C., Le Bever, H., Cynober, L., De Bandt, J.P., and Carsin, H. (2000). Ornithine alpha-ketoglutarate improves wound healing in severe burn patients: a prospective randomized double-blind trial versus isonitrogenous controls. Crit Care Med *28*, 1772-1776.
- Cruje, C., and Chithrani, D.B. (2014). Polyethylene Glycol Functionalized Nanoparticles for Improved Cancer Treatment. Reviews in Nanoscience and Nanotechnology *3*, 20-30.
- Cruz, L., Romero, J.A.A., Iglesia, R.P., and Lopes, M.H. (2018). Extracellular Vesicles: Decoding a New Language for Cellular Communication in Early Embryonic Development. Frontiers in cell and developmental biology *6*, 94.
- Damodaran, V.B., Fee, C.J., Ruckh, T., and Popat, K.C. (2010). Conformational studies of covalently grafted poly(ethylene glycol) on modified solid matrices using X-ray photoelectron spectroscopy. Langmuir *26*, 7299-7306.
- Debats, I.B.J.G., Deutz, N.E.P., Vd Hogen, E., Boeckx, W.D., and Vd Hulst, R.R.W. (2003). Ornithine pathway stimulated in human wound healing during arginine suppletion. Clinical Nutrition *22*, S30.

- Del Conde, I., Shrimpton, C.N., Thiagarajan, P., and Lopez, J.A. (2005). Tissue-factor-bearing microvesicles arise from lipid rafts and fuse with activated platelets to initiate coagulation. Blood *106*, 1604-1611.
- Deng, N.-N., Vibhute, M.A., Zheng, L., Zhao, H., Yelleswarapu, M., and Huck, W.T.S. (2018). Macromolecularly Crowded Protocells from Reversibly Shrinking Monodisperse Liposomes. Journal of the American Chemical Society *140*, 7399-7402.
- Deshpande, P.P., Biswas, S., and Torchilin, V.P. (2013). Current trends in the use of liposomes for tumor targeting. Nanomedicine (Lond) *8*, 1509-1528.
- Deshpande, S., Caspi, Y., Meijering, A.E.C., and Dekker, C. (2016). Octanol-assisted liposome assembly on chip. Nature Communications *7*, 10447.
- Dezi, M., Di Cicco, A., Bassereau, P., and Lévy, D. (2013). Detergent-mediated incorporation of transmembrane proteins in giant unilamellar vesicles with controlled physiological contents. Proceedings of the National Academy of Sciences *110*, 7276-7281.
- Di Bonito, P., Chiozzini, C., Arenaccio, C., Anticoli, S., Manfredi, F., Olivetta, E., Ferrantelli, F., Falcone, E., Ruggieri, A., and Federico, M. (2017). Antitumor HPV E7-specific CTL activity elicited by in vivo engineered exosomes produced through DNA inoculation. Int J Nanomedicine *12*, 4579-4591.
- Dioufa, N., Schally, A.V., Chatzistamou, I., Moustou, E., Block, N.L., Owens, G.K., Papavassiliou, A.G., and Kiaris, H. (2010). Acceleration of wound healing by growth hormone-releasing hormone and its agonists. Proc Natl Acad Sci U S A *107*, 18611-18615.
- Draffehn, S., and Kumke, M.U. (2016). Monitoring the Collapse of pH-Sensitive Liposomal Nanocarriers and Environmental pH Simultaneously: A Fluorescence-Based Approach. Molecular Pharmaceutics *13*, 1608-1617.
- Einfalt, T., Witzigmann, D., Edlinger, C., Sieber, S., Goers, R., Najer, A., Spulber, M., Onaca-Fischer, O., Huwyler, J., and Palivan, C.G. (2018). Biomimetic artificial organelles with in vitro and in vivo activity triggered by reduction in microenvironment. Nat Commun *9*, 1127.
- El Andaloussi, S., Mäger, I., Breakefield, X.O., and Wood, M.J.A. (2013). Extracellular vesicles: biology and emerging therapeutic opportunities. Nature Reviews Drug Discovery *12*, 347.

- El-Sayed, A., Futaki, S., and Harashima, H. (2009). Delivery of macromolecules using arginine-rich cell-penetrating peptides: ways to overcome endosomal entrapment. Aaps j *11*, 13-22.
- Elkin, S.R., Bendris, N., Reis, C.R., Zhou, Y., Xie, Y., Huffman, K.E., Minna, J.D., and Schmid, S.L. (2015). A systematic analysis reveals heterogeneous changes in the endocytic activities of cancer cells. Cancer research *75*, 4640-4650.
- Fearnley, C.J., Roderick, H.L., and Bootman, M.D. (2011). Calcium signaling in cardiac myocytes. Cold Spring Harb Perspect Biol *3*, a004242.
- Fernando, M.R., Jiang, C., Krzyzanowski, G.D., and Ryan, W.L. (2017). New evidence that a large proportion of human blood plasma cell-free DNA is localized in exosomes. PLoS One *12*, e0183915.
- Finetti, F., Cassioli, C., and Baldari, C.T. (2017). Transcellular communication at the immunological synapse: a vesicular traffic-mediated mutual exchange. F1000Res *6*, 1880.
- Frey, C., Göpfrich, K., Pashapour, S., Platzman, I., and Spatz, J.P. (2020). Electrocoalescence of Water-in-Oil Droplets with a Continuous Aqueous Phase: Implementation of Controlled Content Release. ACS Omega *5*, 7529-7536.
- Friend, J., and Yeo, L. (2010). Fabrication of microfluidic devices using polydimethylsiloxane. Biomicrofluidics *4*, 026502.
- Fujii, T. (2002). PDMS-based microfluidic devices for biomedical applications. Microelectronic Engineering *61-62*, 907-914.
- Fuqua, W.C., Winans, S.C., and Greenberg, E.P. (1994). Quorum sensing in bacteria: the LuxR-LuxI family of cell density-responsive transcriptional regulators. J Bacteriol *176*, 269-275.
- Garcia-Manrique, P., Gutierrez, G., and Blanco-Lopez, M.C. (2018). Fully Artificial Exosomes: Towards New Theranostic Biomaterials. Trends Biotechnol *36*, 10-14.
- Garrod, D., and Chidgey, M. (2008). Desmosome structure, composition and function. Biochimica et Biophysica Acta (BBA) - Biomembranes *1778*, 572-587.
- Geiger, A., Walker, A., and Nissen, E. (2015a). Human fibrocyte-derived exosomes accelerate wound healing in genetically diabetic mice. Biochem Biophys Res Commun *467*, 303-309.

- Geiger, A., Walker, A., and Nissen, E. (2015b). Human fibrocyte-derived exosomes accelerate wound healing in genetically diabetic mice. Biochemical and Biophysical Research Communications *467*, 303-309.
- Geminard, C., De Gassart, A., Blanc, L., and Vidal, M. (2004). Degradation of AP2 during reticulocyte maturation enhances binding of hsc70 and Alix to a common site on TFR for sorting into exosomes. Traffic *5*, 181-193.
- Gibbings, D.J., Ciaudo, C., Erhardt, M., and Voinnet, O. (2009). Multivesicular bodies associate with components of miRNA effector complexes and modulate miRNA activity. Nat Cell Biol *11*, 1143-1149.
- Gilbert, D.F., Erdmann, G., Zhang, X., Fritzsche, A., Demir, K., Jaedicke, A., Muehlenberg, K., Wanker, E.E., and Boutros, M. (2011). A novel multiplex cell viability assay for high-throughput RNAi screening. PLoS One *6*, e28338.
- Gonzalez Gomez, A., Syed, S., Marshall, K., and Hosseinidoust, Z. (2019). Liposomal Nanovesicles for Efficient Encapsulation of Staphylococcal Antibiotics. ACS Omega *4*, 10866-10876.
- Gopfrich, K., Platzman, I., and Spatz, J.P. (2018). Mastering Complexity: Towards Bottom-up Construction of Multifunctional Eukaryotic Synthetic Cells. Trends Biotechnol *36*, 938-951.
- Göpfrich, K., Haller, B., Staufer, O., Dreher, Y., Mersdorf, U., Platzman, I., and Spatz, J.P. (2019). One-pot assembly of complex giant unilamellar vesicle-based synthetic cells. ACS Synthetic Biology.
- Haller, B., Gopfrich, K., Schroter, M., Janiesch, J.W., Platzman, I., and Spatz, J.P. (2018). Charge-controlled microfluidic formation of lipid-based single- and multicompartment systems. Lab Chip *18*, 2665-2674.
- Halvaei, S., Daryani, S., Eslami, S.Z., Samadi, T., Jafarbeik-Iravani, N., Bakhshayesh, T.O., Majidzadeh, A.K., and Esmaeili, R. (2018). Exosomes in Cancer Liquid Biopsy: A Focus on Breast Cancer. Mol Ther Nucleic Acids *10*, 131-141.
- Hansen, M.M.K., Meijer, L.H.H., Spruijt, E., Maas, R.J.M., Rosquelles, M.V., Groen, J., Heus, H.A., and Huck, W.T.S. (2016). Macromolecular crowding creates heterogeneous environments of gene expression in picolitre droplets. Nature Nanotechnology *11*, 191-197.
- Harding, C.V., Heuser, J.E., and Stahl, P.D. (2013). Exosomes: looking back three decades and into the future. J Cell Biol *200*, 367-371.

- Has, C., and Sunthar, P. (2019). A comprehensive review on recent preparation techniques of liposomes. J Liposome Res, 1-30.
- He, F., Liu, H., Guo, X., Yin, B.C., and Ye, B.C. (2017). Direct Exosome Quantification via Bivalent-Cholesterol-Labeled DNA Anchor for Signal Amplification. Anal Chem *89*, 12968-12975.
- Heath, T.D., Montgomery, J.A., Piper, J.R., and Papahadjopoulos, D. (1983). Antibody-targeted liposomes: increase in specific toxicity of methotrexate-gamma-aspartate. Proc Natl Acad Sci U S A *80*, 1377-1381.
- Hikita, T., Miyata, M., Watanabe, R., and Oneyama, C. (2018). Sensitive and rapid quantification of exosomes by fusing luciferase to exosome marker proteins. Scientific Reports *8*, 14035.
- Hillaireau, H., and Couvreur, P. (2009). Nanocarriers' entry into the cell: relevance to drug delivery. Cell Mol Life Sci *66*, 2873-2896.
- Hopkinson, S.B., Hamill, K.J., Wu, Y., Eisenberg, J.L., Hiroyasu, S., and Jones, J.C.R. (2014). Focal Contact and Hemidesmosomal Proteins in Keratinocyte Migration and Wound Repair. Advances in wound care *3*, 247-263.
- Huebner, S., Battersby, B.J., Grimm, R., and Cevc, G. (1999). Lipid-DNA Complex Formation: Reorganization and Rupture of Lipid Vesicles in the Presence of DNA As Observed by Cryoelectron Microscopy. Biophysical Journal *76*, 3158-3166.
- Hurley, J.H. (2008). ESCRT complexes and the biogenesis of multivesicular bodies. Curr Opin Cell Biol *20*, 4-11.
- Ilina, O., and Friedl, P. (2009). Mechanisms of collective cell migration at a glance. Journal of Cell Science *122*, 3203-3208.
- Immordino, M.L., Dosio, F., and Cattel, L. (2006). Stealth liposomes: review of the basic science, rationale, and clinical applications, existing and potential. Int J Nanomedicine *1*, 297-315.
- Irion, U., and St Johnston, D. (2007). bicoid RNA localization requires specific binding of an endosomal sorting complex. Nature *445*, 554-558.
- Ishida, T., Harashima, H., and Kiwada, H. (2002). Liposome clearance. Biosci Rep *22*, 197-224.
- Jang, S.C., Kim, O.Y., Yoon, C.M., Choi, D.S., Roh, T.Y., Park, J., Nilsson, J., Lotvall, J., Kim, Y.K., and Gho, Y.S. (2013). Bioinspired exosome-mimetic

nanovesicles for targeted delivery of chemotherapeutics to malignant tumors. ACS Nano *7*, 7698-7710.

- Janiesch, J.W., Weiss, M., Kannenberg, G., Hannabuss, J., Surrey, T., Platzman, I., and Spatz, J.P. (2015). Key factors for stable retention of fluorophores and labeled biomolecules in droplet-based microfluidics. Anal Chem *87*, 2063-2067.
- Jassal, B., Matthews, L., Viteri, G., Gong, C., Lorente, P., Fabregat, A., Sidiropoulos, K., Cook, J., Gillespie, M., Haw, R.*, et al.* (2020). The reactome pathway knowledgebase. Nucleic Acids Res *48*, D498-d503.
- Jenkins, E., Santos, A.M., O'Brien-Ball, C., Felce, J.H., Wilcock, M.J., Hatherley, D., Dustin, M.L., Davis, S.J., Eggeling, C., and Sezgin, E. (2018). Reconstitution of immune cell interactions in free-standing membranes. J Cell Sci *132*.
- Jia, H., and Schwille, P. (2019). Bottom-up synthetic biology: reconstitution in space and time. Curr Opin Biotechnol *60*, 179-187.
- Jo, W., Jeong, D., Kim, J., Cho, S., Jang, S.C., Han, C., Kang, J.Y., Gho, Y.S., and Park, J. (2014). Microfluidic fabrication of cell-derived nanovesicles as endogenous RNA carriers. Lab Chip *14*, 1261-1269.
- Johnsen, K.B., Gudbergsson, J.M., Skov, M.N., Pilgaard, L., Moos, T., and Duroux, M. (2014). A comprehensive overview of exosomes as drug delivery vehicles - endogenous nanocarriers for targeted cancer therapy. Biochim Biophys Acta *1846*, 75-87.
- Juliano, R.L., and Stamp, D. (1975). The effect of particle size and charge on the clearance rates of liposomes and liposome encapsulated drugs. Biochemical and Biophysical Research Communications *63*, 651-658.
- Kalluri, R., and LeBleu, V.S. (2020). The biology, function, and biomedical applications of exosomes. Science *367*.
- Karamdad, K., Law, R.V., Seddon, J.M., Brooks, N.J., and Ces, O. (2015). Preparation and mechanical characterisation of giant unilamellar vesicles by a microfluidic method. Lab Chip *15*, 557-562.
- Kaufmann, S., Borisov, O., Textor, M., and Reimhult, E. (2011). Mechanical properties of mushroom and brush poly(ethylene glycol)-phospholipid membranes. Soft Matter *7*, 9267-9275.
- Kern, A.D., Oliveira, M.A., Coffino, P., and Hackert, M.L. (1999). Structure of mammalian ornithine decarboxylase at 1.6 Å resolution: stereochemical implications of PLP-dependent amino acid decarboxylases. Structure *7*, 567-581.

- Kim, D., Woo, H.-K., Lee, C., Min, Y., Kumar, S., Sunkara, V., Jo, H.-G., Lee, Y.J., Kim, J., Ha, H.K.*, et al.* (2020). EV-Ident: Identifying Tumor-Specific Extracellular Vesicles by Size Fractionation and Single-Vesicle Analysis. Analytical Chemistry.
- Kliesch, T.-T., Dietz, J., Turco, L., Halder, P., Polo, E., Tarantola, M., Jahn, R., and Janshoff, A. (2017). Membrane tension increases fusion efficiency of model membranes in the presence of SNAREs. Scientific reports *7*, 12070-12070.
- Knecht, E., Hernandez-Yago, J., and Grisolia, S. (1984). Regulation of lysosomal autophagy in transformed and non-transformed mouse fibroblasts under several growth conditions. Experimental cell research *154*, 224-232.
- Knudsen, K.B., Northeved, H., Kumar, P.E., Permin, A., Gjetting, T., Andresen, T.L., Larsen, S., Wegener, K.M., Lykkesfeldt, J., Jantzen, K.*, et al.* (2015). In vivo toxicity of cationic micelles and liposomes. Nanomedicine *11*, 467-477.
- Kress, G.J., and Mennerick, S. (2009). Action potential initiation and propagation: upstream influences on neurotransmission. Neuroscience *158*, 211-222.
- Kriebel, P.W., Majumdar, R., Jenkins, L.M., Senoo, H., Wang, W., Ammu, S., Chen, S., Narayan, K., Iijima, M., and Parent, C.A. (2018). Extracellular vesicles direct migration by synthesizing and releasing chemotactic signals. J Cell Biol *217*, 2891-2910.
- Krinsky, N., Kaduri, M., Zinger, A., Shainsky-Roitman, J., Goldfeder, M., Benhar, I., Hershkovitz, D., and Schroeder, A. (2018). Synthetic Cells Synthesize Therapeutic Proteins inside Tumors. Adv Healthc Mater *7*, e1701163.
- Kruk, J., and Duchnik, E. (2014). Oxidative stress and skin diseases: possible role of physical activity. Asian Pac J Cancer Prev *15*, 561-568.
- Lachmann, P.J. (2009). The amplification loop of the complement pathways. Adv Immunol *104*, 115-149.
- Laemmli, U.K. (1970). Cleavage of structural proteins during the assembly of the head of bacteriophage T4. Nature *227*, 680-685.
- Lakhal, S., and Wood, M.J.A. (2011). Intranasal Exosomes for Treatment of Neuroinflammation?: Prospects and Limitations. Mol Ther *19*, 1754-1756.
- Lankford, K.L., Arroyo, E.J., Nazimek, K., Bryniarski, K., Askenase, P.W., and Kocsis, J.D. (2018). Intravenously delivered mesenchymal stem cell-derived exosomes target M2-type macrophages in the injured spinal cord. PLoS One *13*, e0190358.

- Lee, B.R., Kim, J.H., Choi, E.S., Cho, J.H., and Kim, E. (2018a). Effect of young exosomes injected in aged mice. Int J Nanomedicine *13*, 5335-5345.
- Lee, K.Y., Park, S.J., Lee, K.A., Kim, S.H., Kim, H., Meroz, Y., Mahadevan, L., Jung, K.H., Ahn, T.K., Parker, K.K.*, et al.* (2018b). Photosynthetic artificial organelles sustain and control ATP-dependent reactions in a protocellular system. Nat Biotechnol *36*, 530-535.
- Levin, M. (2019). The Computational Boundary of a "Self": Developmental Bioelectricity Drives Multicellularity and Scale-Free Cognition. Frontiers in Psychology *10*.
- Li, B., Antonyak, M.A., Zhang, J., and Cerione, R.A. (2012). RhoA triggers a specific signaling pathway that generates transforming microvesicles in cancer cells. Oncogene *31*, 4740-4749.
- Li, M., Zeringer, E., Barta, T., Schageman, J., Cheng, A., and Vlassov, A.V. (2014). Analysis of the RNA content of the exosomes derived from blood serum and urine and its potential as biomarkers. Philosophical Transactions of the Royal Society B: Biological Sciences *369*.
- Litzinger, D.C., Buiting, A.M.J., van Rooijen, N., and Huang, L. (1994). Effect of liposome size on the circulation time and intraorgan distribution of amphipathic poly(ethylene glycol)-containing liposomes. Biochimica et Biophysica Acta (BBA) - Biomembranes *1190*, 99-107.
- Liu, C., and Su, C. (2019). Design strategies and application progress of therapeutic exosomes. Theranostics *9*, 1015-1028.
- Liu, D., Mori, A., and Huang, L. (1992). Role of liposome size and RES blockade in controlling biodistribution and tumor uptake of GM1-containing liposomes. Biochim Biophys Acta *1104*, 95-101.
- Loor, G., Kondapalli, J., Schriewer, J.M., Chandel, N.S., Vanden Hoek, T.L., and Schumacker, P.T. (2010). Menadione triggers cell death through ROS-dependent mechanisms involving PARP activation without requiring apoptosis. Free Radic Biol Med *49*, 1925-1936.
- Luhtala, N., Aslanian, A., Yates, J.R., 3rd, and Hunter, T. (2017). Secreted Glioblastoma Nanovesicles Contain Intracellular Signaling Proteins and Active Ras Incorporated in a Farnesylation-dependent Manner. J Biol Chem *292*, 611-628.

- Majumder, S., and Liu, A.P. (2017). Bottom-up synthetic biology: modular design for making artificial platelets. Phys Biol *15*, 013001.
- Martin, W.F., Garg, S., and Zimorski, V. (2015). Endosymbiotic theories for eukaryote origin. Philosophical Transactions of the Royal Society B: Biological Sciences *370*, 20140330.
- Mateescu, B., Kowal, E.J., van Balkom, B.W., Bartel, S., Bhattacharyya, S.N., Buzas, E.I., Buck, A.H., de Candia, P., Chow, F.W., Das, S., *et al.* (2017). Obstacles and opportunities in the functional analysis of extracellular vesicle RNA - an ISEV position paper. J Extracell Vesicles *6*, 1286095.
- Matsumura, S., Minamisawa, T., Suga, K., Kishita, H., Akagi, T., Ichiki, T., Ichikawa, Y., and Shiba, K. (2019). Subtypes of tumour cell-derived small extracellular vesicles having differently externalized phosphatidylserine. J Extracell Vesicles *8*, 1579541.
- McConnell, R.E., Higginbotham, J.N., Shifrin, D.A., Jr., Tabb, D.L., Coffey, R.J., and Tyska, M.J. (2009). The enterocyte microvillus is a vesicle-generating organelle. J Cell Biol *185*, 1285-1298.
- Meleard, P., Bagatolli, L.A., and Pott, T. (2009). Giant unilamellar vesicle electroformation from lipid mixtures to native membranes under physiological conditions. Methods Enzymol *465*, 161-176.
- Michael, A., Bajracharya, S., Yuen, P., Zhou, H., Star, R., Illei, G., and Alevizos, I. (2010). Exosomes from human saliva as a source of microRNA biomarkers. Oral Diseases *16*, 34-38.
- Missirlis, D., Haraszti, T., Scheele, C., Wiegand, T., Diaz, C., Neubauer, S., Rechenmacher, F., Kessler, H., and Spatz, J.P. (2016). Substrate engagement of integrins alpha5beta1 and alphavbeta3 is necessary, but not sufficient, for high directional persistence in migration on fibronectin. Scientific reports *6*, 23258.
- Moga, A., Yandrapalli, N., Dimova, R., and Robinson, T. (2019). Optimization of the Inverted Emulsion Method for High-Yield Production of Biomimetic Giant Unilamellar Vesicles. Chembiochem *20*, 2674-2682.
- Mohamed, M., Abu Lila, A.S., Shimizu, T., Alaaeldin, E., Hussein, A., Sarhan, H.A., Szebeni, J., and Ishida, T. (2019). PEGylated liposomes: immunological responses. Sci Technol Adv Mater *20*, 710-724.
- Mok, K.W., and Cullis, P.R. (1997). Structural and fusogenic properties of cationic liposomes in the presence of plasmid DNA. Biophysical journal *73*, 2534-2545.

- Muntasell, A., Berger, A.C., and Roche, P.A. (2007). T cell-induced secretion of MHC class II-peptide complexes on B cell exosomes. Embo j *26*, 4263-4272.
- Nakase, I., Kogure, K., Harashima, H., and Futaki, S. (2011). Application of a fusiogenic peptide GALA for intracellular delivery. Methods Mol Biol *683*, 525-533.
- Niehage, C., Stange, C., Anitei, M., and Hoflack, B. (2014). Liposome-based assays to study membrane-associated protein networks. Methods Enzymol *534*, 223-243.
- Nielsen, M.S., Axelsen, L.N., Sorgen, P.L., Verma, V., Delmar, M., and Holstein-Rathlou, N.H. (2012). Gap junctions. Compr Physiol *2*, 1981-2035.
- Nightingale, A.M., Leong, C.L., Burnish, R.A., Hassan, S.-u., Zhang, Y., Clough, G.F., Boutelle, M.G., Voegeli, D., and Niu, X. (2019). Monitoring biomolecule concentrations in tissue using a wearable droplet microfluidic-based sensor. Nature Communications *10*, 2741.
- Nolte-'t Hoen, E., Cremer, T., Gallo, R.C., and Margolis, L.B. (2016). Extracellular vesicles and viruses: Are they close relatives? Proc Natl Acad Sci U S A *113*, 9155-9161.
- Oh, J.W., Hsi, T.-C., Guerrero-Juarez, C.F., Ramos, R., and Plikus, M.V. (2013). Organotypic skin culture. The Journal of investigative dermatology *133*, 1-4.
- Ollech, D., Pflästerer, T., Shellard, A., Zambarda, C., Spatz, J.P., Marcq, P., Mayor, R., Wombacher, R., and Cavalcanti-Adam, E.A. (2020). An optochemical tool for light-induced dissociation of adherens junctions to control mechanical coupling between cells. Nature Communications *11*, 472.
- Osteikoetxea, X., Balogh, A., Szabó-Taylor, K., Németh, A., Szabó, T.G., Pálóczi, K., Sódar, B., Kittel, Á., György, B., Pállinger, É*., et al.* (2015). Improved characterization of EV preparations based on protein to lipid ratio and lipid properties. PloS one *10*, e0121184.
- Overland, J., Hodge, J.C., Breik, O., and Krishnan, S. (2016). Surgical anatomy of the spinal accessory nerve: review of the literature and case report of a rare anatomical variant. J Laryngol Otol *130*, 969-972.
- Pang, B., Zhu, Y., Ni, J., Thompson, J., Malouf, D., Bucci, J., Graham, P., and Li, Y. (2020). Extracellular vesicles: the next generation of biomarkers for liquid biopsy-based prostate cancer diagnosis. Theranostics *10*, 2309-2326.

- Patel, G.K., Khan, M.A., Zubair, H., Srivastava, S.K., Khushman, M.d., Singh, S., and Singh, A.P. (2019a). Comparative analysis of exosome isolation methods using culture supernatant for optimum yield, purity and downstream applications. Scientific Reports *9*, 5335.
- Patel, S., Ryals, R.C., Weller, K.K., Pennesi, M.E., and Sahay, G. (2019b). Lipid nanoparticles for delivery of messenger RNA to the back of the eye. J Control Release *303*, 91-100.
- Pathan, M., Keerthikumar, S., Chisanga, D., Alessandro, R., Ang, C.S., Askenase, P., Batagov, A.O., Benito-Martin, A., Camussi, G., Clayton, A.*, et al.* (2017). A novel community driven software for functional enrichment analysis of extracellular vesicles data. J Extracell Vesicles *6*, 1321455.
- Perez-Hernandez, D., Gutierrez-Vazquez, C., Jorge, I., Lopez-Martin, S., Ursa, A., Sanchez-Madrid, F., Vazquez, J., and Yanez-Mo, M. (2013). The intracellular interactome of tetraspanin-enriched microdomains reveals their function as sorting machineries toward exosomes. J Biol Chem *288*, 11649-11661.
- Perry, J.L., Reuter, K.G., Kai, M.P., Herlihy, K.P., Jones, S.W., Luft, J.C., Napier, M., Bear, J.E., and DeSimone, J.M. (2012). PEGylated PRINT Nanoparticles: The Impact of PEG Density on Protein Binding, Macrophage Association, Biodistribution, and Pharmacokinetics. Nano Letters *12*, 5304-5310.
- Petrie, R.J., and Yamada, K.M. (2015). Fibroblasts Lead the Way: A Unified View of 3D Cell Motility. Trends Cell Biol *25*, 666-674.
- Piccin, A., Murphy, W.G., and Smith, O.P. (2007). Circulating microparticles: pathophysiology and clinical implications. Blood Rev *21*, 157-171.
- Platkiewicz, J., and Brette, R. (2010). A threshold equation for action potential initiation. PLoS Comput Biol *6*, e1000850.
- Pomatto, M.A.C., Bussolati, B., D'Antico, S., Ghiotto, S., Tetta, C., Brizzi, M.F., and Camussi, G. (2019). Improved Loading of Plasma-Derived Extracellular Vesicles to Encapsulate Antitumor miRNAs. Mol Ther Methods Clin Dev *13*, 133-144.
- Quan, P.L., Sauzade, M., and Brouzes, E. (2018). dPCR: A Technology Review. Sensors (Basel) *18*.
- Raffa, V., Falcone, F., De Vincentiis, S., Falconieri, A., Calatayud, M.P., Goya, G.F., and Cuschieri, A. (2018). Piconewton Mechanical Forces Promote Neurite Growth. Biophys J *115*, 2026-2033.

- Rauch, I., Müller, M., and Decker, T. (2013). The regulation of inflammation by interferons and their STATs. Jakstat *2*, e23820.
- Reinkemeier, C.D., Girona, G.E., and Lemke, E.A. (2019). Designer membraneless organelles enable codon reassignment of selected mRNAs in eukaryotes. Science *363*.
- Rejman, J., Oberle, V., Zuhorn, I.S., and Hoekstra, D. (2004). Size-dependent internalization of particles via the pathways of clathrin- and caveolae-mediated endocytosis. Biochem J *377*, 159-169.
- Romoren, K., Thu, B.J., Bols, N.C., and Evensen, O. (2004). Transfection efficiency and cytotoxicity of cationic liposomes in salmonid cell lines of hepatocyte and macrophage origin. Biochim Biophys Acta *1663*, 127-134.
- Rossjohn, J., Gras, S., Miles, J.J., Turner, S.J., Godfrey, D.I., and McCluskey, J. (2015). T Cell Antigen Receptor Recognition of Antigen-Presenting Molecules. Annual Review of Immunology *33*, 169-200.
- Rustom, A., Saffrich, R., Markovic, I., Walther, P., and Gerdes, H.H. (2004). Nanotubular highways for intercellular organelle transport. Science *303*, 1007-1010.
- Santiago-Dieppa, D.R., Steinberg, J., Gonda, D., Cheung, V.J., Carter, B.S., and Chen, C.C. (2014). Extracellular vesicles as a platform for 'liquid biopsy' in glioblastoma patients. Expert Rev Mol Diagn *14*, 819-825.
- Sebastian, A., Syed, F., McGrouther, D.A., Colthurst, J., Paus, R., and Bayat, A. (2011). A novel in vitro assay for electrophysiological research on human skin fibroblasts: degenerate electrical waves downregulate collagen I expression in keloid fibroblasts. Exp Dermatol *20*, 64-68.
- Sercombe, L., Veerati, T., Moheimani, F., Wu, S.Y., Sood, A.K., and Hua, S. (2015). Advances and Challenges of Liposome Assisted Drug Delivery. Front Pharmacol *6*, 286.
- Shannon, C.E. (1948). A mathematical theory of communication. The Bell System Technical Journal *27*, 379-423.
- Shen, B., Fang, Y., Wu, N., and Gould, S.J. (2011). Biogenesis of the posterior pole is mediated by the exosome/microvesicle protein-sorting pathway. J Biol Chem *286*, 44162-44176.

- Shi, H.P., Fishel, R.S., Efron, D.T., Williams, J.Z., Fishel, M.H., and Barbul, A. (2002). Effect of supplemental ornithine on wound healing. J Surg Res *106*, 299-302.
- Shibuya, S., Yamamoto, T., and Itano, T. (2009). Glial and axonal regeneration following spinal cord injury. Cell Adh Migr *3*, 99-106.
- Shim, J.-u., Ranasinghe, R.T., Smith, C.A., Ibrahim, S.M., Hollfelder, F., Huck, W.T.S., Klenerman, D., and Abell, C. (2013). Ultrarapid Generation of Femtoliter Microfluidic Droplets for Single-Molecule-Counting Immunoassays. ACS Nano *7*, 5955-5964.
- Shiue, S.J., Rau, R.H., Shiue, H.S., Hung, Y.W., Li, Z.X., Yang, K.D., and Cheng, J.K. (2019). Mesenchymal stem cell exosomes as a cell-free therapy for nerve injury-induced pain in rats. Pain *160*, 210-223.
- Shui, L., van den Berg, A., and Eijkel, J.C.T. (2011). Scalable attoliter monodisperse droplet formation using multiphase nano-microfluidics. Microfluidics and Nanofluidics *11*, 87-92.
- Sigal, A., Bleijs, D.A., Grabovsky, V., van Vliet, S.J., Dwir, O., Figdor, C.G., van Kooyk, Y., and Alon, R. (2000). The LFA-1 integrin supports rolling adhesions on ICAM-1 under physiological shear flow in a permissive cellular environment. J Immunol *165*, 442-452.
- Simmel, F.C. (2019). Synthetic organelles. Emerging Topics in Life Sciences *3*, 587-595.
- Smith, B.R., and Gambhir, S.S. (2017). Nanomaterials for In Vivo Imaging. Chemical Reviews *117*, 901-986.
- Sofou, S., and Sgouros, G. (2008). Antibody-targeted liposomes in cancer therapy and imaging. Expert opinion on drug delivery *5*, 189-204.
- Staufer, O., Hernandez, B.J., and Rustom, A. (2018). Protease-resistant cell meshworks: An indication of membrane nanotube-based syncytia formation. Exp Cell Res *372*, 85-91.
- Staufer, O., Schroter, M., Platzman, I., and Spatz, J.P. (2020). Bottom-Up Assembly of Functional Intracellular Synthetic Organelles by Droplet-Based Microfluidics. Small, e1906424.
- Steenbeek, S.C., Pham, T.V., de Ligt, J., Zomer, A., Knol, J.C., Piersma, S.R., Schelfhorst, T., Huisjes, R., Schiffelers, R.M., Cuppen, E.*, et al.* (2018). Cancer

cells copy migratory behavior and exchange signaling networks via extracellular vesicles. The EMBO journal *37*.

- Stickney, Z., Losacco, J., McDevitt, S., Zhang, Z., and Lu, B. (2016). Development of exosome surface display technology in living human cells. Biochem Biophys Res Commun *472*, 53-59.
- Stoeckli, E.T., and Landmesser, L.T. (1995). Axonin-1, Nr-CAM, and Ng-CAM play different roles in the in vivo guidance of chick commissural neurons. Neuron *14*, 1165-1179.
- Street, J.M., Koritzinsky, E.H., Glispie, D.M., and Yuen, P.S.T. (2017). Urine Exosome Isolation and Characterization. Methods Mol Biol *1641*, 413-423.
- Stuffers, S., Sem Wegner, C., Stenmark, H., and Brech, A. (2009). Multivesicular endosome biogenesis in the absence of ESCRTs. Traffic *10*, 925-937.
- Suk, J.S., Xu, Q., Kim, N., Hanes, J., and Ensign, L.M. (2016). PEGylation as a strategy for improving nanoparticle-based drug and gene delivery. Advanced drug delivery reviews *99*, 28-51.
- Tabrizi, M., Bornstein, G.G., and Suria, H. (2010). Biodistribution mechanisms of therapeutic monoclonal antibodies in health and disease. Aaps j *12*, 33-43.
- Termini, C.M., and Gillette, J.M. (2017). Tetraspanins Function as Regulators of Cellular Signaling. Front Cell Dev Biol *5*, 34.
- Thakur, B.K., Zhang, H., Becker, A., Matei, I., Huang, Y., Costa-Silva, B., Zheng, Y., Hoshino, A., Brazier, H., Xiang, J.*, et al.* (2014). Double-stranded DNA in exosomes: a novel biomarker in cancer detection. Cell Res *24*, 766-769.
- Thayanithy, V., Dickson, E.L., Steer, C., Subramanian, S., and Lou, E. (2014). Tumor-stromal cross talk: direct cell-to-cell transfer of oncogenic microRNAs via tunneling nanotubes. Transl Res *164*, 359-365.
- Thery, C., Witwer, K.W., Aikawa, E., Alcaraz, M.J., Anderson, J.D., Andriantsitohaina, R., Antoniou, A., Arab, T., Archer, F., Atkin-Smith, G.K.*, et al.* (2018). Minimal information for studies of extracellular vesicles 2018 (MISEV2018): a position statement of the International Society for Extracellular Vesicles and update of the MISEV2014 guidelines. J Extracell Vesicles *7*, 1535750.
- Thompson, A.M., Paguirigan, A.L., Kreutz, J.E., Radich, J.P., and Chiu, D.T. (2014). Microfluidics for single-cell genetic analysis. Lab Chip *14*, 3135-3142.

- Tian, L., Li, M., Patil, A.J., Drinkwater, B.W., and Mann, S. (2019). Artificial morphogen-mediated differentiation in synthetic protocells. Nat Commun *10*, 3321.
- Tian, Y., Li, S., Song, J., Ji, T., Zhu, M., Anderson, G.J., Wei, J., and Nie, G. (2014). A doxorubicin delivery platform using engineered natural membrane vesicle exosomes for targeted tumor therapy. Biomaterials *35*, 2383-2390.
- Tiruvayipati, S., Wolfgeher, D., Yue, M., Duan, F., Andrade, J., Jiang, H., and Schuger, L. (2020). Variability in protein cargo detection in technical and biological replicates of exosome-enriched extracellular vesicles. PLoS One *15*, e0228871.
- Trajkovic, K., Hsu, C., Chiantia, S., Rajendran, L., Wenzel, D., Wieland, F., Schwille, P., Brugger, B., and Simons, M. (2008). Ceramide triggers budding of exosome vesicles into multivesicular endosomes. Science *319*, 1244-1247.
- Trelis, M., Galiano, A., Bolado, A., Toledo, R., Marcilla, A., and Bernal, D. (2016). Subcutaneous injection of exosomes reduces symptom severity and mortality induced by Echinostoma caproni infection in BALB/c mice. Int J Parasitol *46*, 799-808.
- Valadi, H., Ekstrom, K., Bossios, A., Sjostrand, M., Lee, J.J., and Lotvall, J.O. (2007). Exosome-mediated transfer of mRNAs and microRNAs is a novel mechanism of genetic exchange between cells. Nat Cell Biol *9*, 654-659.
- van den Pol, A.N., di Porzio, U., and Rutishauser, U. (1986). Growth cone localization of neural cell adhesion molecule on central nervous system neurons in vitro. J Cell Biol *102*, 2281-2294.
- van Niel, G., Charrin, S., Simoes, S., Romao, M., Rochin, L., Saftig, P., Marks, M.S., Rubinstein, E., and Raposo, G. (2011). The tetraspanin CD63 regulates ESCRT-independent and -dependent endosomal sorting during melanogenesis. Dev Cell *21*, 708-721.
- van Niel, G., D'Angelo, G., and Raposo, G. (2018). Shedding light on the cell biology of extracellular vesicles. Nat Rev Mol Cell Biol *19*, 213-228.
- van Nies, P., Westerlaken, I., Blanken, D., Salas, M., Mencía, M., and Danelon, C. (2018). Self-replication of DNA by its encoded proteins in liposome-based synthetic cells. Nature Communications *9*, 1583.
- van Oppen, L.M.P.E., Abdelmohsen, L.K.E.A., van Emst-de Vries, S.E., Welzen, P.L.W., Wilson, D.A., Smeitink, J.A.M., Koopman, W.J.H., Brock, R., Willems,

P.H.G.M., Williams, D.S., *et al.* (2018). Biodegradable Synthetic Organelles Demonstrate ROS Shielding in Human-Complex-I-Deficient Fibroblasts. ACS Central Science *4*, 917-928.

- Vangasseri, D.P., Cui, Z., Chen, W., Hokey, D.A., Falo, L.D., Jr., and Huang, L. (2006). Immunostimulation of dendritic cells by cationic liposomes. Mol Membr Biol *23*, 385-395.
- Vasquez, C., Benamer, N., and Morley, G.E. (2011). The cardiac fibroblast: functional and electrophysiological considerations in healthy and diseased hearts. J Cardiovasc Pharmacol *57*, 380-388.
- Villarroya-Beltri, C., Gutierrez-Vazquez, C., Sanchez-Cabo, F., Perez-Hernandez, D., Vazquez, J., Martin-Cofreces, N., Martinez-Herrera, D.J., Pascual-Montano, A., Mittelbrunn, M., and Sanchez-Madrid, F. (2013). Sumoylated hnRNPA2B1 controls the sorting of miRNAs into exosomes through binding to specific motifs. Nat Commun *4*, 2980.
- Vishwakarma, M., Di Russo, J., Probst, D., Schwarz, U.S., Das, T., and Spatz, J.P. (2018). Mechanical interactions among followers determine the emergence of leaders in migrating epithelial cell collectives. Nat Commun *9*, 3469.
- Vogel, R., Pal, A.K., Jambhrunkar, S., Patel, P., Thakur, S.S., Reátegui, E., Parekh, H.S., Saá, P., Stassinopoulos, A., and Broom, M.F. (2017). High-Resolution Single Particle Zeta Potential Characterisation of Biological Nanoparticles using Tunable Resistive Pulse Sensing. Scientific reports *7*, 17479.
- Wang, F., Chen, L., Zhang, R., Chen, Z., and Zhu, L. (2014). RGD peptide conjugated liposomal drug delivery system for enhance therapeutic efficacy in treating bone metastasis from prostate cancer. Journal of Controlled Release *196*, 222-233.
- Wang, Q., Bosch, B.J., Vlak, J.M., van Oers, M.M., Rottier, P.J., and van Lent, J.W.M. (2016). Budded baculovirus particle structure revisited. J Invertebr Pathol *134*, 15-22.
- Wang, X., Tian, L., Du, H., Li, M., Mu, W., Drinkwater, B.W., Han, X., and Mann, S. (2019). Chemical communication in spatially organized protocell colonies and protocell/living cell micro-arrays. Chemical Science *10*, 9446-9453.
- Warner, A., and Mittag, J. (2012). Thyroid hormone and the central control of homeostasis. J Mol Endocrinol *49*, R29-35.

- Weiss, M., Frohnmayer, J.P., Benk, L.T., Haller, B., Janiesch, J.W., Heitkamp, T., Borsch, M., Lira, R.B., Dimova, R., Lipowsky, R.*, et al.* (2017). Sequential bottom-up assembly of mechanically stabilized synthetic cells by microfluidics. Nat Mater.
- Weiss, M., Tura, A., Kautzky-Willer, A., Pacini, G., and D'Argenio, D.Z. (2016). Human insulin dynamics in women: a physiologically based model. Am J Physiol Regul Integr Comp Physiol *310*, R268-274.
- Whitehead, B., Wu, L., Hvam, M.L., Aslan, H., Dong, M., Dyrskjøt, L., Ostenfeld, M.S., Moghimi, S.M., and Howard, K.A. (2015). Tumour exosomes display differential mechanical and complement activation properties dependent on malignant state: implications in endothelial leakiness. Journal of extracellular vesicles *4*, 29685-29685.
- Whitesides, G.M. (2006). The origins and the future of microfluidics. Nature *442*, 368-373.
- Wiklander, O.P., Nordin, J.Z., O'Loughlin, A., Gustafsson, Y., Corso, G., Mäger, I., Vader, P., Lee, Y., Sork, H., Seow, Y.*, et al.* (2015). Extracellular vesicle in vivo biodistribution is determined by cell source, route of administration and targeting. J Extracell Vesicles *4*, 26316.
- Xu, B.Y., Xu, J., and Yomo, T. (2019). A protocell with fusion and division. Biochem Soc Trans *47*, 1909-1919.
- Yamashita, T., Takahashi, Y., and Takakura, Y. (2018). Possibility of Exosome-Based Therapeutics and Challenges in Production of Exosomes Eligible for Therapeutic Application. Biol Pharm Bull *41*, 835-842.
- Yamashita, Y., Oka, M., Tanaka, T., and Yamazaki, M. (2002). A new method for the preparation of giant liposomes in high salt concentrations and growth of protein microcrystals in them. Biochimica et Biophysica Acta (BBA) - Biomembranes *1561*, 129-134.
- Yang, J.M., and Gould, S.J. (2013). The cis-acting signals that target proteins to exosomes and microvesicles. Biochem Soc Trans *41*, 277-282.
- Yerneni, S.S., Lathwal, S., Shrestha, P., Shirwan, H., Matyjaszewski, K., Weiss, L., Yolcu, E.S., Campbell, P.G., and Das, S.R. (2019). Rapid On-Demand Extracellular Vesicle Augmentation with Versatile Oligonucleotide Tethers. ACS Nano *13*, 10555-10565.

- Yu, B., Lee, R.J., and Lee, L.J. (2009). Microfluidic methods for production of liposomes. Methods Enzymol *465*, 129-141.
- Yue, K., Zhu, Y., and Kai, L. (2019). Cell-Free Protein Synthesis: Chassis toward the Minimal Cell. Cells *8*.
- Zakeri, A., Kouhbanani, M.A.J., Beheshtkhoo, N., Beigi, V., Mousavi, S.M., Hashemi, S.A.R., Karimi Zade, A., Amani, A.M., Savardashtaki, A., Mirzaei, E.*, et al.* (2018). Polyethylenimine-based nanocarriers in co-delivery of drug and gene: a developing horizon. Nano reviews & experiments *9*, 1488497-1488497.
- Zhang, B., Korolj, A., Lai, B.F.L., and Radisic, M. (2018). Advances in organ-on-a-chip engineering. Nature Reviews Materials *3*, 257-278.
- Zhang, S.J., Zou, M., Lu, L., Lau, D., Ditzel, D.A., Delucinge-Vivier, C., Aso, Y., Descombes, P., and Bading, H. (2009). Nuclear calcium signaling controls expression of a large gene pool: identification of a gene program for acquired neuroprotection induced by synaptic activity. PLoS Genet *5*, e1000604.
- Zheng, J., Lamoureux, P., Santiago, V., Dennerll, T., Buxbaum, R.E., and Heidemann, S.R. (1991). Tensile regulation of axonal elongation and initiation. J Neurosci *11*, 1117-1125.

7 Appendix

7.1 Abbreviations

aa – Amino acids
ATP – Adenosine tri-phosphate
BV – Baculoviruse
CD – Cluster of differentiation
cryoTEM – Cryogenic transmission electron microscopy
CRG – CellRox Green
CV – Coefficient of variation
DEG – Differentially expressed gene
DLS – Dynamic light scattering
DMEM – Dulbecco's Modified Eagle Medium
DNA – Deoxyribonucleic acid
DOBAQ – N-(4-carboxybenzyl)-dimethyl-2,3-bis(oleoyloxy)propan-1-aminium
dsDNA – Double-stranded DNA
dsGUV – Droplet-stabilized GUV
ED2 – Extracellular domain 2
EGFR – Epidermal growth factor receptor
ELISA – Enzyme-linked immunosorbent assay
ER – Endoplasmic reticulum
ESCRT – Endosomal sorting complex required for transport
EVs – Extracellular vesicles
FasL – Fas ligand
FC – Fold changes
FIA-MS – Flow Injection MS
fsEVs – Fully-synthetic extracellular vesicles
GFP – Green fluorescent protein
GLP1 – Glucagon-like peptide 1
GSEV – German Society of Extracellular Vesicles
GUV – Giant unilamellar vesicle
H/E – Haematoxylin/eosin
HIV – Human immunodeficiency virus

HPTS – 8-Hydroxypyrene-1,3,6-trisulfonic acid
HSC70 – Heat shock cognate 71 kDa
HSP70 – Heat shock 70 kDa protein
IC_{50} – Half maximal inhibitory concentration
ICAM – Intercellular adhesion molecule
IgG – Immunoglobulin G
ILV – Intraluminal vesicle
ISEV – International Society of Extracellular Vesicles
LC/MS – Liquid chromatography/ mass spectrometry
MHC – Major histocompatibility complex
miRISC – miRNA-induced silencing complex
miRNA – Micro RNA
mRNA – Messenger RNA
MS – Mass Spectrometry
MVB – Multivesicular bodies
MVs – Microvesicles
N.A. – Not applicable
NADH – Nicotinamide adenine dinucleotide
NASA – National Aeronautics and Space Administration
NCAM – Neuronal cell adhesion molecule
NHS – Hydroxysuccimid
NIH – National Institute of Health
npEGTA – Nitrophenyl EGTA
N.s. – Not significant
ODC – Ornithine decarboxylase
P_{adj} – Adjusted p-value
PAGE – Polyacrylamide gel electrophoresis
PBS – Phosphate buffered saline
PC – Principle component
PCR – Polymerase chain reaction
PDMS – Polydimethylsiloxan
PEG – Poly-ethylenglycol
PEI – Poly-ethylene-imine
PFA – Paraformaldehyde

PLL – Poly-L-lysine
pN – Piconewton
PS – Polystyrene
psi – Pound-force per square inch
QCM-D – Quartz crystal microbalance with dissipation monitoring
REF – Rat embryonic fibroblasts
RNA – Ribonucleic acid
ROS – Reactive oxygen species
rpm – Rounds per minute
SD – Standard deviation
SOs – Synthetic organelles
SM – Sphingomyelin
SUV – Small unilamellar vesicle
TCR – T-Cell Receptor
TEM – Transmission electron microscopy
tRNA – Transfer RNA
TSG – Tumour susceptibility gene
WGA – Wheat germ agglutinin
w/o – Water in oil

7.2 List of figures

7.3 List of tables